Dissertation

submitted to the

Combined Faculty of Natural Sciences and Mathematics of

the Ruperto Carola University Heidelberg, Germany

for the degree of

Doctor of Natural Sciences

Presented by

M.Sci. Matthew Boucher

born in Enfield, United Kingdom

Oral Examination: 16th November, 2021

Exploring combination treatment with a HER2 and a Pirin inhibitor in HER2-overexpressing breast cancer cells

Referees:

Prof. Dr. Stefan Wiemann

Dr. Alexander Aulehla

I would like to dedicate this thesis to Veronique Derndinger.

The most important result of my entire
scientific career was finding my best friend;
I love you very much.

Acknowledgements

There are many people that I would like to thank for making this PhD thesis possible, both on a scientific and personal level. First and foremost, I would like to thank my supervisor, **Martin Jechlinger** for engaging my scientific interest in this project, and his support and mentorship throughout my PhD studies. I would also like to thank the members of the Jechlinger lab for their encouragement and support. To **Marta Garcia Montero**, for showing me the ins and outs of the lab, for her humour, and friendship. To **Lucas Chaible**, for his supervision, showing me various practical techniques, and incredible barbeque food. To **Savannah Jackson**, for her fantastic and hilarious conversations over a cup of tea, and helping on humid afternoons in the mouse house. To **Ashna Alladin**, for her office chats and for her discussion about various scientific and practical questions. To **Ksenija Radic-Shechter** for her humour, support and scientific support. To **Sylwia Gawrzak**, for her support with scientific questions and practical techniques, and for engaging lunchtime conversations.

I want to thank the **EMBL Advanced Light Microscopy Facility**, specifically **Sabine Reither** for her help and training on the Leica SP8 DLS and Olympus ScanR, **Marco Lampe** for all of his help with the Leica SP8 DLS image deconvolution, and **Christian Ticher** for his help with establishing ImageJ programs such as the LazyRatioViewer and BigDataProcessor2, as well as his guidance and training for various elements of ImageJ-based image analysis.

I also want to thank **Joe Lewis** for his guidance for this project, specifically with regard to EMBL-703625. By extension, I want to thank the **EMBL Chemical Biology Core Facility** for producing EMBL-703625 and generating all the excellent data that a large part of this project was based off.

I want to thank the **EMBL GeneCore Facility**, and in particular, **Vladimir Benes** and **Laura Villacorta** for their guidance and assistance with my RNAseq experiments.

Thank you also to **Matt Rogon** for his consulting and help with the RNAseq analysis, and analysis with Cytoscape, as well as his guidance and training. By extension, I would like to thank the **Centre for Biomolecular Network Analysis** at EMBL.

I want to thank the members of my thesis advisory committee: **Alexander Aulehla, Pierre Neveu**, and **Stefan Wiemann** for their excellent guidance and support for the duration of my PhD. Thank you also to **Alexander Aulehla**, **Stefan Wiemann**, **Ursula Klingmüller**

and **Stefan Wölfl** for taking the time to be a part of my thesis defence committee.

I would like to thank all the organisers of the **19th EMBL International PhD Sympsosium** for helping me to organise a successful and engaging conference for attendees from all around the world. I also want to thank the **EMBL Graduate Office** for all of their help over the years, and all my various PhD student colleagues. Thank you to **Philipp Hoess** for helping with the German translation of this thesis abstract.

I want to also thank the **EMBL Health and Safety Office** and various individuals and departments who took a leadership role at EMBL during the COVID-19 pandemic, for their incredible organisation and diligence in ensuring our safety, allowing us to return to EMBL after the first lockdown to continue with our important experiments.

On a personal level, I want to thank my Mum, **Sally Boucher**, and my Dad, **Anthony Boucher** for their love and support to me through all of my education, starting from school, to university and finally through my PhD, and also for doing my laundry and buying me pies during my visits home. Thank you also to my sister, **Jessica Boucher** and my brother, **Thomas Boucher** for all of their support.

I also want to thank several people from my time at university in Nottingham for making it such an enjoyable experience and giving me a well needed balance between work and fun; people like **Alastair Gibbons, Victoria Foster, Emma Vincent, Hannah Jackson, James Gregory, Hugh Brash, Laura Millett, Ollie Steels, Simona Sevdina, Lisa Shraine, Joel Pope, Chris Stirrup** and **Ste Lawlor**.

From my time at The University of Nottingham, I would like to give a special and heartfelt thank you to **Rita Tewari**. Rita was my mentor throughout my four years at Nottingham, and coincidentally also my masters thesis supervisor. It is because of Rita's motivation, energy and critique that I gained the self confidence and motivation to pursue a PhD after my time at Nottingham finished. I am incredibly grateful. I am also very happy that we published work together that based off my masters research. By extension, I also want to thank the various members of Rita's lab that supported and helped me during my masters thesis, as well as the authors of our publication for their collaboration and input.

I would like to thank my friends from school: **Christopher Fidler, Damon Gray, Michael Grayston, Luke Howley** and **Robert Kuzik**. I'm very appreciative of your presence through thick and thin, for the evenings in my parents computer room drinking three ciders and playing on the PS4, and for only laughing at my small calves when I'm not there. I feel incredibly privileged to know that no matter how long and difficult the road ahead may appear, I can look to you for your example and how you live your lives, and think, "Well, it could be worse." I also want to thank **Sarah Irving** who was my biology teacher between the ages of 15-17. Her engaging lessons, coupled with lots of humour, helped me to decide that I wanted to study biology at a more advanced level.

I would also like to thank **Ute Kowalczyk-Lang** and **Stefan Lang** for the various weekend dinners and beers. Also thank you to my favourite four-legged friend **Nala** for all of the stink eye and sassiness.

Finally, I would like to thank my wonderful girlfriend, **Veronique Derndinger**. It is difficult to articulate in a few sentences how lucky and privileged I feel to have you in my life. Quite simply, I came to Heidelberg and met my best friend. Du machst mich sehr glücklich und ich liebe dich so sehr.

Abstract

HER2 over-expressing breast cancer (HER2+ BC) is an aggressive breast cancer subtype that is responsible for approximately 20% of overall cases. Targeted therapies have been developed against the HER2 driver oncogene which has significantly improved patient outcomes. However, HER2+ BC still has comparatively high rates of relapses following first-line neoadjuvant or adjuvant therapy, compared to other breast cancer sub-types. These relapses are characterised by a poor prognosis, and metastatic tumors (*de novo* origin or relapsed) are considered incurable. This presents a continued need to identify therapeutic drugs that can be administered alongside first-line HER2-targeted therapy to kill or prevent re-growth of residually surviving tumor cells in order to prevent subsequent relapses.

Pirin (encoded by PIR) is a comparatively under-characterised iron-binding protein that serves as a transcriptional regulator through interactions with NF-$\varkappa\beta$. It has been suggested in the literature as a potentially attractive target for cancer therapy. Preliminary functional characterisation of a pirin ligand generated and characterised by the EMBL Chemical Biology Core Facility (CBCF), named EMBL-703625, suggested anti-tumor efficacy and excellent *in vivo* tolerability in mice. Transcriptomic data from HeLa cells treated with EMBL-703625 from the EMBL-CBCF have identified multiple de-regulated cellular processes as a result of pirin inhibition, such as glycolysis and the expression of heat shock proteins. Many of these same processes have also been identified as mechanisms of treatment evasion or relapse in HER2-targeted therapy resistant breast cancer cells.

This project characterised treatment with EMBL-703625 alongside lapatinib, which is a clinically licensed HER2 tyrosine kinase inhibitor. Using a combination of biochemical assays, synergy modelling and transcriptomic experiments, we demonstrated that this combination synergistically reduces cell viability and increases toxicity in 3D grown, human, HER2-overexpressing breast cancer cell lines: BT-474 and SK-BR3. This appears to be conferred through their largely unique effects on the cell transcriptome. Additionally, it appears that this drug combination could also prevent re-growth of BT-474 cells following treatment removal. Experiments on tumor-inducible primary mouse mammary cells suggest that their combinatorial effect applies uniquely to neoplastically transformed cells. As well as this, it is possible that lapatinib and EMBL-703625 confer their synergy, in part, through glycolytic inhibition. One drug given after another may also enhance tumor killing, which could allow patients to potentially avoid more severe side effects compared

to simultaneous treatment.

Additionally, this project aimed to use light-sheet microscopy to characterize intercellular cell heterogeneity on a 3-dimensional spatial and temporal basis. This was performed through the light-sheet imaging of SK-BR3 cells transfected with a fluorescent sensor named SoNar[1], which reads out on the NAD+/NADH ratio of cells. Image analysis pipelines were established, with deconvolution of raw-light sheet images potentially allowing an understanding of cell-cell heterogeneity in the future.

Finally, as part of a parallel analysis with data generated in the Jechlinger Lab, an integrated metabolomic and transcriptomic analysis from experiments on tumor-inducible *in vitro* primary mouse mammary gland cells was performed. This highlighted potential cellular pathways and processes related to cell metabolism that could serve as nodes of vulnerability for residually surviving cells and/or tumor cells, which could inform on similar experimental strategies in the future.

Overall, these results provide pre-clinical data that could provide a rationale for the progression of combined HER2 and Pirin inhibition into a clinical setting, pending additional results from *in vivo* mouse experiments that are planned.

Zusammenfassung

HER2-positiver Brustkrebs (HER2+ BK) ist ein aggressiver Untertyp des Mammakarzinoms bei dem das HER2-Gen überexprimiert ist und der für ca. 20% der Gesamtfälle verantwortlich ist. Obwohl zielgerichtete Therapien gegen das HER2-Onkogen entwickelt wurden, wodurch sich die Behandlungsergebnisse für die Patientinnen deutlich verbessert haben, gibt es beim HER2+ BK immer noch relativ hohe Raten von Rückfällen nach einer neoadjuvanten oder adjuvanten Erstlinientherapie. Diese Rezidive sind von einer schlechten Prognose gekennzeichnet, und metastasierte Tumore (neu entstandene oder rezidivierte) gelten als unheilbar. Daher besteht weiterhin Bedarf an der Identifizierung von therapeutischen Medikamenten, die zusätzlich zur HER2-gerichteten Erstlinientherapie verabreicht werden können, um verbliebene überlebende Tumorzellen abzutöten oder deren erneutes Wachstum zu verhindern und damit weitere Rückfälle zu vermeiden.

Pirin (kodiert durch das Gen PIR) ist ein relativ unzureichend charakterisiertes eisenbindendes Protein, das durch Interaktionen mit NF-$\varkappa\beta$ als Transkriptionsregulator dient. Es wurde in der Literatur als potentiell attraktives Ziel für die Krebstherapie vorgeschlagen. Eine vorläufige funktionelle Charakterisierung eines Pirin-Liganden, der von der EMBL Chemical Biology Core Facility (CBCF) generiert und charakterisiert wurde und den Namen EMBL-703625 trägt, deutet auf eine anitumorale Wirksamkeit und eine sehr gute Verträglichkeit in Mäusen hin. Transkriptomische Daten von HeLa-Zellen, die mit EMBL-703625 aus der EMBL-CBCF behandelt wurden, haben mehrere deregulierte zelluläre Prozesse als Folge der Pirin-Inhibition identifiziert, wie z.B. die Glykolyse und die Expression von Hitzeschockproteinen. Viele dieser Prozesse wurden auch als Mechanismen identifiziert, die in Brustkrebszellen, die resistent gegenüber einer auf HER2 abzielenden Therapie sind, für einen Rückfall oder eine Umgehung der Behandlung sorgen.

Mithilfe einer Kombination aus biochemischen Testverfahren, Synergiemodellierung und Analyse des Transkriptoms wurde in diesem Projekt festgestellt, dass Lapatinib, ein klinisch zugelassener HER2-Tyrosinkinase-Inhibitor, bei gleichzeitiger Verabreichung mit EMBL-703625 die Zellviabilität synergistisch reduziert. Darüber hinaus sorgte das Zusammenwirken der beiden Wirkstoffe dafür, dass sich die Toxizität in zwei humanen HER2- überexprimierenden Brustkrebszelllinien (BT-474 und SK-BR3) erhöht, die in 3D-Zellkultur gezüchtet wurden. Diese Ergebnisse werden offenbar durch die größtenteils einzigartigen Effekte der beiden Medikamente auf das Transkriptom der Zellen bewirkt. Außerdem scheint es, dass diese Medikamentenkombination auch das erneute Wachstum von BT-

474-Zellen nach Ende der Behandlung verhindern kann. Experimente an tumorinduzierbaren primären Brustdrüsenzellen der Maus deuten darauf hin, dass die kombinatorische Wirkung ausschließlich auf neoplastisch transformierte Zellen entfaltet wird. Darüber hinaus ist es möglich, dass Lapatinib und EMBL-703625 ihre Synergie zum Teil durch die Inhibierung der Glykolyse vermitteln. Die sequenzielle Gabe der beiden Medikamente könnte die gleiche Wirkung wie die gleichzeitige Gabe haben, wodurch den Patientinnen schwere Nebenwirkungen erspart bleiben könnten.

Des Weiteren wurde in diesem Projekt die Lichtblattmikroskopie genutzt, um die Heterogenität zwischen verschiedenen Zellen auf 3-dimensionaler und zeitlicher Ebene zu charakterisieren. Dafür wurden SK-BR3-Zellen mit dem Fluoreszenzsensor SoNar[1], der das intrazelluläre NAD+/NADH-Verhältnis anzeigt, transfiziert und per Lichtblattmikroskopie untersucht. Für die Bildanalyse der so gewonnenen Daten wurden Pipelines etabliert, wobei die Dekonvolution der Roh-Mikroskopiedaten in Zukunft zum Verständnis der Zellheterogenität beitragen könnte.

Parallel dazu wurden experimentelle Daten aus dem Jechlinger-Labor, die an tumorinduzierbaren primären Brustdrüsenzellen von Mäusen in Zellkultur gewonnen wurden, mit Hilfe einer integrierten metabolomischen und transkriptomischen Analyse ausgewertet. Dabei hat sich herausgestellt, dass es zelluläre Vorgänge und Prozesse des Zellstoffwechsels gibt, die potenziell verwundbare zentrale Knotenpunkte für verbleibende überlebende Zellen und/oder Tumorzellen darstellen könnten. Darauf basierend könnten in der Zukunft ähnliche experimentelle Strategien aufgebaut werden.

Insgesamt beinhaltet diese Arbeit präklinische Daten, die eine Grundlage für die Weiterentwicklung der kombinierten HER 2 und Pirin Inhibition in eine klinische Umgebung darstellen könnten, unter der Voraussetzung, dass weitere Ergebnisse aus *in vivo* Experimenten an Mäusen vorliegen.

Contents

1 Introduction **21**

1.1 Introduction to Cancer . . . 22

1.2 Breast Cancer . . . 25

1.2.1 Introduction . . . 25

1.2.2 Anatomy of the breast . . . 26

1.2.3 Formation of breast cancer . . . 26

1.2.4 Sub-types of breast cancer . . . 28

1.3 HER2 driven breast cancer, therapeutic challenges and future perspectives . . . 30

1.3.1 Introduction . . . 30

1.3.2 The HER2 receptor: A member of the HER receptor family . . . 30

1.3.3 HER2 over-expression and induction of a neoplastic phenotype . . . 31

1.3.4 'Addiction' to the HER2 oncogene in HER2 overexpressing breast cancer . . . 33

1.3.4.1 Oncogene addiction . . . 33

1.3.4.2 Experimental evidence of 'addiction' to HER2 in HER2 overexpressing breast cancer . . . 33

1.3.5 Therapeutic exploitation of "addiction" to HER2 over-expression in breast cancer: Targeted therapies . . . 34

1.3.6 Therapeutic challenges: tumor relapse . . . 36

1.4 Tumor relapses after HER2-targeted therapy . . . 37

1.4.1 Tumor heterogeneity: a driving force behind tumor relapse . . . 37

1.4.2 A HER2 "blockade" as the current combination treatment strategy – successes and ongoing issues . . . 38

1.5 Resistance mechanisms of HER2+ breast cancer cells to current HER2-targeted treatment regimens . . . 40

1.5.1 Resistance mechanisms: Maintaining HER2 signalling through re-activation of downstream signalling pathways, or HER2 mutations . . . 40

1.5.2 Resistance mechanisms: Utilisation of "escape" pathways . . . 41

1.5.2.1 CDK4/6 expression . . . 41

1.5.2.2 HSP protein expression . . . 41

1.5.2.3 NF-$\kappa\beta$ signaling . . . 42

1.5.3 Resistance mechanisms: Altered metabolism . . . 42

1.5.3.1 Metabolism as a hallmark of cancer . . . 42

1.5.4 Altered metabolism in HER2 over-expressing breast cancer . . . 43

1.5.4.1 Altered metabolism as a route of therapeutic resistance to HER2-targeted therapy . . . 44

1.5.5 A lack of ongoing clinical trials combining HER2-targeted therapies in combination with non-HER2 targeted agents: an unmet need for reducing numbers of patient relapses . . . 45
1.6 Pirin inhibition alongside targeted HER2 therapy as a potential therapeutic regimen 47
1.6.1 Pirin: an iron-binding transcriptional regulator . . . 47
1.6.2 Pirin in cancer . . . 47
1.6.3 Development of a small molecule inhibitor of Pirin, EMBL-703625, by the EMBL-CBCF: promising anti-tumor activity, and a rationale for combination with HER2-targeted therapy in breast cancer . . . 48
1.7 Project Hypothesis and Aims . . . 50
1.7.1 Introduction summary and context for project hypothesis . . . 50
1.7.2 Project Hypothesis . . . 51
1.7.3 Project Aims . . . 51
1.8 Experimental systems used in this project: human HER2+ breast cancer cell lines and transgenic primary mouse mammary gland cells . . . 52
1.8.1 BT-474 and SK-BR3: human, HER2 over-expressing breast cancer cell lines 52
1.8.2 Transgenic, doxycycline inducible mouse primary cells . . . 53

2 Results and Discussion 55
2.1 Assessing combinatorial interactions between Lapatinib and EMBL-703625 in BT-474 and SK-BR3 cells . . . 56
2.1.1 Lapatinib and EMBL-703625 have a large combinatorial effect on cell viability over time . . . 56
2.1.2 Assessing drug synergy between lapatinib and EMBL-703625 in BT-474 and SK-BR3 cells . . . 59
2.1.2.1 The importance of testing for drug synergy, and synergy modelling strategies . . . 59
2.1.2.2 Experimental design to assess drug synergy between lapatinib and EMBL-703625 . . . 61
2.1.2.3 Lapatinib and EMBL-703625 synergistically affect cell viability in BT-474 and SK-BR3 cells . . . 64
2.1.3 Discussion of Section 2.1: synergy between lapatinib and EMBL-703625 . 69
2.1.4 Future experiments (with relevance to results discussed in Section 2.1.2) . 70
2.2 Transcriptomic data reveal fundamental differences between the actions of lapatinib and EMBL-703625 on BT-474 and SK-BR3 cells, and a large combined effect . . . 71
2.2.1 Rationale and experimental design . . . 71
2.2.2 Variance Stabilising Transformation of count data and sample-to-sample relationships . . . 72
2.2.3 Lapatinib and EMBL-703625 have largely independent effects on gene expression . . . 76
2.2.4 Pathway analysis of transcriptomic data . . . 80
2.2.5 De-regulated pathways associated with cancer hallmarks are higher in combination treatment, compared to lapatinib or EMBL-703625 monotherapy . 83
2.2.6 Discussion of Section 2.2: Distinct effects of lapatinib and EMBL-703625, and a large combination effect . . . 85
2.2.6.1 General context and therapeutic implications . . . 85
2.2.6.2 De-regulated pathways . . . 86
2.2.7 Future experiments (with relevance to results discussed in Section 2.2) . . 88

2.3 Assessing the ability of BT-474 or SK-BR3 cells to re-grow following lapatinib or EMBL-703625 monotherapy, or in combination 89
2.3.1 Experimental design and rationale 89
2.3.2 Imaging of cell regrowth using high throughput imaging on the Olympus ScanR 89
2.3.3 EMBL-703625 and Lapatinib act together to compromise the ability of BT-474 cells to re-grow after treatment removal 90
2.3.4 Discussion of Section 2.3: Lapatinib and EMBL-703625 inhibit re-growth in BT-474 cells when in combination, but not in SK-BR3 93
2.3.4.1 Discussion of results 93
2.3.4.2 Extrapolation of re-growth results into a clinical setting: *in vivo* considerations, and experimental future directions 94
2.3.5 Future experiments (with relevance to results discussed in Section 2.3). . . 96
2.4 Co-inhibition of cellular glycolysis alongside HER2 or Pirin inhibition 97
2.4.1 Oxamate and EMBL-703635 show strong synergy together in reducing the viability of BT-474 and SK-BR3 cells 97
2.4.2 Discussion of Section 2.4: Inhibition of pirin and glycolysis show strong synergy in BT-474 and SK-BR3 cells, inhibition of HER2 alongside glycolysis shows additivity 101
2.4.3 Future experiments (with relevance to results discussed in Section 2.4) . . 102
2.5 Comparison of the response of non-neoplastic and neoplastic mouse mammary cells treated with lapatinib and/or EMBL-703625 103
2.5.1 Combination treatment with lapatinib and EMBL-703625 more strongly reduces viability in induced primary mouse mammary tumor cells, compared to never induced mammary cells 103
2.5.2 Discussion of Section 2.5: Experiments on mouse-derived primary cells suggest a preferential effect on neoplastically transformed cells, compared to normal 107
2.5.3 Future experiments (with relevance to results discussed in Section 2.5) . . 108
2.6 Consecutive treatment 109
2.6.1 BT-474 cells are sensitised to pirin inhibition following treatment with lapatinib110
2.6.2 BT-474 cells begin to lose sensitivity to HER2-targeted therapy after initial treatment, whereas SK-BR3 cells do not 111
2.6.3 Discussion of Section 2.6: Lapatinib may sensitise BT-474 cells to subsequent EMBL-703625 treatment 112
2.6.4 Future experiments (with relevance to results discussed in Section 2.6) . . 114
2.7 Establishment of a spatial and temporal light microscopy pipeline, aimed at assessing intercellular metabolic heterogeneity via the use of a fluorescent metabolic sensor115
2.7.1 The SoNar Sensor: a sensor for the cytosolic NAD+/NADH ratio 116
2.7.2 Establishment of SK-BR3 and BT-474 stably expressing SoNar and cpYFP using lentiviral transfection 117
2.7.3 Light-sheet imaging of the SoNar sensor on the Leica SP8 DLS 118
2.7.4 Development of a mounting method to allow multi-positioning light-sheet imaging 119
2.7.5 Image analysis workflow 120
2.7.6 Establishment of an automated big data image analysis pipeline 121
2.7.6.1 Processing of raw data to workable sizes 121
2.7.6.2 Ratiometric viewing using lazy loading: The Lazy Ratio Viewer . . 123
2.7.6.3 Image artefact correction and noise reduction: 3D mean blurring . 124

2.7.6.4 Generalised image analysis: Generation of histograms and normalised means . . . 125
2.7.7 Testing and characterising the functionality of the SoNar sensor with a oxamate, known NAD+/NADH ratio reducing agent . . . 126
2.7.8 Lapatinib treatment at close to IC50 concentrations reduces the NAD+/NADH ratio of SK-BR3 cells over time . . . 129
2.7.9 Lapatinib and EMBL-703625 act synergistically to reduce the NAD+/NADH ratio of SK-BR3 cells . . . 130
2.7.10 Image fusion and deconvolution, aimed to be able to improve image resolution to visualise cell-cell heterogeneity . . . 133
2.7.10.1 Background and Theory . . . 133
2.7.10.2 Image deconvolution is able to better resolve cells in 3D . . . 134
2.7.11 Discussion of Section 2.7: Light-sheet imaging of breast cancer cells to obtain a spatial and temporal read-out of the redox status of cells on cell-cell resolution . . . 136
2.7.11.1 Discussion of results and further directions to further develop and optimise the microscopy and image analysis pipeline . . . 136
2.7.11.2 Other possible future uses for the SoNar sensor, or similar sensors 137
2.8 Changes in tumor cells and during the formation of minimal residual disease . . . 139
2.8.1 Gene expression changes during tumor regression towards a residual state 139
2.8.2 Residual cells resemble tumors, but have a unique metabolic phenotype . 147
2.8.3 Discussion of section 2.8: Metabolic differences of tumor and residual cells, compared to normally mammary epithelial cells . . . 151
2.8.3.1 Sugar metabolism: potential shifting towards an altered state of sugar metabolism in residual cells . . . 151
2.8.3.2 Sugar metabolism: up-regulation of keratan sulfate biosynthesis in tumor and residual cells . . . 152
2.8.3.3 Amino acid metabolism: potential for a deregulated urea cycle contributing to HER2+ breast cancer relapses . . . 152
2.8.3.4 Mitophagy: a source of macromolecule production as cells enter a residual state . . . 153
2.8.3.5 TGF-β and FoxO signalling pathways: regulators of tumor metabolism153

3 General Discussion and Future Perspectives 155
3.1 Recap and overview of results . . . 156
3.2 Future directions: Characterising synergy between dual HER2 and Pirin inhibition, or pirin inhibition monotherapy across other cancer types . . . 157
3.2.1 Multiple different tumor types over-express or express HER2 and therefore could be susceptible to dual HER2 and pirin inhibition . . . 157
3.2.1.1 An example of a cancer type that dual HER2 and Pirin inhibition may benefit: Non-Small Cell Lung Cancer . . . 158
3.2.2 Evidence to support further characterisation of pirin inhibiton in monotherapy, or alongside other targeted treatments, across multiple tumor types . . 159
3.2.3 Methods to characterise HER2 and Pirin inhibition across other tumor types 160
3.2.3.1 Cell lines . . . 160
3.2.3.2 *In vivo* approaches . . . 160
3.2.4 Patient-derived organoids . . . 161
3.3 Future directions: Single cell -omics based approaches to understand cell heterogeneity in response to drug treatment . . . 161

3.4 Future directions: Progressing with HER2 and Pirin inhibition into a clinical setting 162
3.4.1 HER2+ breast cancer clinical trials involving Pirin inhibiton 162

4 Materials and Methods 165
4.1 Biochemical Assays 166
4.1.1 Cell Toxicity Assay 166
4.1.2 3D Cell Viability Assay 166
4.2 General cloning methods 166
4.2.1 Restriction Digestions 166
4.2.2 Ligation Reactions 167
4.2.3 Heat Shock Transformation of competent *E. coli* 167
4.3 Transfection and imaging of the SoNar Sensor in SK-BR3 cells 168
4.3.1 Cloning of lentiviral vectors to generate SoNar or cpYFP-expressing BT-474 and SK-BR3 cells 168
4.3.2 Production and counting of lentiviral particles for transduction 168
4.3.3 Production and counting of lentiviral particles for transduction 169
4.4 Light-sheet Microscopy on the Leica SP8 DLS 169
4.4.1 Mounting for Light-Sheet Microscopy 169
4.4.2 Light-sheet imaging on the Leica SP8 DLS 169
4.5 Cell Lines 170
4.5.1 Cell line authentication 170
4.5.2 Culturing of cell lines (2D) 170
4.5.2.1 Media 170
4.5.2.2 Passaging 170
4.5.2.3 Generating liquid nitrogen stocks of cell lines or primary mouse cells 170
4.6 Mouse Genotyping 171
4.7 Harvesting of primary mouse mammary gland cells and culturing 171
4.7.1 3D seeding of Cell lines 172
4.7.2 3D seeding of primary mouse cells 172
4.7.3 High-throughput seeding 173
4.7.4 Re-seeding of cell lines for re-growth experiments 173
4.7.5 High throughput imaging: Olympus ScanR 173
4.8 Transcriptomic experiments 174
4.8.1 RNA isolation, processing and analysis 174
4.8.2 Transcriptomic Data analysis 174
4.8.3 Image fusion and deconvolution 174
4.9 Inhibitors: lapatinib, EMBL-703625 and Oxamate 175
4.10 Analysis and integration of GCMS, LCMS and transcriptomic data 175

5 Supplementary Figures 177

Bibliography 232

List of Tables 233

List of Figures 237

List of Abbreviations 239

Chapter 1

Introduction

1.1 Introduction to Cancer

Cancer is a disease caused by the uncontrolled division of abnormal cells in the body. This is due to the accumulation of genetic mutations, which usually occur gradually over time, making cancer generally an age related disease. However, certain factors can increase the rate of gain of these mutations. For example, DNA damaging agents (mutagens) such as those found in tobacco smoke which cause some forms of lung cancer, or ultraviolet light causing some forms of melanoma. They can also include signalling molecules, such as the presence of estrogen in the blood, which is majorly implicated in many subtypes of breast cancer. Additionally, certain bacteria and viruses can also lead to cancers. For example, *Helicobacter pylori* is associated with forms of stomach cancer[2], and Human Papilloma Virus is associated with forms of cervical cancer[3]. Background genetic factors also play a role in increasing or decreasing each individuals lifetime likelihood of developing particular cancers. In the vast majority of individuals, their overall genetic profile is likely to increase or decrease their predisposition for a lifetime risk of a certain cancer. However, there are certain examples of inherited genetic mutations which can drastically increase an individuals chance of developing a certain cancer in their lifetimes. For example, mutations in the RB1 gene significantly increase incidences of childhood retinoblastoma, often occurring in both retinas of a patient (bilateral retinoblastoma)[4], or mutations in the DNA repair BRCA1 or BRCA2 genes, which are associated with heritable forms of breast and ovarian cancer[5].

Whatever their causes, these mutations can alter the fundamental characteristics of these cells. Mutations that cause increased cell growth and division rates, decreased responsiveness to apoptotic signals, or increased genomic instability, can in turn increase the probability of these cells to gain further mutations. In this regard, cancer cell evolution has many parallels with Darwinian evolution; cells that have acquired mutations that increase survival probability (“fitter” from an evolutionary perspective) are more likely to become over-represented in their cellular niche, in turn, meaning they are more likely to acquire further mutations that could further increase their survival probability[6]. The mutations in these cells can accumulate to the extent that they become unresponsive to normal cell cycle regulatory mechanisms, both intrinsic and extrinsic, become immortalised, and divide in an unregulated fashion, to form a growth of cells called a hyperplasia. As genetic mutations further accumulate and the phenotypic characteristics of these cells are further altered, these cells can gain invasive properties through a loss of cell polarity and adhesion, and become more de-differentiated, with an altered cellular metabolism and cell signalling, which can allow them to evade immune responses and recruit new blood vessels (known as angiogenesis). This can lead them to leave their primary site and be able to invade and divide in surrounding tissues and, eventually, other organs, which is known as metastasis. Acquiring these invasive properties along with uncontrolled division and immortality is referred to as a neoplastic phenotype. Cells that have acquired a neoplastic phenotype are defined as cancerous.

The phenotypic differences that cancer cells have, relative to normal cells, are often re-

ferred to as cancer cell hallmarks (summarised in Figure 3). Each of these hallmarks can be considered a way that cancer cells are able to gain a selective growth advantage over their normal counterparts; in combination they come together to be permissive of a neoplastic phenotype. These neoplastic characteristics allow them to eventually grow and migrate around the body which can lead to severe patient health problems. tumors can grow and migrate to an extent that they can block capillaries and compromise organ function, and/or lead to cachexia (body wasting due to competition for nutrients). In turn, this leaves the patient vulnerable to secondary infections, internal bleeding, anaemia and loss of pharmacological homeostasis. Combinations of these symptoms can eventually lead to patient death.

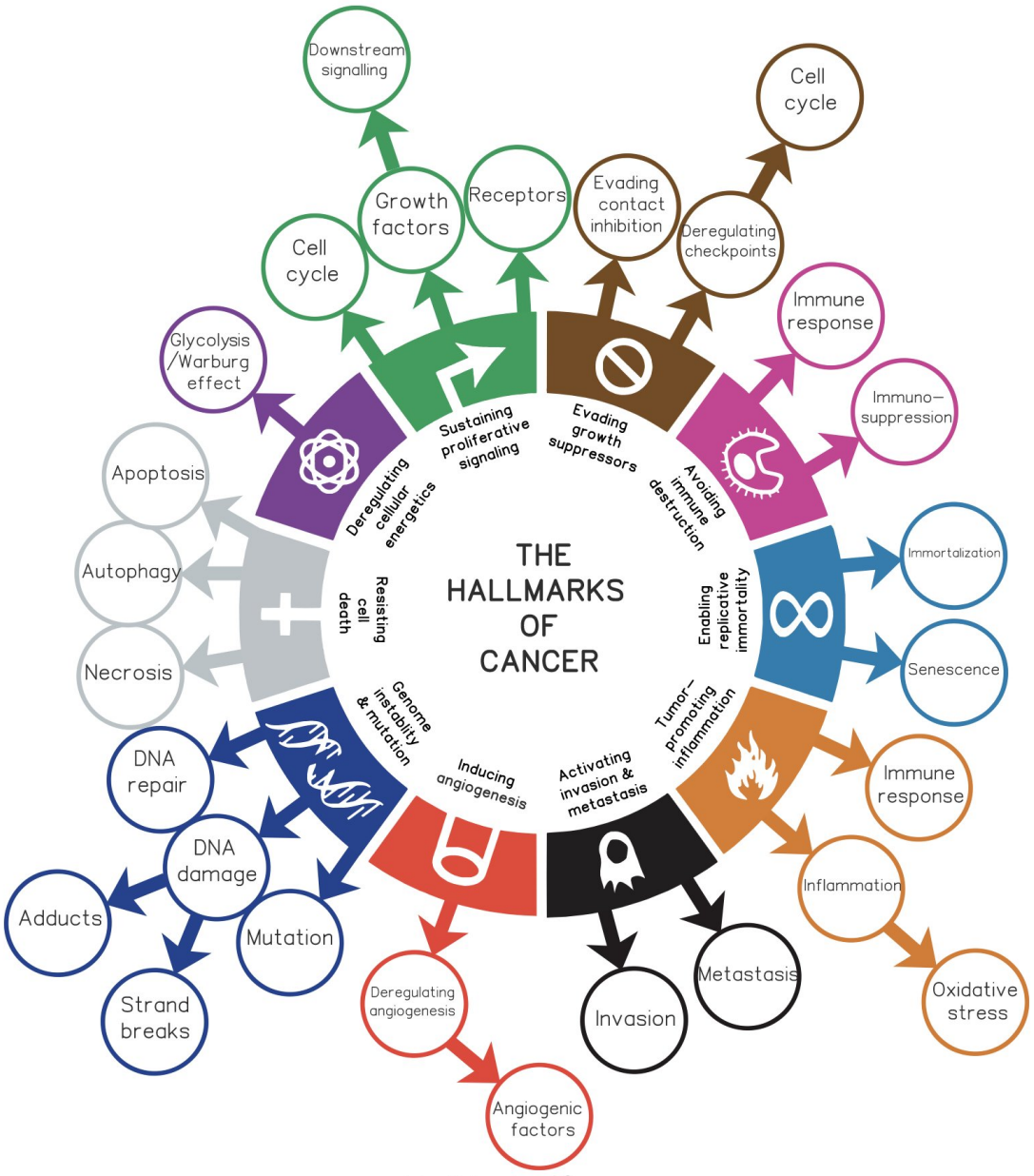

Figure 1: **The hallmarks of cancer, with examples of sub-hallmarks (outer circle).** Although the hallmarks are not unanimously agreed on, and definitions may differ between driving hallmarks and "passenger" hallmarks, a combination of these hallmarks can cause a cancerous phenotype to develop. Figure adapted from Ref.[7].

Significant amounts of biological and clinical research have gone into slowing or stopping cancer progression. The first modern anti-cancer therapies are now often referred to as “shotgun” therapies, because they targeted actively proliferating cells, not delineating between cancerous cells and normal “healthy” cells, therefore often causing significant side effects in a patient. This originally involved radiation therapy and later chemotherapy to induce DNA damage in actively dividing cells, leading to mitotic catastrophe. These treatments were, and often still are, in combination with surgery (where possible). As scientific understanding has improved, cancer therapy has gradually begun to take on more patient tailored approaches, which is based on the unique complement of mutations, and phenotypic characteristics that each patient has, in order to capitalise on their altered cancer hallmarks, which can provide cancer-specific vulnerabilities. As specific molecular drivers of a cancer-like phenotypes, called oncoproteins (coded for by oncogenes) have been identified and characterised, therapeutics that specifically target these drivers have also been developed and used in the clinic; this is often referred to as targeted therapy.

To further increase treatment effectiveness, modern therapies are often administered to patients in combination to elicit the largest tumor killing effects, whilst minimising adverse side-effects[8], which is known as combination therapy. Also, in general, identifying cancers at an earlier stage is associated with an improved prognosis, which has led to research into diagnostic procedures, resulting in improvements in this area too[9]. Alongside these biological and diagnostic improvements, better surgical techniques have also further improved treatment effectiveness[10]. Because of a combination of these reasons, cancer death rates have decreased. Across all cancers, races and ages, overall US yearly death rates per 100,000 people decreased by 17.4% between 1953 and 2013[11].

Despite these improvements, cancer is still a major worldwide killer, being responsible for approximately 9.5 million worldwide deaths in 2018[12]. As the human population becomes proportionally older, it is likely that cancer will affect an increasing number of people in their lifetime, meaning that there is a need to continue improving cancer treatment[13]. In this regard, there remain significant clinical challenges that still need to be addressed; many patients have cancers that are still able to progress, despite treatment, and eventually lead to death. One prominent issue is tumor recurrence, where a tumor returns after apparently successful initial treatment, leading to significant research efforts to identify mechanisms behind this, and develop therapeutics aimed at reducing or eliminating this risk. Prevention of tumor recurrences will form a major part of the discussion of this thesis, in the context of HER2 over-expressing breast cancer.

1.2 Breast Cancer

1.2.1 Introduction

Breast cancer is formed by tumors developing in the glandular tissues in the breast, most commonly from the milk producing mammary epithelium. Breast cancer can occur in both sexes, but over 99% of cases occur in women. It is the most common form of female cancer worldwide, accounting for approximately 2.08 million new cases in 2018, and approximately 627,000 deaths in the same year (11.6% of all worldwide cancer-related deaths)[12].

Apart from 5-10% of cases that are caused by inherited genetic mutations (such as BRCA1 and BRCA2 mutations)[5], breast cancers primarily occur due to an accumulation of mutations over time, primarily in epithelial cells lining the ducts and lobules of the glandular tissues in the breast (responsible for producing milk after childbirth).

Breast cancer incidence is primarily associated with age, but lifetime probability of developing breast cancer is also influenced by higher long-term levels of the sex hormones estrogen and progesterone, which can occur through lifestyle based factors such as obesity, estrogen based therapies or having more lifetime estrous cycles because of a lack of pregnancies and breastfeeding, or due to biological factors, such as a late menopause[14]. These hormones are thought to increase breast cancer incidence because they induce proliferation of the mammary epithelium, leading to a higher probability of mutational acquisition after cell division. It is also possible that the presence of hormones such as estrogen can also have chemical effects aside of their normal receptor based signalling, that could also increase the rate of DNA damage[15].

Because of the close association of the growth dynamics of the mammary epithelium with hormonal cues, breast cancers are often found to be associated with the over-expression or mutation of the cell surface receptors, such as the estrogen receptor (ER), progesterone receptor (PR) and Human Epidermal Growth Factor Receptor 2 (HER2). The presence of different combinations of these receptors often form the basis for different molecular sub-classifications of breast cancer, which are further discussed in Section 1.2.4.

In the developed world, across all sub-types, 5-year survival rates are currently around 80-90%, improving from approximately 75% in the 1970's[11]. Research by Narod *et al.* (2015)[16] suggested that this is mainly due to improved treatment. Notably, the development of targeted therapies (for example, tamoxifen targeting the estrogen receptor, or trastuzumab (Herceptin®) targeting the HER2 receptor) has led to demonstrable increases in patient prognosis, particularly for primary cancers that have not yet metastasised. Less improvement has been demonstrated in patients with recurrent or metastatic tumors[16].

1.2.2 Anatomy of the breast

In order to understand how breast cancer first forms, it is important to consider the structure and function of the breast, particularly in the context of hormonal signalling. The female breast primarily consists of adipose (fatty) tissue and glandular tissue, the latter of which functions to produce milk in women following childbirth. In the glandular tissue, milk is produced in the lobules, which consist of a cluster of acini. Surrounding each acinus are luminal and myo-epithelial cells. Luminal cells function to produce milk, whereas myo-epithelial cells act to contract, forcing the milk out of the lobule. From the lobule, milk travels through the extra-lobular terminal duct, which connects it to the main duct, which leads to the nipple. Each breast contains approximately 40 lobules.

These functional units of the breast are also known as Terminal Ductal Lobular Units (TDLU's). Each TDLU is surrounded by a layer basement membrane, contractile myo-epithelial cells and luminal epithelial cells. The myo-epithelial cells serve to allow contraction, pushing the milk out of the lobule and into the duct, and the milk itself is produced in the luminal epithelial cells.

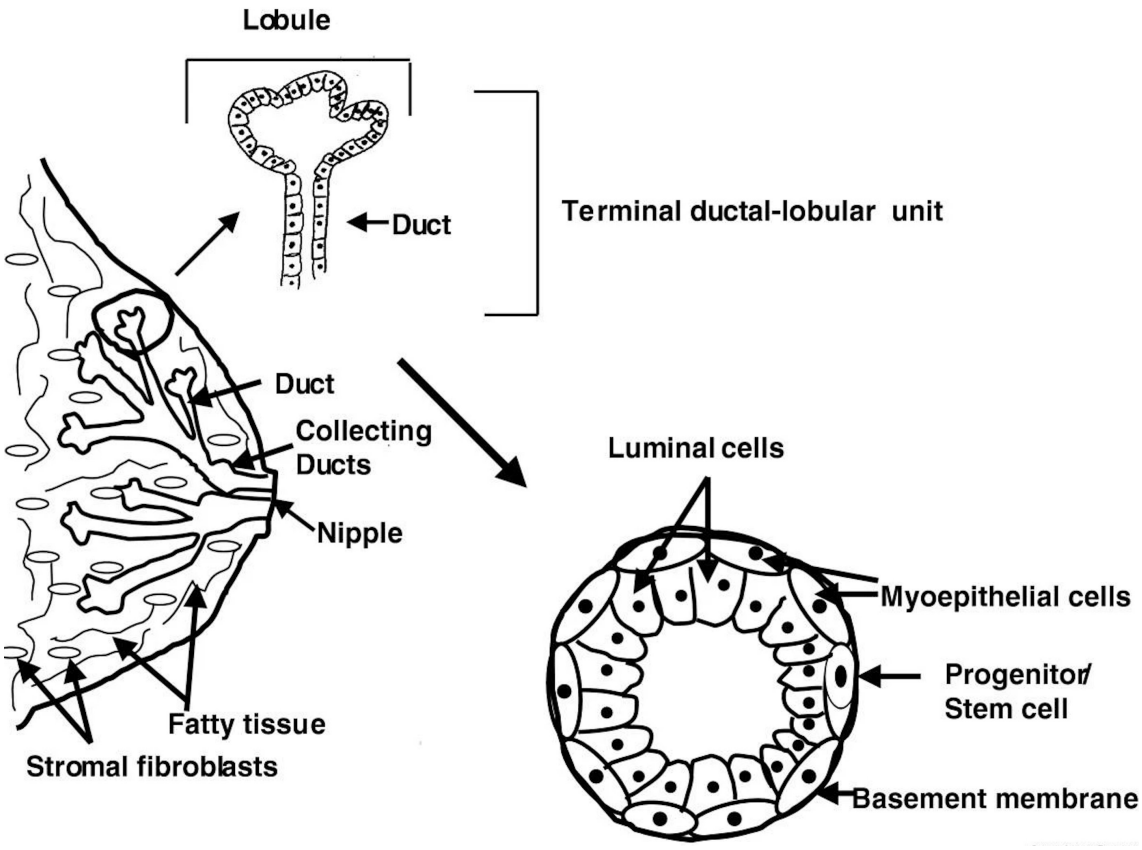

Figure 2: Cross sections showing the anatomy of the breast, Terminal Ductal Lobular Units and the cell types in a duct or lobule. Adapted from Pluchinotta *et al.,* (2015)[17].

1.2.3 Formation of breast cancer

Luminal cells in the TDLUs that have undergone malignant transformation lead to invasive breast cancer. In the majority of breast cancer cases, tumors originate from luminal ep-

ithelial cells in the mammary ducts or lobules. As these cells gain mutations that promote increased rates of division and acquisition of DNA damage, they increase in numbers, often forming a hyperplasia. Further genetic mutations can lead to changes in phenotypic properties of these cells, for example, a loss of E-cadherin, which leads to the formation of an atypical hyperplasia[18]. In a clinical setting, individuals diagnosed with an atypical hyperplasia are considered at a higher risk of developing breast cancer and are often subjected to further tests. An atypical hyperplasia can continue to divide, and acquire further mutations and undergo resulting phenotypic changes to form a cancerous growth that has not yet invaded surrounding tissues. This can form in the mammary ducts, or in the lobules. These are known as Ductal Carcinoma In Situ or Lobular Carcinoma In Situ (DCIS and LCIS, respectively).

DCIS may remain in a non-invasive state and never undergo a full malignant transformation to give rise to a invasive breast tumor, but are considered precursors to an invasive state that has been able to infiltrate local surrounding tissues, known as invasive ductal carcinomas (IDC). These invasive properties mean that IDC's are considered to be in a full cancerous state, and account for approximately 80% of breast cancer cases[19]. LCIS, however, is unlikely to follow a similar trajectory; the majority of invasive lobular carcinomas originate as a DCIS. However, the presence of a LCIS is considered to be indicative of a risk for eventual breast tumor formation, as it is possibly reminiscent of the fact that cells in the TDLUs have accumulated mutations to put them into an atypical state.

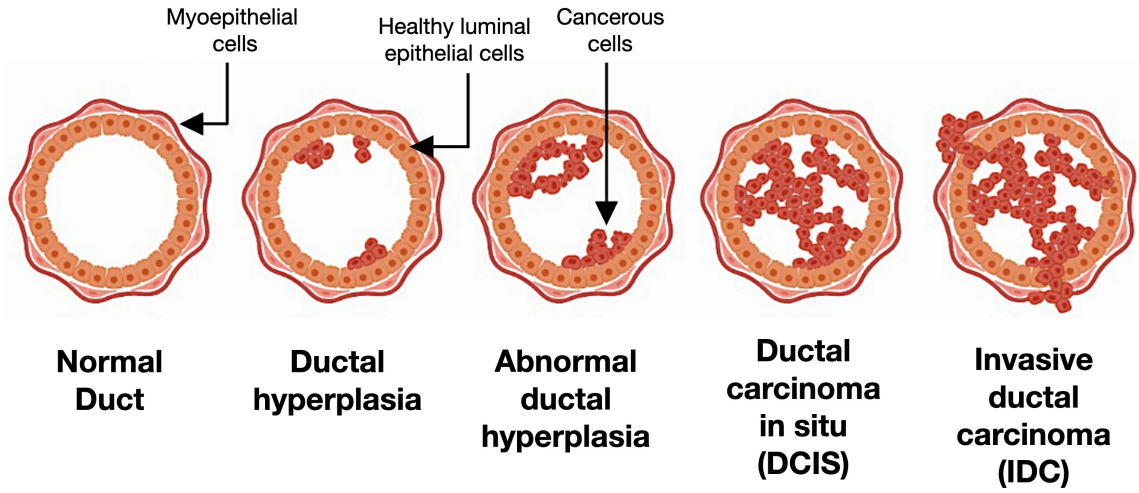

Figure 3: **Different stages of intitial breast cancer development, originating from the mammary duct.** A ductal hyperplasia (also called usual hyperplasia) is usually characterised by a growth of cells that appear relatively normal, relative to epithelial cells. An atypical ductal hyperplasia is formed when these cells appear to be arranged in an abnormal way. A ductal carcinoma in situ is formed when cells have acquired a cancerous stage, but have not yet invaded surrounding tissues. This stage of breast cancer is referred to as stage 0, and rarely produces symptoms, and is usually only discovered through a routine mammography. An invasive ductal carcinoma is when these cancerous cells have been able to invase surrounding tissues. At this stage, the lesion is considered cancerous. Figure adapted from Ref.[20].

1.2.4 Sub-types of breast cancer

Each individual case of breast cancer has its own unique complement of mutations that drive tumor growth, progression and eventual likelihood to metastasise to new organs. As breast cancer is primarily driven by the over-expression or mutation of hormone receptors, each tumor is typically assigned a sub-type based on these, which more precisely provides a general prognosis and strategy for tumor treatment. The three main receptors implicated in breast cancer: ER, PR and HER2, provide the framework for this, along with Ki67, a nuclear protein that is associated with cell proliferation and used as a marker for it. The presence of different combinations of these tumor markers gives rise to the four molecular breast cancer sub-types: Luminal A, Luminal B, HER2 over-expressing, and triple negative (basal-like) (Table 1).

Sub-type	**Receptor Status**	**Incidence (%)**[21]	**10-year rates of metastatic recurrence**[22]	**5-year survival**[21]	
				Localised	**Metastatic**
Luminal A	ER+ and/or PR+, HER2- Low levels of Ki67.	74.6%	9.5 %	100%	30.6 %
Luminal B	ER+ and/or PR+, HER2+ or HER2- High levels of Ki67.	10.5%	20 %	98.9 %	44.7 %
Triple Negative (TNBC)	ER-,PR-, HER2-	10.8%	23.2 %	91.2 %	12.2 %
HER2 over-expressing (HER2+)	ER-, PR-, HER2+	4%	25.6%	96.7%	37.9%

Table 1: Breast cancer sub-types and incidence (2018). Incidence and 5-year survival is based off U.S. data[21], and 10-year rates of metastatic recurrence is based on Netherlands data[22], which is approximately consistent with other similar studies performed from other countries. It is important to note that data from patients of different ethnicities and/or countries that the analysis was performed in can result in different sub-type prevalence data and outcomes. For example, studies of Indian breast cancer sub-types tend to have proportionally lower levels of Luminal A breast cancer, and higher Luminal B, TNBC and HER2+[23].

Of the four sub-types, Luminal A is the least aggressive and has the best prognosis. This is because it is more likely to respond to anti-hormone therapy, for example Tamoxifen, which compromises estrogen receptor function, or aromatase inhibitors, which reduce estrogen production[24].

Triple negative breast cancer (TNBC) does not over-express any of the three main hormone receptors; it has been postulated that risk factors for this sub-type originate from common and rare causative germline mutations[25]. For example, BRCA1 mutations most often result in TNBC compared to other subtypes[26] Because of the lack of identifiable driver mutations, it means that TNBC does not respond to targeted hormone therapy, and in general, finding an optimal treatment regime is often challenging. In fact, TNBC is considered highly heterogenous, and identifying further biomarkers within this subtype is likely to be important in finding more patient-tailored treatments[27]. For example, an integrated genomic analysis identified that tumors that had androgen receptor and FOXA1 pathway

mutations had an increased sensitivity to currently avaliable chemotherapy treatments[28].

Luminal B breast cancer is characterised by the presence of ER and/or PR, with high levels of Ki67, and is often further sub-divided into further sub-types, based on whether the HER2 receptor is over-expressed or not. Occasionally, Luminal B breast cancer that over-expresses HER2 is grouped as HER2 over-expressing breast cancer. Generally, Luminal B (with or without HER2 over-expression) has a relatively good prognosis, second only to Luminal A. This is partially due to its sensitivity to hormone therapy because of the presence of ER/PR. Targeted therapies against HER2 can also be administered if it is present[29;30].

The final sub-type, HER2 breast cancer, is driven by the over-expression of the HER2 receptor, with an absence of ER and PR, meaning that it is not sensitive to hormone therapy. Along with TNBC, HER2 over-expressing breast cancer is considered one with a relatively poor prognosis, and is characterised by high rates of tumor relapses following therapy, a statistic that has been improved by the development of targeted therapies against the HER2 receptor.

The rest of this literature review, and thesis, will focus on HER2 over-expressing breast cancer, both with and without the presence of the estrogen receptor.

1.3 HER2 driven breast cancer, therapeutic challenges and future perspectives

1.3.1 Introduction

HER2 over-expressing breast cancer is a particularly aggressive breast cancer sub-type with a relatively poor patient prognosis, and accounts for approximately 15-20% of worldwide breast cancer cases. It is characterised by over-expression of the ERBB2 gene, which codes for the human epidermal growth factor receptor 2 (HER2) receptor. Because of this, many therapies targeting the HER2 receptor have been developed. The introduction of these therapies have improved prognosis, but the disease still has relatively high rates of metastatic recurrence (see Table 1), relative to other sub-types. Metastatic breast cancer, regardless of sub-type, is considered incurable.

1.3.2 The HER2 receptor: A member of the HER receptor family

The HER2 receptor is a member of a the highly conserved HER family of membrane traversing receptor tyrosine kinases, which has four members; HER1-4. Each member of the HER family has a similar structure: an extracellular domain consisting of four sub-domains, a transmembrane domain, and an intracellular kinase domain (See Figure 4). The extracellular domain of each HER protein is required to induce dimer formation, which happens through co-interactions of the sub-domain II. On HER2, the extracellular domain is in a conformation that makes sub-domain II readily available for interaction[31;32], but HER1 (commonly referred to as EGFR), HER3 and HER4 require ligand binding to change the extracellular domain conformation in a way that permits sub-domain II interactions[33;34;35]. A variety of extracellular signalling ligands have been identified that interact with EGFR (7 in total)[36], HER3 (4 in total)[37;38], and HER4 (9 in total)[33]. HER2 has no known extracellular signalling ligands. Formation of these dimers allows interactions between their respective kinase domains, leading to auto-phosphorylation of different residues; this auto-phosphorylation mediates which downstream molecules are phosphorylated, and in turn, which pathways are activated[39].

The signalling of the HER family of proteins is highly conserved, and has evolved into a complex, multifaceted signalling network in higher eukaryotes across a multitude of different tissue types. This complexity is due to a variety of reasons. Firstly, the HER receptor proteins have an apparent hierarchy of preferred dimerisation partners, which is important for the specific down-stream signalling pathways that are activated. HER2 is the preferred dimerisation partner of each of the other HER family members[40]. Secondly, the individual extracellular ligands that bind to HER-1, -3 or -4 can also influence their bias to form certain dimers[41]. Thirdly, there is a high degree of cross-talk between the HER-signalling network and other pathways, for example with SRC kinases, which interact with the catalytic tyrosine kinase activity of the HER2 receptor, and potentiate its activity[42;43;44].

Taken together, the expression dynamics of each HER receptor, coupled with the unique

complement of extracellular signalling ligands found in each tissue, and presence of interacting RTKs and effector proteins, plethora of possible effects within each tissue, this includes effects on cell proliferation, apoptosis, migration, adhesion and differentiation.

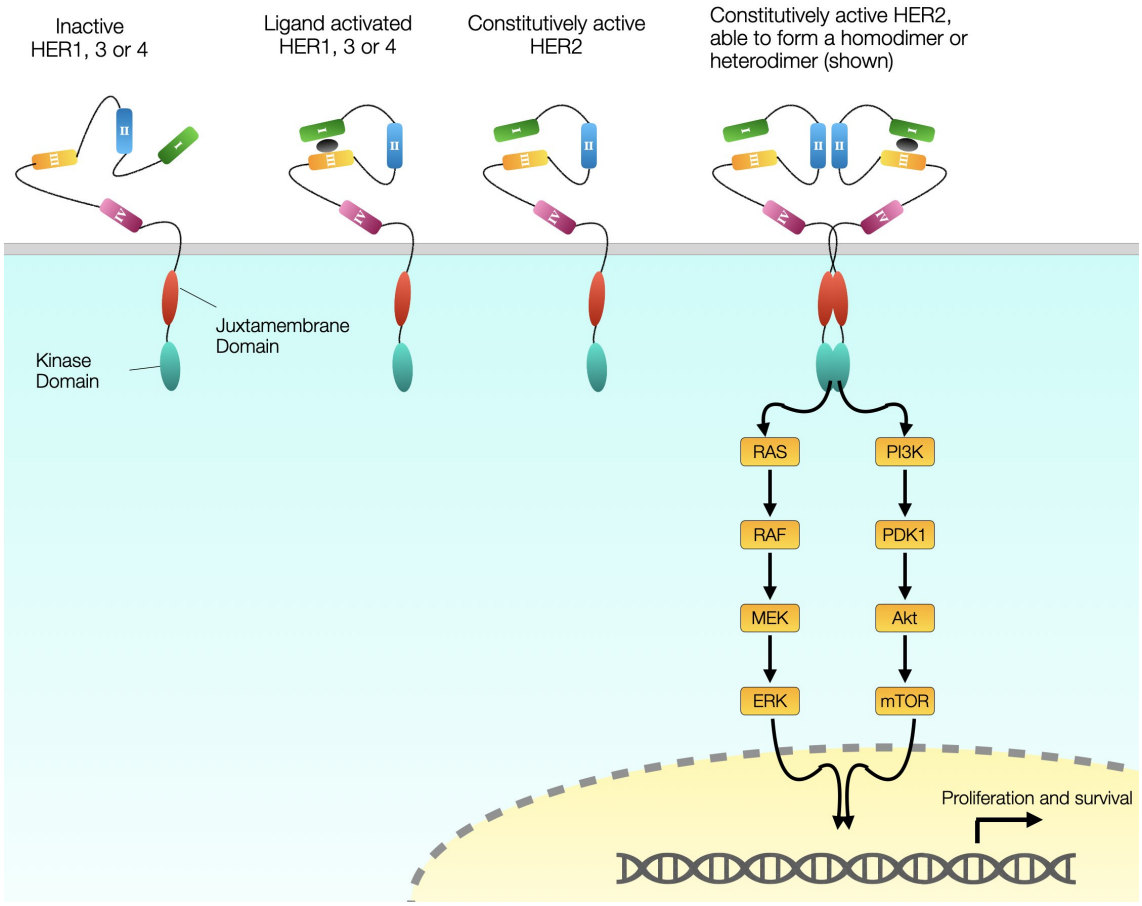

Figure 4: **The HER-family of receptors, showing how protein domains interact with ligands to induce dimer formation.** EGFR (HER1), HER3 and HER4 are naturally in an inactive conformation that is not permissive of dimer formation until they are bound by an extracellular ligand. HER2 is naturally in a conformation that is permissive of dimer formation. Members of the HER family can then form homo- or heterodimers with one another which causes interactions between their kinase domains, allowing downstream protein phosphorylation and induction of signalling cascades.

1.3.3 HER2 over-expression and induction of a neoplastic phenotype

Of the four HER- family members, EGFR and HER2 are the most commonly implicated in a variety of cancers due to their ability to fundamentally change the characteristics of the cell when mutated or over-expressed[45;46]. The transforming effect of HER2 in breast cancer shall be the focus of this section.

In 1984, the first link between the HER2 oncogene and an aggressive form of breast cancer was identified[47;48] and major research efforts have since been conducted to further characterise this tumor driver. The oncogenic effects of HER2 are important to understand in the context of HER- family signalling. HER2-driven breast cancer is primarily caused by gene duplication resulting in over-expression[48], and sometimes also acquiring

activating mutations[49]. At normal expression levels, HER2 is already a more potent signaller; HER2 is the preferred dimerisation partner of the other HER- family members[40], and has the strongest kinase activity of any of the receptors[40;50], and these complexes have more potent oncogenic signalling[51;52;53]. In particular, the HER2-HER3 heterodimer transforms a cell towards a neoplastic phenotype more potently than any other HER-based dimer[54;55;56]. In HER2 over-expressing breast cancer, the membrane density of HER2 is increased[57], which allows it to potentiate its signalling in multiple ways. HER2 distributes on the membranes in areas of localised high density, which is permissive for homodimer formation[58]. Along with this, as HER2 is the preferred dimerisation partner of the other HER family members, heterodimer formation is also increased, which has critically important functions in cell transformation[59]. The increased HER2 signalling also functions to increase its own stability in a positive feedback loop; HER2 over-expression activates HSF-1, which increases HSP90 expression[60], which in turn, functions to increase EGFR and HER2 receptor membrane stability[61]. Further, EGFR signalling is also indirectly increased because EGFR-HER2 heterodimers are not susceptible to endosomal digestion, meaning that the membrane density of EGFR is partially de-regulated[62].

The increased amount of HER2 based homodimers and heterodimers drives multiple phenotypic changes that can contribute to a neoplastic phenotype. Their signalling primarily acts through the PI3K/AKT/mTOR and Ras/Raf/ERK signalling pathways, leading to a multitude of different effects on the cell, these include: driving losses in cell polarity, adhesion, cell proliferation, anti-apoptotic signals, migration, cell cycle deregulation and metabolic changes[63;64]. HER2 homodimers and heterodimers are both integral to induction of a neoplastic phenotype. Inhibition of homodimer formation through treatment of cells with the monoclonal antibody Trastuzumab (see section 1.3.5 for a comprehensive discussion on targeted therapeutics) preferentially effects cells with higher homodimer levels. With regard to heterodimers, different heterodimers have been associated with tumor progression and resistance. For example, the EGFR-HER2 heterodimer has been implicated in tumor cell motility through signalling of the STAT1 transcription factor[65]. Similarly, the relevance of the HER2/HER3 heterodimer has become a large focus of research in recent years due to its association with tumor relapse and metastasis because of its strong transforming effect. This dimer has an rapid rate of tyrosine kinase activity and potentiates multiple signalling pathways[66]. It has been demonstrated that HER3 provides ways for HER2 to continue its signalling activity despite treatment with HER2-specific tyrosine kinase inhibitors[67]. Levels of HER2-HER3 dimers in a tumor are also positively correlated with the probability of a metastastic relapse in patients[68], and associated with a poor response to targeted treatment[69]. As well as heterodimer formation being important for HER2 over-expressing breast cancer progression and resistance to treatment, homodimer formation is also important. Cells with a lack of HER2 homodimers were found to be less responsive to drug treatment[70]. It has also been demonstrated that HER2 interacts with a wide array of RTKs outside of the HER family; this is important for maintaining a tumor phenotype in the absence of HER2 homodimer formation, and is therefore implicated in therapy resistant tumors[59].

1.3.4 'Addiction' to the HER2 oncogene in HER2 overexpressing breast cancer

1.3.4.1 Oncogene addiction

With our modern understanding, it is now evident that cancer, including HER2 over-expressing breast cancer, arises through a multi-stage process of sub-clonal evolution, where many fundamental characteristics of the cell change due to genetic mutations, accelerated by increased genomic instability, and also through selection due to micro-environmental effects, such as access to nutrients and oxygen. This Darwinian-like selection, typically over the course of multiple decades, eventually allows a neoplastic phenotype to develop.

An inherent result of genomic instability and diverse tumor micro-environments is a high degree of inter- and intra-tumor heterogeneity (discussed in Section 1.4.1). However, remarkably, despite this, the reliance of the vast majority of tumor cells on a single or few driver oncogenes to maintain their neoplastic phenotype has long been identified and characterised, dating back to the work by Duesberg and Vogt in 1970[71]. This phenomenon had been coined as 'oncogene addiction'[72].

The notion that oncogenes can solely be responsible for tumor establishment and progression provided an attractive rationale for the development of molecules that compromise their downstream functions[73], potentially inhibiting cancer cell division and survival. This research interest eventually gave rise to the advent of targeted cancer therapy, which is now a major foundation of modern cancer therapy, along with more traditional systemic therapies (chemotherapy and radiotherapy) along with surgery.

1.3.4.2 Experimental evidence of 'addiction' to HER2 in HER2 overexpressing breast cancer

Multiple experimental models have helped to verify that the concept of oncogene addiction carries over to the HER2 oncogene in breast cancer. Silencing of HER2 expression in HER2 over-expressing human breast cancer cell lines with siRNAs has been demonstrated to inhibit proliferation and induce apoptosis[74], whilst conversely, MCF10a cells, considered a non-neoplastic human breast cell line, can take on tumor properties when HER2 is over-expressed or mutated into a constitutively active form[75], and can even cause non-transformed neighbouring cells to take on a neoplastic phenotype by the release of exogenous signalling factors[76]. Inducible mouse models that over-express Neu (rodent HER2 homologue) specifically in the mammary epithelium are also a well established model of *in vitro* and *in vivo* tumorigenesis, particularly when it is co-over-expressed along with the MYC oncogene[77;78]. When the over-expression of these oncogenes is de-induced (mimicking a "perfect" drug treatment), tumors regress *in vitro* and *in vivo*.

1.3.5 Therapeutic exploitation of “addiction" to HER2 over-expression in breast cancer: Targeted therapies

The notion that cancer cells are reliant on oncogene over-expression has led to a large pharmaceutical effort to develop therapeutics that compromise their function. In 1998, the FDA approved the first targeted therapeutic against the HER2 receptor called Trastuzumab (marketed as Herceptin®, Genentech)[79]. This is a monoclonal antibody that binds to the receptors extracellular domain, preventing homodimerisation and subsequent activation of downstream signalling pathways[32;70]. Consistent with HER2 knock-down and de-induction experimental models, treatment of patients with HER2 over-expressing breast cancer cell lines with trastuzumab ablates cell proliferation and survival[80]. On a clinical level, trastuzumab has improved long-term prognosis for breast cancer patients in clinical trials and is demonstrated as a safe method of treatment[81;82].

In the time since the original licensing of Trastuzumab, further HER2-targeted agents have been approved. These are often used as an adjuvant or neo-adjuvant therapy along with trastuzumab and other chemotherapeutics, with some combinations being specifically licensed to target metastatic tumors. The current FDA-licensed HER2 targeted agents primarily have three mechanisms of action. These are listed below and the corresponding agents are listed in Table 2.

1. Attachment to the extracellular domain of the HER2 receptor (Trastuzumab, Pertuzumab and Margetuximab).
2. Inhibition of the intracellular tyrosine kinase activity of the receptor (Lapatinib, Neratinib, Pyrotinib[83] (Tucatinib)
3. Targeted delivery of a cytotoxic agent to HER2 over-expressing cells (Trastuzumab Emantisine and Trastuzumab deruxtecan).

The year 2020 and early 2021 was perhaps the most encouraging time for HER2+ breast cancer treatment, since the FDA approval of Trasutuzumab (Herceptin®, Genentech) in 1998. This is due to the regulatory approval in this period of Tucatinib (Tukysa®, Seagen) and two drugs involving trastuzumab covalently linked to a cytotoxic payload (known as an antibody-drug conjugate (ADC)): trastuzumab emtansine (Kadcyla®, Genentech) and the very recently approved trastuzumab deruxtecan (Enhertu®, Daiichi-Sankyo/AstraZeneca). In their respective Phase III clinical trials, each of these drugs improved patient outcomes, relative to the comparator group. For example, Tucatinib, which is used in patients with advanced or metastastic breast cancer, yielded a improved overall survival time, with a 1 year hazard ratio (relative risk of death) of 0.48[84]. This is partially due to the fact that Tucatinib is able to cross the blood-brain barrier, allowing treatment of brain metastases that are often inoperable through surgical methods.

Drug (Marketed name)	Mechanism of action	Current licensed therapeutic use	Year of first regulatory approval	Key Data
Trastuzumab (Herceptin®	Anti-HER2 mAb	+ paclitaxel for HER2+ metastatic breast cancer	1998 (FDA)	Overall survival HR of 0.76 compared to chemotherapy alone[85].
Pertuzumab (Perjeta®)	Anti-HER2 mAb	Alongside trastuzumab and docetaxel in neoadjuvant HER2+ breast cancer	2013 (FDA)	pCR rate: pertuzumab + trastuzumab + docetaxel; 45.0%, trastuzumab + docetaxel; 29.0%[86]
		+ trastuzumab and pertuzumab for adjuvant HER2+ breast cancer treatment	2017 (FDA)	PFS HR of 0.82 of all 3 agents compared to trastuzumab + chemotherapy alone[87].
Margetuximab (Margenza®)	Anti-HER2 mAb	+ chemotherapy for metastatic disease, with at least 2 prior treatment regimens (at least 1 in the metastatic setting)	2020 (FDA)	PFS HR of 0.76 (median of 5.8 vs 4.9mos; margetuximab vs trastuzumab)[88]
Trastuzumab emtansine (Kadcyla®)	Anti-HER2 ADC	Metastatic breast cancer patients who have received prior taxane + trastuzumab	2013 (FDA)	PFS HR of 0.65 compared to lapatinib + capecitabine[89].
		Patients with residual-invasive disease after neoadjuvant taxane + trastuzumab	2019 (FDA)	PFS HR of 0.50 compared to trastuzumab. 10.5% of recurrences were metastatic, compared to 15.9 when treated with trastuzumab[90].
Trastuzumab deruxtecan (Enhertu®)	Anti-HER2 ADC	Unresectable or metastatic HER2+ breast cancer after at least two prior failed lines of therapy	2020 (FDA)	Single arm Phase II clinical trial. 60.3% ORR, mPFS: 14.3 months. These data currently exceed efficacy statistics from other HER2 targeted treatments at this HER2+ breast cancer stage. Two confirmatory Phase III double-blinded trials are currently ongoing[91;92;93].
Lapatinib (Tykerb®)	EGFR and HER2 TKI	+ capecitabine for previously treated HER2+ metastatic breast cancer	2007 (FDA)	PFS HR of 0.57 compared to capecitabine alone[94].
Neratinib (Nerlynx®)	EGFR and HER2 TKI	+ capecitabine for advanced or metastatic HER2+ BC	2020 (FDA)	PFS HR of 0.76 of neratinib + capecitabine compared to lapatinib + capecitabine[95].
		Extended adjuvant treatment following trastuzumab therapy	2017 (FDA)	After 2 years, DFS HR of 0.66 compared to placebo[96].
Tucatinib (Tukysa®)	HER2 TKI	+ trastuzumab + capecitabine for advanced unresectable or metastatic HER2+ BC, including patients with brain metastases	2020 (FDA)	PFS HR of 0.54: tucatinib + trastuzumab + capecitabine compared to placebo + trastuzumab + capecitabine[97].

Table 2: Currently approved HER2-targeted therapies, along with the mechanism of action, the therapeutic setting the drug is used in, year of original regulatory approval, and the key data that led to that approval. Abbreviations: PFS - Progression Free Survival, HR - Hazard Ratio, pCR - Pathological complete response, ORR - Overall response rate, DFS - Disease Free Survival, ADC - Antibody-drug conjugate, TKI - Tyrosine kinase inhibitor.

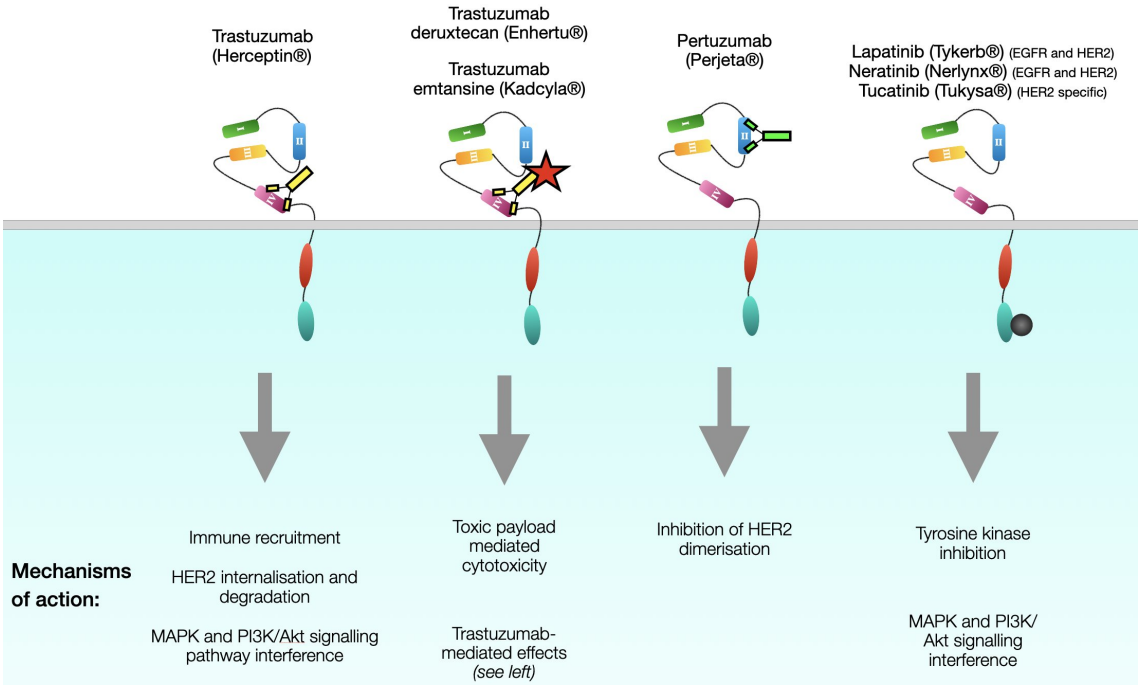

Figure 5: **The binding and mechanisms of action of currently licensed HER2-targeted therapeutics.** Currently, anti-HER2 drugs fall into three main categories for their mechanism of action: anti-HER2 antibodies (such as Trastuzumab) HER2 or pan-HER tyrosine kinase inhibitors (such as lapatinib or Tucatinib), and more recently, antibody-drug conjugates (such as trastuzumab emtansine) which are able to specifically deliver a cytotoxic payload to HER2-expressing cells and induce mitotic catastrophe, similarly to how non-targeted chemotherapeutic agents work.

However, despite encouraging clinical data, there are still significant clinical challenges in HER2+ breast cancer that need to be addressed as HER2+ breast cancer is still considered as one with a relatively poor prognosis. One particular challenge is tumor relapse - tumors that re-occur in the body after apparently successful original treatment, often being less responsive to treatment than previously because of tumor resistance. The following section will discuss the clinical challenges brought on by tumor relapse in HER2+ breast cancer, and how targeting tumor heterogeneity could help to prevent this from happening.

1.3.6 Therapeutic challenges: tumor relapse

A significant clinical challenge for HER2 positive breast cancer is tumor relapse, particularly metastatic relapse. A large portion of mortality from any cancer is due to eventual metastatic spread, which compromises organ viability and function, which can occur in a *de novo* fashion, or due to tumor relapse. As with all breast cancer metastases, HER2 driven breast cancer metastases, occurring in either way, are largely considered incurable. This means that drugs such as tucatinib and trastuzumab deruxtecan, which are currently only approved in advanced/metastatic patients, only prolong survival, and almost never cause full disease remission. For example, tucatinib + trastuzumab + capecitabine led to a median progression free survival of 7.6mos, compared from 5.6mos on the control treatment (placebo + trastuzumab + capecitabine)[84]. Of concern in the context of tumor relapse is that HER2+ breast cancer tumors that have recurred in a metastatic setting give rise to particularly poor survival statistics[98]. On top of this, current treatment regimens

that are licensed for earlier stages of breast cancer (before relapse or metastasis) appear to lead to proportionally higher incidences of problematic brain metastases; the current proportion of patients that develop brain metastases following targeted HER2 therapy is now estimated to be 30-50%.[99;100;101]. As a first metastatic site, patients with metastatic relapses are approximately 3.1 times more likely to be in the brain than *de novo* metastases[98].

Despite these statistics, HER2-targeted therapies have improved patient outcomes in all lines of therapy, and are likely to continue to do so, particularly with the recent approval of newer generation HER2-targeted treatment regimens (see Section 1.3.5). The approval of trastuzumab emtansine in the adjuvant setting is likely to improve relapse statistics, as it is a more effective treatment than the previous standard of care (although these statistics will take approximately 8-10 more years to be fully mature). However, as it is still a HER2-directed treatment, and resistance mechanisms to it have already been identified[102], it is also likely that subsequent relapses will remain a significant therapeutic challenge to overcome.

1.4 Tumor relapses after HER2-targeted therapy

1.4.1 Tumor heterogeneity: a driving force behind tumor relapse

Because of the problems associated with tumor relapses, significant amounts of research have been directed into understanding the processes that lead to them, so that they can be treated or prevented. Central to this is the concept of tumor heterogeneity.

It has long been understood that cancer cells arise through a multi-stage process of subclonal evolution, where many fundamental characteristics of the cell change due to genetic mutations, accelerated by increased genomic instability. Because of the propensity of tumor cells to mutate, and the different micro-environmental conditions found within a single tumor (for example, cells in the middle of a tumor experiencing more hypoxia) individual cancers experience a high degree of intra-tumor heterogeneity both on a genetic and non-genetic level, including in HER2 positive breast cancer patients. For similar reasons, patients with the same sub-types of cancer can still experience high degrees of between-patient (inter-tumor) heterogeneity[103].

Understanding both levels of tumor heterogeneity has, and is, likely to drive clinical advances in relation to tumor relapses. On a patient level, understanding the unique tumor drivers and conditions that are unique to each patient has led to increasingly more personalised treatment approaches. These will be continue to improve patient prognosis statistics. Eventually, approaches such as this may even make metastatic disease considered to be curable in some patients. However, whilst improving treatment of tumor relapses (particularly metastases) is important, the presence of these relapsed tumors leads to decreases in quality of life, economic and practical burdens on healthcare systems, and will involve significant amounts of financial and time investment to see a gradual improvement in patient outcome statistics. From all of these standpoints, relapse and/or

metastasis prevention would be a more effective and beneficial therapeutic strategy.

Earlier cancer prognosis is highly predictive of patient outcomes, and so developing reliable and affordable screening techniques would be effective at helping to improve patient outcomes. On top of this, finding methods to target cells that would otherwise be able to evade therapy could lead to improved treatment outcomes. Theoretically, increased intra-tumor heterogeneity increases the probability that some cells will be able to survive initial targeted treatment through compensatory survival mechanisms, possibly relocate to other organs, and re-grow to form relapsed tumors. Consistent with this, a recent study demonstrated that increased intra-tumor heterogeneity is associated with an increased risk of metastasis and a decrease in overall patient survival[104], backed up by another study focusing on HER2 copy number[105]. To further lower the probability of tumor progression or recurrence despite treatment, a therapeutic regime would have to also compromise the escape mechanisms in these cellular sub-populations.

1.4.2 A HER2 "blockade" as the current combination treatment strategy – successes and ongoing issues

As will be discussed in Section 1.5.1, one major way that HER2+ breast cancer is able to evade therapy is through sustaining HER2 oncogenic signalling, either through HER2 mutations that render it insensitive to treatment, or through the reactivation of downstream signalling.

To combat this, the majority of currently licensed treatment regimens involving HER2-targeted agents focus on a dual-HER2 blockade, both in the neoadjuvant/adjuvant setting, and also in the metastatic setting. For example, trastuzumab, pertuzumab and chemotherapy are the standard of care for first-line HER2 positive breast cancer (although this is likely to be overtaken by trastuzumab emtansine in the coming years). For metastatic and relapsed patients, the newly-approved tucatinib is exclusively licensed for treatment alongside trastuzumab and chemotherapy. Trastuzumab deruxtecan, also newly approved, is currently approved as a monotherapy. The current late-phase clinical pipeline also suggests that a general clinical strategy is a HER2-blockade. In line with this, a relatively high proportion of Phase PII/III or Phase III clinical trials still involve a HER2 blockade (38/81 (46.9%) ongoing or planned, as of August 2021)[106].

Whilst it is that using a HER2 blockade has improved initial treatment outcomes, it may not be optimally effective at preventing tumor relapses. Whilst more comprehensively inhibiting the main tumor driver (HER2) will cause more tumor cells to lose their driver and therefore succumb to oncogene addiction, it does not account for cells that may be able to survive through alternative pathways that are not reliant on HER2 expression. In line with this, clinical evidence demonstrates that patients that did not achieve a pathological complete response (pCR[‡]) had a 9.55x increased chance of subsequent relapse after targeted HER-2 therapy (trastuzumab and/or lapatinib treated). As a percentage of total

[‡]Pathological complete response - the absence of any detectable residual cancer cells following treatment

patient population, 14.7% of patients have HER2 negative residual disease[§] after targeted treatment, and these patients have a 2.41x higher chance of subsequent disease relapse, compared to patients with HER2+ residual disease[107]. A longer-term follow up data further confirmed these data; patients with HER2+ residual disease after adjuvant therapy had a 84% 5-year overall survival, patients with HER2- residual disease had a 50% 5-year overall survival. As well as this, other clinical data suggest that approximately 24% of metastatic relapsed tumors lose HER2-expression, and this loss is positively associated with a poorer outcome[108]. Trastuzumab treatment did not significantly influence the likelihood of this discordance, but in patients that did lose HER2 expression after initial trastuzumab treatment, patient prognosis was particularly poor, with all patients on the study in this subgroup dying within two years[108]. This suggests that loss of HER2 expression could be selected for in some patients for metastatic progression, and that these selected for cells are particularly aggressive.

[§]Residual disease - Surviving cancer cells following therapy

1.5 Resistance mechanisms of HER2+ breast cancer cells to current HER2-targeted treatment regimens

The following sub-sections discuss resistance mechanisms to HER2 targeted anti-cancer therapies. A summary of these resistance mechanisms is displayed in Figure 6.

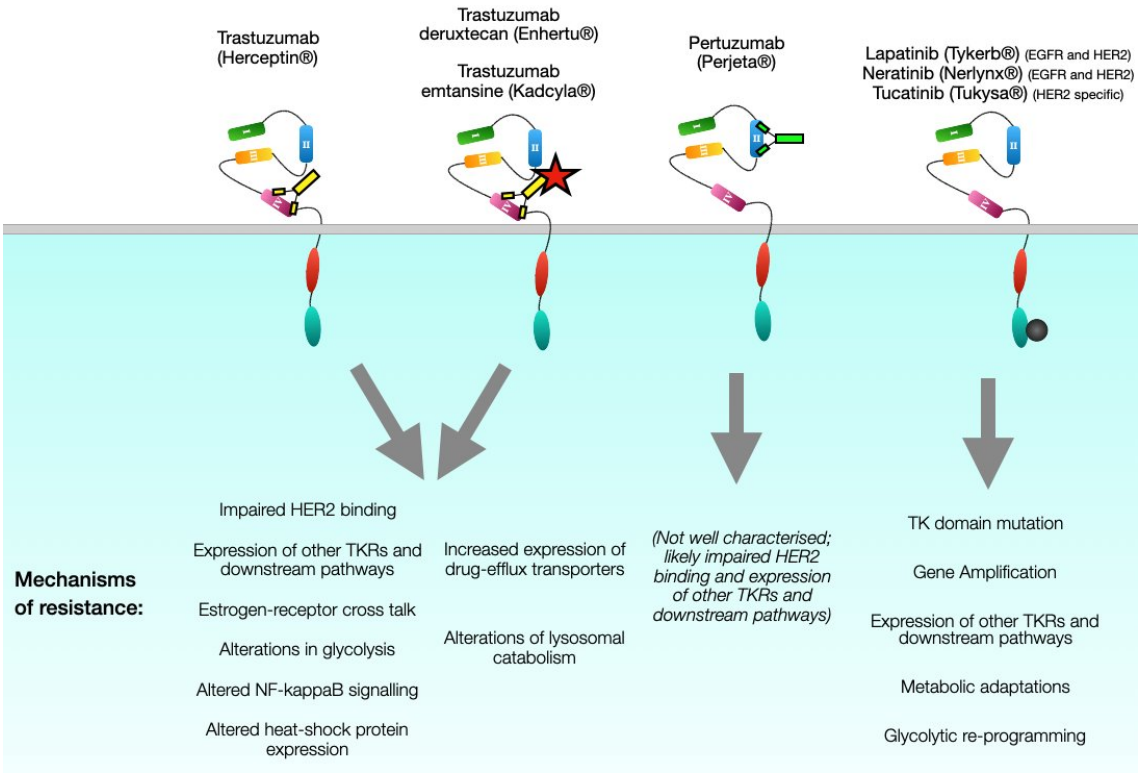

Figure 6: Mechanisms of drug resistance to currently licensed therapeutics. Text references (top to bottom): Trastuzumab:[109;110;111;112;113;114;115;116;117;118] Trastuzumab emtansine:[119;120;121] Tyrosine kinase inhibitors: Lapatinib:[122;123;124] Neratinib:[124] Tucatinib:[124]. Margetuximab is not included in this figure as there are no mature data about it yet in this context.

1.5.1 Resistance mechanisms: Maintaining HER2 signalling through re-activation of downstream signalling pathways, or HER2 mutations

Evidence suggests that one reason for resistance to HER2 targeted therapies could be the re-activation of downstream pathways that allow the effects of HER2 signalling to be propagated, even when HER2 function is compromised by the presence of targeted therapies. For example, dual inhibition of HER2 signalling and the downstream PI3K protein is implicated in overcoming HER2 resistance[125;126]. Evidence also exists to suggest that resistance to HER2 targeted therapies can also come at the level of the receptor through the acquisition of activating mutations[127]. In fact, resistance to originally non-HER2 over-expressing, ER+ breast cancer can occur through HER2 activating mutations[128], highlighting a need for improved anti-HER2 therapy outside of this specific sub-type of breast cancer. Furthermore, resistance in this way can also occur at the level of drug interactions; for example, increased levels of mucins are implicated in trastuzumab resistance[129]. Evidence also suggests that resistance to tyrosine kinase inhibitors such as lapatinib is asso-

ciated with an increased resistance to the TRAIL apoptosis pathway which occurs through differential phosphorylation of AKT, leading to changes in BCL-2 family members - inhibition of these is correlated with increased sensitivity in lapatinib resistant cells.[130].

1.5.2 Resistance mechanisms: Utilisation of “escape” pathways

“Escape” pathways could be utilised to allow oncogenic effects to be propagated in the absence of HER2 signalling. There are multiple lines of evidence to suggest that this is a significant driver of tumor resistance. Examples of some prominent mechanisms of this is described in the following sub-sections, relating to CDK4/6 expression, heat shock protein (HSP) expression, and NF-$\varkappa\beta$ signalling.

1.5.2.1 CDK4/6 expression

Alterations of CDK4/6 expression in cancer are common, and have emerged as an attractive therapeutic target[131]. In HR+/HER2- breast cancer, the CDK4/6 inhibitor Palbociclib was approved by the FDA in 2016[132], after a successful Phase III clinical trial[133]. Activation of CDK4/6 signalling has become an area of significant scientific and clinical interest in HER2 breast cancer[126], with certain studies currently in Phase II and III clinical trails[134;135;136]. It has long been known that CDK4/6 signalling is important in breast cancer survival[137], and experimentally demonstrated to be synergistic in cell lines, and have a significant combinatorial effect in xenograft models with no increases in toxicity in mice[138]. On top of this, work with transgenic mouse models have identified that resistance to HER2-targeted therapy is overcome by using CDK4/6 inhibitors[139].

1.5.2.2 HSP protein expression

HSP protein expression is modulated by HSF-1. Alterations in their expression can reprogram tumor cell metabolism (discussed in depth in Section 1.5.3). Human breast cancer cell lines over-expressing HER2, BT-474 and SK-BR3, have over-expression of HSF-1 and down-stream heat shock proteins, and resistance to both trastuzumab and lapatinib comes through the failure of these drugs to regulate HSF-1 expression[60]. Cells that are resistant to either of these drugs are sensitive to HSF-1 inhibition[123;114], and it was demonstrated that lapatinib resistant cells are also sensitive to downstream HSP-90 inhibition. Six of the eight RTKs that were de-regulated in the lapatinib resistant mammary tumors were HSP-90 clients[140]. Lapatinib resistant BT-474 cells maintain sensitivity to heat shock protein inhibition, which is mediated through heat shock factor 1 (HSF-1) activity[140]. Consistent with this, ganetspib, which is involved in HSP90 inhibition, was demonstrated to preferentially reduce viability in BT-474 and SK-BR3 cells, compared to their non-HER2-over-expressing counterparts[141]. Additionally, in line with this study, they also established that ganetspib potentiates the effects of lapatinib in each cell line, with stronger combined effects in BT-474, relative to SK-BR3[141].

On top of this, a recent study found that 17-DMAG, a HSP90 inhibitor, was able to overcome resistance to lapatinib in BT-474 and SK-BR3 cells. Interestingly, this same study

also found that a combination of both lapatinib and 17-DMAG were able to more effectively treat these resistant cell lines compared to either in monotherapy, which was also the case in xenograft tumors as well, suggesting that the effects of this drug interaction may carry over to resistant cells as well[142].

1.5.2.3 NF-$\varkappa\beta$ signaling

NF-$\varkappa\beta$ expression is associated with HER2 over-expression[143], and its signalling is activated by HER2 through a canonical pathway with results in an invasive phenotype[144]. Clinical evidence suggests that NF-$\varkappa\beta$ is a biomarker that is predictive of an aggressive phenotype and poor prognosis[145]. Because of these reasons, the link between HER2+ and NF-$\varkappa\beta$ has long been identified and characterised as a potentially attractive node of interference for therapy resistant breast cancer[146;147]. In the context of HER2+ breast cancer specifically, there is also evidence for this. Trastuzumab-resistant BT-474 cells have demonstrated activation of NF-$\varkappa\beta$[115]. It has also been demonstrated that NF-$\varkappa\beta$ is hyperactivated in breast cancer cells, and that combination inhibition of HER2 and NF-$\varkappa\beta$ was effective in killing lapatinib resistant cells[148]. As well as this, RANK signalling, through ERK and NF-$\varkappa\beta$ signaling mediates resistance to lapatinib in multiple HER2+ breast cancer cell lines[149].

1.5.3 Resistance mechanisms: Altered metabolism

1.5.3.1 Metabolism as a hallmark of cancer

It has long been understood that cancer cells fundamentally alter their metabolism, dating back to the pioneering work by Otto Warburg in the 1920s, who determined that cancer cells preferentially undergo anaerobic metabolism (glycolysis as the main source of ATP production) despite the presence of readily available oxygen being present in the cellular microenvironment[150;151]. Since then, altered metabolism has gone from being considered a by-product of a neoplastic phenotype, to an active driver of tumorigenesis[152].

The original work by Otto Warburg postulated that this increased glycolysis was due to an accumulation of mitochondrial damage in cancer cells, meaning that glycolysis was required as the preferential source of energy production to maintain cell viability and support growth[150;151]. Since then, it has become clear that mitochondrial metabolism is an essential part of cancer cell metabolism, albeit in an altered state. In quiescent, non-actively dividing cells, ATP production preferentially comes from mitochondrial metabolism; this form of aerobic respiration is more energy efficient. However, in actively proliferating cells, including cancer cells, cell metabolism is shifted from ATP production to macromolecule production. This system of metabolism is less energy efficient, but is important to meet the macromolecular requirements for actively dividing cells. HER2 over-expressing breast cancer cells have an altered metabolic phenotype, which, similar to many other cancers, is shifted towards a state of macromolecule production, including with increased fatty acid synthesis[153] which preferentially comes through exogenous fatty acid uptake[154],

nucleotide biosynthesis[155], and reliance on the pentose phosphate pathway[156] which is implicated in amino acid, nucleotide and fatty acid biosynthesis.

1.5.4 Altered metabolism in HER2 over-expressing breast cancer

The fundamental metabolic alterations in HER2 over-expressing breast cancer cells are controlled through alterations in molecular signalling pathways, including the PI3K/Akt/mTOR and RAS/RAF/ERK pathways, both important pathways in HER2+ breast cancer. In particular, the PI3K/Akt pathway is implicated many altered downstream metabolic effects, across many different cancers[157]. In this pathway, phosphoinositide 3-kinase (PI3K) binds to phosphorylated tyrosine residues following receptor trans-autophosphorylation, causing it to become activated. In turn, this activated form of PI3K binds to membrane bound PIP2, causing an extra phosphate group to bind to it, converting it to PIP3. PIP3 is then able activate the AKT kinase, which in turn can activate mTOR. mTOR has a multitude of effects on a cells metabolism[158]. In HER2+ breast cancer, glucose uptake is enhanced through increased levels of sodium-dependent Glucose Transporter 1 (SGLT1), which in turn acts in a positive feedback loop to activate the PI3K/AKT/mTOR pathway. This pathway is also implicated in the expression of an pyruvate kinase isozyme M2 (PKM2) in HER2 over-expressing breast cancer[159]. This isoform is functional in glycolysis and is associated with a highly proliferative phenotype. It is important for the survival of HER2 over-expressing cells; demonstrated by the fact that PKM2 inhibition compromises cell viability[160]. mTOR also stimulates activation of lactate dehydrogenase in HER2 breast cancer (LDH)[161], through the activation of Heat Shock Factor 1 (HSF-1)[162] to produce lactate. The amount of exogenous lactate is correlated with the level of HER2 addiction and response to targeted therapy[163]. There is also evidence to suggest lactate acts in a positive feedback loop to further activate mTOR through activation of BCL-2 in cancer cells[164]. HSF-1 also stimulates the expression of heat shock proteins (HSPs) such as HSP-70 and HSP90, both of which also are implicated in influencing the metabolic characteristics of a variety cancers[165;166]. Both have been implicated in having a role in HER2 over-expressing breast cancer and resistance to targeted therapy[167;60]. In particular, HSP90 has been a subject of particular interest, with many HSP90-targeting drugs being tested in Phase I clinical trials[168]. A notable example is Ganetspib, due to its effectiveness across a range of breast cancer sub-types[118]. A Phase I clinical trial data testing this inhibitor in combination with trastuzumab and paclitaxel produced encouraging safety data[169]. As well as promoting a glycolytic phenotype, mTOR also promotes Acetyl-CoA production, *de novo* lipogenesis and changes in mitochondrial physiology in HER2 over-expressing breast cancer cells[170].

Similarly, RAS/RAF signalling is also implicated in driving metabolic changes in a variety of cancers[171], and this includes an important role in in HER2 over-expressing breast cancer, which is mediated through heterodimer formation with EGFR, HER3 and CDKN1B[172]. Up-regulation of this signalling pathway is is implicated in regulating the MYC transcription factor[173], which also promotes a glycolytic phenotype. MYC itself is widely implicated in multiple cancers, and in HER2 over-expression alongside MYC over-expression is as-

sociated with faster tumor progression and an increased probability of metastasis, which was associated with higher levels of intra-tumor heterogeneity[174].

1.5.4.1 Altered metabolism as a route of therapeutic resistance to HER2-targeted therapy

Re-programming of metabolism is a common way that HER2-driven breast cancer cells escape targeted therapies. Work from the Jechlinger Lab used an inducible mouse system of tumorigenesis in 3D culture to characterise adaptations in cells following oncogene induction and de-induction. Using doxycycline as an expression activator, Neu (Rodent homologue of HER2) and MYC could be conditionally over-expressed using the reverse tetracycline trans-activator (rtTA), which was specifically expressed in the mouse mammary gland using the (MMTV) promoter. This experimental system is further discussed and shown in Section 1.8.2. Using this methodology, oncogene expression could be de-induced (through doxycycline removal), mimicking a "perfect" drug treatment. The surviving fraction of cells could then be analysed to explore their alterations. Using a combination of transcriptomics, targeted and un-targeted metabolomics, fundamental metabolic alterations were identified in residually surviving cells, including an up-regulation of glycolysis (Preprint:[175]). Consistent with this, resistance of HER2 over-expressing cell lines grown in 2D culture to trastuzumab or lapatinib also have fundamentally altered glycolysis[123;114;140].

Microarray and transcriptomic data from our lab using the system of inducible primary mouse organoids also identified that fatty acid metabolism is up-regulated in residually surviving cells[176]. Similarly to a re-programming of glycolysis, it is possible that changes in fatty acid metabolism could also provide targetable vulnerabilities that could be capitalised on with combination therapy. For example, BT-474 and SK-BR3 cells have a Warburg-like phenotype, and this phenotype supports fatty acid synthesis and invasive tumor-like properties. When palmitate supplementation was used to inhibit glycolysis in these cells, fatty acid synthesis was decreased and β-oxidation (catabolism of lipids) was increased, suggesting a phenotypic shift away from the macromolecule -generating based metabolic phenotype that cancer cells have[177]. In the context of combination therapy, compromising fatty acid synthase function alongside HER2 targeted inhibition has increased anti-tumor activity. Blankafort *et al.* (2015) generated SK-BR3 cells resistant to lapatinib, trastuzumab and a combination of both. All three lines showed an increase of EGFR, ERK1/2 and PI3KCA mutations, and dual resistant lines also had increased levels of AKT. mTOR and fatty acid synthase (FASN) levels were stable in all three lines[178]. Together, this suggests that a re-activation of downstream signalling is important for the resistance of these cells to targeted therapy. When pertuzumab, a HER2 targeted agent that compromises receptor dimerisation was used alongside FASN inhibitors, a synergistic effect was identified in cell lines, and in patients with primary and trastuzumab and lapatinib resistant HER2+ tumors, without signs of toxicity[178]. Similar sensitivity of HER2 targeted therapy resistant cells to fatty acid synthase inhibition has also been identified in xenograft experiments[179].

Other areas of metabolism are also implicated in resistance to targeted therapies. ERRα is a master regulator of cell metabolism, and its expression is important in cells that are lapatinib resistant, which occurs through mTOR signalling. In these cells, ERRα triggers metabolic adaptations favouring increased glutamine metabolism which facilitates mitochondrial energy metabolism[180]. Compromising activity of mitochondrial MAPK phosphatase 1, which is not well characterised, alongside HER2 inhibition also enhanced killing of breast cancer cells that were resistant to HER2 targeted therapy[181].

1.5.5 A lack of ongoing clinical trials combining HER2-targeted therapies in combination with non-HER2 targeted agents: an unmet need for reducing numbers of patient relapses

In a neoadjuvant/adjuvant clinical setting, there are strikingly few currently ongoing therapeutic strategies to combine HER2-targeted therapy with other forms of targeted therapy. As shown in Table 3, there are only a total of 5 current Phase II or III approaches in localised breast cancer that do this. These involve strategies of immune recruitment, a cancer vaccine, or a CDK4/6 inhibitor.

The strategy of immune recruitment is currently a highly active area in cancer therapy. This is typically through monoclonal antibodies targeting PD-1 (expressed on the surface of immune cells), or PD-L1 or CTLA-4 (Antigens on cancer cells that allow them to evade the immune system). Atezolizumab and Pembrolizumab, which are being tested in clinical trials (Table 3) have already been approved for the treatment of various different cancers. There is clinical evidence to support this therapeutic strategy in breast cancer treatment also, as tumors that have recurred after trastuzumab therapy have increased PD-L1 expression[182]. This same rationale also supports the efforts to introduce a cancer vaccine to reduce the probability of relapses. Over recent years, cancer vaccines have been a clinical approach of increasing interest, but no cancer vaccine has yet been approved for use in any type of cancer. Preliminary data from the Phase II trial in Table 3 suggest that nelipeptimut-S + trastuzumab leads to no more side effects than trastuzumab alone[183], but efficacy data is not yet mature.

As discussed in Section 1.5.2.1, the combination of SHR-6390 (CDK4/6 inhibitor) and HER2-targeted therapy are relevant in the context of currently existing evidence for resistance to HER2-targeted therapy. However, there are multiple more trials of CDK4/6 inhibitors alongside HER2-targeted therapy in the metastatic setting, including two phase III trials (PATINA and DETECT V).

In general, there is a disparity between the number of these approaches taken in the (neo)adjuvant setting and advanced/metastatic setting[184] This is likely to be largely due to commercial interests; the 5-year survival rate for non-metastatic HER2+ breast cancer is already favourable (96.7% across all races in the US[11]). A new therapeutic regimen would have to at least be comparable to the safety and efficacy of these existing treatments to obtain regulatory approval, and a strategy of licensing a therapeutic regimen based on relapse statistics inherently takes a long amount of time to obtain statistically significant

data. From this standpoint, it is more commercially attractive to test these drugs in the metastatic setting first, which helps to provide clinical data to support a rationale for testing in earlier lines of therapy.

Breast cancer clinical setting	**HER2-targeted agent**	**Non-HER2-targeted agent**	**Mechanism of action (non-HER2-targeted agent)**	**Clinical Trial phase *(Reg. number)***
HER2+, adjuvant	Trastuzumab emtansine	Atezolizumab	Anti-PD-L1 mAb (Immune recruitment)	III *(2020-003681-40)*
HER2+, neoadjuvant	Trastuzumab + pertuzumab + chemo	Atezolizumab	Anti-PD-L1 mAb (Immune recruitment)	III *(NCT03595592)*
HER2+, neoadjuvant	Trastuzumab + pertuzumab	Pembrolizumab	Anti-PD-L1 mAb (Immune recruitment)	II *(NCT03988036)*
HER2+, adjuvant, patients at high risk of relapse*	Trastuzumab	Nelipeptimut-S + GM-CSF	Cancer vaccine + immunoadjuvant	II *(NCT02297698)*
HER2+, ER+, neoadjuvant	Trastuzumab + pyrotinib	SHR-6390 + Anastrozole	CDK4/6 inhibitor + anti-estrogen	II *(NCT04236310)***

Table 3: Ongoing or planned phase II or III clinical trials in the neoadjuvant or adjuvant setting of HER2-targeted agents in combination with non-HER2-targeted agents. The displayed HER2-targeted and non-HER2 targeted agents are all in combination with each other, not in comparison. *Patients did not achieve a pCR from initial neoadjuvant therapy **This trial is not yet recruiting, the others are recruiting or have finished recruiting.

1.6 Pirin inhibition alongside targeted HER2 therapy as a potential therapeutic regimen

1.6.1 Pirin: an iron-binding transcriptional regulator

One relatively poorly characterised, yet promising candidate for targeting metabolism in tumor therapy is a protein known as Pirin (encoded by PIR). Pirin, a member of the cupin superfamily, is a highly conserved, nuclear[185], nonheme iron-binding protein that functions as a sensor of oxidative stress. Like other members of the cupin superfamily, it has two β-barrel domains, and is able to bind to iron in two states (Fe^{2+}, Fe^{3+}) in the domain towards the N-terminus[186]. The binding of these different oxidised forms of iron mediates its function; only Fe^{3+} facilitates the binding of pirin to the p65-DNA complex (an NF-$\varkappa\beta$ subunit)[187]. Therefore, pirin is a sensor of iron cellular redox[188;189]. Pirin is known to interact with the NF-$\varkappa\beta$ interacting BCL-3, and through this interaction, co-regulate the NF-$\varkappa\beta$ pathway[188;190]. Recently, it was identified that pirin plays a role in modulating autophagy-dependent ferroptosis[191]. Evidence also exists from data on fungi for a role of pirin in pyruvate catabolism, suggesting that it could be a regulator of cell metabolism[192].

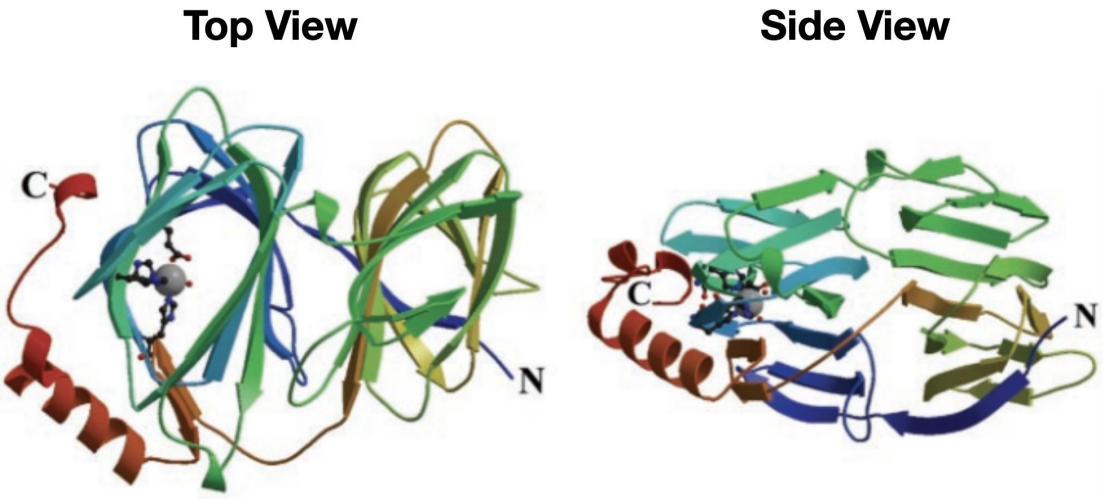

Figure 7: Top and side view of pirin (crystal structure). Adapted from Pang *et al.* (2004)[186]. Colored red to blue from the C-terminus to N-terminus. The side and top views both show the two β-barrel domains. β-barrel domain closest to the C-terminus (left) is able to bind iron (grey sphere) which mediates the function of pirin.

1.6.2 Pirin in cancer

Although there is currently little literature about the function of pirin, there are multiple lines of evidence that suggest an association between pirin and cancer. Recently, Perez-Dominiguez *et al.* (2021) published an excellent review of the evidence in the current literature to support the role of pirin in epithelial carcinogenesis[193]. However, no current direct evidence exists in the literature on the role of pirin directly in HER2+ breast cancer. In non-HER2 over-expressing breast cancer cell lines, pirin has been demonstrated to up-regulate E2F1, which is important for their proliferation *in vitro*, and in mouse

xenografts[194]. Pirin has also been shown to play a role in E-cadherin expression, but independently of BCL3-Slug signalling, suggesting that it also could play independent roles, and also provides evidence that pirin could have a functional role in cancer metastasis through activating an epithelial to mesenchymal transition (EMT)[195].

1.6.3 Development of a small molecule inhibitor of Pirin, EMBL-703625, by the EMBL-CBCF: promising anti-tumor activity, and a rationale for combination with HER2-targeted therapy in breast cancer

The EMBL Chemical Biology Core Facility (CBCF) identified and developed a series of ligands against pirin, which have been confirmed through co-crystal structures of these ligands with the pirin protein (data not shown). Through the characterization of these ligands, they have developed an encouraging rationale for the anti-tumor activity of these compounds. One molecule, named EMBL-703625, has been characterized in multiple tumor settings. *In vitro* data on cell lines from the EMBL-CBCF showed a broad antitumor activity range, including activity against cancers of the colon, brain, breast, lung, ovary, bone, pancreas and stomach (data not shown). The breast cancer cell lines also included the HER2 over-expressing SK-BR3.

Transcriptomic data performed on HeLa cells also showed results that were relevant in the context of current clinical and preclinical data for HER2 relapses. Firstly, many aspects of cellular metabolism were down-regulated following EMBL-703625 treatment, including in glycolysis (shown in Figure 8) and many signalling pathways involved in metabolism, and also HER2 treatment resistance, such as the EGFR and IGF1R receptors, and PI3K/AKT /mTOR signaling (data not shown). All of these have been implicated in HER2-targeted treatment resistance. On top of this, many heat shock protein genes were also down-regulated, including HSF1, one of the main transcription factors that regulates their expression. As previously discussed (Section 1.5.2.2, altered heat shock protein expression is also a mechanism of HER2-targeted treatment resistance. On top of this, solute carrier expression was also down-regulated by treatment with EMBL-703625. Recent evidence has also shown that trastuzumab emtansine resistant cell lines have altered solute carrier expression[196], indicating that this is also a potential node of HER2-targeted therapeutic resistance to what is likely to take over as the standard of care in early-stage HER2+ breast cancer treatment. EMBL-703625 also showed inhibition of multiple histone deacetylases (HDACs) and Sirtuin (SIRT) proteins, implying that it could also interfere with DNA replication and damage repair.

Taken together, these results from the EMBL-CBCF suggest an anti-tumor function of pirin inhibition through EMBL-703625, and provide an exciting rationale for co-treatment alongside HER2 inhibition, as it inhibits many of the cellular mechanisms known to be associated with resistance to HER2 targeted therapy.

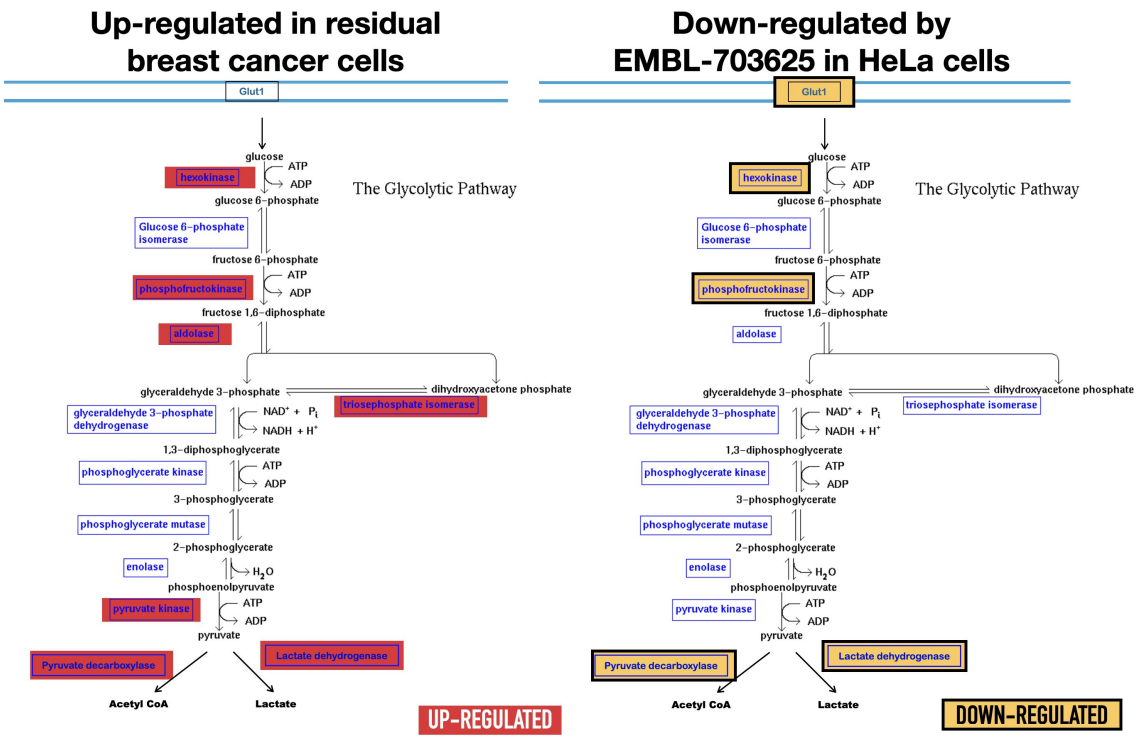

Figure 8: An example of overlap of glycolytic enzymes inhibited by EMBL-703625 and those that were up-regulated in residual breast cancer cells in mice. Results such as this suggest that pirin may impact nodes that residual cells use to survive. The mouse data were generated by Radic-Shechter *et al.* (2020)[175] and transcriptomic results were found on HeLa cells by the EMBL Chemical Biology Core Facility.

1.7 Project Hypothesis and Aims

1.7.1 Introduction summary and context for project hypothesis

As discussed, advances have been made in HER2+ breast cancer, significantly improving patient prognosis through more advanced surgical techniques, earlier cancer diagnosis, and the development of novel HER2-targeted therapies, to kill cancer cells that are "addicted" to the over-expression of the HER2 oncogene.

Despite these advances, tumor relapses after targeted therapy still present a significant problem in the clinic for HER2+ breast cancer patients. Because of this, large amounts of research are being focused on identifying ways in which some cells are able to evade targeted therapy and re-grow to form tumors.

There are various ways that HER2+ breast cancer cells are able to evade treatment, for example, through an altered cellular metabolism, signalling pathways such as the NF-$\varkappa\beta$ pathway, truncated HER2 proteins, drug efflux transporters, and altered heat shock protein activity. Partially successful efforts have been made to overcome some acquired resistance characteristics, through targeting the HER2 receptor with more than one drug in order to more comprehensively ablate its function. This is referred to as a "HER2 blockade".

Whilst a HER2 blockade during initial neoadjuvant or adjuvant treatment has led to decreased rates of tumor relapse and prolonged patient survival, many patients still relapse. Because of this, some pre-clinical and clinical lines of enquiry are now to target other proteins alongside the HER2 receptor, in order to prevent cells utilising "escape" pathways. A comprehensive understanding of how inhibition of other proteins impacts on cell survival and their characteristics are of critical importance to successfully develop clinical strategies that use this approach.

Targeting of Pirin, an iron binding transcriptional co-regulator that binds to NF-$\varkappa\beta$, could serve as a promising strategy alongside HER2-targeted treatment. A ligand against pirin, EMBL-703625, developed by the Chemical Biology Core Facility (CBCF) at EMBL has been demonstrated to show promising activity against lung tumor cell xenografts in mice, and is very well tolerated by mice. A transcriptomic analysis, also performed by the EMBL CBCF also showed that pirin inhibition through EMBL-703625, de-regulates many of the processes that are shown to play a role in acquired resistance to HER2-targeted therapy, such as a de-regulation of glycolysis and altered expression of heat-shock proteins.

1.7.2 Project Hypothesis

Due to the overlap between the effects of pirin inhibition and mechanisms of tumor resistance in HER2, and that EMBL-703625 is well tolerated in mice, and that is shows anti-tumor effects against tumor xenografts, this project has the following hypothesis:

Pirin inhibition through EMBL-703625 administration targets pathways that HER2 over-expressing breast cancer cells may use to evade targeted therapy and re-grow into relapsed tumors, therefore meaning in combination, dual HER2 and Pirin inhibition could effectively kill these cells and reduce their ability to re-grow.

1.7.3 Project Aims

To address this hypothesis, this project has the following aims:

1. Develop and implement high-throughput experimental techniques on 3D grown cells that will allow a comprehensive assessment of combination therapy with two different drugs, that is reproducible and can be implemented in the future for different cancer types and drugs
2. Use these experimental techniques to functionally characterise how combination therapy with lapatinib and EMBL-703625 behave in combination with each other to impact upon the survival and re-growth ability of HER2 over-expressing breast cancer cells
3. Develop a microscopy pipeline that will allow a 3D spatio-temporal assessment of the metabolic state of cells, and will allow an understanding of intra-tumor heterogeneity.
4. Analyse previously generated data from tumor-inducible transgenic mice, in order to understand nodes of vulnerability in tumor and residual cells, compared to normal mammary gland cells.

1.8 Experimental systems used in this project: human HER2+ breast cancer cell lines and transgenic primary mouse mammary gland cells

1.8.1 BT-474 and SK-BR3: human, HER2 over-expressing breast cancer cell lines

To address the aims of this project, two main experimental systems were used: human, HER2+ breast cancer cell lines, BT-474 and SK-BR3, and transgenic mouse primary cells. For both experimental systems, all experiments were conducted in 3D culture using matrigel. The reason for 3D is because of the closer resemblance to *in vivo* conditions than 2D culture allows; it has been argued that culturing in 2D is a large reason as to why pre-clinical data often do not correlate with clinical data[197]. As seen in Figure 9, these cell lines both grow in matrigel, and form distinct 3D structures.

BT-474[198] and SK-BR3[199] are both well-characterised and studied breast cancer cell lines. They have the advantage of convenience, low cost, and generating reproducible results. As well as this, they can be used in many different experimental settings. To inhibit HER2 and pirin in these cell lines, Lapatinib, an approved HER2 TKI (see Table 2) and EMBL-703625 were used, respectively. The initial characterisation of combination HER2 and pirin inhibition was performed on these lines (Section 2.1.1), before in-depth high-throughput experiments were performed to determine whether this interaction was synergistic (Section 2.1.2). Further understanding of these results then came through transcriptomic experiments of cells treated with lapatinib or EMBL-703625 in monotherapy, or in combination with one another (Section 2.2). To gain an understanding into the abilities of cells to re-grow following this treatment, re-growth experiments were also performed, by selecting for persister cells following initial treatment, and then removing treatment to observe if re-growth was more compromised by combination therapy, compared to either agent in monotherapy (Section 2.3). As well as this, lapatinib or EMBL-703635 were characterised alongside treatment with oxamate, an inhibitor of cellular glycolysis, based on the hypothesis that these drugs may interact, in part, through cellular metabolism (Section 2.4). BT-474 and SK-BR3 were also assessed to observe their responses to consecutive treatment with lapatinib and EMBL-703625 (or vice versa) (Section 2.6). In order to understand cell-cell heterogeneity SK-BR3 was transfected with a high dynamic range fluorescent sensor for the NAD+/NADH ratio named SoNar, was characterised using light-sheet microscopy, where methods were established with the aim of being able to understand cell-cell heterogeneity on a spatial and temporal basis (Section 2.7). Finally, this project also re-analysed data generated by Radic-Shechter *et al.* (2020)[175] in order to observe metabolic nodes of vulnerability in mouse tumor and residual cells (Section 2.8). These results could be used in future directions to inform on further pre-clinical strategies in HER2-overexpressing cells.

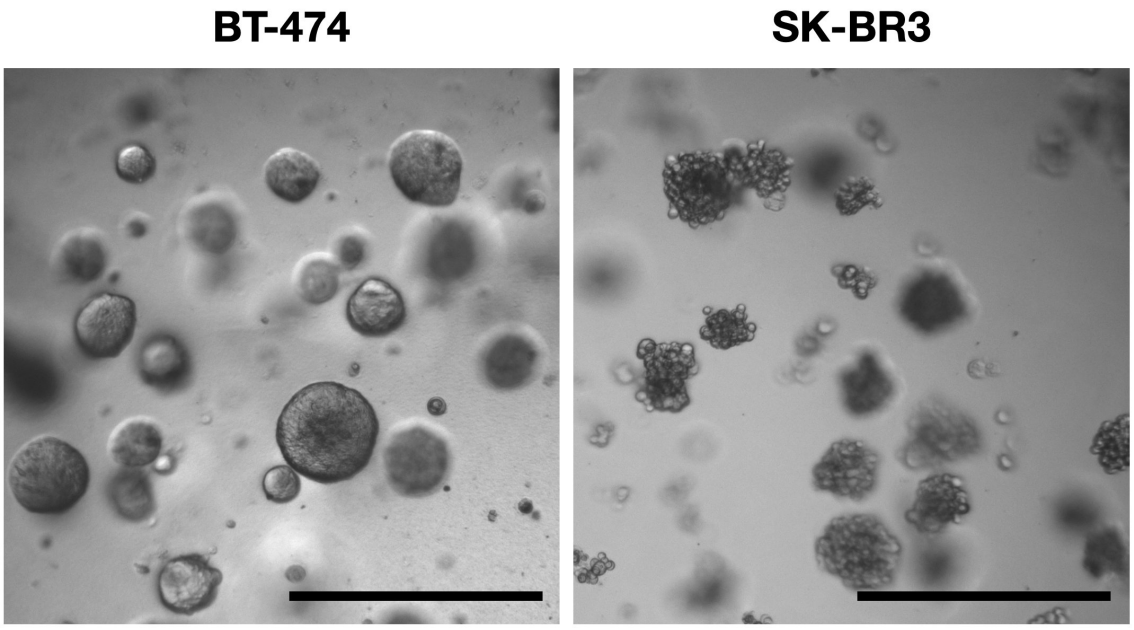

Figure 9: **BT-474 and SK-BR3 organoids grown for 14 days in matrigel.** BT-474 cells grown in 3D culture using matrigel form "ball" like structures, where it is difficult to distinguish the boundaries of each cell. SK-BR3 cells are more loosely associated with each other, forming "grape" like structures. Scale bar = 500µm.

1.8.2 Transgenic, doxycycline inducible mouse primary cells

Transgenic mouse primary cells were used to compare neoplastic cells with non-neoplastic cells. Using the doxycycline inducible system described in Figure 10, mammary gland derived cells were induced *in vitro* to induce oncogene over-expression and induce a neoplastic transformation. These were compared to cells that were not induced (never induced) to gain a direct comparison of how therapy with lapatinib and/or EMBL-703625 affected tumor cells compared to non-tumor cells (Section 2.5). Experiments are planned *in vivo* to compare first-line efficacy of lapatinib and EMBL-703625 in combination therapy, compared to either agent in monotherapy. This same murine experimental system was also used *in vitro* by Ashna Alladin and Ksenija Radic-Shechter (*et al.*) to generate transcriptomic and metabolomic data to assess differences between never induced, tumorigenic, and residual cells (following oncogene de-induction). As part of this project, these data were analysed to identify any differing cellular processes or pathways that could potentially serve as nodes of vulnerability in tumorigenic or residual cells (Section 2.8).

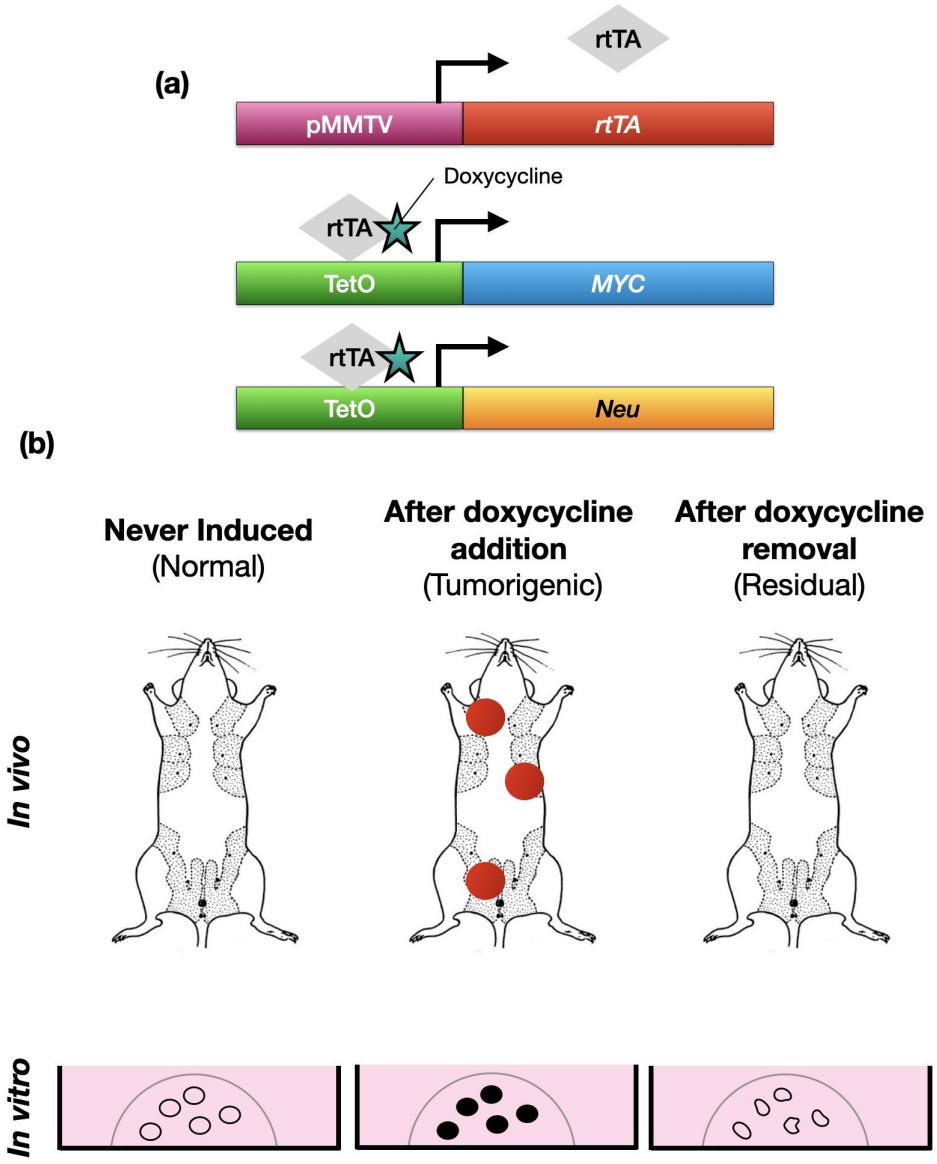

Figure 10: **The transgenic, doxycycline inducible mouse experimental system utilised by the Jechlinger Lab** (a) The mice are transgenic for the reverse tetracycline transactivator (rtTA) under the control of the mouse mammary tumor virus (MMTV) promoter, causing it to be uniquely and constitutively expressed in the mouse mammary gland. The mice are also transgenic for MYC and/or Neu, under the control of the Tet operon (TetO). When doxycycline is introduced to these cells, it interacts with rtTA, meaning that it can bind to the TetO and induce expression of MYC and Neu. (b) This system can be used *in vivo*, through introducing doxycycline through their food. It can also be used *in vitro*. 3-D grown organoids form a hollow acinus structure, upon doxycycline addition to the media, the cells begin to divide and lose polarity[77] and the acinus grows and becomes filled. In the *in vivo* and *in vitro* systems, removal of doxycycline causes the cells to lose "addiction" to these oncogenes and regress towards a residual state. In the *in vivo* system, a large number of these mice will eventually relapse, making them an ideal system to study how particular treatment regimens affect tumor growth, and rates of relapse.

Chapter 2

Results and Discussion

In the Results and Discussion chapter, each section describes results from this project, followed by a discussion of those results. A more generalised discussion with wider contexts and future directions for this project can be found in Chapter 3 (Page 155).

2.1 Assessing combinatorial interactions between Lapatinib and EMBL-703625 in BT-474 and SK-BR3 cells

2.1.1 Lapatinib and EMBL-703625 have a large combinatorial effect on cell viability over time

Evidence from the literature surrounding mechanisms of relapses in HER2 overexpressing breast cancer patients following HER2-targeted therapies suggest that there are mechanisms of vulnerability that could be targeted to prevent tumor recurrence. Data from the EMBL CBCF, coupled with data from the literature (see Section 1.6) suggest that targeted inhibition of pirin, an iron binding transcriptional regulator that interacts with the NF-$\kappa\beta$ complex, coupled with HER2-targeted therapy, could potentially reduce the probability of relapses. This is the hypothesis of this project.

To address this hypothesis, this project used lapatinib, an already licenced HER2 tyrosine kinase inhibitor, and EMBL-703625, an inhibitor of pirin developed by the EMBL-CBCF. This project used a combination of human HER2 overexpressing cell lines known as BT-474 and SK-BR3 as well as tumor-inducible mouse primary mammary gland cells (these are described in detail in Section 1.8).

In order to establish if lapatinib and EMBL-703625 had a combinatorial effect on BT-474 or SK-BR3 cell viability over time, combination treatment was compared to either agent in monotherapy. In order to assess this, a time-designed experiment was used using the CellTitre Glo viability assay (See Supplementary Figure S.1) using a black-walled 96-well plate. This assay measures ATP levels in each individual well and gives a luminescent read-out, which can be normalised to other wells to give relative values. BT-474 and SK-BR3 cells were treated with lapatinib and EMBL-703625 at varying concentrations, with or without a constant concentration of the other drug. Preliminary experiments determined appropriate concentration ranges to gain sensitivity in these experiments (data not shown). This would allow a first assessment of how how differing concentrations of EMBL-703625 and lapatinib would have effects in monotherapy, and also as part of a combination therapy. This also allowed an assessment of what particular combination concentrations appeared to elicit the biggest combinatorial effects on cell viability; these concentrations (displayed later in Table 4 (Page 71)) were used in further experiments comparing monotherapy to combination therapy for transcriptomic (Section 2.2), consecutive treatment (Section 2.6) and, specifically for SK-BR3, for light-sheet microscopy experiments (Section 2.7).

As shown in Figure 11(a and c), lapatinib monotherapy (blue bars) had a concentration-dependent effect on cell viability for both lines. For SK-BR3 (part a), the lower concentra-

tions of lapatinib (0.1-0.2µM) appeared to have a moderate effect, with viability read-outs tending to remain relatively close to levels before treatment. In combination, treatment at 0.2µM lapatinib and 1µM EMBL-703625 appeared to have the most dramatic effect, and so 0.2µM lapatinib was chosen as the constant concentration for varying concentrations of EMBL-703625 (shown in part b). In BT-474 it was less apparent what concentration combination yielded the most obvious change in effect (part c), and so 1µM lapatinib was chosen as the constant concentration for part d. In both lines, EMBL-703625 showed concentration-dependent effects on cell viability (part b and d) in a similar fashion to lapatinib.

In combination (red bars), the viability was lower across all concentrations tested compared to monotherapy (blue bars). At certain concentrations, the difference more pronounced, for example, in SK-BR3 cells at 1µM EMBL-703625 and 0.2µM lapatinib, monotherapy treatment caused an approximate +0.2 and -0.1 fold change in viability, compared to before treatment, respectively. However, in combination, there was an approximately -0.7 fold change in viability. Similarly, in BT-474, 1µM of EMBL-703625 or 1µM of lapatinib in monotherapy caused +0.25 and -0.45 fold changes in viability, respectively. These two same concentrations in combination led to an approximately -0.75 fold change in viability.

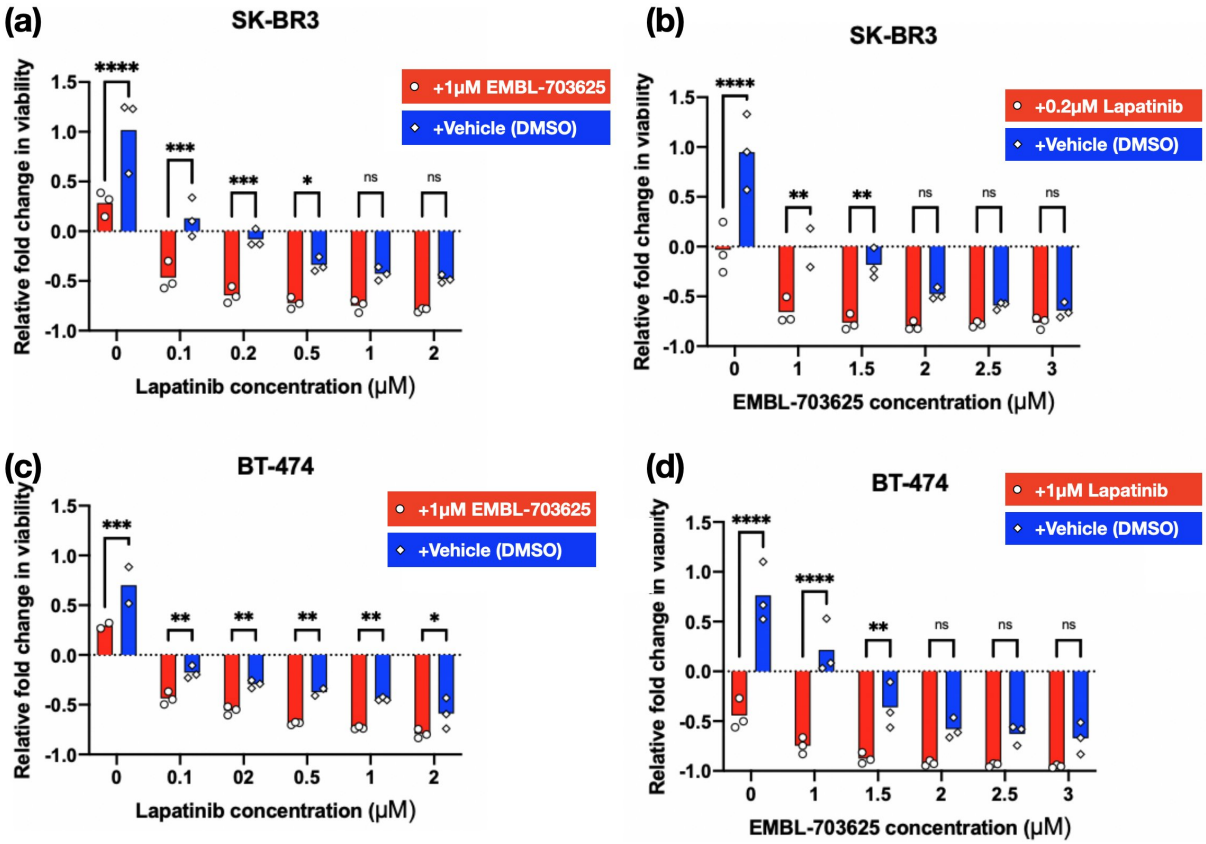

Figure 11: **Changes in cell viability measured over 72 hours in BT-474 and SK-BR3 cells, comparing singular drug treatment (blue bars) to combination treatment (red bars).** Relative fold changes in viability are normalised to viability readings taken from 10 randomized wells from a parallel plate at the point of treatment addition. Five technical replicates were taken for each treatment and the mean was taken. Data points for each experimental replicate (Repeated 3 times) are plotted. Each bar shows the mean for these three replicates. Statistical significance between bars were calculated using Šidák's multiple comparisons test. Significance notation is as follows: ns (not significant) - $p \geq 0.05$; * - $p < 0.05$; ** - $p < 0.01$; *** - $p < 0.001$; **** - $p < 0.0001$.

2.1.2 Assessing drug synergy between lapatinib and EMBL-703625 in BT-474 and SK-BR3 cells

2.1.2.1 The importance of testing for drug synergy, and synergy modelling strategies

Combination treatment is used in cancer therapy in order to have a stronger therapeutic effect and reduce the probability of tumor recurrence and/or resistance, whilst minimising the patient side effects. Each drug administered to treat a tumor has its own level of potency, and administering multiple drugs that are known to have anti-tumor properties will likely have a larger tumor killing effect than any single drug on its own. However, this often comes with the trade-off that off-target patient side effects are also increased, causing many treatment regimens to fail to progress from early phase clinical trials. To optimise treatment, drug combinations that have a greater than expected effect on cancer cells (higher than the expected sum effects of all the individual drugs), also known as drug synergy, are often considered attractive treatment regimens if they do not also lead to increases in toxicity to healthy body tissues. This would allow lower dosages of each drug to be administered to each patient, reducing the probability or severity of serious side effects arising, whilst maximising tumor killing effects.

Although assessing drug synergy in cancer is designed to bring benefits at the level of the patient, experimental synergy assessments are performed at a cellular level, because it requires testing multiple drug concentrations on the same set of cells. There have been multiple mathematical models developed to assess synergy. These are all based off distinct null hypotheses and assumptions, and therefore utilise different mathematical models to achieve their effects, which inherently also bring their own set of strengths and weaknesses. The most commonly referred to models are the Bliss independence model[200], and the Loewe additivity model[201]. The Bliss independence model assumes the null hypothesis that each drug has stochastic, independent effects. In other words, that there is no added effect from drug-drug interactions. For example, if Drug A and B, both at 1.0µM, reduced cell viability to 60% of the control, then the predicted combined additive effect, assuming no synergy or antagonism, would be 36% (0.6 x 0.6 = 0.36) (Figure 12(a)). A combined effect that leads to less than 36% remaining viability would be synergistic (Figure 12(b)), and more than 36% would suggest drug antagonism (Figure 12(c)).

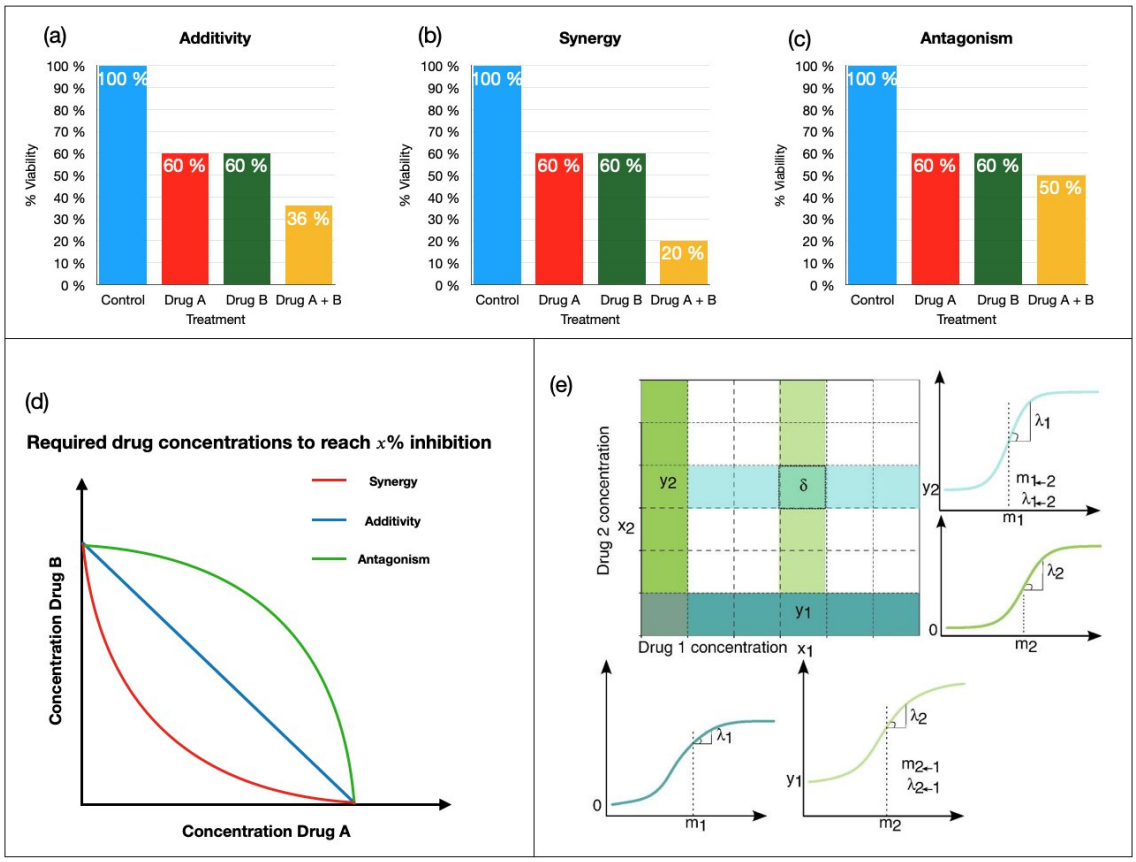

Figure 12: **Representations of Bliss Independence, Loewe Additivity and ZIP synergy models of drug interaction testing.** Representations of the Bliss Independence Model (a),(b) and (c). (a) Each drug has its own effect on cell viability; the null hypothesis of no interaction suggests that the drugs elicit their combined effects as expected. (b) Drug synergy is when the combined killing effect is more than expected under the null hypothesis. (c) Drug antagonism is when their combined killing effect is less than expected under the null hypothesis. Representation of the Loewe Additivity Model (d). The graph displayed shows hypothetical dose response curves of combinations of drugs to reach a 50% reduction in cell viability. The Loewe Additivity model suggests that each drug has a linear relationship with its effects, therefore, a combination of drugs that have no interaction would also have a linear relationship (grey line). Drug synergism is shown when a lower than expected concentration of one or both drugs is required to reach the same level of killing. Drug antagonism is when a higher than expected concentration is required to do the same. Representation of ZIP synergy model (e). ZIP synergy modelling focuses on the changes in the dose response curve, taking into account the dose response curves of each individual drug, and when in combination with the other drug, at each concentration. *((e) is adapted from Yadav et al., (2015)[202].)*

In contrast, the Loewe additivity model focuses on the relationship between drug dosages and effects. This model has the null hypothesis that each drug will elicit exactly the same effect on the cells (thereby not being synergistic when in combination), and the effect of each drug has a linear relationship to its dosage. For example, if Drug A had a concentration of 2.0µM to elicit a 50% reduction in cell viability, and Drug B had a concentration of 1.0µM to elicit a 50% reduction in cell viability, then half of their respective concentrations (1.0µM Drug A + 0.5µM Drug B) in combination would also reduce viability by 50% (both contributing to 25% of reduction of cell viability each). Any deviation from this linear relationship would either be drug synergy, or drug antagonism, depending on if the combined effect was larger or smaller than the expected linear relationship under the null hypothesis. A visualisation of this is illustrated in Figure 12(d)).

Both of these models are widely used, but however, have disadvantages. The Bliss model fails to account for combined effects over a maximum possible drug effect threshold. For example, if Drug A's effect on cell viability plateaued at 75% (regardless of concentration), then any added effect of Drug B would be, by definition, synergistic. The Loewe model assumes a linear relationship between drug concentration and effect, but many drugs have a non-linear effect on cell viability when their own concentration is increased. Steeper or shallower parts of this dose-response curve, would indicate that a drug is synergistic, or antagonistic, with itself, which is impossible.

The Zero Interaction Potency (ZIP) model is a more recently proposed model[202] that is designed to capitalise on the advantages of both the Bliss and Loewe models, without their drawbacks. It focuses on the gradient of dose response curves of each individual drug. If two drugs had no interaction, then there would be theoretically no changes to the steepness of the drug-response curve. However, if there was a synergistic drug-drug interaction, then the steepness of the curve would be increased. Conversely, antagonistic drug-drug interactions would cause a decrease in the steepness of the curve.

2.1.2.2 Experimental design to assess drug synergy between lapatinib and EMBL-703625

Because of the advantages of the ZIP synergy model, this model was chosen for the following synergy experiments. These experiments were designed using BT-474 and SK-BR3 cells grown in 3D culture to observe if lapatinib and EMBL-703625 had synergistic interactions. These experiments involved increasing the concentration of each drug, individually, and in combination with one another.

In order to assess possible synergy between lapatinib and EMBL-703625 using the ZIP synergy model, experiments were designed using black-walled 96 well plates. Using multiplexing of the luminescent Promega CellTitre Glo^{TM} 3D cell viability and CellTox^{TM} green flourescent cytotoxicity assay, a comprehensive overview of the effect of combinatorial treatment with the two drugs could be assessed. ZIP synergy calculations were based on the results of the luminescent cell viability assay. This is because this assay is highly sensitive with relatively little noise, and also because of the assay read-out; the viabil-

ity assays give a read-out of 100% relative viability (only vehicle treated) to 0% viability (absence of any ATP) whereas the cell-toxicity assay increases in read-out relative to the control and it is not possible to determine what the upper limit of the assay is. This means that ZIP synergy calculations are not possible with this assay. Therefore, the cell toxicity assay was used as a secondary validation method to compare with the viability assay results.

In this experimental design, it is important to have multiple drug concentration increments as well as an appropriate number of technical replicates for accuracy. To serve both of these purposes, a black-walled 96 well plate format was used, with the black-walls allowing good quality read-outs from both the luminescent viability assay and the fluorescent toxicity assay. To allow for multiple drug increment concentrations for accurate synergy calculations, along with at least three technical replicates for each treatment, two 96 well plates were used for each experiment, with the concentration of one drug at more specific increments on one plate, and the other at more specific increments on the other (Figure 13).

To calculate the ZIP synergy scores, SynergyFinder 2.0, an open-source "R" based package, was used[203]. Data was outputted from SynergyFinder 2.0, and the synergy landscape was visualised in "R", using the "ggplot2" package. To combine the separate plates for each experiment into a single landscape, data were interpolated using linear interpolation and combined with each other, taking the mean of any specific treatments that overlapped between the plates. Linear interpolation was used because it had very minimal influence on the LL-4 dose response curves relative to the non-interpolated version (data not shown). Quality control runs were also used on single plates (without combining with the other) to verify that resulting synergy landscapes were not influenced by the interpolation, relative to non-interpolated data (data not shown).

Figure 13 (next page) shows an illustration of this experimental design.

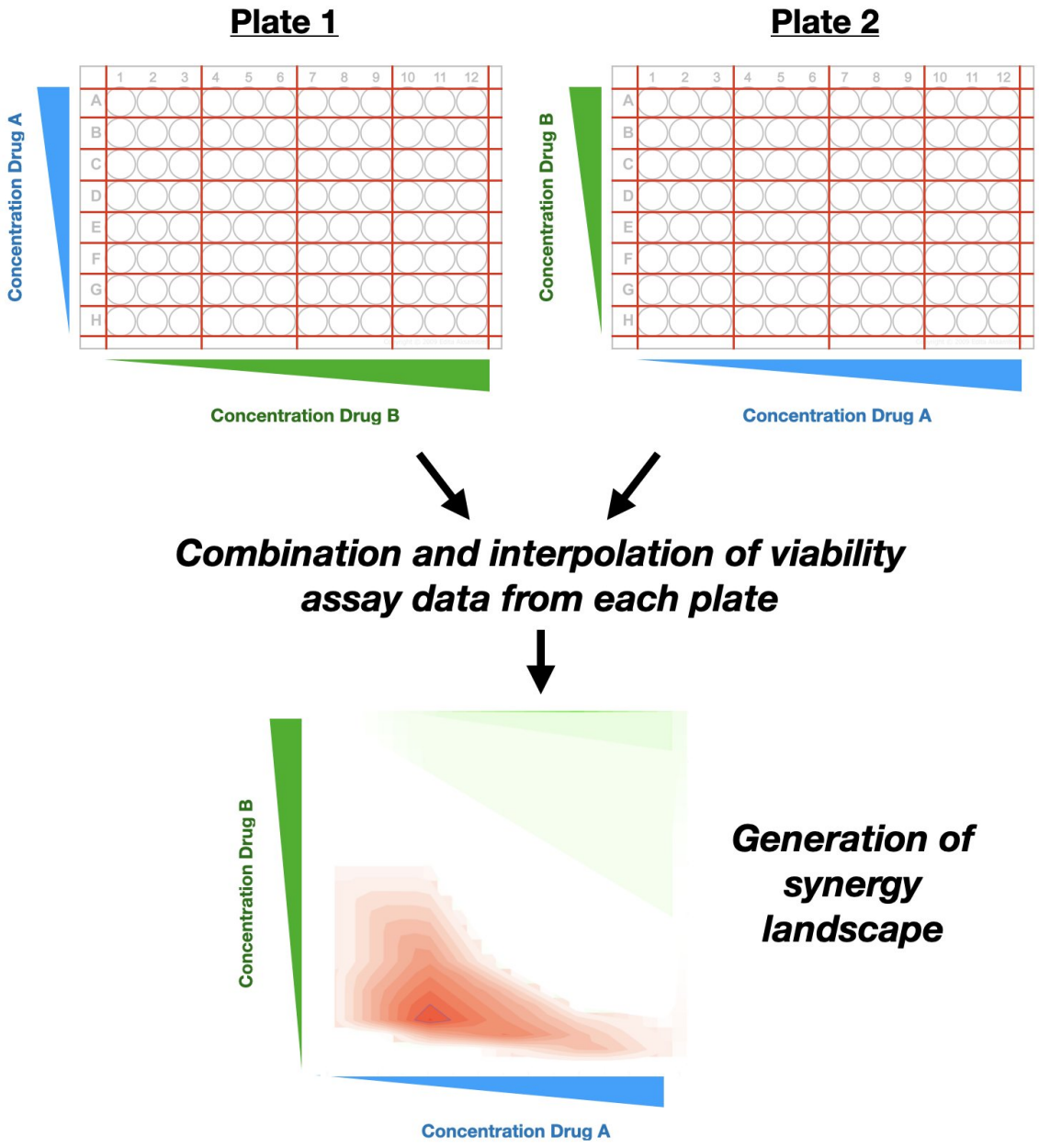

Figure 13: **Schematic of how viability data was processed and outputted as synergy landscapes**. The CellTitre Glo™ Viability Assay was used on cells grown in black-walled 96-well plates in order to obtain viability readings, which were normalised as a percentage to vehicle (DMSO) treated cells. To obtain viability readings for lapatinib and EMBL-703625 at a good number of concentration increments, whilst also using three technical replicates in each experiment, 8 concentrations of one drug and four of another could be used on each 96-well plate. To allow for more resolution in the synergy landscape, two 96-well plates were used in each experiment, with the drugs used transposed between them, meaning that both drugs had 8 incremental concentrations in the resulting synergy landscape after result combination. To combine the results, the viability readings were interpolated to account for specific concentration combinations that were only available on one plate, and then averaged (mean). The open-source "R" package "SynergyFinder 2.0" was then used to calculate ZIP Synergy scores using these data, which is presented in a landscape, to visualise which concentration areas yield different synergy scores.

2.1.2.3 Lapatinib and EMBL-703625 synergistically affect cell viability in BT-474 and SK-BR3 cells

Viability assay read-outs across the drug concentration ranges showed a large combinatorial effect in both cell lines, with the combination treatment consistently having lower viability read-outs than their corresponding single drug treatments. Consistent with this, the cell toxicity data showed a similar trend, with toxicity read-outs consistently being higher in the combination treatments, relative to either of their corresponding singular treatments. However, in contrast to the viability read-outs, the trends with the toxicity assay were not as consistent. Certain combination treatments showed higher toxicity readings than others at higher drug concentrations (for example, in Figure 14, 1.0µM EMBL-703625 + 1.0µM Lapatinib gave a toxicity read-out of 649.7%, compared to 2.0µM EMBL-703625 and 3.0µM Lapatinib with a read-out of 524.1%). This could be due to simple noise from the assay read-outs, or due to the nature of the assay; the cell toxicity assay gives a read-out of exposed nucleotides, in more compromised cells in higher concentration treatments, higher levels of cell lysis could mean a higher rate of diffusion of DNA into the cell media. The diffuse DNA (and therefore flourescent signal) could possible lead to less intense plate reader read-out values, particularly as flourescence was read from the bottom of the well due to the position of the matrigel droplets.

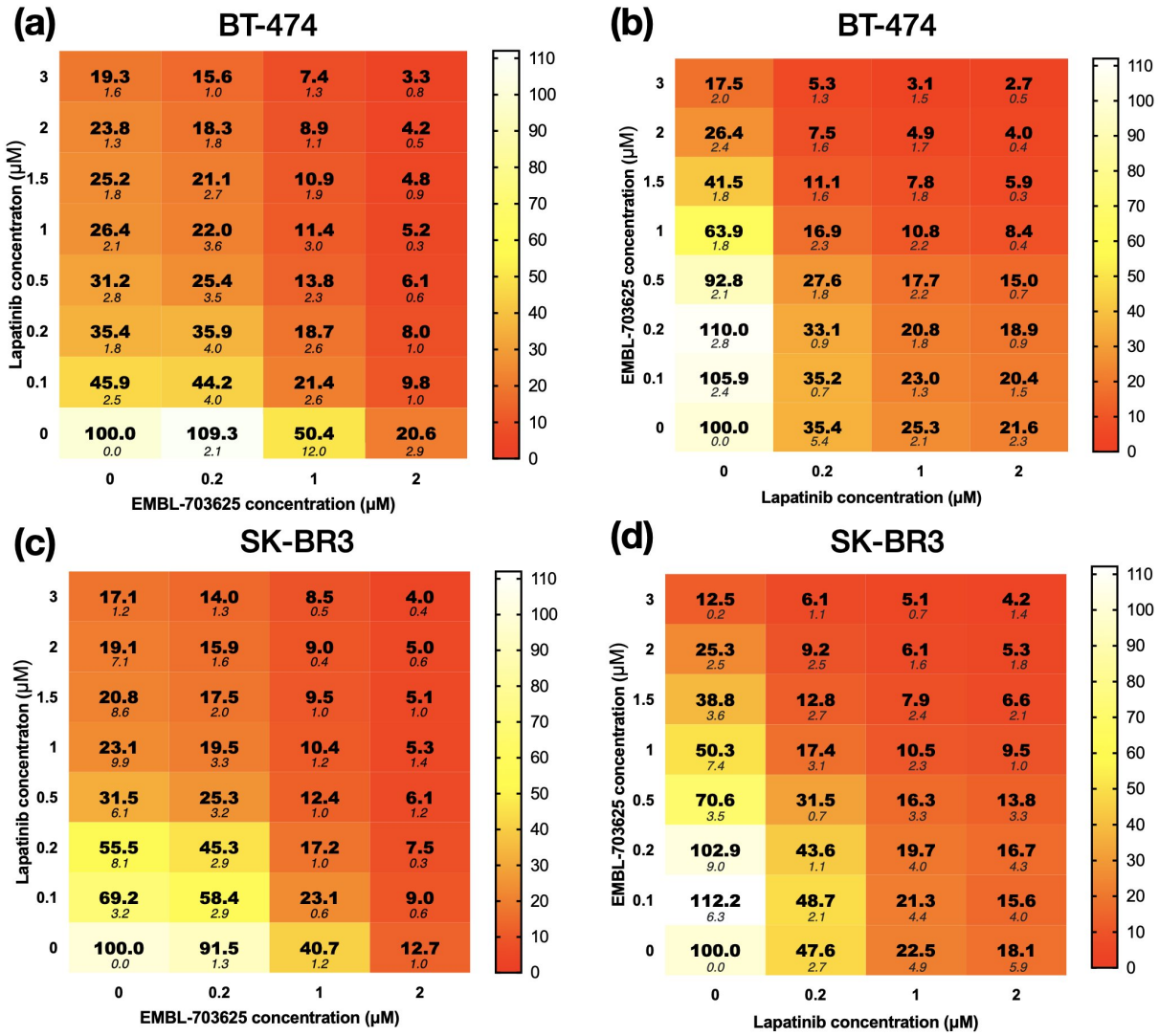

Figure 14: Viability heatmaps (from the Promega CellTitre Glo™ 3D cell viability assay) for BT-474 (a) and (b) and SK-BR3 (c) and (d) cells treated with lapatinib and EMBL-703625 at varying concentrations. The experiment was repeated 3 times, and each experiment had 3 technical replicates.

Figure continued on next page.

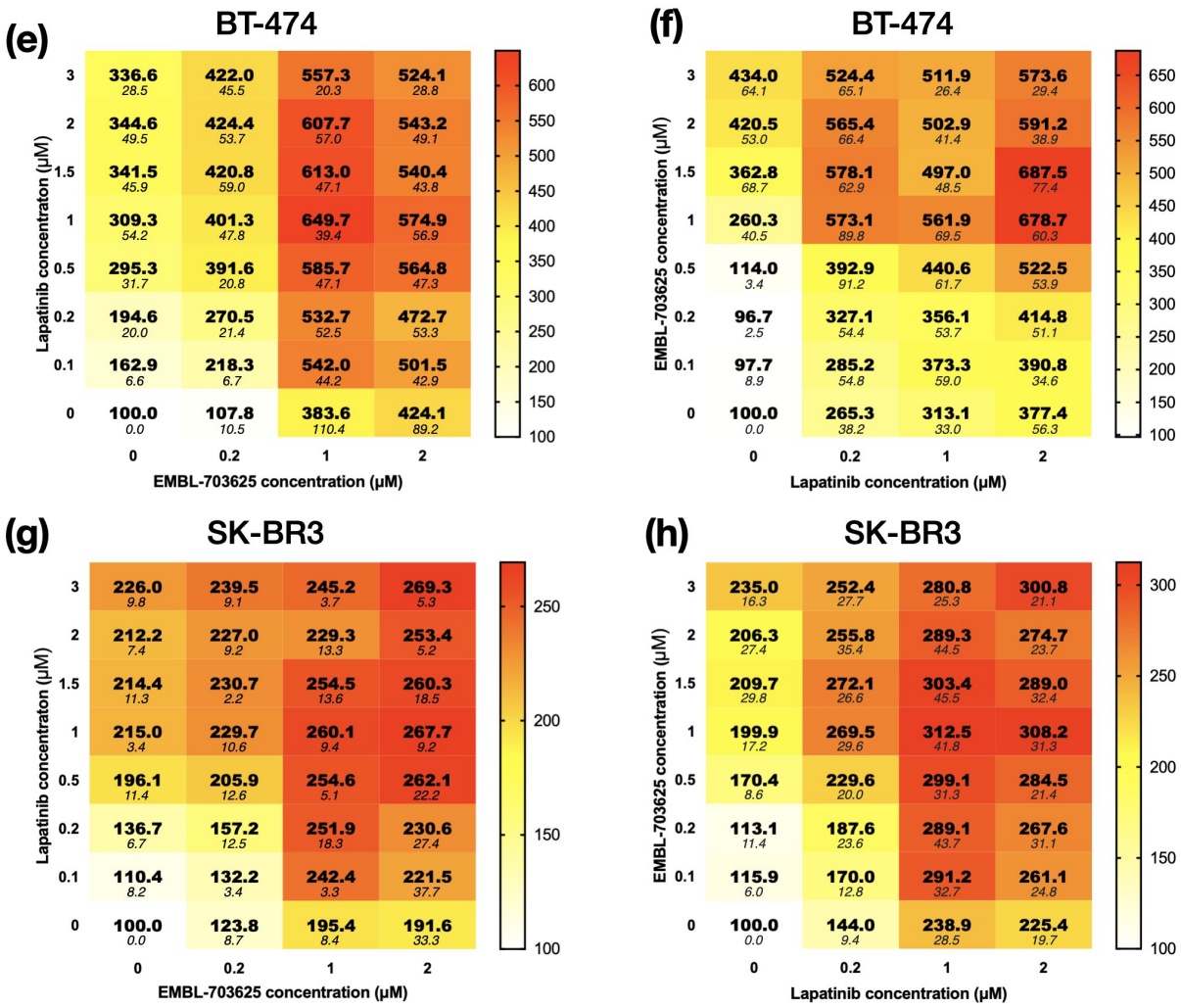

Figure 14: **Heat-maps of relative cell viability (using the Promega CellTitre Glo™ 3D cell viability assay) (a-d) and toxicity (using the CellTox™ green fluorescent cytotoxicity assay) (e-h) for BT-474 and SK-BR3 cells treated with varying concentrations of lapatinib and EMBL-703625.** Displayed values in bold are the means of 3 experimental replicates, which each had 3 technical replicates, the smaller text in italics is the SEM. Experiments were performed on 96 well plates; in order to get a good resolution of different drug concentrations and appropriate amounts of technical replicates, treatments were performed on separate plates, which each drug regime transposed (see Figure 13).

An interesting note from Figure 14 (a) and (b) is that lower concentrations of EMBL-703625 (0.1-0.2μM) led to small increases in viability of BT-474 cells, relative to the control. It is unclear why this is, but also notable that this increase in viability is not carried over to when in combination with lapatinib (relative to either single dose).

Although the combination treatments showed lower levels of viability and higher levels of toxicity compared to either of their corresponding singular treatments, this is not necessarily indicative of drug synergy. In fact, two drugs can kill more cells than either one in monotherapy, and still be considered antagonistic (see Figure 13) for a full explanation). To assess if these interactions were in fact synergistic, additive or antagonistic, ZIP synergy scores were calculated for each specific concentration using SynergyFinder 2.0 after data were interpolated and combined. These data were visualised as a landscape

(Figure 15). There is no consensus over which synergy score suggests drug synergy, antagonism, or additivity, but it is largely agreed that scores above 10, or below -10 suggest drug synergy or antagonism, respectively. Scores within this range suggest possible additivity. To visualise this, a blue line was added in the synergy landscape to highlight which areas had a synergy score above 10 or below -10 (although no results from any experiements in this project had a ZIP synergy score below -10).

As shown in Figure 15(a) (BT-474) and (b) (SK-BR3), all ZIP-synergy scores were positive values, suggesting a lack of drug antagonism across the concentration ranges used. BT-474 showed drug a ZIP synergy score $>$10 (surrounded by blue line) across a wider range of drug-concentrations tested than SK-BR3, reaching a peak score of 20 at between 0.25 - 1.0µM lapatinib, and 0.1 and 0.5µM EMBL-703625. SK-BR3 showed ZIP synergy score peaks at two concentration ranges, 0.1-0.75µM Lapatinib and 0.1 - 0.25µM EMBL-703625, and also 0.1 - 0.3µM Lapatinib and 0.6-1.3µM EMBL-703625. The data for the non-interpolated and combined plates are shown in Supplementary Figure S.2. Overall, this suggests that BT-474 and SK-BR3 both display drug synergy at certain lapatinib and EMBL-703625 concentrations, but that synergy is generally stronger in BT-474 cells, both in terms of the peak ZIP-synergy score and also in terms of the range of lapatinib/EMBL-703625 concentrations.

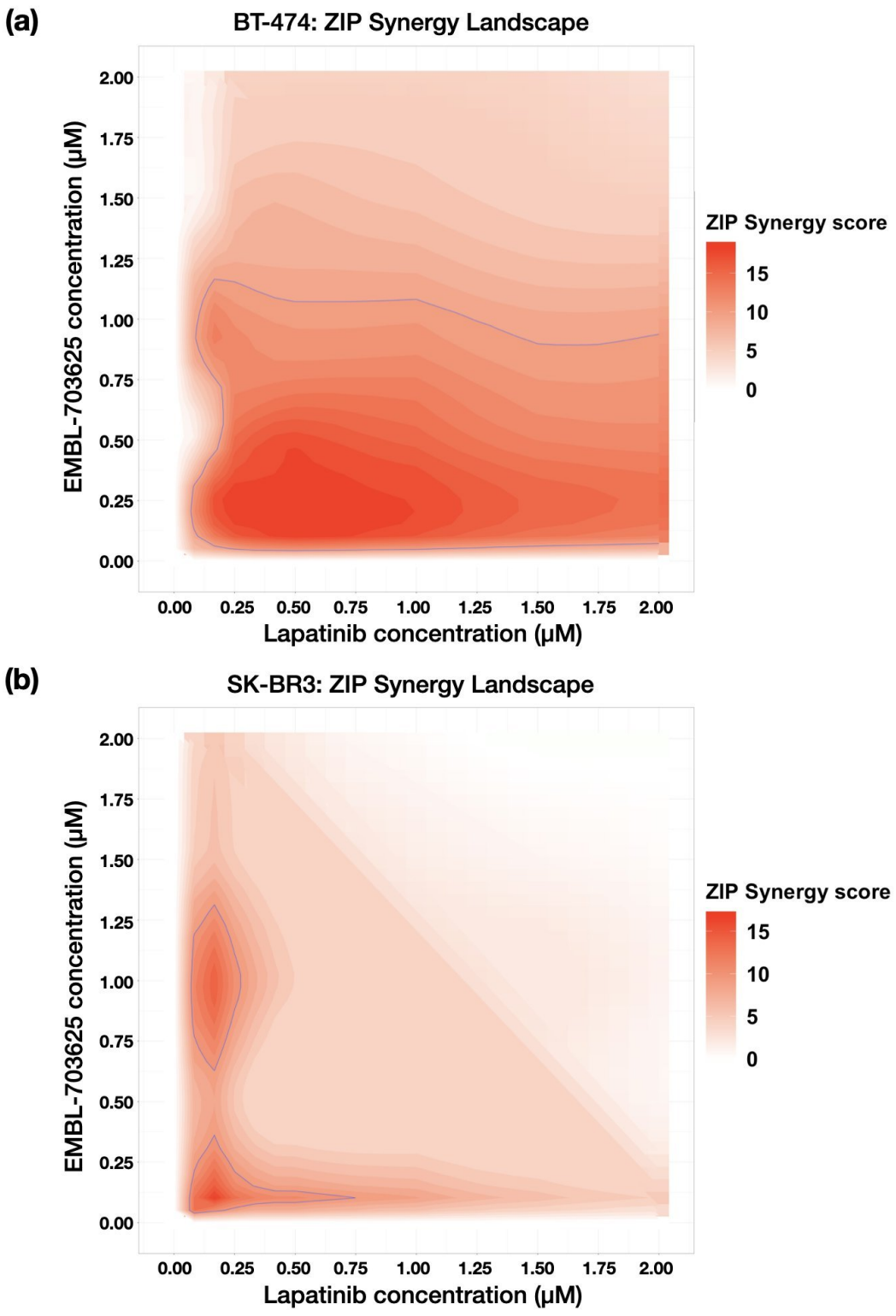

Figure 15: **ZIP Synergy landscape of Lapatinib and EMBL-703625 for BT-474 (a) and SK-BR3 (b)** ZIP synergy data was generated by SynergyFinder 2.0, and plotted in R using the ggplot2 package. The blue line denotes ZIP synergy scores that are higher than 10; there is no consensus of which synergy scores denote synergy, but it is widely agreed that a synergy score above 10 is confidently synergistic. To generate a combined synergy map from multiple plates, viability data from each plate layout were interpolated using linear interpolation (total of 25 data points for each concentration range) and processed using SynergyFinder 2.0 (See Figure 13 for a more detailed explanation). The mean of data points that had overlapping values between plates were taken. As a quality control, interpolation was performed on individual plates and synergy landscapes were generated, which minimal changes to the Synergy landscape using this method (data not shown).

2.1.3 Discussion of Section 2.1: synergy between lapatinib and EMBL-703625

To address the criteria that a drug combination would need to be effective in initial tumor reduction, lapatinib and EMBL-703625 were tested in the human HER2 over-expressing breast cancer cells lines, BT-474 and SK-BR3. BT-474 represents a HER2+/ER+ subtype[198] (also known as Luminal B), whereas SK-BR3 represents a HER2+/ER- subtype[199]. The latter subtype is associated with a worse prognosis and response to treatment, which is partially because ER+ tumors respond relatively well to endocrine therapy[204;205]. However, growing evidence suggests that cross-talk between the estrogen receptor and HER2 receptor could serve as a mechanism of tumor resistance, including to modern and widely used HER2-targeted therapies, such as trastuzumab[206;207;208].

A drug combination that kills a larger than expected amount of cancer cells could translate into high clinical efficacy. Figure 11 shows how combination treatment reduced viability of these cell lines over time. In both cell lines, it is apparent that a combination of these drugs are able to cause meaningful reductions in viability, whereas in monotherapy at certain concentrations, they simply led to growth inhibition (viability was not increased). Figure 14 and 15 further validated these data, both by using a cell toxicity assay to validate the viability data, but also because the experimental design allowed synergy modelling of these drug interactions. In both cell lines, synergy between lapatinib and EMBL-703625 was demonstrated, but this was higher across a wider range of concentrations in BT-474 cells compared to SK-BR3, considering the concentration range of each drug had comparable effects on cell viability and toxicity readings in monotherapy. There are different possible reasons that synergy is stronger in BT-474 cells, and it is likely due to the specific genetic and transcriptomic profile that these cells have. To assess this, transcriptomic experiments were conducted, and the results of these are further discussed in Section 2.2.

The fact that synergy was observed is particularly important when considering the clinical setting, both from an efficacy and safety standpoint. The safety profile of a treatment regimen is of critical importance when assessing new drugs or treatment combinations for use in cancer patients; an acceptable safety profile is almost always the main assessment criteria in Phase I trials, and is essential for a treatment to progress to further clinical trials. Often, therapeutic regimens do not progress through clinical trials because an acceptable dosage that is both safe and effective cannot be met. Synergistic interactions between drugs make it more likely that their combination elicits a clinically meaningful effect, whilst avoiding too many serious side effects.

The importance of drug interactions in cancer therapy is becoming more well understood. Recent large-scale efforts have aimed to establish drug synergy predictions based on responses of cancer cells in monotherapy[209;210]. As well as this, deep learning methods have been established that also allow a more comprehensive prediction of how different agents may act in combination with one another[211].

Other studies have showed synergistic interactions between inhibitors in HER2+ breast

cancer cells, which then went on to be approved for clinical use. A pre-clinical study using BT-474 and SK-BR3 cells, using dual inhibition with trastuzumab along with lapatinib or gefitinib (HER2 and EGFR TKIs, respectively) showed a synergistic effect by enhancing apoptosis induction[212]. Along with this, pre-treatment with these combinations also enhanced the effect of chemotherapy, and also showed encouraging efficacy in pre-clinical *in vivo* mouse models. Similar results were also found with trastuzumab and pertuzumab, both anti-HER2 monoclonal antibodies, in BT-474 and SK-BR3 cells, with the combination inhibiting the cell cycle, particularly in BT-474 cells[213]. *In silico* approaches have also provided a rationale for how these two antibodies are both able to independently bind to the HER2 receptor and lead to synergy[214].

2.1.4 Future experiments (with relevance to results discussed in Section 2.1.2)

Experiment	Rationale
Antibody staining of cell viability biomarkers	Antibody staining of key cell viability markers, such as caspase, give another validation and read-out of these results, as well as potentially giving more functional information about how each drug in monotherapy, or in combination therapy elicits its effects
***In vivo* validation of first-line safety and efficacy**	Using the transgenic, inducible mouse models from the Jechlinger Lab, lapatinib and EMBL-703625 can be administered together to test their effect on mouse mammary gland tumors that overexpress MYC and Neu. Protocols have already been established along with the EMBL Animal Facility in order to do this. EMBL-703625 can be delivered intra-peritoneally, whereas lapatinib can be delivered by oral gavage.
Characterisation of EMBL-703625 alongside targeted therapy in cells lines from other cancer types	This will allow an assessment of whether EMBL-703625 elicits synergy alongside already established targeted treatment regimens in other cancer types, which will allow a first assessment of whether pirin inhibition is a possibly effective therapeutic strategy in other forms of cancer.

2.2 Transcriptomic data reveal fundamental differences between the actions of lapatinib and EMBL-703625 on BT-474 and SK-BR3 cells, and a large combined effect

2.2.1 Rationale and experimental design

It is often hypothesised that synergistic interactions between different drugs is due to each drug having a distinct effect on the cell phenotype. At a molecular level, this means that compensatory pathways that are usually utilised to evade cell death in response to one drug are compromised by the action of the other drug. To gain a further understanding of the molecular mechanisms that lead to synergy between lapatinib and EMBL-703625 in BT-474 and SK-BR3 cells, transcriptomic experiments were performed using treatments with either a combination lapatinib and EMBL-703625, either drug in monotherapy, or vehicle (DMSO) treatment as a control. These were performed at pre-selected concentrations of both drugs that were previously known to elicit a relatively large combinatorial effect on viability, relative to either individual drug, based on the data from Figure 11. This is shown in Table 4.

Cell Line	**Lapatinib conc.** ***(viability change in monotherapy)***	**EMBL-703625 conc.** ***(viability change in monotherapy)***	***Viability change in combination***
BT-474	1µM *(-0.45)*	1µM *(+0.2)*	*-0.75*
SK-BR3	0.2µM *(-0.1)*	1µM *(+0.2)*	*-0.60*

Table 4: Table of chosen lapatinib and EMBL-703625 concentrations, and the corresponding changes in viability over 72h (see Figure 11) in monotherapy and also combination therapy. These concentrations were chosen and used for transcriptomic and consecutive experiment treatments (This section and Section 2.6, respectively) due to the differences between viability changes in monotherapy, compared to combination therapy. For SK-BR3, these concentrations were also used in the light-sheet experiments (Section 2.7).

Time course experiments were designed, taking measurements at 0h, 2h, 4h, 8h, 12h and 24h post-treatment addition in order to also observe how gene expression was altered over time. After pre-processing of raw transcriptomic count data to produce reads-to-genes data-sets, differential expression analysis using DeSeq2 was performed to allow comparisons between each treatment over the time series.

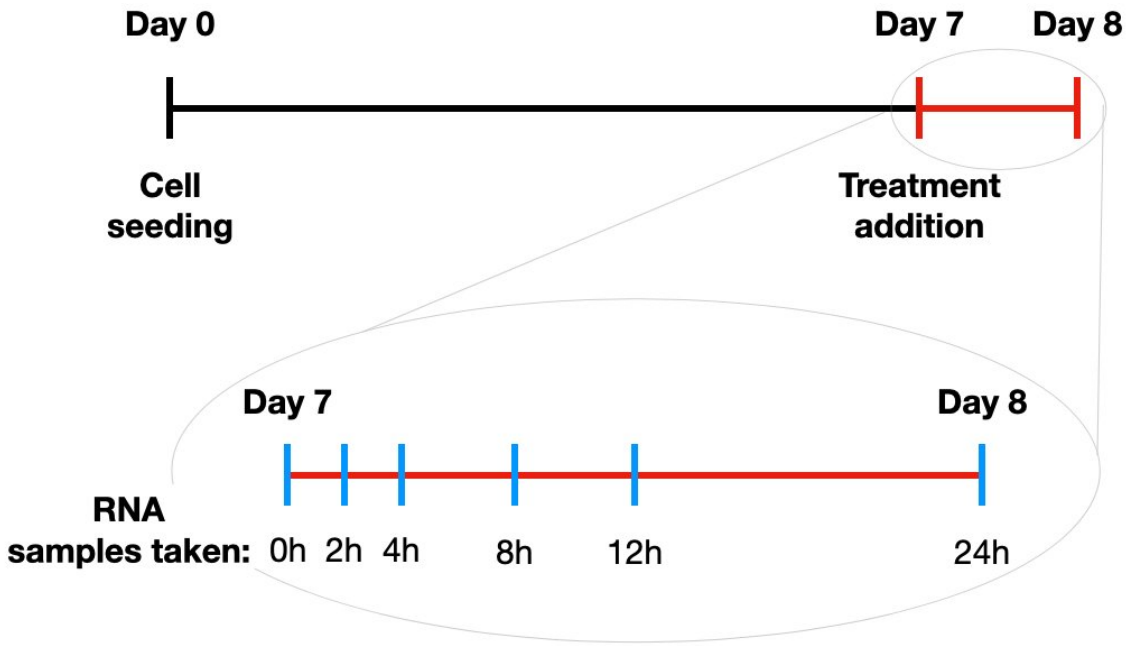

Figure 16: **Schematic of transcriptomic experiment.** After a 7 day growth period, total RNA samples were taken at 0h, 2h, 4h, 8h, 12h and 24h post-treatment addition. Note: for SK-BR3, samples taken at 4h were omitted because one of the experiments RNA sample did not pass the quality control.

2.2.2 Variance Stabilising Transformation of count data and sample-to-sample relationships

To understand the relationships between different treatments and time points, sample distance maps and PCA plots were generated. In order to perform these comparisons accurately, it is important to transform the data to allow a distribution of data where the variation remains the same across multiple mean values (known as a homoskedastic distribution). To achieve this, a variance stabilising transformation (VST) was performed on the data using DeSeq2, which removes the emphasis on low counts (data not shown). Low counts have a high variance in nature; this statistical noise can erroneously contribute to perceived variances between datasets. To remove any batch effects between the two experimental replicates, "R"'s limma program was utlised. This fits a linear model to the data, and removes unwanted variance that is caused by the effect of batch (see Supplementary Figure S.5).

To observe the similarities between each sample, principle component analyses (PCA) and sample-sample distances were plotted. As shown in Figure 17 (a - BT-474) and (c -SK-BR3), PCA plotting of VST transformed data revealed that lapatinib (square symbols) and EMBL-703625 ("+" symbols) had unique effects on the transcriptome of each cell lines, and the combination treatment (triangle symbols) was a combination of both effects, in both cell lines. The vehicle treatment (circle symbols) saw little changes throughout the time course. Interestingly, more variance was accounted for by EMBL-703625 compared to lapatinib, despite having less of a severe effect on cell viability at the chosen concentrations (see Table 4).

In line with the PCA data, the sample-sample distance heat map plotting (Figure 17b - BT-474; d - SK-BR3) further confirmed the unique effect that lapatinib and EMBL-703625 had on the transcriptome of both cell lines. These could broadly be separated into three different main groups:

1. Early time points and vehicle (control) treated
2. Lapatinib treated
3. EMBL-703625 and combination treated

Taken together, these results demonstrate that EMBL-703625 and lapatinib treatment in monotherapy have distinct transcriptional effects on BT-474 and SK-BR3 cells, and in combination, both partially account for the transcriptional effect, although more-so by EMBL-703625.

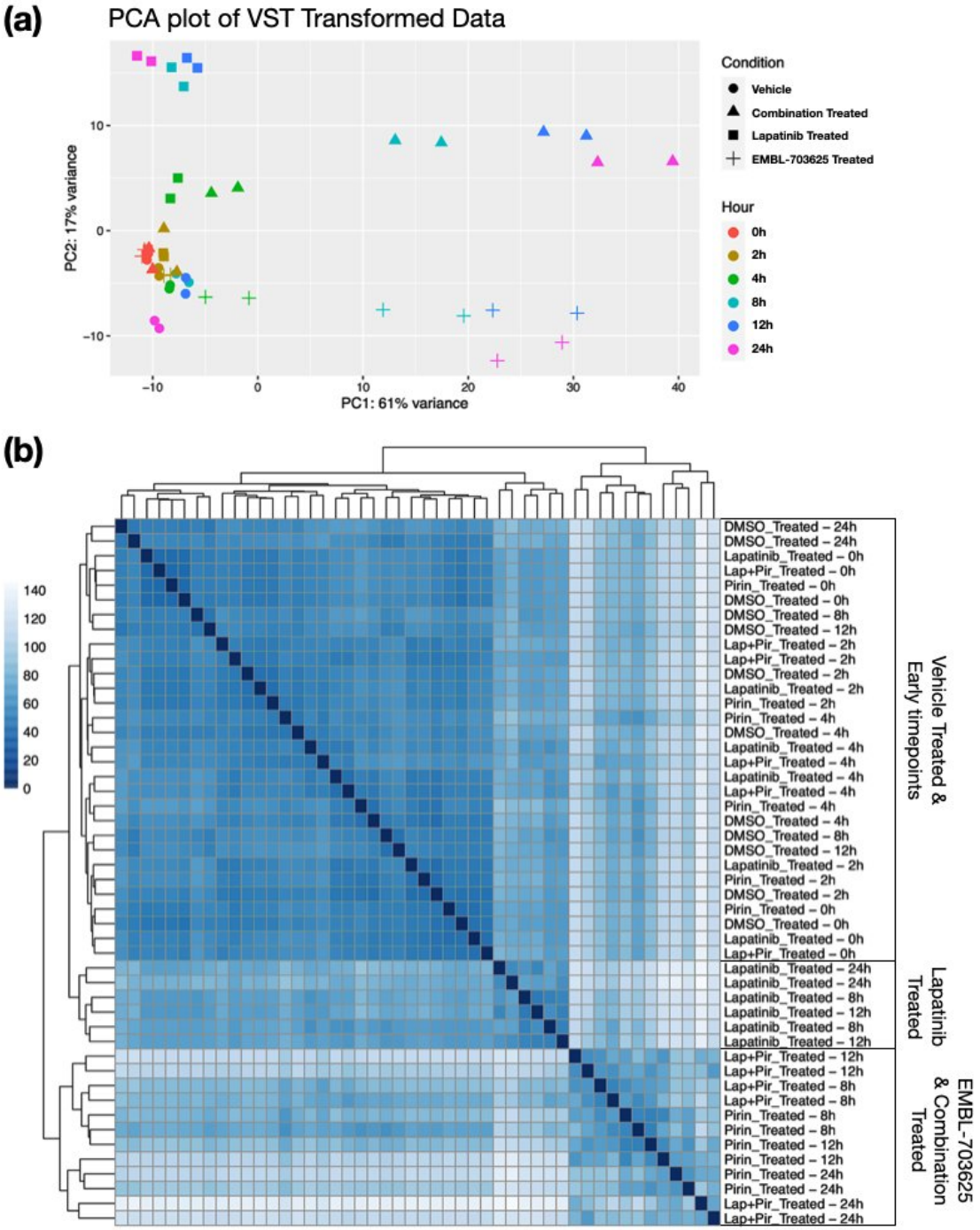

Figure 17: Figure continued on next page.

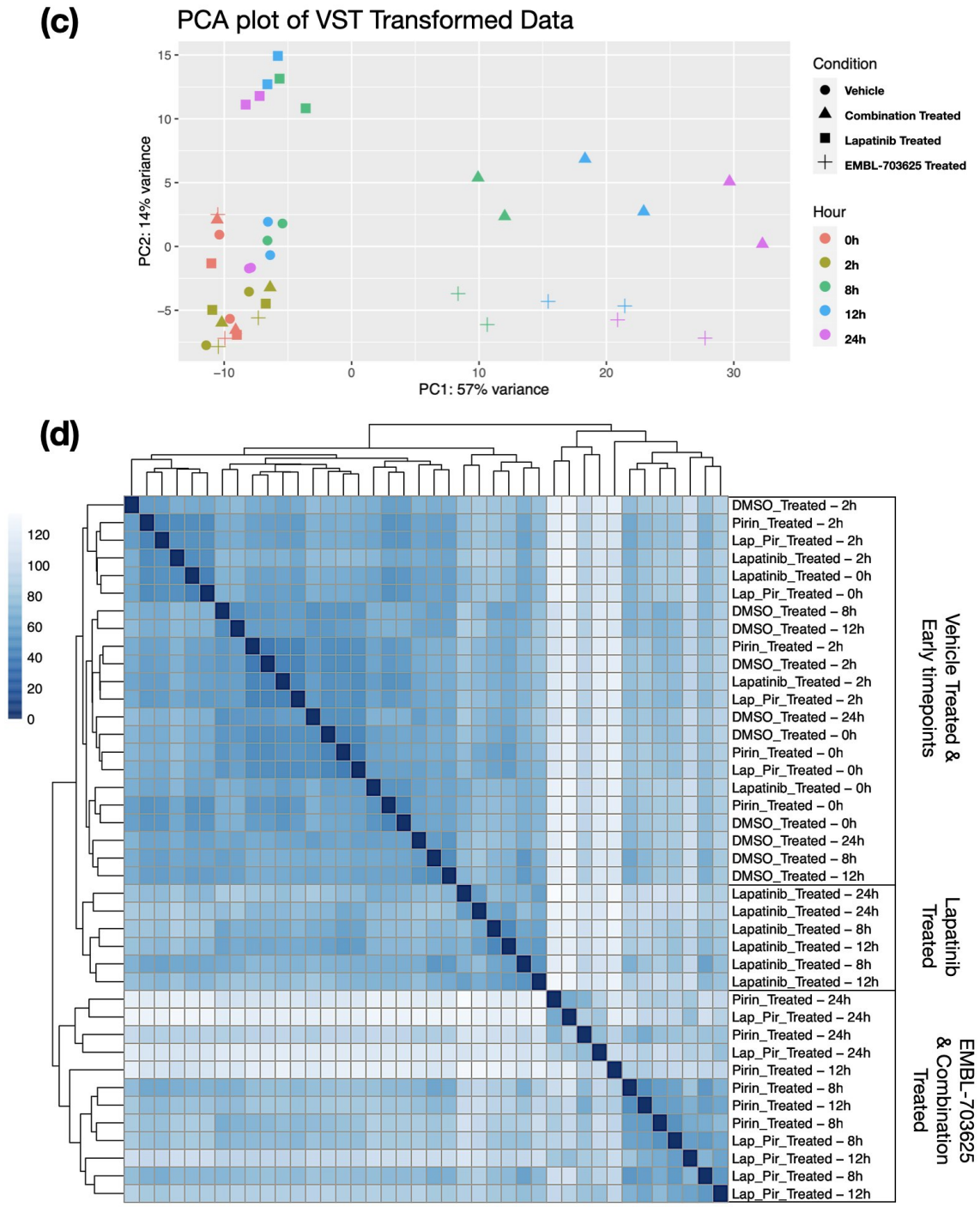

Figure 17: **PCA plot of VST transformed transcriptomic data (a) and (c) (BT-474 and SK-BR3, respectively) and sample-sample distances (b) and (d) (BT-474 and SK-BR3, respectively)** (a) and (c): PCA plots for the 1st and 2nd prinicple component were plotted on VST-transformed data for each sample. Symbols denote treatment, and colours denote the time point. (b) and (d): Sample-sample distance relationships of VST transformed data for each sample used in the analysis. The three major groups that the samples segmented into were manually imposed after the generation of the figure in "R". The scale bar displays the Euclidean distance between samples. The experiment was repeated twice, the data points show all technical replicates.

2.2.3 Lapatinib and EMBL-703625 have largely independent effects on gene expression

The distinct differences between the effects of lapatinib and EMBL-703625 on overall gene expression in both cell lines supported the hypothesis that each drug had an independent effect on the cell, which could possibly explain the synergistic interactions observed. Following this logic, it would be expected that the de-regulation of genes through the action of each drug would have minimal overlap, and that each monotherapy treatment would contribute to a larger amount of de-regulated genes in the combination treatment.

To understand how different genes were de-regulated by each treatment, DeSeq2 was used with a multi-factoral design, factoring in experimental replicates, time points and treatments, and testing the interaction between the time points and treatment profiles. Prior to this analysis, surrogate variable analysis (SVA) was performed on the DeSeq data, which accounts for unknown and unwanted sources of noise in the data. It produces surrogate variables, which can be used as covariates in subsequent analysis. Data processing in this way has been previously demonstrated to remove artefacts and improve experimental reproducibility[215].

Using the time course designed, SVA-corrected DeSeq2 dataset, gene expression was analysed and compared between the different treatments, using adjusted p-values that take the entire time series into account. As shown in Figure 18(a) and (b), for both cell lines, there was strikingly little overlap between significantly de-regulated ($p<0.01$) genes from lapatinib or EMBL-703625 monotherapy, with a total of 55 genes in BT-474, and 4 genes in SK-BR3. As well as this, as expected, the number of significantly de-regulated genes was greater in the combination therapy treated cells than in monotherapy, for both cell lines. Consistently with the results from extracellular 17, EMBL-703625 in monotherapy had a larger number of de-regulated genes compared to lapatinib in monotherapy (1841 vs 1248 in BT-474 and 1026 vs 287 in SK-BR3, both respectively). As well as this, EMBL-703625 also had more overlap with the combination treatment than lapatinib in monotherapy (1346 vs 594 genes in BT-474, and 814 vs 126 genes in SK-BR3, both respectively), suggesting that it accounts for more changes in the transcriptional profile of the combination treatment, compared to lapatinib.

To view these data in terms of expression profiles, as well as significant p-values, the top 500 differentially expressed genes for each treatment was plotted. These were then directly compared to the expression trajectories of these same genes in the other treatments. For example, in Figure 18(c)(iii), the top 500 differentially expressed genes for EMBL-703625 monotherapy treated BT-474 cells were plotted in a heatmap, and these same genes were compared to lapatinib monotherapy and combination treatment.

Consistent with the sample-to-sample plots and PCA data, genes that had significant de-regulation with one drug in monotherapy, did not generally experience the same de-regulation by the other, suggesting an independent drug effect. This was the case for both cell lines. In the combination treatment, there was an apparent association with each singular treatment; the trajectories of the monotherapies were generally in the same

direction, but weaker than the combination therapy. This suggests that for these genes, each drug helped to contribute to the de-regulation. Considering this, it is possible that there are many genes that were de-regulated by EMBL-703625 or lapatinib on their own, but the effect size was only large enough in the combination treatment to have an adjusted p-value below the cut off (p = 0.01), and therefore were shown as not statistically significant in the monotherapy treatments.

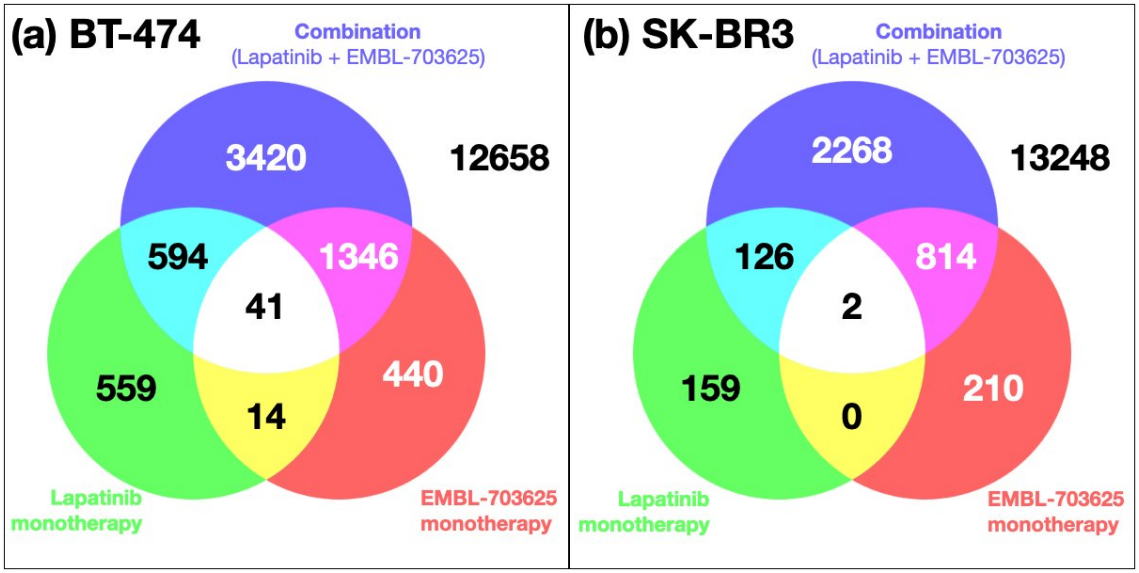

Figure 18: **(a) and (b) (BT-474 and SK-BR3, respectively): Genes de-regulated by lapatinib and/or EMBL-703625 treatment, relative to vehicle (DMSO) treated cells.** Adjusted p-value threshold was set at $p<0.01$. The number displayed outside the venn diagram is the number of genes that were not significantly de-regulated.
Figure continued on next page.

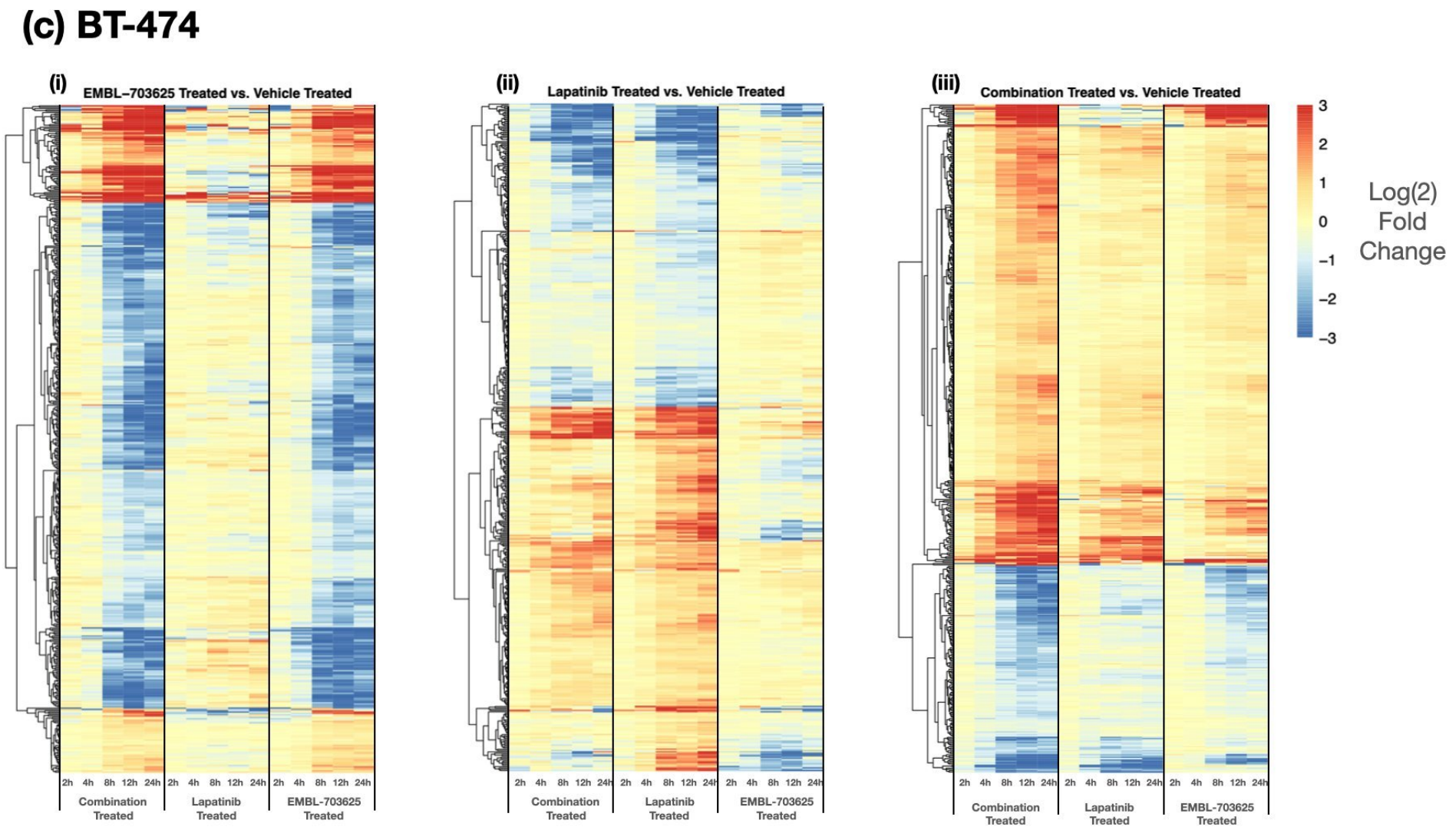

Figure 18: Figure continued on next page.

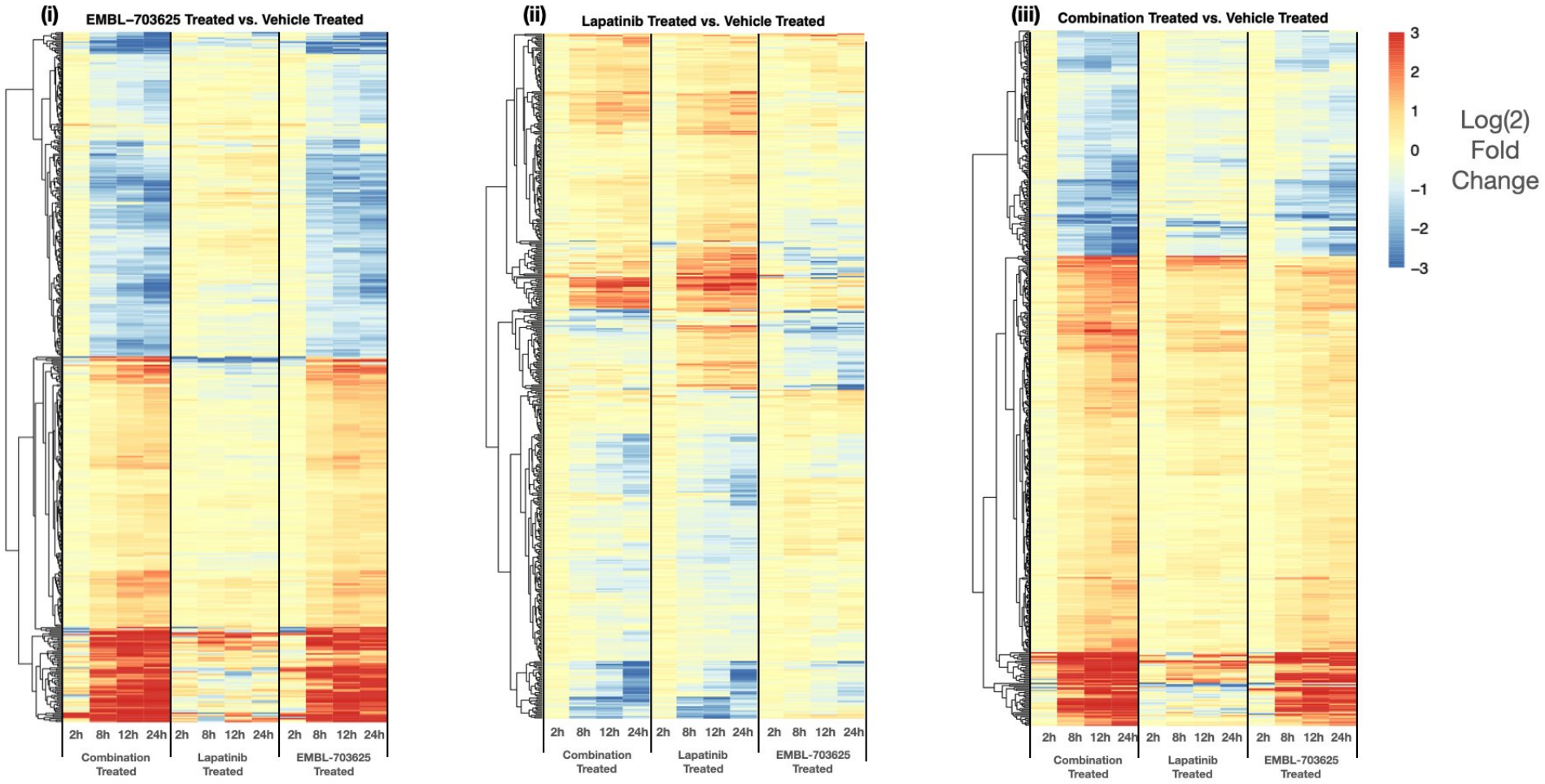

Figure 18: **Gene expression changes (relative to non-treated) for the top 500 de-regulated genes for BT-474 (c) or SK-BR3 (d) cells treated with EMBL-703625 (i), Lapatinib (ii) or a combination of both (iii).** For each panel, these expression patterns are shown across the three different treatments for a comparison visualisation. Red denotes an increase in expression, and blue denotes a decrease.

2.2.4 Pathway analysis of transcriptomic data

In both cell lines, lapatinib and EMBL-703625 appear to have unique effects on the transcriptomic profile of the cell, which both contribute to a larger overall combinatorial effect. To characterise how these transcriptional changes may translate to effects on cellular pathways, pathway enrichment analysis was performed using the "R" package "PathfindR" to identify the most significantly de-regulated pathways in the different treatment conditions, using the log(2)fold changes and adjusted P-values from across all time points from the DeSeq2 analysis. PathfindR works by using information from protein-protein interaction networks to identify sub-networks based on differential gene expression. Enrichment analysis is then performed on these sub-networks. The p-value cut-off was chosen as 0.01, and the Gene Ontology (GO) database was used for this analysis.

Once these significantly de-regulated GO terms were obtained, they were hierarchically clustered (also using PathfindR) into distinct subgroups based on their similarity to each other, which was based on the genes that were de-regulated within these pathways. These clusters each have a representative member, which was the member of the cluster that had the lowest p-value. This clustering helps to present the data in a format that shows the main aspects of cell biology that were de-regulated by each treatment. In Supplementary Tables 14 - 19, the individual pathways, clusters, and de-regulated individual genes are listed for each cell line and treatment.

As seen in Figure 19, combination treatment in both cell lines led to a higher number of de-regulated clusters, compared to either drug in monotherapy. Interestingly, and consistently with overall significant gene expression (see Figure 18(a) and (b)), EMBL-703625 had showed more overall similarity to the combination treatment, compared to lapatinib, with more overlap. In line with this, the amount of de-regulated clusters were similar between lapatinib and EMBL-703625 in BT-474 cells (20 and 21, respectively), but different in SK-BR3 (14 vs 39, respectively), which is roughly proportional to the amount of genes de-regulated by either agent in monotherapy. Another result that was consistent with the overall gene expression analysis, was that there was very minimal overlap between EMBL-703625 and lapatinib, further suggesting that these two drugs have largely independent effects on these cell lines, at the level of the gene and pathway.

The individual GO terms are represented in extracellular 18 (Corresponding GO IDs are displayed in Supplementary Tables 14 - 19 (Pages 189 - 212)). In both cell lines, a multitude of different areas of cell biology were de-regulated in combination treatment (82 in BT-474, and 68 in SK-BR3). In broad terms, both cell lines experienced similar types of de-regulation in their corresponding treatments. In combination therapy, protein ubiquitination and general cellular responses to stress were de-regulated, as well as DNA replication, DNA repair, transcription factors and signalling pathways, such as NF-$\chi\beta$ or SMAD signalling. EMBL-703625 in monotherapy also had a generally wide range of effects, including protein ubiquitination related pathways, protein and DNA binding, and kinase and phosphatase activity. Lapatinib had less of a range of different effects, primarily affecting DNA repair and DNA binding, transcriptional effects, and translation and protein folding.

(a) BT-474

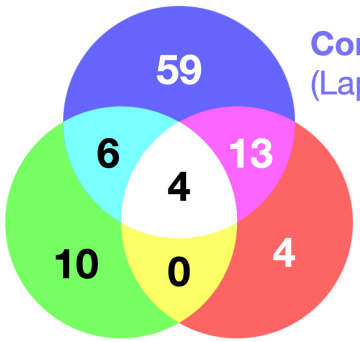

EMBL-703625 monotherapy
cyclin-dependent protein serine/ threonine kinase inhibitor activity
protein serine/threonine phosphatase activity
protein binding, bridging
gamma-tubulin binding
Combination and Lapatinib
protein phosphatase binding
transcription factor binding
chaperone binding
beta-catenin binding
protein domain specific binding
rRNA binding
Combination + EMBL-703625
calmodulin binding
histone acetyltransferase activity
transcription regulatory region sequence-specific DNA binding
RNA binding
protein N-terminus binding
protein-containing complex binding
single-stranded DNA binding
protein serine/threonine kinase activity
polyubiquitin modification-dependent protein binding
CARD domain binding
SNARE binding
nuclear receptor activity
actin filament binding
All three treatments
ubiquitin-protein transferase activity
thiol-dependent ubiquitin-specific protease activity
ubiquitin protein ligase binding
protein tyrosine kinase activity

Combination Therapy only	
p53 binding	SH3 domain binding
chromatin binding	double-stranded RNA binding
GDP binding	cullin family protein binding
I-SMAD binding	ATPase binding
NF-kappaB binding	protease binding
nuclear hormone receptor binding	thioesterase binding
DNA-binding transcription factor activity, RNA polymerase II-specific	mRNA 3'-UTR AU-rich region binding
androgen receptor binding	phosphoprotein binding
histone deacetylase binding	protein heterodimerization activity
SUMO transferase activity	receptor tyrosine kinase binding
SMAD binding	poly(A) binding
structural constituent of ribosome	single-stranded DNA-dependent ATP-dependent DNA helicase activity
ubiquitin conjugating enzyme activity	low-density lipoprotein particle receptor binding
protein kinase A catalytic subunit binding	
translation initiation factor activity	WW domain binding
GTPase activator activity	methyl-CpG binding
ATPase activity	scaffold protein binding
proximal promoter sequence-specific DNA binding	signaling receptor binding
K63-linked polyubiquitin modification-dependent protein binding	ubiquitin-ubiquitin ligase activity
RNA polymerase II transcription factor binding	RNA polymerase binding
cyclin binding	tubulin binding
ion channel binding	insulin-like growth factor I binding
zinc ion binding	calcium ion binding
protein phosphatase regulator activity	enzyme inhibitor activity
RNA polymerase II complex binding	calcium-dependent protein binding
epidermal growth factor receptor binding	poly(A)-specific ribonuclease activity
GTPase binding	peroxidase activity
unfolded protein binding	histone-lysine N-methyltransferase activity
phosphatase activity	enzyme activator activity
kinase binding	ubiquitin binding

Lapatinib monotherapy only	
protein kinase activity	ribosome binding
transcription coactivator activity	insulin-like growth factor receptor binding
transcription corepressor activity	guanyl-nucleotide exchange factor activity
damaged DNA binding	transforming growth factor beta binding
structural molecule activity	MAP kinase kinase activity

Figure 19: *Figure continued on next page*

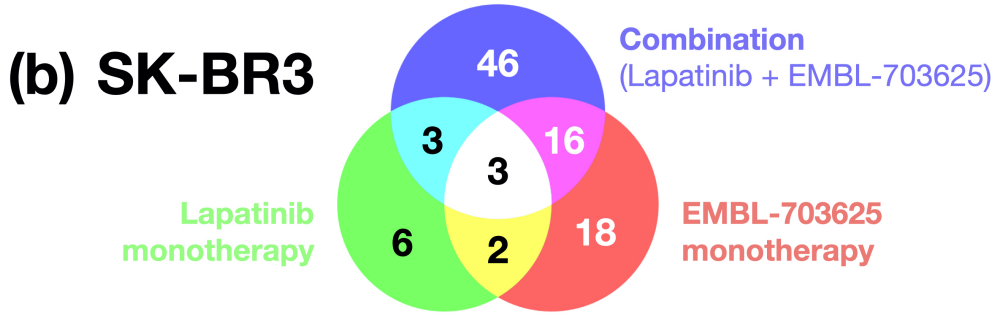

EMBL-703625 monotherapy
transcription regulatory region sequence-specific DNA binding
mRNA binding
chromatin binding
p53 binding
ubiquitin-like protein ligase binding
translation initiation factor binding
core promoter sequence-specific DNA binding
14-3-3 protein binding
phosphatase activity
zinc ion binding
GTPase binding
ribosome binding
protein phosphatase regulator activity
ubiquitin-specific protease binding
GTP binding
methylated histone binding
kinase activity
double-stranded RNA binding

Combination + EMBL-703625
ubiquitin conjugating enzyme activity
thiol-dependent ubiquitin-specific protease activity
protein serine/threonine kinase activity
histone binding
protein C-terminus binding
RNA polymerase II proximal promoter sequence-specific DNA binding
histone acetyltransferase activity
protein N-terminus binding
protein tyrosine kinase activity
histone acetyltransferase binding
calmodulin binding
beta-catenin binding
protein heterodimerization activity
K63-linked polyubiquitin modification-dependent protein binding
polyubiquitin modification-dependent protein binding
protein-containing complex binding

Combination and Lapatinib
damaged DNA binding
ubiquitin-protein transferase activity
NF-kappaB binding

Lapatinib monotherapy and EMBL-703625 monotherapy
DNA-binding transcription repressor activity, RNA polymerase II-specific
R-SMAD binding

Lapatinib monotherapy only
Lys63-specific deubiquitinase activity
promoter-specific chromatin binding
proximal promoter sequence-specific DNA binding
insulin-like growth factor receptor binding
tau protein binding
DNA-binding transcription activator activity, RNA polymerase II-specific

Combination Therapy only	
transcription corepressor activity	ubiquitin-ubiquitin ligase activity
transcription coactivator activity	small GTPase binding
I-SMAD binding	phosphatidic acid binding
RNA binding	sodium channel regulator activity
GTPase activator activity	histone methyltransferase activity (H3-K4 specific)
SMAD binding	GTPase inhibitor activity
DNA-binding transcription factor activity, RNA polymerase II-specific	protein domain specific binding
transcription coregulator activity	dynein complex binding
epidermal growth factor receptor binding	thioesterase binding
miRNA binding	lipid binding
guanyl-nucleotide exchange factor activity	Rho guanyl-nucleotide exchange factor activity
kinase binding	protein phosphatase 2A binding
androgen receptor binding	receptor tyrosine kinase binding
protein phosphatase binding	microfilament motor activity
Rac GTPase binding	protease binding
pre-mRNA binding	phosphoprotein binding
RNA polymerase II complex binding	protein kinase A catalytic subunit binding
myosin V binding	SNARE binding
Hsp90 protein binding	poly(A)-specific ribonuclease activity
G-rich strand telomeric DNA binding	nuclear receptor activity
ATPase activity	cyclin binding
chaperone binding	methyl-CpG binding
integrin binding	structural constituent of ribosome

All three treatments
ubiquitin-protein transferase activity
phosphotyrosine residue binding
actin binding

Figure 19: **Venn diagrams of the number significantly de-regulated clusters ($p<0.01$) for BT-474 cells (a) or SK-BR3 cells (b) treated with Lapatinib, EMBL-703625, or a combination of both, with the corresponding representative terms for each cluster listed below**. Data about the individual pathways de-regulated in each cell line and treatment, as well as p-values and GO-terms are displayed in Supplementary Tables 14 - 19.

2.2.5 De-regulated pathways associated with cancer hallmarks are higher in combination treatment, compared to lapatinib or EMBL-703625 monotherapy

The transcriptomic results shown thus far suggested that lapatinib and EMBL-703625 come together to have a multitude of effects on cell biology. In the context of cancer therapy, it is important to be able to tackle different cancer hallmarks, which is what make cancer cells unique, and potentially vulnerable, relative to normal cells.

To do this, representative GO terms for the different cancer hallmarks were used. These were obtained after personal discussion with Bálint Mészáros, who has also now published this work (Mészáros *et al.,* 2021)[102]. This study manually curated these terms, and confirmed that these terms were over-represented in publicly-available datasets[102]. These GO terms were then compared to the significantly de-regulated pathways (before hierarchical clustering as in the previous section) from the different treatments in both cell lines. Significantly de-regulated GO terms ($p<0.01$) that matched the ones by Mészáros *et al.* were summarised and displayed in Table 5 for BT-474, and Table 6 for SK-BR3.

As seen in both tables, the amount of hallmark-related deregulated GO terms was higher in the combination treatment, compared to either agent in monotherapy, and there were multiple de-regulated GO-terms that were not statistically significant with either agent in monotherapy. Consistent with the gene expression data and pathway clustering (Figure 18 and 19, respectively), EMBL-703625 de-regulated more GO-terms than lapatinib in both cell lines. In BT-474, there was minimal overlap between them, but between them, they accounted for at least one de-regulated pathway in each hallmark. In SK-BR3, the only two GO Terms that were de-regulated by lapatinib were "Cellular response to DNA damage stimulus" and "DNA repair", both of which were also de-regulated by EMBL-703625. In combination therapy for SK-BR3 cells, the only hallmark that did not have de-regulated pathways was "Evading growth suppressors", which, however, was the case for EMBL-703625 monotherapy.

Hallmark	GO Term	Treatment		
		Combination	Lapatinib	EMBL-703625
Activating invasion and metastasis	Cell migration	✓	✓	
	Epithelial to mesenchymal transition	✓		
Avoiding immune destruction	Innate immune response	✓	✓	✓
De-regulating cellular energetics	Regulation of glycolytic process	✓		
	Glucose homeostasis	✓	✓	
	Generation of precursor metabolites and energy	✓		
	Cellular response to hypoxia	✓		
Enabling replicative immortality	Somatic stem cell population maintenance	✓		
	Telomere maintenance	✓		
	Cell aging	✓		
	Cellular senescence			✓
	Regulation of telomere maintenance	✓		
Evading growth suppressors	Cell cycle arrest	✓		✓
	Negative regulation of cell growth	✓		✓
Genome instability and mutation	Cellular response to DNA damage stimulus	✓		✓
	DNA repair	✓		✓
	DNA damage checkpoint			✓
	mismatch repair			✓
Sustaining proliferative signalling	Regulation of cell proliferation	✓		
	Cell division		✓	
Tumor promoting inflammation	I-kappaB kinase/NF-$\varkappa\beta$ signaling	✓	✓	
	Fc-epsilon receptor signaling pathway	✓		✓
	Regulation of inflammatory response	✓		
	Inflammatory response	✓		

Table 5: **BT-474 cells:** GO-terms and corresponding cancer Hallmarks, as per Mészáros et al. (2021), for significantly de-regulated (adj. p value < 0.01) GO-terms. Displayed for combination therapy, or lapatinib or EMBL-703625 monotherapy, compared to vehicle (DMSO) treated.

Hallmark	GO Term	Treatment		
		Combination	Lapatinib	EMBL-703625
Activating invasion and metastasis	Cell migration	✓		
	Epithelial to mesenchymal transition	✓		✓
Avoiding immune destruction	Innate immune response	✓		✓
De-regulating cellular energetics	Cellular response to hypoxia	✓		✓
Enabling replicative immortality	Cell aging			✓
	Somatic stem cell population maintenance	✓		
	Regulation of telomere maintenance	✓		
	Telomere maintenance	✓		
Evading growth suppressors	Negative regulation of cell growth			✓
	Negative regulation of cell cycle			✓
Genome instability and mutation	Cellular response to DNA damage stimulus	✓	✓	✓
	DNA damage checkpoint	✓		
	DNA repair	✓	✓	✓
Sustaining proliferative signalling	Regulation of cell cycle	✓		
	Regulation of cell proliferation	✓		
Tumor promoting inflammation	Fc-epsilon receptor signaling pathway	✓		✓

Table 6: **SK-BR3 cells:** GO-terms and corresponding cancer Hallmarks, as per Mészáros et al. (2021), for significantly de-regulated (adj. p value < 0.01) GO-terms. Displayed for combination therapy, or lapatinib or EMBL-703625 monotherapy, compared to vehicle (DMSO) treated.

2.2.6 Discussion of Section 2.2: Distinct effects of lapatinib and EMBL-703625, and a large combination effect

This discussion is divided into two parts. The first sub-section discusses general contexts and implications for these results, and the second sub-section discusses the specific de-regulated pathways that were found in this section.

2.2.6.1 General context and therapeutic implications

All currently licensed HER2-targeted breast cancer treatment regimens are based on a HER2-targeted therapeutic along with another HER2-targeted therapeutic and/or chemotherapy. This approach has been coined as a "HER2-blockade". As stated before, this approach has been demonstrated as effective. For example, a long term follow up study demonstrated that adjuvant trastuzumab treatment significantly increased relapse-free survival rates over 10 years, compared to chemotherapy[216]. However, relapses are still an issue for HER2+ breast cancer patients, particularly those that are hormone negative[216]. Therefore, experiments were conducted to assess if co-pirin and HER2 inhibition were able to minimise the risk of tumor relapses. This was addressed by comparing

monotherapy with either inhibitor to combination therapy in BT-474 and SK-BR3 cells with two types of experiment. Firstly, transcriptomic experiments were conducted to assess how each drug affected the transcriptional profile of the cell (This section); if they were largely different, it could be suggestive that resistant-sub-populations would be less likely to form. Secondly, re-growth experiments were conducted, where cells would be treated with either or both drugs, surviving cells would be selected and further treatment, before treatment was finally removed to see if re-growth could be observed. These regrowth experiments are displayed and discussed in the next section (Section 2.3).

To achieve less surviving cancer cells, it would be optimal to treat them in such a way that each drug in the combination has a largely distinct effect, which could simultaneously enhance toxicity in cells that are susceptible to both drugs, and also increase the likelihood of killing cells that have inherent or acquired resistance to either drug in monotherapy. In line with this, the transcriptomic results presented in this thesis suggested that lapatinib and EMBL-703625 had largely independent effects on gene expression, both at the level of individual genes, and also at the level of the pathway (Figure 18 and 19). This helps to validate the notion that these two drugs act synergistically with each other (as shown in Figure 15), but also potentially means that monotherapy resistant cells could be more likely to be killed by combination treatment. In line with this, a study from Palmer and Sorger (2017)[217] suggests that the added benefit from combination therapy can come about because cells or individuals that may be unaffected by one drug can be affected by the other. For example, a patients cancer that is not affected by lapatinib could be affected by EMBL-703625 to achieve tumour remission, and vice versa. In this case, the combination does not need to be synergistic or even additive to confer a combination benefit. This means that on top of the benefit that is brought about by the synergistic drug interaction between lapatinib and EMBL-703625, there is also an added benefit of the lack of overlap between these two drugs.

2.2.6.2 De-regulated pathways

The de-regulated pathways referred to in this section can be seen in the clustering that was done in Figure 19 (Page 82), and also in Supplementary Tables 14 - 19 (Pages 189 - 212).

De-regulation of heat-shock proteins by combination therapy and EMBL-703625 monotherapy

One group of genes that were found to be de-regulated by combination therapy in this project, and also from transcriptomic data on HeLa cells from the EMBL CBCF were heat shock proteins. Pirin has been linked to heat shock proteins previously in the literature. A phenotypic screen that inhibited different heat-shock proteins identified that an inhibitor of pirin had inhibitory downstream affects on heat shock factor 1 (HSF1) related pathways[218].

There have also been a number of studies that highlight the link between heat shock proteins and resistance to HER2-targeted therapy, as has been discussed in Section 1.5.2.2

(Page 41). As dual treatment targets these pathways, it is possible that this treatment regimen could help to overcome the formation of resistance through mechanisms related to HSP activity.

With respect to the particularly strong synergy shown in BT-474 cells, estrogen receptor signalling has been known to interact with heat shock proteins, suggesting that this subtype may be particularly reliant on the function of heat shock proteins. A previous study established that lapatinib resistant BT-474 cells maintained sensitivity to heat shock protein inhibition, which is mediated through heat shock factor 1 (HSF-1) activity[140]. Consistent with this, ganetspib, which is involved in HSP90 inhibition, was demonstrated to preferentially reduce viability in BT-474 and SK-BR3 cells, compared to their non-HER2-over-expressing counterparts[141]. In line with this project, they also established that ganetspib potentiates the effects of lapatinib in each cell line, with stronger combined effect in BT-474, relative to SK-BR3[141].

De-regulation of ubiquitination related pathways by combination therapy and EMBL-703625 monotherapy

In both cell lines, multiple pathways involved ubiquitination were de-regulated by combination treatment. Ubiquitin and HSP pathways show degrees of cross talk, both being involved in cellular responses to stress. It has been suggested that targeting the ubiquitin degradation pathway could be effective in HER2+ breast cancer treatment. For example, the histone H2B ubiquitin ligase RNF40 was recently demonstrated to be essential for HER2-driven breast cancer tumorigenesis across multiple experimental models[219]. In certain types of cancer, ubiqutin pathway inhibitors have shown encouraging data in a clinical setting. For example, Pevonedistat, which targets NEDD-4, a ubiquitin-like protein, has recently been given breakthrough-therapy designation by the US FDA[220], which is a designation that allows fast-tracking of therapeutics that have demonstrated encouraging preliminary data.

In this study, it appeared that genes involved in proteasomal degradation were particularly de-regulated. Evidence from the literature supports the notion that regulation of proteasomal degradation is a point of vulnerability in the context of HER2-targeted therapy resistance. It has been observed that proteasome inhibitors prevent cross-talk between HER2 and the estrogen receptor, and leave them vulnerable to cell death in lapatinib or endocrine therapy resistant cells[221]. A recent study on pirin itself has also shown that it is a modulator of autophagy-dependent ferroptosis[191].

De-regulation of NF-$\varkappa\beta$ pathways by combination therapy and EMBL-703625 monotherapy

Another de-regulated pathway from combination treatment that was consistent between both cell lines was the NF-$\varkappa\beta$ pathway. NF-$\varkappa\beta$ expression is associated with HER2 over-expression[143], and its signalling is activated by HER2 through a canonical pathway with results in an invasive phenotype[144]. On top of this, clinical evidence suggests that NF-$\varkappa\beta$ is a biomarker that is predictive of an aggressive phenotype and poor prognosis[145]. Because of these reasons, the link between HER2+ and NF-$\varkappa\beta$ has long been identi-

fied and characterised as a potentially attractive node of interference for therapy resistant breast cancer[146;147]. In the context of HER2+ breast cancer specifically, there is also evidence for this, as discussed in the introduction (Section 1.5.2.3). To recap, trastuzumab-resistant BT-474 cells have demonstrated activation of NF-κβ[115]. It has also been demonstrated that NF-κβ is hyperactivated in breast cancer cells, and that combination inhibition of HER2 and NF-κβ was effective in killing lapatinib resistant cells[148]. Although pirin is generally relatively poorly characterised, it has been shown that it is an iron-dependent regulator of NF-κβ signalling[188;222] when it is activated by active Fe(III) form of Pirin[187]. In oral cancer, pirin has also been demonstrated to act with NF-κβ[223].

2.2.7 Future experiments (with relevance to results discussed in Section 2.2)

Experiment	Rationale
Integrated analysis with metabolomics	The role that cell metabolism plays in the survival of residual cells and tumor relapse makes it an area of key interest. Therefore, performing metabolomics would allow an understanding of how this plays a role in lapatinib and EMBL-703625 synergy. Strategies to efficiently extract metabolites from 3D grown cell lines have already been established as part of this project, as well as a metabolite processing and analysis pipeline in collaboration with the Zimmerman Lab at EMBL.
Fewer starting samples with a higher read depth	The experiments described in this thesis have established that lapatinib and EMBL-703625 have distinct effects on the cellular transcriptomic profile, and gives some insights into cellular processes that may be deregulated because of them in monotherapy or combination therapy. Further experiments using a higher concentration of starting material would make it more likely to achieve a higher read depth, which would be important for an integrated analysis alongside metabolomics. Certain pathways, for example, glycolysis, did not have a sufficient read-depth in this project that conclusions about them could be made in these experiments.

Table 7: Future experimental directions with regard to the data discussed in Section 2.2.

2.3 Assessing the ability of BT-474 or SK-BR3 cells to re-grow following lapatinib or EMBL-703625 monotherapy, or in combination

2.3.1 Experimental design and rationale

A major challenge facing modern cancer therapy is reducing the incidences of problematic tumor relapses. Even with a synergistic drug response, tumor cell heterogeneity could mean that certain cells are still able to re-grow following treatment removal. To assess this in BT-474 and SK-BR3 cell lines, experiments were designed to treat cells with singular treatments and combination treatments, remove these treatments, and assess their ability to regrow. As displayed graphically in Figure 20, after a treatment period of 7 days, with a drug replenishment every 3.5 days, cells were re-seeded to select for surviving cells. This allowed an increase of sensitivity and also visualisation; re-growth of surviving cells could be difficult to visualise with a large amount of surrounding cellular debris. This also helped to control for possible micro-environmental effects; contact inhibition from cellular debris could also potentially compromise re-growth, or slow it to an extent that would be difficult to experimentally assess. It was also possible that certain cells may not have been accessible by the drug due to blocking from other cells. Following re-seeding, cells were kept on their respective treatments for a further 7 days to allow for further selection. Following this, some cells were removed from their treatment, and others remained on as a control. Multi-positioning was used on the Olympus ScanR to image the entirety of the re-seeded gel, with image stitching used on the projected images to produce a single image for each well (see Supplementary Figures S.3 and S.4; Pages 181 and 182, respectively).

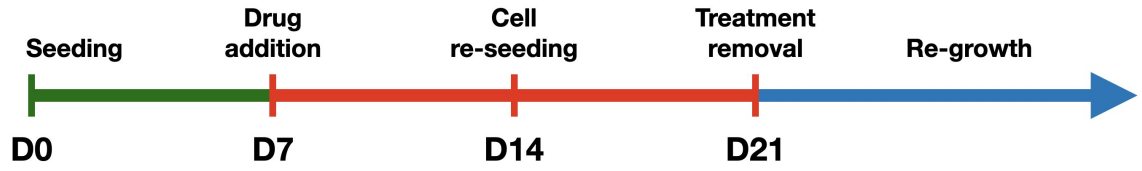

Figure 20: **Schematic of experimental design for BT-474 and SK-BR3 re-growth removal following EMBL-703625/Lapatinib monotherapy or combination therapy**. As a control, some wells were left on treatment following day 21.

2.3.2 Imaging of cell regrowth using high throughput imaging on the Olympus ScanR

The Olympus ScanR was used in order to visualise cell re-growth over long time periods in a high throughput manner. This microscope had the capability of imaging matrigel droplets in 3D in a 96 well plate format, meaning that multiple different treatment conditions could be imaged simultaneously. The 96 well plate format also meant that same 3D structures could be consistently re-imaged, allowing for accurate comparisons. 3D projection (Supplementary Figure S.3) and stitching (Supplementary Figure S.4) macros

on ImageJ were used to provide a single overview image of each individual gel, giving a comprehensive overview of all the structures within each gel.

2.3.3 EMBL-703625 and Lapatinib act together to compromise the ability of BT-474 cells to re-grow after treatment removal

BT-474 cells were treated with varying concentrations of EMBL-703625, with or without a combination of 1.0µM Lapatinib. This concentration of lapatinib had been previously determined in preliminary experiments to be selective to BT-474 cells on its own, but consistently allow these cells to re-grow after it was removed (data not shown).

Images were taken on the Olympus ScanR following re-seeding, immediately after drug removal, and 7, 14 and 28 days after that. Across multiple concentrations, EMBL-703625 and Lapatinib together reduced the levels of re-growth in BT-474, relative to either treatment alone. At a combination of 2.3µM of EMBL-703625 and 1.0µM of lapatinib, re-growth was almost entirely compromised (Figure 21).

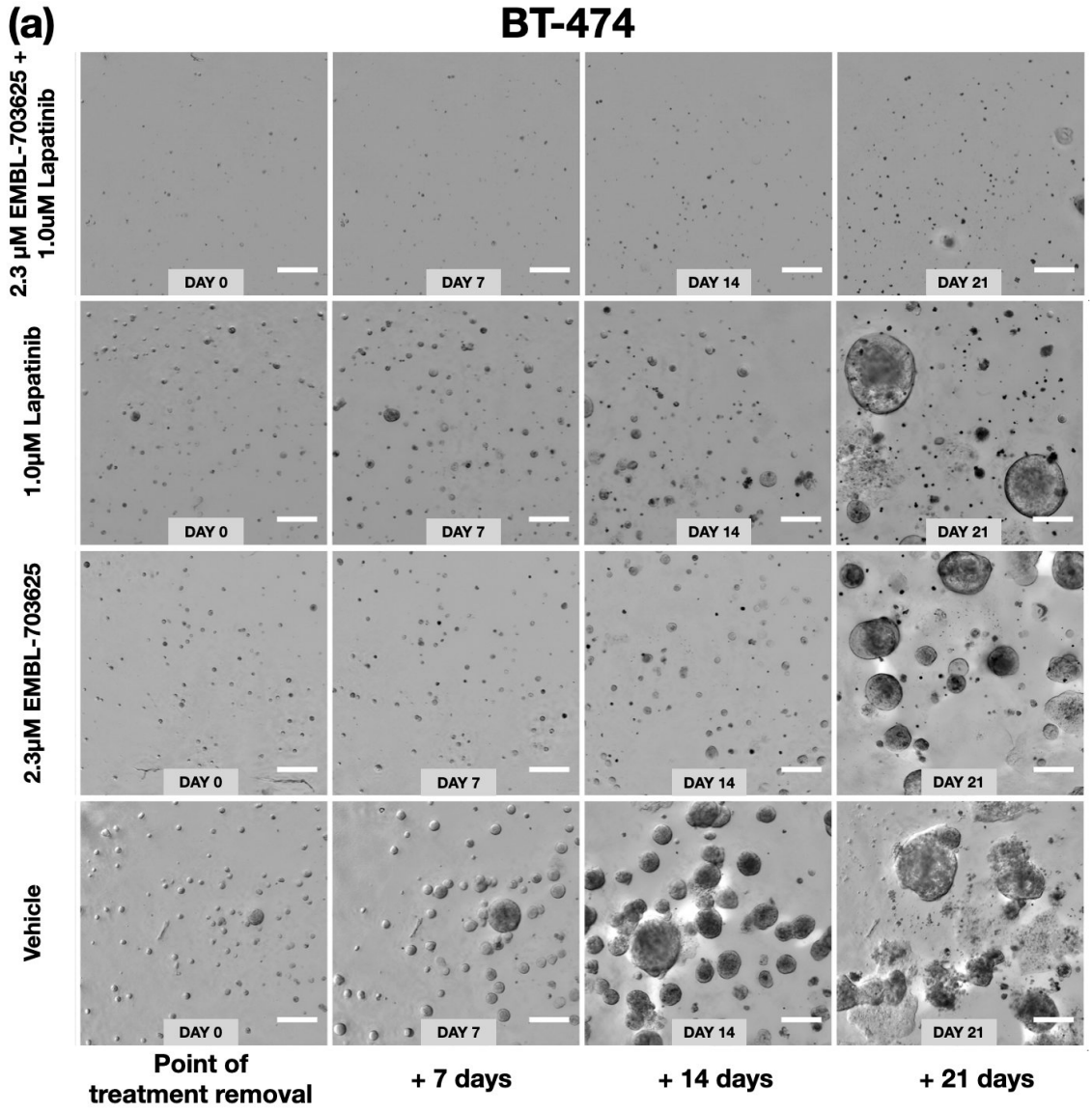

Figure 21: *Figure continues on next page.*

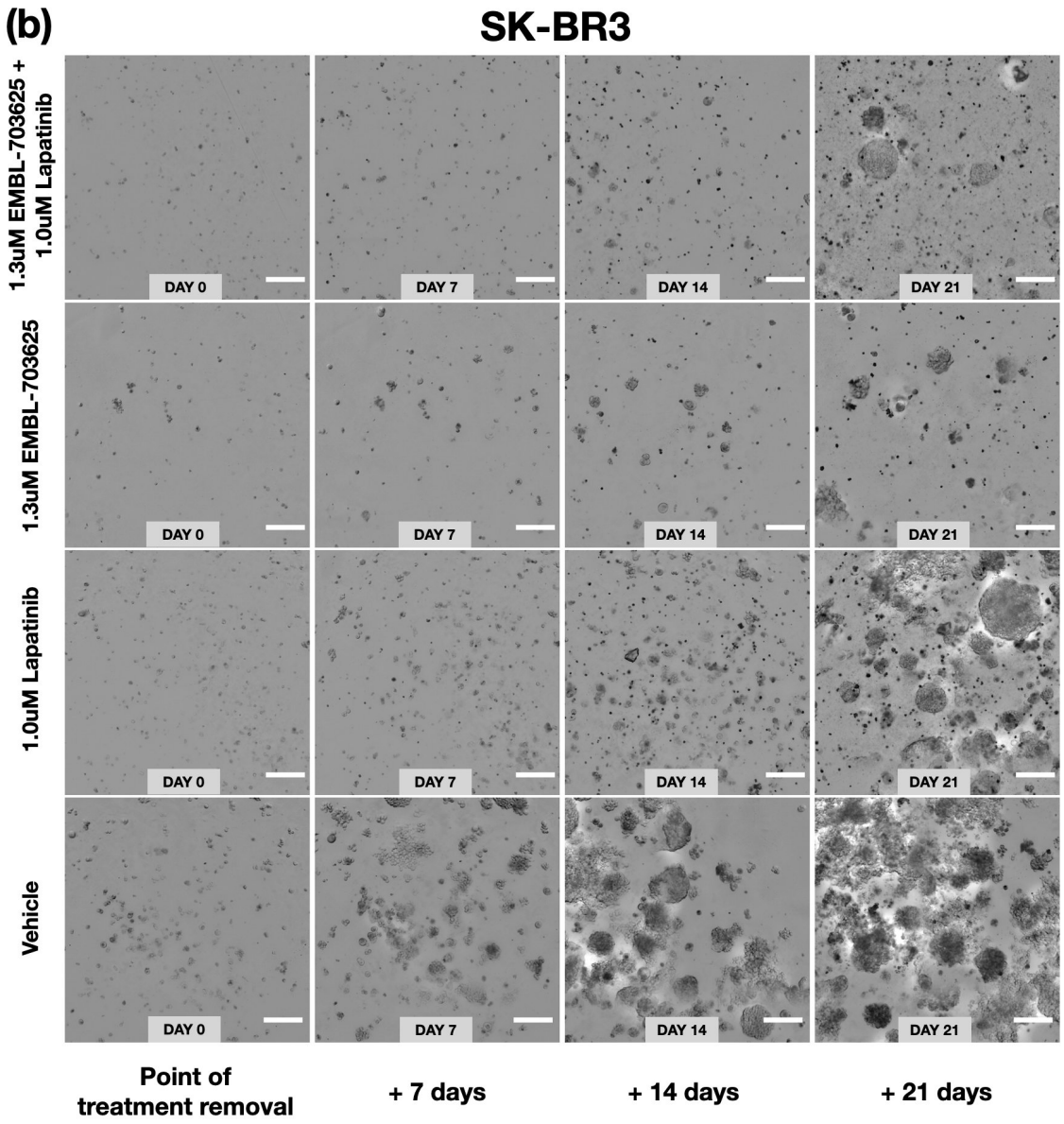

Figure 21: **Projected and stitched ScanR images showing re-growth following treatment removal in BT-474 (a) and SK-BR3 (b) cells.** Regions of interest were taken from larger stitched images to reflect representative re-growth. The experiment was repeated three times with consistent results. Scale bar = 500µm.

In contrast to BT-474, SK-BR3 cells did not experience an overall reduction in their ability to regrow following treatment removal, when comparing singular treatments to double treatments (Figure 21). However, interestingly, the ability of SK-BR3 to re-grow was more compromised by singular EMBL-703625 treatment when compared to BT-474. For example, BT-474 is able to actively grow in the presence of 2.3µM of EMBL-703625, whereas the ability of SK-BR3 to re-grow is nearly completely ablated in the presence of 1.3µM EMBL-703625, despite the fact that BT-474 has an approx. 80% reduction in cell viability, compared to an approx. 50% reduction in the SK-BR3 cells (See Figures 11 and 15).

Interestingly, BT-474 appeared to be relatively resilient to singular EMBL-703625 treatments. As shown in Figure 22, BT-474 was able to actively begin to grow in the continued

presence of certain concentrations of EMBL-703625 (albeit at slower than normal rates) despite viability assay results demonstrating an approximately 80% reduction in viability, suggesting there were cellular adaptations to allow cell survival and re-growth.

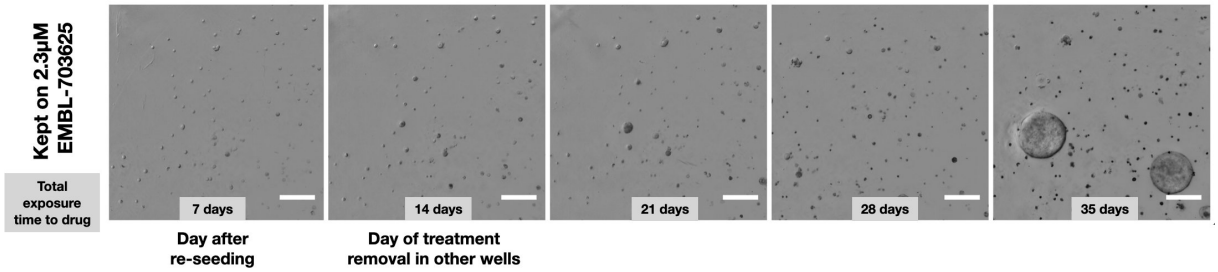

Figure 22: Time lapse of BT-474 cells re-growing in the presence of 2.3µM of EMBL-703625. The experiment was repeated three times, with consistent results. Regions of interest were taken from larger stitched images to reflect representative re-growth. Scale bars = 500µm.

2.3.4 Discussion of Section 2.3: Lapatinib and EMBL-703625 inhibit re-growth in BT-474 cells when in combination, but not in SK-BR3

2.3.4.1 Discussion of results

In an experimental setting, a functional way of validating whether lapatinib and EMBL-703625 combination therapy may help to prevent relapses is to assess the ability of treated cells to re-grow after treatment removal. The hypothesis brought forward by the transcriptomic results is that EMBL-703625 and lapatinib having largely different impacts on gene expression could make it more difficult for persister sub-populations to arise to each drug. If this holds true, their combined effect should reduce the ability of these cells to re-grow, more than either agent in monotherapy. To do this, experiments were set up that assessed the re-growth in BT-474 and SK-BR3 cells. To be able to mimic a real-life situation more accurately, these experiments involved a relatively long treatment period, and also a re-seeding step to clear cellular debris that may adversely impact on cell growth or behaviours, or make it more difficult to observe.

The results suggest that this mechanism of drug independence holds true for BT-474, with an apparent negative impact on in the ability of these cells to re-grow in combination therapy, but not for SK-BR3. This is reminiscent of the current clinical setting when considering the cancer sub-type that each cell line represents: HER2+ HR- (represented by SK-BR3) is more likely relapse after targeted therapy than HER2+ HR+ (represented by BT-474), although this is largely due to the sensitivity of HR+ tumors to anti-estrogen therapy. Although cell lines are likely to be relatively homogenous compared to a real-life tumor situation which has a much more diverse array of different micro-environmental conditions and also degrees of genomic instability, a pre-print submitted by Roden *et al*. (2018)[224], using single cell transcriptomics on different breast cancer cell lines (including BT-474 and SK-BR3), demonstrated a striking degree of heterogeneity. Along with this, another recently submitted pre-print by Chang *et al*. (2020) that also used single cell transcriptomics[225], shows that surviving cells after lapatinib treatment form two distinct molecular sub-types, reminiscent of an epithelial and mesenchymal state.

2.3.4.2 Extrapolation of re-growth results into a clinical setting: *in vivo* considerations, and experimental future directions

Patient variability and micro-environmental interactions

If these results carried over to an clinical setting, it could mean that patients with a HER2+ HR- tumor sub-type could still experience eventual tumor re-growth, despite apparent initial treatment success. HER2+ HR+ tumors, however, could be less likely to undergo relapses. This is reflected in the clinical evidence, as has been previously discussed. However, it is important to consider aspects of clinical treatment that are not reflected in an *in vitro* experimental setting, and how these could be addressed in future experiments. Firstly, patient-patient variability could translate into varying probabilities of tumor relapse, highlighting the need of parallel strategies to appropriately stratify patients according to bio-marker expression or transcriptomic, proteomic or metabolomic profiles. To this end, various bio-markers are being characterised across multiple clinical trials[225]. Secondly, a real life setting involves a high degree of micro-environmental and immune effects, including endocrine, immune and ECM interactions, which are also likely to influence the ability of a cell to remain dormant or not.

Immune system interactions: co-culturing with immune cells as a future direction

The cross-talk between cancers and the immune system is currently an area of extensive clinical development, with anti-PD-L1, PD-1 or CTLA-4 monoclonal antibodies taking precedent. Pembrolizumab (Keytruda®), an anti-PD-1 monoclonal antibody, has been approved across a wide range of cancers, and is now the best selling and most widely approved targeted-cancer therapy in history[226], having been approved for use across a wide range of cancers. It has shown encouraging results in Phase II clinical trials in HER2+ breast cancer when administered along with trastuzumab[227]. In *in vitro* cell culture experiments such as these, the relevance and importance of co-culturing HER2+ cell lines with immune cells has been shown. On their own in culture, HER2+ murine breast cancer cell lines do not over-express PD-L1, but this was induced once they were co-cultured with human peripheral blood mono-nuclear cells[228]. Future co-culture experiments would be useful to observe how interactions with the immune system impact on HER2 and pirin inhibition synergy, and the ability of cells to re-grow. In the context of immune effects, it would be useful to characterise this HER2 and Pirin synergy when using trastuzumab as the HER2-inhibitor, given the immune recruiting effects that trastuzumab has been demonstrated to have[229].

Experimental vs real-life time scales, and tumor metastasis: *in vivo* experiments as a future direction

Finally, the time scale of these experiments are different than the time scale of experiments in a real-life setting, both in terms of treatment duration (months to years) and also the time to tumor relapse, which normally takes place over years or even decades, rather than the weeks in these experiments. Over these time scales, and given the inherent tumor cell instability of tumor cells, and also the different tissues that these cells may have metastasised to, a whole plethora of different cellular scenarios that impact on their ability

to re-grow or not re-grow could be at play. The only appropriate way to experimentally validate this on a practical experimental time scale (outside of real-world clinical trials) is by performing *in vivo* mouse experiments and observing rates of relapses. As discussed in Section 3.2.3.2, efforts for this are already planned and have been discussed with the EMBL LAR Facility, by performing first-line treatment by comparing lapatinib or EMBL-703625 monotherapy to combination therapy.

An equally as important experiment is to characterise how these combinations impact on tumor relapses in local or metastatic sites, or whether HER2 and pirin inhibition is appropriate after relapse (second-line treatment). Current evidence suggests that pirin could plays a role in tumor metastasis. Importantly, long-term follow-up studies on breast cancer patients found that pirin expression was positively associated with the likelihood of tumor metastasis[230]. As well as this, evidence linking pirin expression to metastasis exists from other tumor types. In cervical cancer cells, pirin has been shown to play a role in metastasis through mediating EMT, which can be overcome with circumin treatment[231]. Similarly, in HeLa cells, pirin has been shown to regulate EMT independently of Bcl3-Slug signalling[195]. Additionally, mir-155, a microRNA encoded by the MIR155 gene has been identified and characterised as an important regulator of metastasis, and also as a regulator of pirin[232]. When inhibited, it has been shown to prevent metastasis of breast tumor cells to the lung through EMT inhibition[233].

The cell line experiments discussed thus far have demonstrated a large combinatorial effect on cell viability and toxicity, and demonstrated synergy between lapatinib and EMBL-703625. As well as this, re-growth experiments have shown that this combination also could inhibit the ability of HER2+ breast cancer cells to re-grow. Previous results from the EMBL CBCF on HeLa cells suggest that EMBL-703625 has large impacts on cellular metabolism, including glycolysis. Results from our lab (Section 2.8) also indicate that metabolism is an attractive area of molecular targeting, and, in line with this, EMBL-703625 and lapatinib show synergistic interactions, have largely distinct effects on the cellular transcriptome, and may compromise the ability of some cells to re-grow after therapy.

2.3.5 Future experiments (with relevance to results discussed in Section 2.3).

Experiment	Rationale
***In vivo* relapse experiments using transgenic inducible mice**	The experiments performed in this section suggest that lapatinib and EMBL-703625 may come together to reduce the ability of cell lines to re-grow after treatment removal. However, the complexity of the in vivo environment makes in vivo experiments that characterise relapse rates more applicable to a real life clinical setting. Lapatinib and EMBL-703625 can be administered together in a first-line setting, with continued Doxycycline administration until tumor remission. If enough mice have remission to have an appropriate sample size, the average time to relapse and lifetime rates of tumor relapse can be characterised. If EMBL-703625 has an acceptable toxicity profile, this also gives rise to the possibility that it could also separately be tested as a maintenance therapy. These approaches would involve removal of the affected mammary fat pads by surgery as part of the experiment, to mimick a real life clinical situation more accurately.

Table 8: Future experimental directions with regard to the data discussed in Section 2.3. Although the immune-co-culture experiments would be a good further direction, these experiments have not yet been explicitly planned or discussed.

2.4 Co-inhibition of cellular glycolysis alongside HER2 or Pirin inhibition

2.4.1 Oxamate and EMBL-703635 show strong synergy together in reducing the viability of BT-474 and SK-BR3 cells

Data from transcriptomic and metabolomic experiments on mice (see Section 2.8) and[175] along with evidence from the literature[152] suggest that metabolism is fundamentally altered in tumor and residual cells, and therefore serves as an attractive point of interference in combination therapy. In particular, data from the Jechlinger Lab[175], data from the EMBL-CBCF (See Figure 8 (Page 49), and data from various sources in the literature (See Section 1.5.3), suggest that glycolysis is of particular importance in the acquisition of resistance against HER2 targeted therapy.

To test how glycolytic inhibition potentiates the effects EMBL-703625 and Lapatinib on BT-474 and SK-BR3 cells, cells were treated with oxamate, a lactate dehydrogenase inhibitor, at varying concentrations along with varying concentrations of Lapatinib and EMBL-703625, in an experimental design similar to the Lapatinib and EMBL-703625 synergy experiments described in Section 2.1.2.

Preliminary experiments were conducted to determine appropriate concentration ranges of oxamate to use (50mM to 175mM). For both cell lines, oxamate had a severe impact on cell viability at the highest concentration measured (175mM), with a comparatively more severe effect on SK-BR3 cells compared to BT-474. The lowest concentration measured (50mM) had a more moderate effect, with an approximately 20% reduction of viability in BT-474 and 10% reduction in SK-BR3.

As seen in Figure 23, oxamate alongside lapatinib or EMBL-703625 had a combination effect in both cell lines. However in both cell lines, for lapatinib and oxamate, this difference appeared less severe than for EMBL-703625 and oxamate. For example, in BT-474 cells, 0.1µM of lapatinib, or 1.0µM of EMBL-703625 had a similar effect on viability in monotherapy (Figure 23(a) and (b), respectively), reducing viability to approximately 55% of the vehicle treated control. 125mM of oxamate reduced viability to approximately 40% of the control. When in combination, 0.1µM of lapatinib with 125mM of oxamate reduced viability to 20.5% of the control, whereas 1µM of EMBL-703625 and 125mM oxamate reduced viability to 4.7% of the control.

ZIP synergy calculations (using the same approach as in Section 2.1.2, but without the plate interpolation and combination) supported these findings[‡]. As shown in Figure 23(e) and (g), lapatinib and oxamate had generally less of an overall synergistic effect than EMBL-703625 and oxamate (Figure 23(f) and (h)), both in terms of overall range, and top synergy peak. For the majority of the SK-BR3 oxamate + lapatinib landscape, the interaction was approximately around 0, or slightly above or below, generally being suggestive

[‡]In these oxamate combination experiments, plate interpolation was not used, as the number of different treatments would have led to an unpractical number of plates if each plate was transposed, as the number of plates would have doubled.

of additivity, but tending towards synergy in particular concentration areas. Overall, these data suggests that HER2 inhibition alongside glycolytic inhibition is generally more additive, whereas pirin inhibiton alongside glycolytic inhibition is more synergistic.

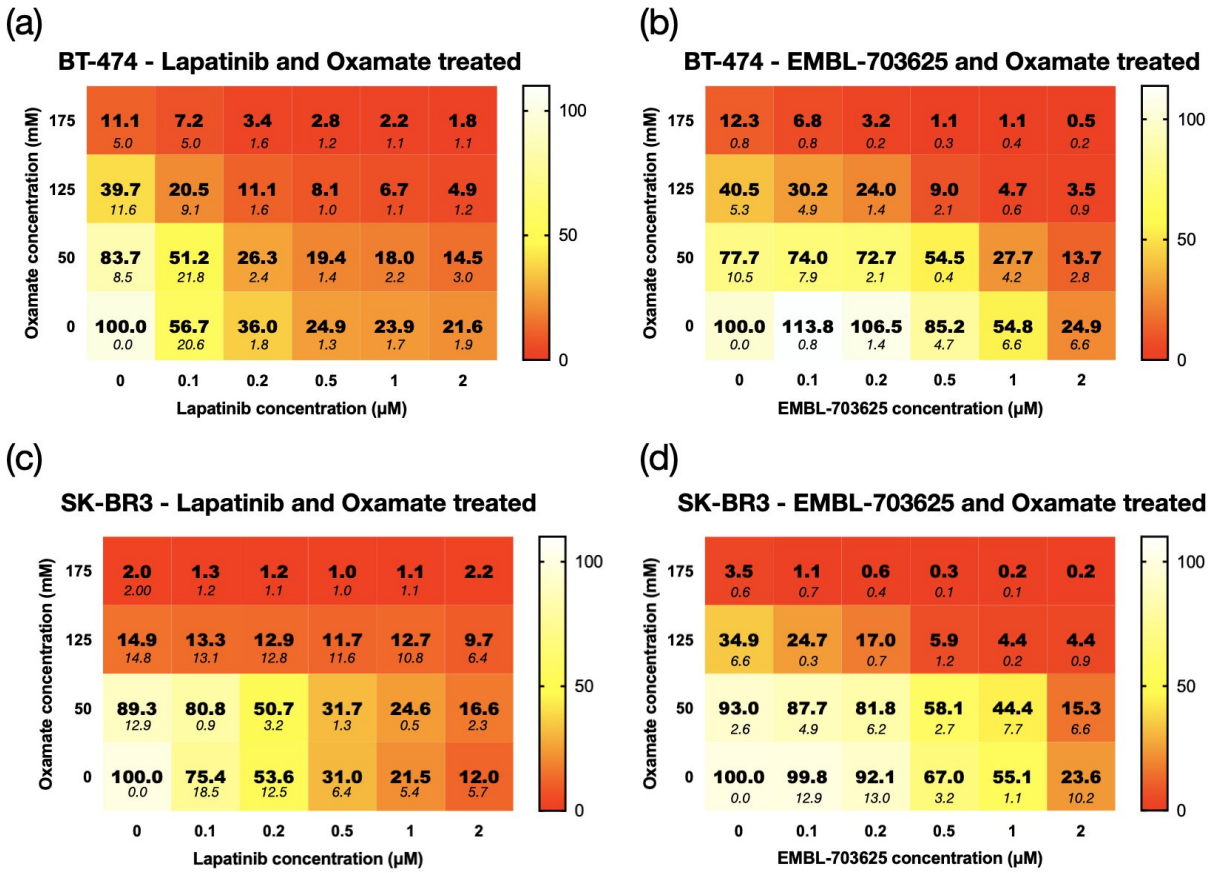

Figure 23: Heat-maps of relative viability (normalised to dual vehicle treatment) with BT-474 cells (a and c) and SK-BR3 cells (b and d) treated for 72 hours with oxamate and Lapatinib, following 7 days of 3D growth. Displayed values in bold are the means of 3 experimental replicates, which each had 3 technical replicates. The smaller written values in italics are the SEM. Experiments were performed on black-walled 96 well plates.

Figure continued on next page.

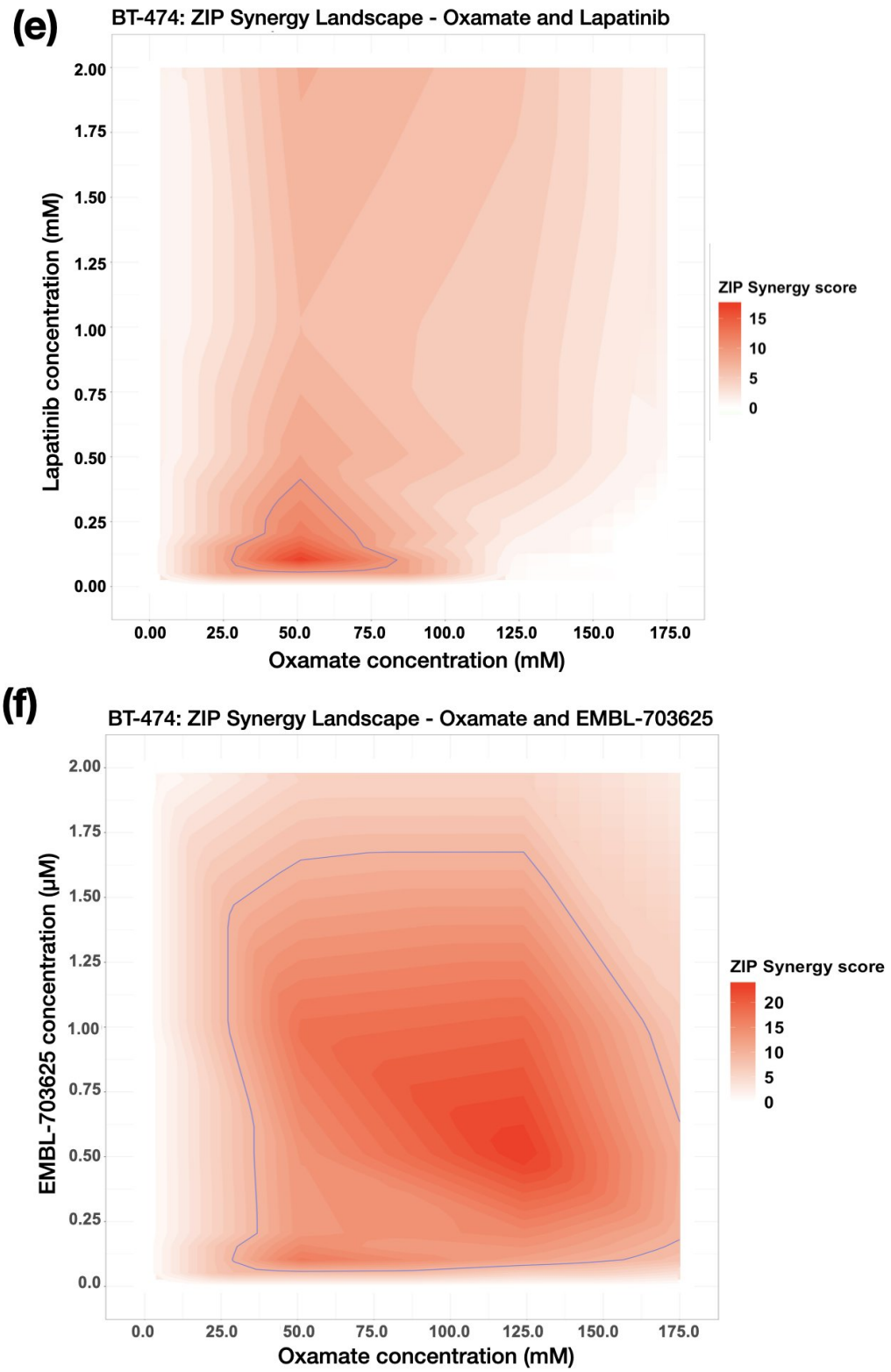

Figure 23: *Figure continued on next page.*

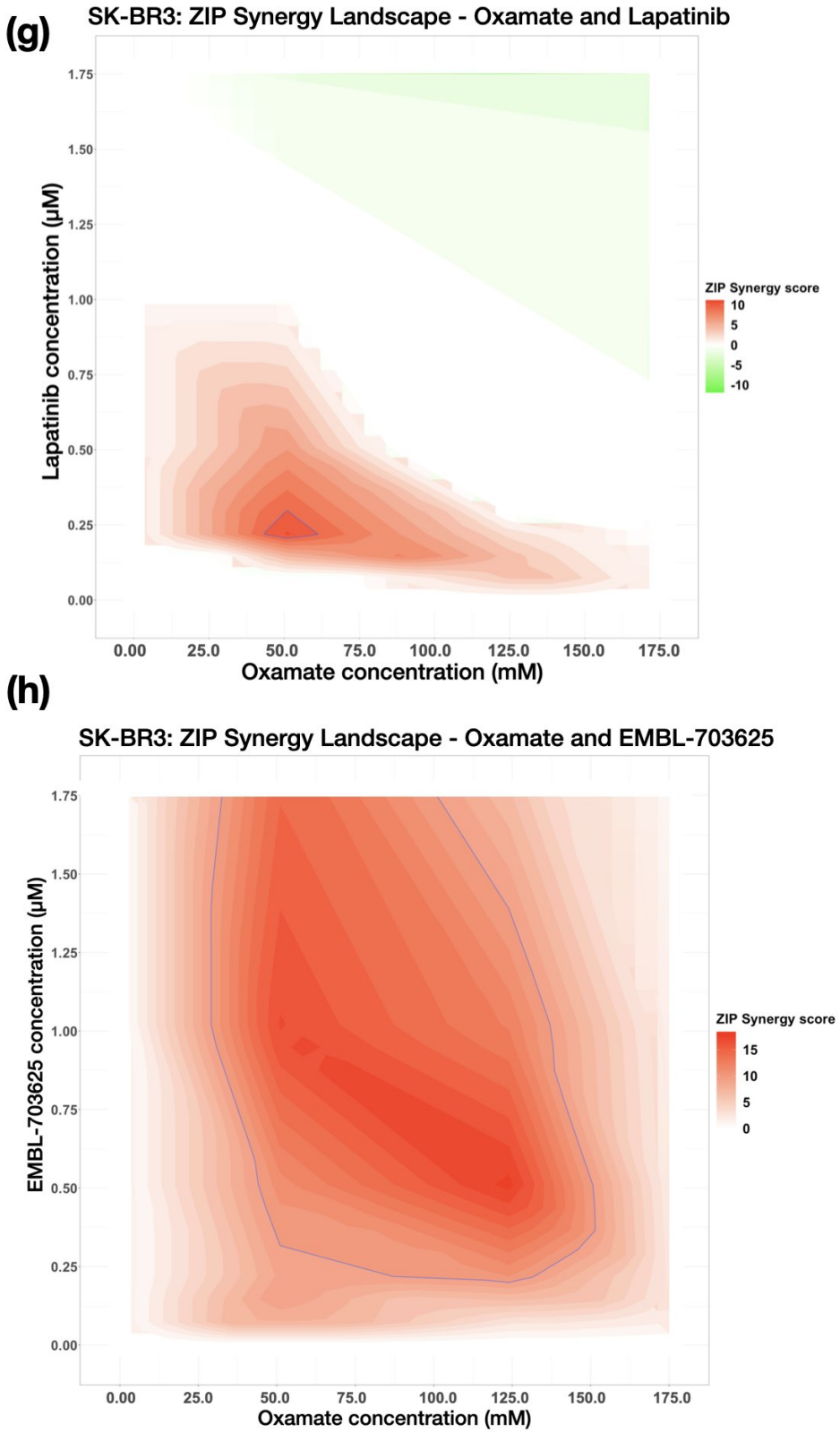

Figure 23: **BT-474 (g) and SK-BR3 (h) ZIP Synergy landscape of cells co-treated with oxamate and Lapatinib, and of cells co-treated with oxamate and EMBL-703625 (c: BT-474, d: SK-BR3)**. Data were processed as described in Figure 13. ZIP synergy data was generated by SynergyFinder 2.0, and plotted in R using the "ggplot2" package. The blue line denotes ZIP synergy scores that are higher than 10; there is no consensus of which synergy scores denote synergy, but it is widely agreed that a synergy score above 10 is confidently synergistic.

2.4.2 Discussion of Section 2.4: Inhibition of pirin and glycolysis show strong synergy in BT-474 and SK-BR3 cells, inhibition of HER2 alongside glycolysis shows additivity

Oxamate was used to functionally characterise how metabolic inhibition works alongside each individual inhibitor, and the results showed that oxamate and EMBL-703625 showed strong synergy with one another, and weaker synergy or additivity with lapatinib. The strong synergy showed between oxamate and EMBL-703625 suggests a “blockade” mechanism, where metabolism is more comprehensively inhibited due to the action of more than one inhibitor on it.

Figure 23 (Page 100) shows that oxamate, a lactate dehydrogenase A inhibitor, and EMBL-703625 show strong synergy in combination with each other in BT-474 and SK-BR3 cells, but show additivity (apart from a small areas of synergy) when in combination with lapatinib at concentrations that lead to similar treatment effectiveness. This suggests that oxamate and EMBL-703625 act together to blockade glycolysis to a stronger degree than oxamate and lapatinib do. Taken together, this suggests that lapatinib and EMBL-703625 may converge on glycolysis, through separate mechanisms, which, in part, allows them to elicit their combination effects.

There is evidence to support this notion in the literature and from EMBL CBCF-generated data. Firstly, lactate dehydrogenase A, the target of oxamate, is upregulated by HER2 through the action of HSF1, and previous studies on HER2 overexpressing breast cancer cells have shown that oxamate selectively inhibits the growth of these cells[162]. In terms of tumor resistance, changes in glycolysis appear to be a way that resistance to HER2 targeted therapy is acquired, demonstrated in cell lines for trastuzumab and lapatinib resistance[123;114;180] This suggests that HER2 inhibition influences glycolysis, and cells that are able to alter their glycolysis are more likely to survive. As well as this, a transcriptomic-based study using parental and persister BT-474 cells after transient lapatinib treatment showed that many glycolysis based genes are altered in the persister cells that are refractory to glycolysis treatment[234], suggesting a relatively fast time scale for resistant sub-populations to form. Furthermore, targeting glycolysis in HER2+ cells makes them more sensitive to subsequent trastuzumab treatment[114].

With regard to pirin, as it is currently poorly functionally characterised, no such experiments that inhibit pirin alongside any glycolysis enzymes have been performed in the literature. However, transcriptomic data generated from the EMBL CBCF suggested that glycolysis enzyme expression was significantly altered by pirin inhibition in HeLa cells. In the transcriptomic experiments in this thesis, it appears that the read depth on glycolysis specific enzymes were too low to many conclusions in this respect. Nonetheless, the CBCF data on pirin, combined with the HER2-inhibition related evidence from literature led to the hypothesis that a part of EMBL-703625 and lapatinib synergy could be through them both inhibiting certain aspects of glycolysis.

To characterise this in more detail, further experiments would be required to understand how each particular inhibitor specifically influences glycolysis in HER2-over expressing

breast cancer cells. To this end, at the time of this thesis submission, efforts to perform metabolomic experiments had already been undertaken, with optimisation steps required to isolate metabolites from the matrigel that cells are grown in. This partially uses the methods pipeline developed by Radic-Shechter *et al.,* (2020)[175].

2.4.3 Future experiments (with relevance to results discussed in Section 2.4)

Experiment	Rationale
Characterising lapatinib or EMBL-703625 alongside other inhibitors	A combination of the data from the EMBL CBCF and transcriptomic data from this project suggest that there may be various nodes that lapatinib and EMBL-703625 come together to elicit their synergy through, for example, heat shock protein expression or the expression of solute carriers. Using the methodology from this section, the effect of inhibiting proteins involved in these different areas can be explored.

Table 9: Future experimental directions with regard to the data discussed in Section 2.4.

2.5 Comparison of the response of non-neoplastic and neoplastic mouse mammary cells treated with lapatinib and/or EMBL-703625

2.5.1 Combination treatment with lapatinib and EMBL-703625 more strongly reduces viability in induced primary mouse mammary tumor cells, compared to never induced mammary cells

Although synergy is important in being able to minimise drug dosages whilst still achieving effective tumor treatment, it is also important to ensure that this synergy does not affect non-neoplastic cells. As well as this, in an experimental context, it is important to assess drug interactions across multiple systems, to ensure robustness of data in a pre-clinical setting. To address both of these issues, an experimental design was utilised involving in vitro organoids derived from transgenic mouse mammary glands, which could be induced into a tumorigenic state by over-expression of the HER2 and MYC oncogenes upon the addition of doxycycline to the cell media (see Figure 10). This allowed for an in vitro comparison between normal mammary gland epithelial cells and their tumor correlates.

Mouse mammary epithelial gland cells from mice transgenic for MMTV-rtTA, TetO-MYC, and TetO-Neu were isolated, seeded in matrigel and grown on multiple black walled 96 well plates. After a growth period, half of the cells had doxycycline introduced into their growth media in order to induce tumorigenesis, whilst the other half were kept on normal media, to remain as un-transformed cells. After 6 days with or without doxycyline exposure to induce a tumorigenic transformation, lapatinib and EMBL-703625 were introduced to the cells in combinations at a range of different concentrations, ranging from 25µM to 0µM. Cells were maintained on their respective treatments for 48 hours before viability assays were performed. The schematic for this experiment is displayed in Figure 24.

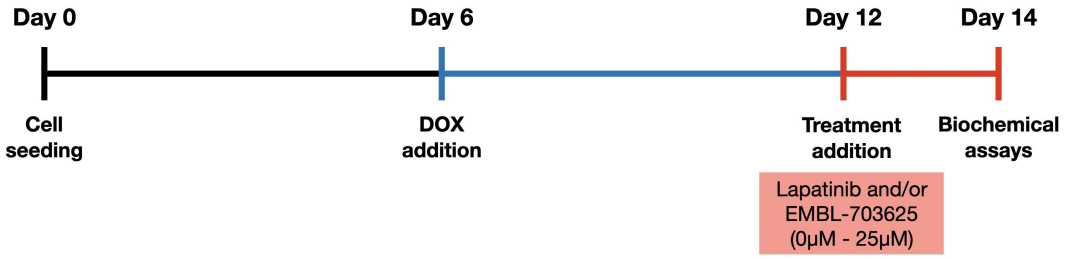

Figure 24: Schematic of experiments performed on non-neoplastic or induced-neoplastic mouse mammary gland cells

This experiment was performed on four separate mice, all positive for MMTV-rtTA, TetO-MYC and TetO-Neu. Figure 25 and 26 show the effects of singular treatment with either drug, and their effects in combination, respectively. As seen in Figure 25(a),(b),(d) and (e), the mice exhibited statistically significant heterogeneity for EMBL-703625 and lapatinib monotherapy. Overall, comparing tumour and never induced cells across all four mice, tumor cells were significantly more sensitive to either treatment, compared to never

induced (normal) cells (Figure 25(c) and (f)). Because of the heterogeneity between mice, creating a synergy landscape, as was done for BT-474 and SK-BR3 cells, would not be appropriate; ZIP synergy calculations rely on changes in dose-response curves, given that these dose-response curves change between each mouse, taking an average for the four replicates would not be reliable.

As shown in Figure 26, lapatinib and EMBL-703625 had a significantly larger inhibitory effect on the viability of tumor cells, compared to never induced cells. The effect size of this was most pronounced at the higher concentrations, as seen in Figure 26(c). Moreover, this effect was consistent between all four mice (Supplementary Figures S.6 - S.9) despite heterogeneity in responses to the individual drugs. Overall, this suggests that the synergy between lapatinib and EMBL-703625 elicits its effects more specifically on tumor cells, and less-so on normal, non-neoplastic cells.

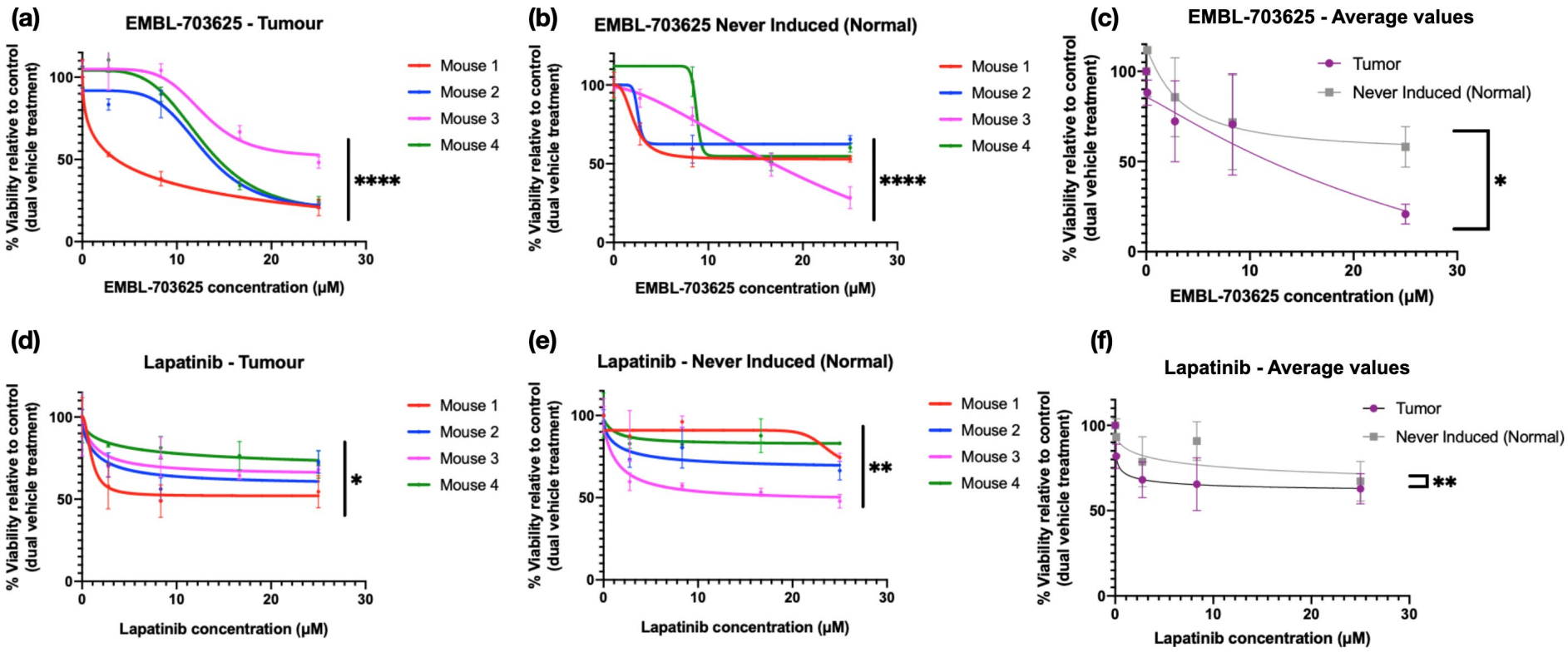

Figure 25: **Dose response curves for each of the four mice used in the experiments, in tumor and never induced cells treated with either lapatinib or EMBL-703625.** (a) and (d) show dose response curves for each mouse in tumor cells for EMBL-703625 and lapatinib, respectively. (b) and (e) show dose response curves for each mouse in never induced cells, for EMBL-703625 and lapatinib, respectively. (c) and (f) show the average for the four mice, comparing tumor and never induced cells. Data points are normalised to sole vehicle treatment (100% viability). Error bars show the SEM for technical replicates (n = 3) for parts a, b, d and e. Error bars show the SEM between all four mice for parts c and f. Curves and statistics were calculated through nonlinear curve fitting (using Prism), and p-values were calculated based on the null hypothesis that one curve could represent the dose response curves on each graph. Significance notation is as follows: ns (not significant) - $p \geq 0.05$; * - $p < 0.05$; ** - $p < 0.01$; *** - $p < 0.001$; **** - $p < 0.0001$.

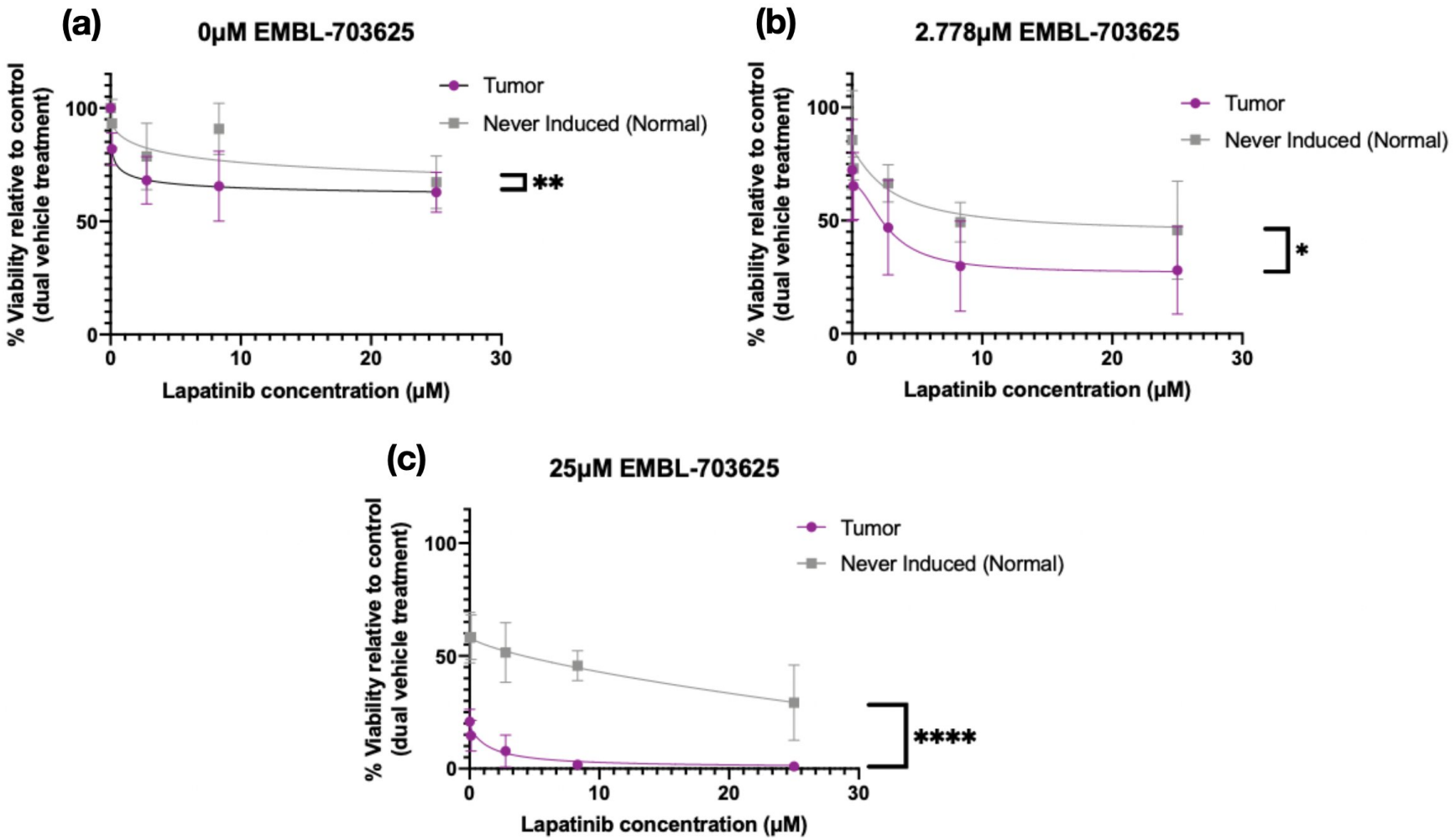

Figure 26: **Dose response curves of Never Induced (Normal) or Induced (Tumor) cells at varying concentrations of lapatinib and EMBL-703625**. (a), (b), and (c) show tumor and never induced (normal) cell dose response curves at 0, 2.778 and 25μM EMBL-703625 with different concentrations of lapatinib. (a) is the same graph as in 25(f). Each data point is the mean of the average normalised viability for the four mice used in this experiment, and error bars show the SEM. Statistics were calculated through nonlinear curve fitting, and p values were calculated based on the null hypothesis that one curve could represent the dose response curves for Tumor and Never Induced cells. Significance notation is as follows: ns (not significant) - $p \geq 0.05$; * - $p < 0.05$; ** - $p < 0.01$; *** - $p < 0.001$; **** - $p < 0.0001$.

2.5.2 Discussion of Section 2.5: Experiments on mouse-derived primary cells suggest a preferential effect on neoplastically transformed cells, compared to normal

As has been discussed previously, safety and efficacy are both important when choosing and characterising new treatment regimes for cancer therapy. It is important that the combination killing effect of drug combinations such as lapatinib and EMBL-703625 do not carry over into non-tumor cells. This phenomenon is sometimes known as “synergistic toxicity”. Currently, there is strong evidence to suggest that both drugs have an acceptable safety profile in monotherapy. Lapatinib is an established clinical therapy, and is therefore known to demonstrate acceptable safety in humans, as well as mice[94;235]. EMBL-703625 has been demonstrated by the EMBL-CBCF to have excellent tolerability in mice (data not shown).

To experimentally deduce if this drug interaction was unique to tumor cells, the inducible mouse systems that are utilized by the Jechlinger Lab were used (see Figure 24, Page 103). This system allows a direct comparison between the HER2-driven tumorigenic and non-tumorigenic state in cells from the same source, allowing for an ideal experimental control. Both drugs were tested in monotherapy at different combinations, and in combination therapy at these different concentrations.

Interestingly, in monotherapy, lapatinib had a comparable killing effect on tumor cells to normal cells. Data do not exist for the effect of lapatinib or other HER2-targeted therapies on the normal mammary gland cells. It is therefore possible that the endogenous HER2 that is expressed by normal mammary gland cells renders them sensitive to HER2 inhibition, but it is also possible that removing primary cells from the context of the mouse breast and growing them in culture renders them more or less sensitive to certain drugs. In contrast, EMBL-703625 did have a steeper dose-response curve in induced (tumor) cells compared to never induced (normal) for 3 of the 4 mice, suggesting that a neoplastic transformation, even without the usual microenvironmental context of a tumor cell, is enough to render cells sensitive to pirin inhibition. However, it is important to note that for any drug in monotherapy, it is most important to test in an *in vivo* setting to test for off-target effects in the many different tissues of the body, as well as immune and other interactions with the tumor micro environment that cannot be properly recapitulated *in vitro*.

In combination, lapatinib and EMBL-703625 had a stronger combined effect on neoplastically transformed cells, compared to non-transformed cells from the same source (Figure 26) showing that in mammary gland epithelial cells, HER2 and MYC-driven neoplastic transformation is required for them to elicit their combinatorial killing effects. This suggests that lapatinib and EMBL-703625 synergy happens solely on neoplastic cells driven by HER2 and MYC oncogenes, which could reduce the incidence of side effects as a result of this synergy. As well as this, these experiments provides a good rationale for progression into *in vivo* experiments. A comprehensive discussion of the experiments that could be conducted in an *in vivo* setting, and the value that these would bring, is

discussed in Section 3.2.3.2.

2.5.3 Future experiments (with relevance to results discussed in Section 2.5)

The main future direction for these experiments is to progress to *in vivo* approaches. The two ways of doing this: assessing first-line efficacy, and monitoring relapse rates. These have previously been discussed in Section 2.1.4 (Page 70) and Section 2.3.5 (Page 96), respectively.

2.6 Consecutive treatment

The results showing an apparent synergy between lapatinib and EMBL-703625 in human cell lines, as well as the increased tumor inhibitory effect compared to normal cells in the mouse system (Section 2.5), suggested that simultaneous combinatorial treatment with both of these drugs could serve as a promising potential tumor treatment regimen in a clinical setting. However, any treatment with multiple drugs comes with an increased risk of serious side effects in the patient, and is a large reason for early phase clinical trial discontinuation. One common way that this is addressed is by performing consecutive drug treatment, where one drug is used as a first-line treatment, followed by the other drug as a secondary or maintenance treatment to treat residual cells and/or relapsed tumors. In breast cancer, there is normally surgery involved (for example, mastectomy or lumpectomy) to remove the affected tissue and/or surrounding lymph nodes. In this case, treatments are referred to as neoadjuvant (before surgery) and adjuvant (after surgery).

In order to assess whether initial lapatinib treatment gave rose to increased sensitivity to EMBL-703625, and vice versa, experiments were designed using BT-474 and SK-BR3 cells that administered these drugs consecutively. The timings of the experiments and methodology used to normalise and compare the data generated are displayed in Figure 27 (a) and (b), respectively.

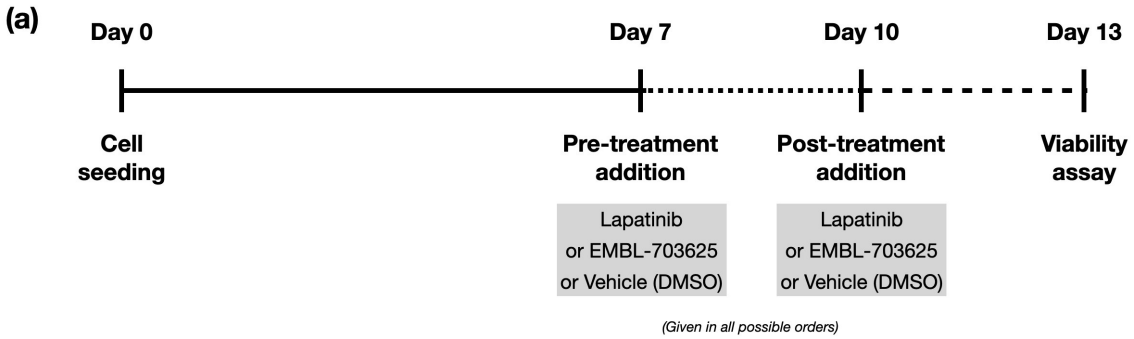

Figure 27: ***Schematics of consecutive treatment experiments.*** *(a) Experimental timings. Cells were grown for 7 days, before they were treated with one treatment (Lapatinib, EMBL-703625 or vehicle (DMSO) for 72 hours followed by washing with PBS and then treatment with the secondary treatment (any of these 3 treatments again). At the end, a viability reading was taken.*
Figure continued on next page.

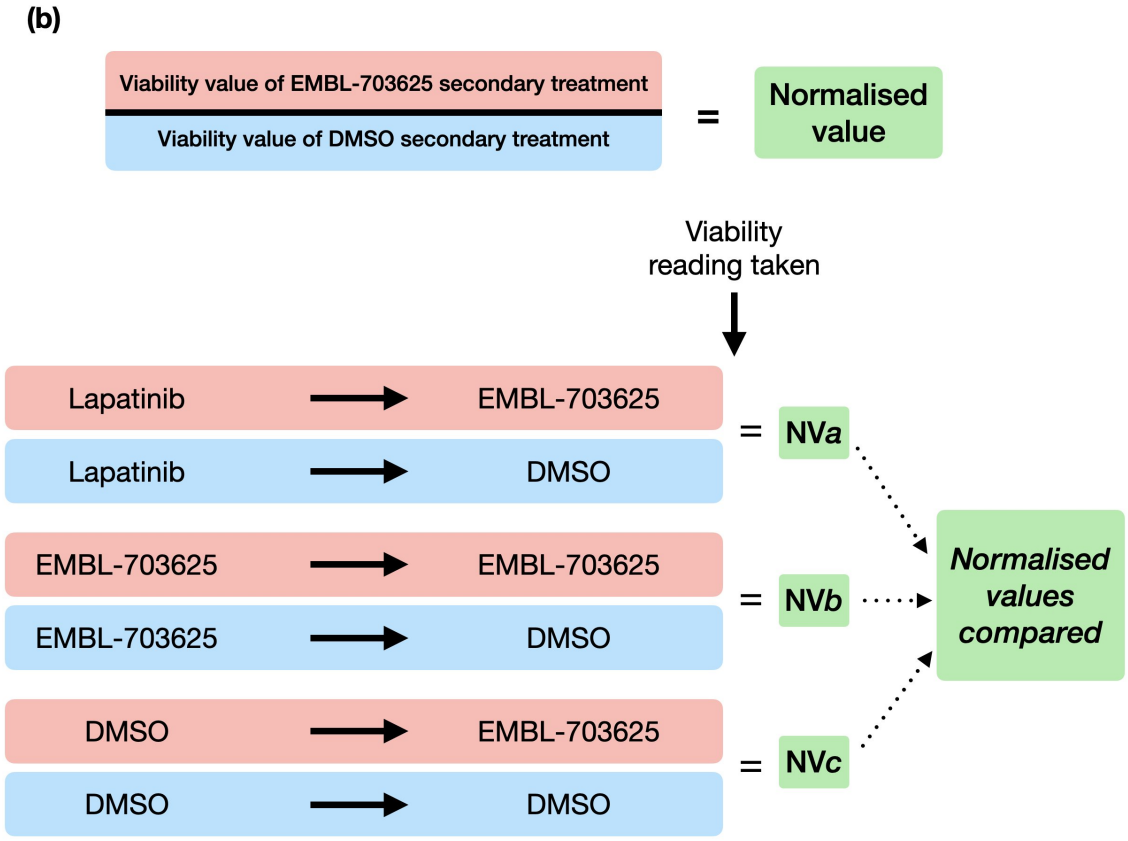

Figure 27: **Schematics of consecutive treatment experiments.** (b) Secondary treatments were compared to DMSO-treated cells to obtain a normalised read-out. These normalised values were then compared to understand which initial treatments had possibly led to tolerance or sensitisation to the secondary treatment. The example shown is for EMBL-703625 as the secondary treatment. This same process was also the case when lapatinib was the secondary treatment.

2.6.1 BT-474 cells are sensitised to pirin inhibition following treatment with lapatinib

As seen in Figure 28, sensitising treatment with lapatinib led to a significantly increased sensitivity to subsequent EMBL-703625 treatment (One-way, two tailed, nested design ANOVA, $p<0.001$), relative to cells not subjected to any sensitising treatment (vehicle treated) in BT-474 cells, but not with SK-BR3 cells. The selected concentration of EMBL-703625 alone does not lead to substantial changes in viability in either cell line (see Figure 11 and Table 4), suggesting that lapatinib is able to predispose cells to EMBL-703625 sensitivity, even at otherwise non-efficacious concentrations. No other comparative treatments were statistically significant, although it is notable that SK-BR3 treated both times with EMBL-703625 was close to the significance cut-off value ($p=0.0505$) when compared to EMBL-703625 followed by vehicle treatment, suggesting that SK-BR3 cells could see increasing sensitivity to continuous EMBL-703625 treatment.

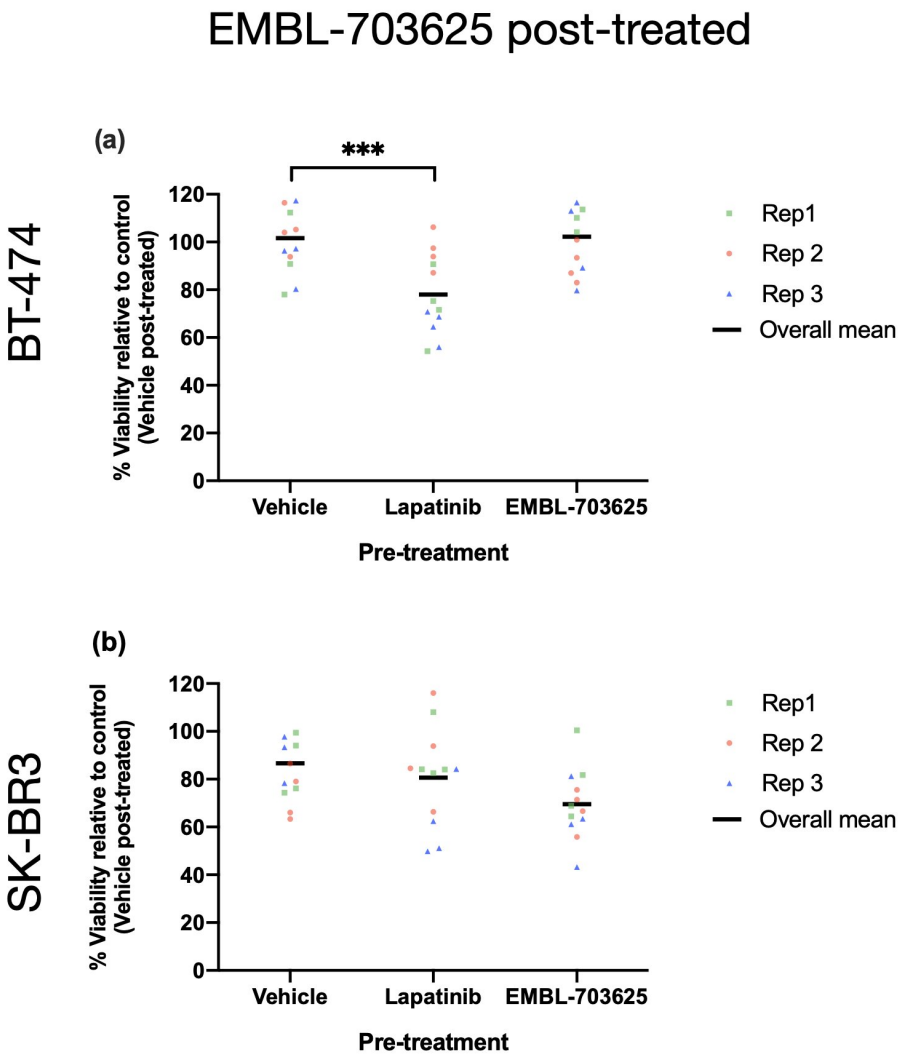

Figure 28: **Viability readings (percentage normalised to vehicle treated) for BT-474 and SK-BR3 cells treated with EMBL-703625 (a and b, respectively) that have been pre-treated for 72h with either vehicle (DMSO), Lapatinib or EMBL-703625.** Each experiment was repeated 3 times. Individual points display each technical replicate, colour coded to denote each experimental repeat. The black line shows the overall mean. *** denotes statistical p-values of <0.001, tested with a one-way, two-tailed, nested design ANOVA. Non-significant differences have no label.

2.6.2 BT-474 cells begin to lose sensitivity to HER2-targeted therapy after initial treatment, whereas SK-BR3 cells do not

The previous subsection showed that BT-474 and SK-BR3 were sensitised to EMBL-703625 treatment, following treatment with lapatinib. In contrast to this, neither BT-474 or SK-BR3 cells were sensitised to lapatinib treatment, following initial sensitising treatment with EMBL-703625. However, BT-474 did see a significant increase in tolerance to Lapatinib, when treated in succession, suggesting that it is quickly able to become tolerant to the drug. Interestingly, these results were not reflected in SK-BR3 cells, who did not lose sensitivity to lapatinib treatment.

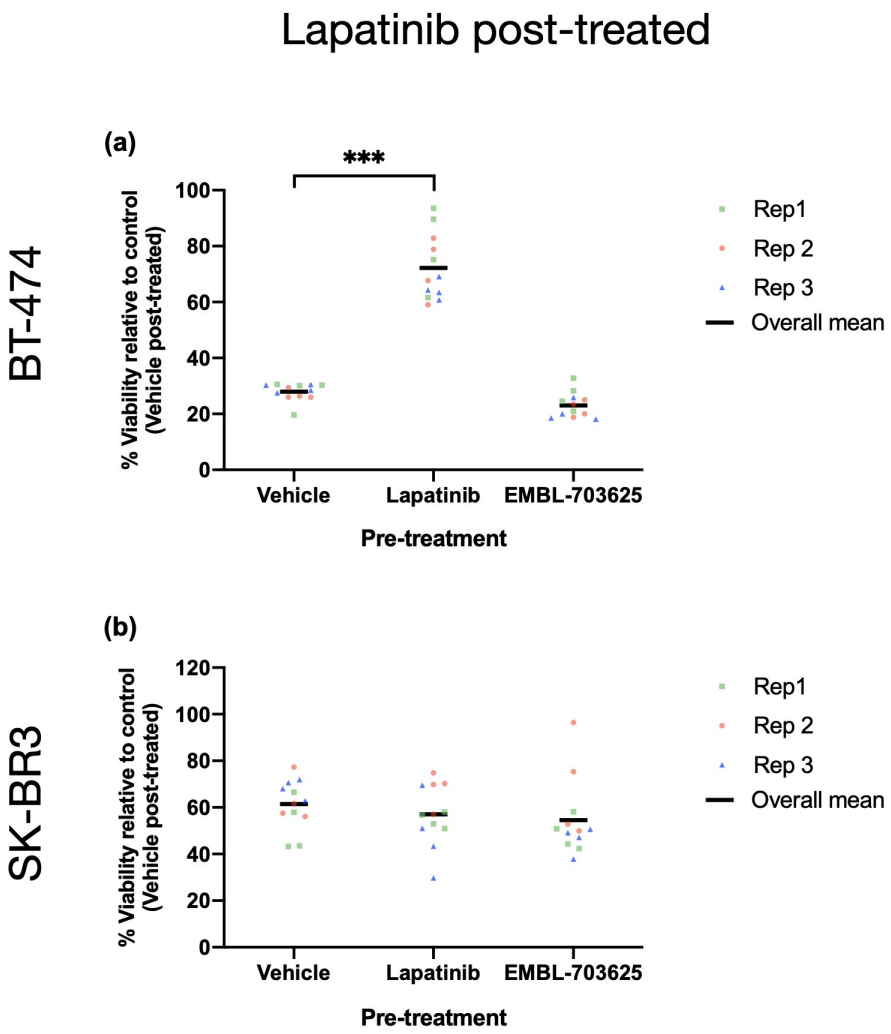

Figure 29: **Viability readings (percentage normalised to vehicle treated) for BT-474 and SK-BR3 cells (a and b, respectively) treated with Lapatinib that have been pre-treated for 72h with either vehicle (DMSO), Lapatinib or EMBL-703625.** Each experiment was repeated 3 times. Individual points display each technical replicate, colour coded to denote each experimental repeat. The black line shows the overall mean. *** denotes statistical p-values of <0.001, tested with a one-way, two-tailed, nested design ANOVA. Non-significant differences have no label.

2.6.3 Discussion of Section 2.6: Lapatinib may sensitise BT-474 cells to subsequent EMBL-703625 treatment

The results in this project have established that lapatinib and EMBL-703625 exhibit synergy in human, HER2+ breast cancer cell lines when administered at the same time. However, in the treatment of many cancers, including HER2+ breast cancer, treatment regimens often involve neoadjuvant (before surgery) and adjuvant (after surgery) treatment regimens. For example, the UK National Institute for Health and Care Excellence (NICE) recommends pertuzumab + trastuzumab + chemotherapy as a neoadjuvant treatment before breast surgery, followed by a variety of possible HER2-targeted treatments based on the specific disease context, including trastuzumab emtansine, pertuzumab, neratinib, or trastuzumab[236]. These decisions are made based on a combination of safety and efficacy data, probability of relapse, and cost effectiveness.

Whilst these have proven to be clinically effective, currently licensed adjuvant/neoadjuvant therapeutic regimens are still all based solely on HER2-targeted therapy, usually in combination with chemotherapy. As discussed in Sections 1.3.5 and 1.4, whilst these approaches are clinically effective, this may allow cells to find "escape" pathways or mechanisms, which gives rise to the possibility of relapses. In fact, approximately 14% of patient tumors lose HER2 expression after neoadjuvant treatment, and these patients are approximately 2-3x more likely to relapse, with disease-free survival being approximately 20% after 5 years[107;237]. On top of this, if these relapses are metastatic, they are disproportionately found in the brain, and are difficult to treat[99;100].

The consecutive treatment experiments were designed with these data in mind, particularly as pirin inhibition may present itself as an attractive treatment regimen in a neoadjuvant or adjuvant setting, to prevent selection for HER2 resistant sub-populations in early-stage treatment. As shown in Figure 28, pre-treatment with lapatinib in BT-474 cells led to sensitisation for later treatment with pirin inhibition, but there was no statistically significant difference in SK-BR3 cells. This could suggest that consecutive treatment could be applicable in a HER2+ HR+ setting, but not in a HER2+ HR- setting. This could suggest that solely HER2-driven cells have a degree of plasticity that allows them to not become more sensitive to pirin inhibition following lapatinib pre-treatment. In this sense, these results are reflective of the results seen from the re-growth experiments (Section 2.3). In line with this, large amounts of evidence show that HER2-targeted therapy resistant cells can utilise alternative oncogenic pathways, such as EGFR, HER3 or IGF-1 signalling[238].

BT-474 also showed a significantly reduced killing effect of lapatinib when also pre-treated with lapatinib, compared to when pre-treated with vehicle (DMSO) or EMBL-703625, suggesting that BT-474 cells quickly acquire lapatinib tolerance. This would back up the fact that BT-474 pre-treated with lapatinib is more sensitive to pirin inhibition, and suggests that there is selection from lapatinib for persister sub-populations, even at early treatment stages. In BT-474 cells, this is also backed up by evidence from the literature. Persister BT-474 cells were able to be relatively quickly derived when treated in 2D culture with lapatinib, and had a largely altered transcriptional profile. Interestingly, these results also showed that lapatinib refractory BT-474 cells were sensitive to ferroptosis, which is mediated in part by pirin[191]. As discussed in section 1.6.3, a multitude of similar genes also appear to be de-regulated in lapatinib refractory cells that are inhibited by EMBL-703625, backing up the data from this project[234].

Pre-treatment with EMBL-703625 did not sensitise either BT-474 or SK-BR3 cells to any subsequent treatment, nor did it cause these cells to develop tolerance to further EMBL-703625 treatment. This suggests that pirin inhibition in these cell lines does not cause sensitization to subsequent HER2 inhibition, suggesting a degree of plasticity. However, it is notable that at the 1µM concentration of EMBL-703625 selected for both cell lines does not have strong effects on their viability, meaning that higher concentrations could have more of a sensitising effect through phenotypic selection, or by influence on cellular pathways. In the future, multiple pre-and post-treatment drug concentrations should be used to understand how the severity of pre-treatment impacts on post-treatment for both

of these drugs. Furthermore, transcriptomic experiments using this experimental design would also help to gain clarity about how drug tolerance or sensitivity is acquired.

2.6.4 Future experiments (with relevance to results discussed in Section 2.6)

Experiment	Rationale
Expanding to multiple concentrations of EMBL-703625 and lapatinib	The experiments outlined in this section were designed with concentrations that elicited the largest possible effect in combination, compared to either agent in monotherapy. However, this was based on concurrent treatment, rather than consecutive treatment. It is possible that maximum efficacy is gained with different concentrations, especially those that are more likely to elicit phenotypic selection on the cell population.
Transcriptomic experiments on successively treated cells	To understand how (or if) cell sensitisation with one agent affects its treatment with the other, transcriptomic analysis could be performed, using similar techniques and analysis pipelines that were used in this project. This would help in gaining an understanding of certain vulnerabilities as a result of treatment with one agent, that the other de-regulates in order to achieve a maximal killing effect.

Table 10: Future experimental directions with regard to the data discussed in Section 2.6.

2.7 Establishment of a spatial and temporal light microscopy pipeline, aimed at assessing intercellular metabolic heterogeneity via the use of a fluorescent metabolic sensor

One aim of this project was to develop an imaging pipeline that would allow a 3D spatial and temporal assessment of the responses of cells to different drug treatments. Multiple methods exist to study tumor metabolism, but rarely are able to resolve over time and space simultaneously. Genetically encoded fluorescent sensors provide a unique way to do this, and can be applied in multiple experimental settings, such as in high-throughput plate reader-based approaches, *in vivo* settings, and *in vitro*, in the setting of light microscopy.

This project aimed to use an *in vitro* approach to characterize the NAD+/NADH ratio over space and time. NAD+ is the oxidized form of NADH. Together, they are some of the most important redox co-factors in cellular metabolism. Their main function is for NAD+ or NADH to serve as an electron acceptor or donor (respectively) in metabolic pathways, including glycolysis, lipid metabolism, the TCA cycle, and the electron transport chain. As well as this, NAD+ has a wider range of non-redox roles as a reaction cofactor, including for PARP and SIRT proteins[239].

In cancer cells, the ratio between NAD+ and NADH tends to be altered, with an increased NAD+/NADH ratio relative to normal cells. Recent work suggests that high levels of NAD+ can lead to a Warburg phenotype; when the amount of NAD+ exceeds the demand for ATP, NAD+ re-generation in the mitochondrial electron transport chain is slowed, which promotes aerobic glycolysis[240]. In breast cancer, SIRT6, which is dependent on NAD+, is associated with disease progression and metastasis[241]. In fact, NAD+-dependent Sirtuins are emerging as an area of interest research surrounding breast cancer metastasis and drug-resistance[242].

Taken together, given the importance of NAD+ and NADH in cellular metabolism, and their central role in cancer cell metabolism, a read-out of the NAD+/NADH ratio is important for informing on the overall metabolic state of the cell, which can have implications for its phenotype. For example, in colon cancer, increased levels of NAD+ was associated with disease progression[243].

2.7.1 The SoNar Sensor: a sensor for the cytosolic NAD+/NADH ratio

The sensor that was used for these experiments is called SoNar (Sensor of NAD(H) Ratio)[1]. It is a flourescent peptide molecule based off subunits of the Rex protein from *Thermus aquaticus* combined chimerically with circulary permutated YFP (cpYFP). The Rex-derived subunits can bind to either NAD+ or NADH, which in turn causes conformational changes in the cpYFP domains of the chimer, changing their fluorescence characteristics (Figure 30(a)). The changes in the fluorescence characteristics can be utilised to obtain a read-out of the cellular NAD+/NADH ratio; when bound to NAD+, the major excitation peak is at approx. 485-490nm, whereas when bound to NADH, it is approx. 405-420nm (Figure 30(b)). SoNar is particularly valuable because of its high dynamic range compared to other sensors, with a 300% increase in the fluorescence ratio observed when NADH was added[1]. Also, compared to other NAD+/NADH sensors, SoNar is relatively resilient to pH changes, and does not have known problems forming tertiary structures which has proven problematic for other sensors in certain cells. Furthermore, it shows an obvious fluorescence response to NAD+, which is useful in the context of high-throughput and *in vivo* experiments, which could be used in future experiments[244] (Discussed further in the discussion of this section: Section 2.7.11.2).

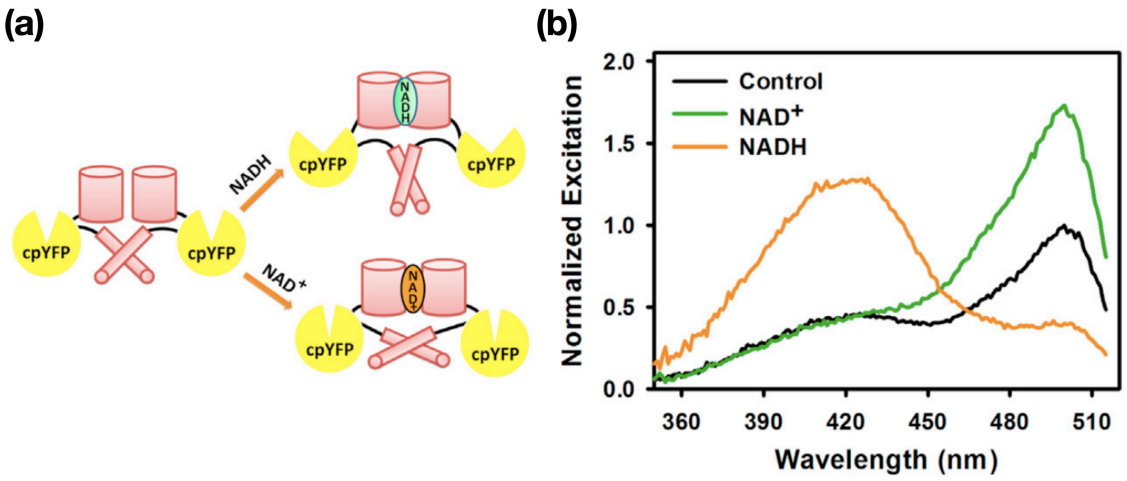

Figure 30: SoNar sensor diagram, and excitation peaks, adapted from Zhao *et al*. (2015)[1]

The SoNar sensor was designed by its creators to be resilient to most environmental condition changes within physiological limits (for example, pH or temperature changes). However, it is still possible that environmental factors could have impacts on its characteristics, as well as microscopy artefacts (for example, altered detection sensitivity between experiments done at different times). It is important to control for this, and also to normalise data so that it can be compared between experiments conducted at different times. In order to do this, SoNar can be calibrated against cpYFP (Shown in Figure 31), which has similar fluorescence properties to SoNar, but does not respond to NAD+ or NADH addition. This can be used alongside the SoNar sensor with the dual purposes of acting as an experimental control (shown in Figure 31), and also as a normalisation benchmark.

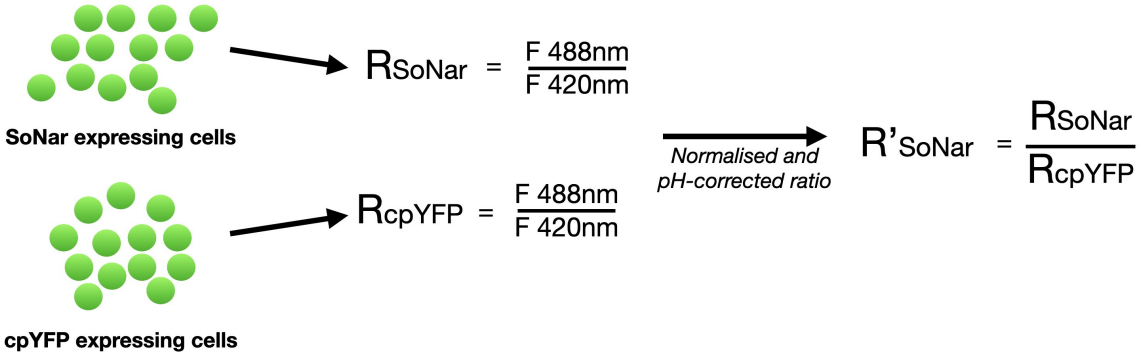

Figure 31: **A schematic, adapted from Zhao *et al*., (2017)[245] of how cpYFP can be used to normalise the ratio of SoNar to account for pH or other imaging artefacts**. Additionally, cpYFP can be used as a non-mathematical control to visually ensure ratio changes past a certain point are genuine.

2.7.2 Establishment of SK-BR3 and BT-474 stably expressing SoNar and cpYFP using lentiviral transfection

To view cell lines expressing SoNar and cpYFP on a fluorescence microscope and get sensitive and reliable readings, it was crucial to generate cells with strong and stable expression of the sensor. Because of this, lentiviral transfection methods were used to generate separate SK-BR3 and BT-474 lines that expressed SoNar and cpYFP under the control of the CMV promoter; preliminary experiments established that the pCMV was effective in expressing enough of each respective fluorophore to achieve a fluorescence intensity that could be used in a microscopy setting (data not shown).

Lentivirally transfected cells were sorted from their non-transfected counterparts by flow cytometry. The cells with the top 5% of fluorescence intensity were further separated using flow cytometry to generate a line of cells with the strongest and brightest SoNar or cpYFP expression, to allow for a high dynamic range when imaging. Whilst BT-474 and SK-BR3 expressing lines were generated (and fluorescence was confirmed) the experiments discussed hereon-in used only SK-BR3 cells– this is because the 3D “grape”-like organoids formed by SK-BR3 cells were easier to potentially analyse heterogeneity on, compared to BT-474 “ball”-like organoids, which had very tightly packed cell-cell connections (3D structures shown in Figure 9, Page 53). BT-474 cells have been stored in liquid nitrogen and are intended to be used in future experiments.

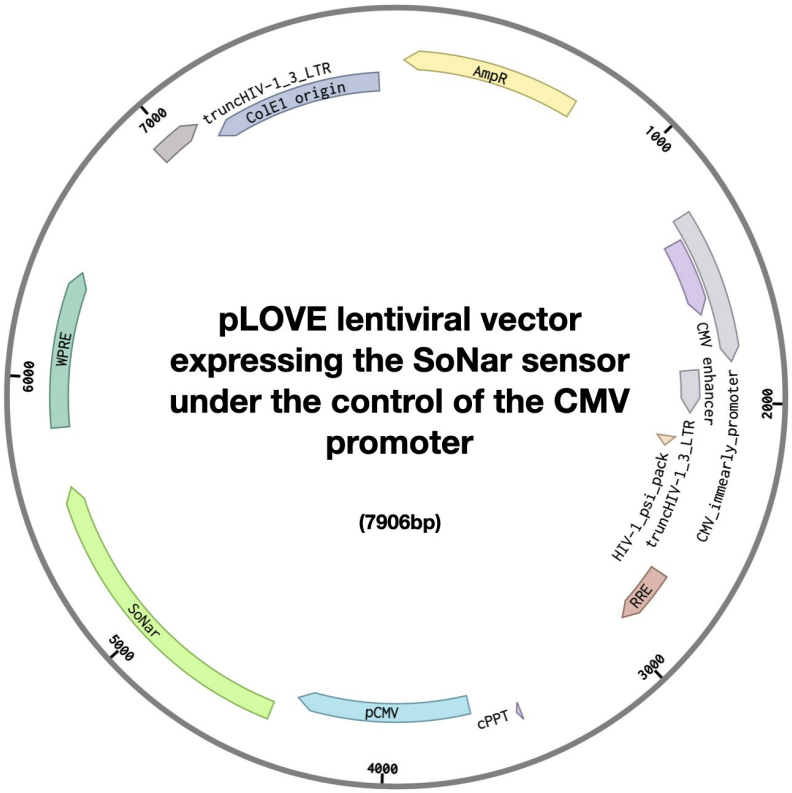

Figure 32: **The pLOVE lentirival vector expressing the SoNar sensor under the control of the CMV promoter.** SoNar (shown) and cpYFP (Supplementary Figure S.10) were kindly provided by the original creators of the sensor[1]. These were cloned into the pLOVE vector using PCR-introduced restriction sites at each end of the gene. SoNar and cpYFP were both cloned into the same position. Lentiviral particles were then produced, before transfection into BT-474 and SK-BR3 cells. The most strongly fluorescent 5% of cells were isolated through FACs to obtain cells with a good dynamic range.

2.7.3 Light-sheet imaging of the SoNar sensor on the Leica SP8 DLS

Light-sheet imaging allows for imaging of fluorescent samples with decreased risks of photo-bleaching or photo-toxicity, a high sample penetrance, and a high dynamic range, compared to more conventional fluorescence microscopy techniques, such as confocal microscopy, making it favourable for longer term 3-D imaging experiments.

The Leica SP8 DLS was used in order to image SK-BR3 cells expressing the SoNar sensor. The Leica SP8 DLS at the EMBL ALMF utilises lasers at multiple excitation wavelengths, including 405nm and 488nm, making it ideal for both of the SoNar's excitation peaks (see Figure 30). Furthermore, multi-positioning techniques can be used to image multiple positions in one experiment, giving more reliable overviews of how overall cell metabolism was responding to drug or inhibitor treatment. On top of this, two magnifications could be used: 10x and 25x. For the figures shown here-on-in, the 10x lens was used; this is because this image pipeline was designed with the aim of being able to gain a representative overview of multiple different structures, which the 10x lens is able to capture in its field of view. The 25x lens, however, provides a higher resolution, and was

used as a secondary validation of the results found (Supplementary Figures S.11 and S.12).

The following sections describe the establishment of experimental techniques used to assess the SoNar sensor, which included: experimental set-up to allow simultaneous imaging of SoNar and also cpYFP-expressing cell populations in normal cell culture conditions, the establishment of an automated image analysis pipeline, and finally image de-convolution, which has the potential to accurately resolve structures in 3D, giving an accurate overview cell-cell heterogeneity.

2.7.4 Development of a mounting method to allow multi-positioning light-sheet imaging

To image on the Leica SP8 DLS, mounting methods had to be established in order to have a sample growing in as close to normal growth conditions as possible, with minimal sample movement or imaging artefacts, whilst allowing the light-sheet from the Leica SP8 DLS to pass freely through the sample. The Leica SP8 DLS operates by using two mirror caps that come down on either side of a sample, these are angled at 45°, so that a beam of fluorescent light coming from the illumination objective below can be directed through it at a 90° angle (shown in Figure 33(c)). The resulting emission can then be read by the detection objective, which is above the sample.

As discussed previously, it was also of crucial importance to be able to simultaneously image cells expressing SoNar and cpYFP, meaning that they needed to be seeded and grown on the same imaging plate. The Leica SP8 DLS had multi-positioning abilities, meaning that more than one structure could be imaged in an experiment. However, this meant that a mounting method was needed that allowed the microscope to move the imaging plate hundreds of times (accounting for multiple time points) without damaging the samples or causing them to drift.

To do this, a method was set up using a small glass “bridge” which was slightly elevated (approximately 2mm) from the glass bottom of the imaging dish, and held in place by a non-reactive glue, appropriate for imaging in this setting. On this bridge, Matrigel containing the two cell populations were seeded adjacent to each other. The glass "bridge" and glass bottom of the imaging plate meant that light from the illumination objective could reach the sample without compromising quality. The thickness of the "bridge" was cut to be between 1.4-1.8mm wide, with a diamond ended pen to stop jagged edges forming, or glass cracking, which could affect imaging. The "bridge" was narrow enough to allow the two mirrors of the Leica SP8 DLS to fit either side of the sample. Being able to seed a relatively small amount of Matrigel (typically 5-10µl) also meant that the samples were less susceptible to drift, and could be imaged on a time period of multiple days (the longest time length tested was 72 hours).

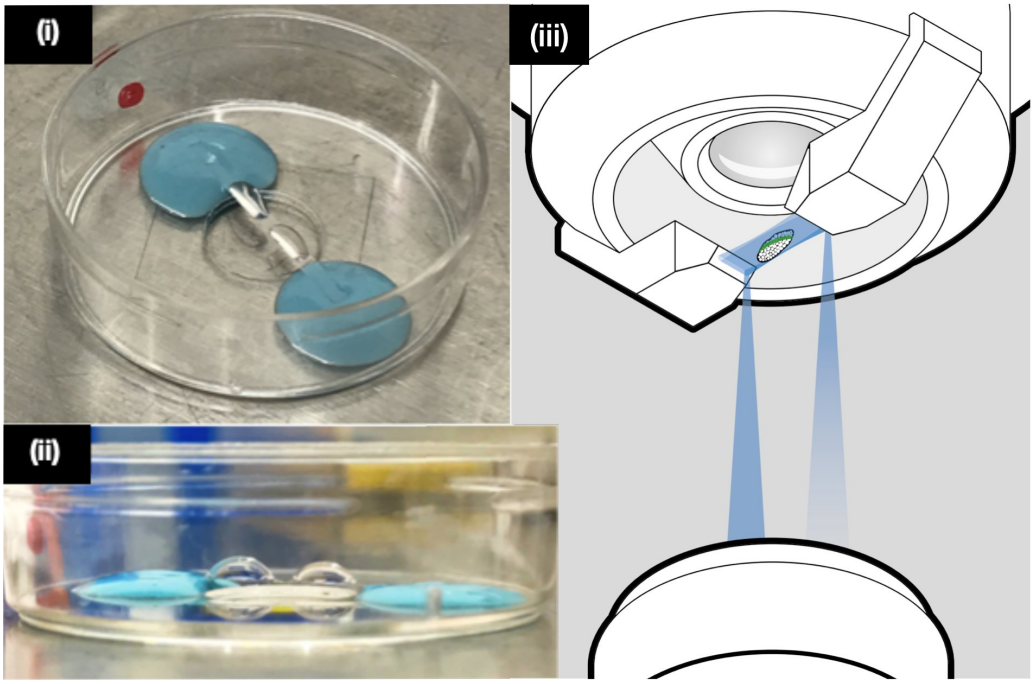

Figure 33: **Sample mouting for the Leica SP8 DLS.** (a) and (b) The imaging chamber used to grow and image cells expressing the SoNar sensor. Glass strips, cut from a microscopy cover slip to a width of 1.4-1.8mm were elevated from the bottom of a glass bottomed plate, and held in place with Picodent Twinsil®, an inert, culture-friendly quickly solidifying paste. Two droplets of matrigel, one containing cells expressing SoNar, and the other containing cells expressing cpYFP were then seeded on the glass strip adjacent to one another. The cells within were left in a tissue culture incubator to grow to an appropriate size, before being imaged on the Leica SP8 DLS. As shown in (b), the surface tension of the matrigel gave each droplet a 3-D appearance. This, along with the elevation of the glass strip, allowed the mirror caps shown in (c) to pass either side of the matrigel droplets, so that a light sheet could be passed through them.

2.7.5 Image analysis workflow

Using the mounting methods described in Section 2.7.4, an image analysis pipeline now needed to be established. In order to do this, two workflows were set up, both using the 10x magnification lens. Firstly, a "fast" workflow was set up, to allow for a generalised temporal overview of how SoNar expressing cells respond to different treatments or conditions. However, as will be described (Section 2.7.6.3), image artefacts in the Z-plane meant that cells could not be resolved on a single cell resolution, due to the 3D mean blurring that was needed to correct for this. Instead, only a general overview of the ratio response could be given. Therefore, another workflow was innovated using image deconvolution to obtain a better 3D resolution, aimed at being able to resolve cells on an individual basis. This workflow involved image fusion of each individual mirrors light-sheet image (in the "fast" workflow the fused images generated by the Leica SP8 DLS were used (Described in Section 2.7.6.1)). These two approaches can be used side-by-side for experiments; the "fast" workflow allows an exploratory identification of conditions or treatments that may influence the NAD+/NADH ratio of cells with a relatively quick and automated workflow. The fusion and de-convolution workflow allows for a more in-depth exploration of these treatments, and may allow a read-out on a cell-cell resolution. Figure 34 summarises the overall workflow, which is described over the next sections.

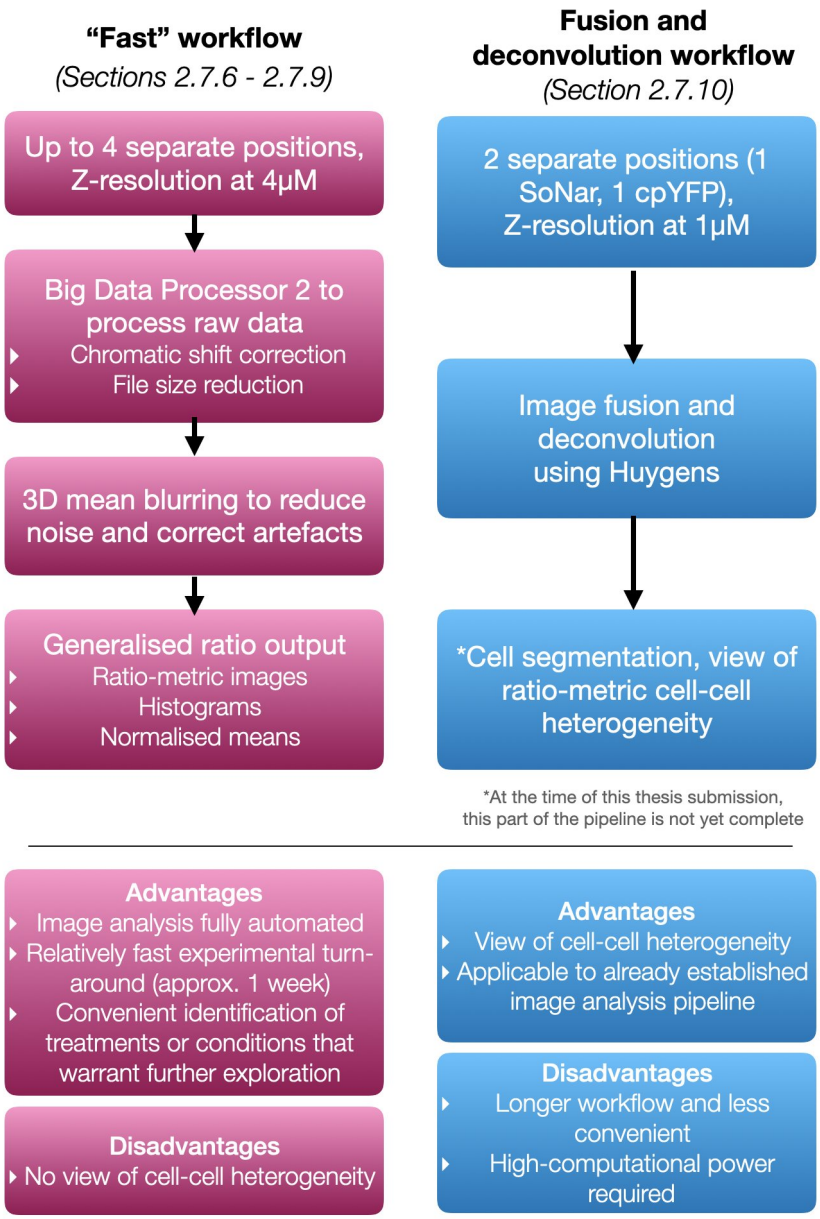

Figure 34: **Workflow of the two image analysis pipelines for the Leica SP8 DLS** This project pioneered two separate work-flow approaches, which allows a trade-off between experimental speed and convenience, and image resolution that could allow resolution of cells on an individual basis.

2.7.6 Establishment of an automated big data image analysis pipeline

2.7.6.1 Processing of raw data to workable sizes

For each Z-plane, the Leica SP8 DLS takes an image with illumination from the right and left light-sheets, and automatically merges them together in order to create a combined image. This is useful for visualising a whole structure, and helps offset the "stripe" effect which is a commonly seen artefact in light-sheet imaging experiments. For the analysis done in this section, the combined images were used, with the individual mirror images being visually inspected to verify that there were no misleading deviations in the combined image.

The combination of 3 high resolution images being taken for each Z plane, large Z-stacks, multiple time points, channels, and positions meant that a single light-sheet experiment typically generated between 400,000 and 800,000 high resolution images (2046x2046 pixels each), equating to approximately 4-6 terrabytes of data for a single experiment.

The large data sizes of each experiment meant that it was essential to reduce the size of the dataset before analysis could be conducted; without this, analysis would require unfeasibly long amounts of time, data storage, and computational power. Because of this, the first step of the image analysis pipeline was to reduce image size through pixel binning.

However, it was still important to be able to visualise data before file size reduction, so that data could be pre-processed (for example, drift correction, chromatic shift correction in the X, Y or Z plane between the two channels, and cropping of regions containing no cells). To do this, Christian Tischer (ALMF, EMBL) developed an ImageJ plug-in called the Big Data Processor 2 (BDP2), which worked via lazy-loading, allowing for image series viewing without opening the whole dataset at once.

Using the BDP2, ImageJ macros were developed that allowed automation of data pre-processing (with the exception of cropping, which was manually performed) and binned the pixels to workable file sizes before saving. This binning was performed at 2-2-2; X-Y-Z. The raw data was backed up to tape for long term storage.

Figure 35: **The processing pipeline of raw Leica SP8 DLS data using the BigDataProcessor 2.** The BigDataProcessor 2 is an ImageJ plug-in, created by Christian Tischer (ALMF, EMBL) that allows visualisation, and automated processing and analysis of large image data sets, through utilising "lazy" loading. In the context of these experiments, the BigDataProcessor 2 was utilised to correct chromatic Z-plane shifts between the 405 and 488 channels, and bin pixels, 2*2*2 (X*Y*Z) to drastically reduce file size, to make further downstream analysis computationally and temporally feasible.

2.7.6.2 Ratiometric viewing using lazy loading: The Lazy Ratio Viewer

Despite significant file reduction size achieved through pixel binning and cropping of areas containing no cells, total experimental file sizes were still large (typically 100-150GB for a single experiment across all positions). However, data could once again be visualised using lazy loading with the BDP2.

In order to view and analyse ratiometric data, it was also necessary to utilise lazy loading to do this because of the large file size. Therefore, Christian Tischer (ALMF, EMBL) developed the “Lazy Ratio Viewer”. Similarly to the BDP2, this utilises Lazy loading to visualise ratiometric images, and works by dividing the pixel intensity of one channel, by the corresponding pixel intensity of the other channel. As shown in Figure 36, this had different parameters that could be adjusted for optimisation. “Background” was used as the baseline (i.e. the “zero” point), and “Threshold” was used to set a cut-off value; pixels below this value would not be calculated in the output ratio image. This was useful for areas of low intensity (for example, “halo” artefacts around the edge of cells) which created noise and gave erroneous values. It was also useful for experiments where cells began to die following drug treatment – these cells would still contain residual SoNar/cpYFP and were also often auto-fluorescent at a low level. These cells would give erroneous ratio values, but were also dimmer in both channels than the live cells, meaning the threshold could be used to ensure these cells were omitted from experimental analysis.

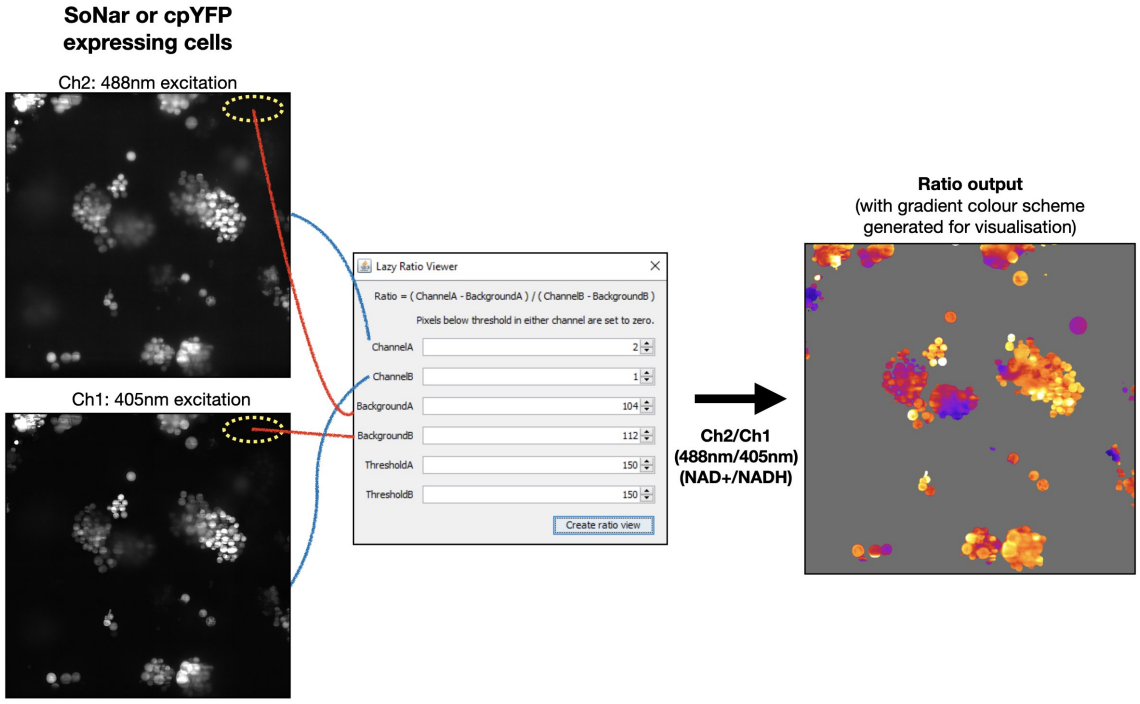

Figure 36: **Creation and visualisation of ratio-metric images using the Lazy Ratio Viewer (ImageJ plug-in)** The Lazy Ratio Viewer was created by Christian Tischer (ALMF, EMBL), to visualise the ratio differences between images taken in each channel. To remove background values and noise from dimmer cells or cell edges, background and threshold values could be set for each channel. On the ratio-output images, look-up tables are applied for more convenient visualisation of differing ratios. Calibration bars, scale bars and time stamps are added to ratio images for real experiments.

2.7.6.3 Image artefact correction and noise reduction: 3D mean blurring

Upon inspection of initial set-up experiments using the Lazy Ratio Viewer and corresponding channel images, it became apparent that further optimisation was also required to reduce image noise, and also to correct for artefacts in the Z-plane. In particular, the output from the 405nm excitation channel appeared spread in the Z-plane, particularly in the direction of the detection objective. In the ratio output, this often created the artefact that the ratio appeared lower at one end of the cell or of a group of cells. Whilst this was largely corrected by setting appropriate background and threshold pixel values in the Lazy Ratio Viewer (see previous subsection), it was important to develop strategies to account for this fully, so that visualisation of the cells was not misleading, and also so that generalised output such as overall statistics were not skewed. To do this in a practical way that did not require high computation power, this was done be performing a 3D mean pixel blur. Blurring inherently comes at the compromise of cell-cell resolution, but at the advantage that overall observations and statistical outputs can be made more reliable, and performed on a feasible time-scale. Despite the blurring, it was still possible to visualise ratiometric images, but was not reliable to do single-cell tracking and conclusions about heterogeneity could only be made in a general sense. As stated before, this project aimed to solve these problems through image deconvolution (Section 2.7.10.2).

Image blurring (particularly in the Z-plane) helped to reduce noise and generate more

reliable ratio-metric images for visualisation (Figure 37) and output statistics such as histograms of pixel ratios, which could then be further used for downstream analysis.

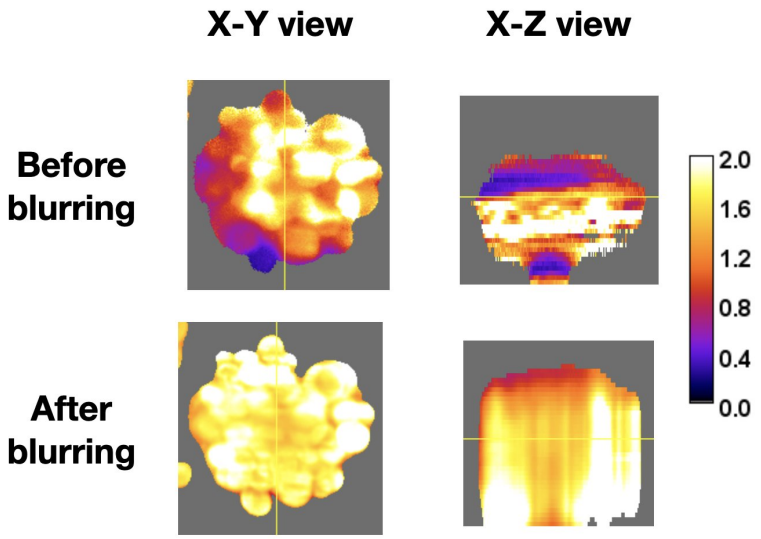

Figure 37: 3D mean blurring of light sheet images to reduce noise and correct for image artefacts

2.7.6.4 Generalised image analysis: Generation of histograms and normalised means

Once image artefacts had been removed and noise had been reduced, it was now also possible to visualise NAD+/NADH ratio changes in cells over their time course. It was also desirable to generate a convenient and simple numeric output. One simple and informative way to do this is to take the mean ratio values for each whole Z-stack, and observe how it changes over multiple time points. Imaging cells expressing cpYFP alongside SoNar-expressing cells was critical for this; the mean value given from SoNar-expressing cells could be normalised to the output from cpYFP-expressing cells variation not caused by the NAD+/NADH ratio. For example, a change in the pH of the cell media that was caused by the small differences in the environment of the microscope compared to the normal cell culture incubator could cause changes in the fluorescence characteristics of SoNar and cpYFP that is not to do with the NAD+/NADH ratio of the cell. Calibrating the SoNar sensor against the cpYFP sensor helps to account for this.

However, whilst calculating the normalised mean of each position was useful and informative, it did not give a read-out of any cell-cell heterogeneity, which was one of the main aims of this experimental pipeline. As stated before, one computationally intensive way that is being established to do this is described in Section 2.7.10.2. However, generating histograms of ratio intensities for all the pixels in each Z-stack could be also used as a convenient visualisation of any heterogeneity in a generalized sense. Similarly to the mean value, these could be compared across time points to observe how the overall data spread shifted when the cells were subjected to a particular treatment or condition.

Because of this, an ImageJ macro was written that would calculate the mean pixel value for each time point, as well as generating a histogram, and saving a 3D TIFF file of Lazy

Ratio Viewer output. These could all be visualised over the whole time series, and the means of the SoNar sensor could be normalised to the cpYFP for each timepoint.

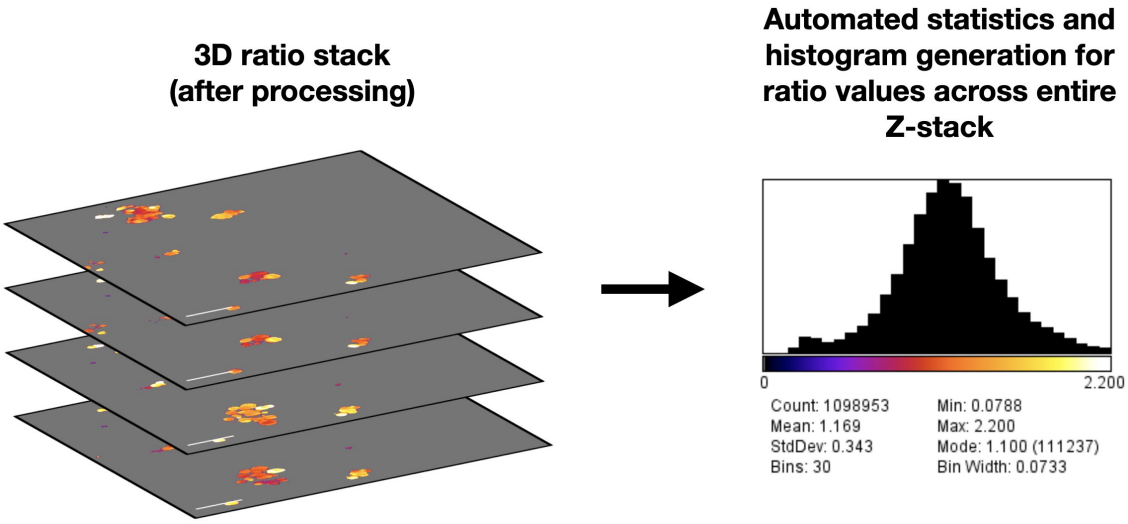

Figure 38: **Histogram generation from 3-D ratio images** 3-D ratio images were generated using the Lazy Ratio Viewer (see Figure 36) and macros were written to automatically generate statistics about the the 3-D ratio stack for each time point, including the generation of a histogram for overall views of how the distribution of ratio values changed over the time course of the experiment.

2.7.7 Testing and characterising the functionality of the SoNar sensor with a oxamate, known NAD+/NADH ratio reducing agent

Once the mounting and image analysis pipeline had been established, it was important to characterise the SoNar sensor. Previously, experiments were conducted to verify that the SoNar sensor and cpYFP fluorophore could be imaged without photobleaching, phototoxicity, or unexpected behavioural changes in the cells for the duration of an experiment (data not shown).

It was now important to establish that the SoNar sensor behaved in ways that were expected. Conveniently, oxamate (also used in combination treatment experiments in Section 2.4), was recommended for this purpose by the creators of the SoNar sensor, due to its known function in drastically reducing the NAD+/NADH ratio.

Oxamate is an non-competitive inhibitor of the lactate dehydrogenase enzyme, which catalyses the conversion of pyruvate to lactate, using NADH as a co-factor to provide a H+ ion (a proton), in turn, converting it to NAD+. When inhibited by oxamate, this means that NADH accumulates in the cell, causing causing the NAD+/NADH ratio to decrease.

To visualise dynamic changes in the NAD+/NADH ratio of SK-BR3 cells, images were taken every 10 minutes for 15 hours, at two positions for the SoNar sensor, and another two for the cpYFP flourophore. Upon addition of 200mM of Sodium Oxamate, SK-BR3 cells expressing the SoNar sensor displayed fast and dramatic reductions in their NAD+/NADH ratio, with a relative increase in brightness in the NADH (405nm) channel

(Figure 39(a)). In contrast, the cpYFP flourophore underwent very minimal changes in either channel (Figure 39(b)). There was a slight increase in the initial ratio of the cpYFP fluorophore over the first few timepoints, which is consistent between multiple experiments. This is possibly because of small changes in environmental conditions between the normal cell incubator and the microscope (for example, small differences in the atmospheric CO_2 concentration, causing a slight pH change).

Using the data generated from the oxamate addition, the three main established parts of the imaging analysis pipeline: ratio-visualisation, histogram generation, and normalised mean generation (shown in Figure 39) could be used. Consistent with the ratio-visualisation and histogram generation, the normalised mean also showed a sharp decrease over the 15 hour time course.

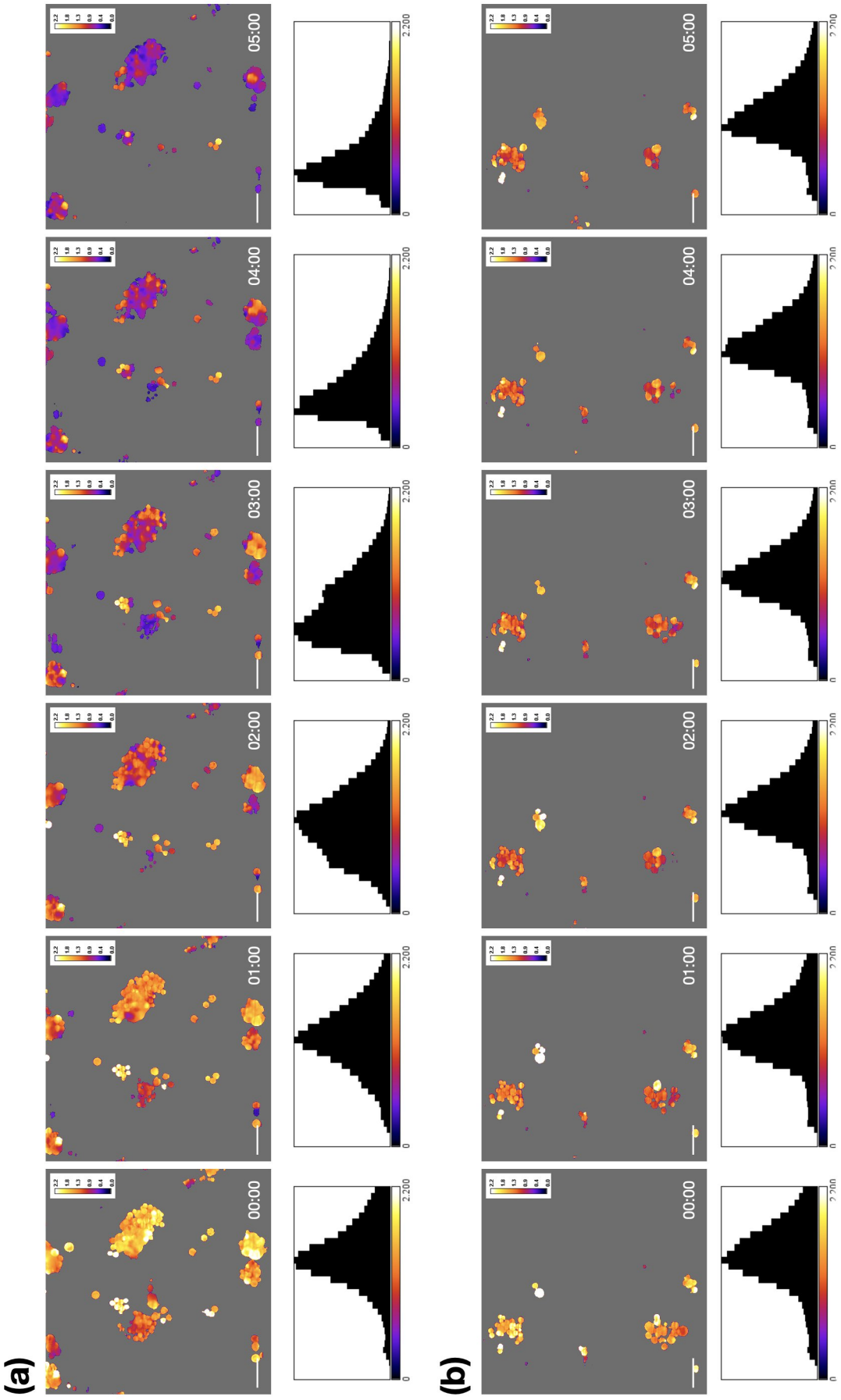

Figure 39: *Figure continued on next page.*

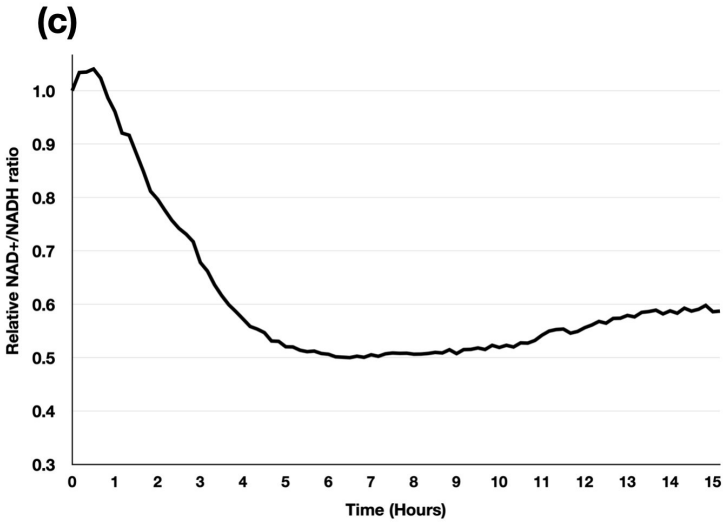

Figure 39: **Ratio changes in SK-BR3 cells expressing the SoNar sensor after the addition of Oxamate.** SoNar (a) and cpYFP (b) expressing SK-BR3 cells after treatment with 100mM Sodium Oxamate, showing representative ratio-metric images (top) and corresponding histograms for the entire Z-stack. (c) The overall mean NAD+/NADH ratio for the SoNar sensor, normalised at each time point to corresponding cpYFP-expressing cells. Ratio shown relative to time point 0.

2.7.8 Lapatinib treatment at close to IC50 concentrations reduces the NAD+/NADH ratio of SK-BR3 cells over time

The image analysis pipeline had now been established, and the SoNar sensor had been characterised with oxamate, showing consistent results with the data presented by the SoNar creators[244]. To observe the effect that HER2 inhibition had on the NAD+/NADH ratio, lapatinib was added to SK-BR3 cells at a concentration of 1.3µM. Prior experiments (see Figure 11 and 15) had shown that 1µM of lapatinib was approximately the IC50 of these cells over 72 hours, so 1.3µM was given to test this over a shorter time period (approx. 24 hours). Separately, Sylwia Gawrzak had also found similar results in independent experiments on these cell lines (data not shown).

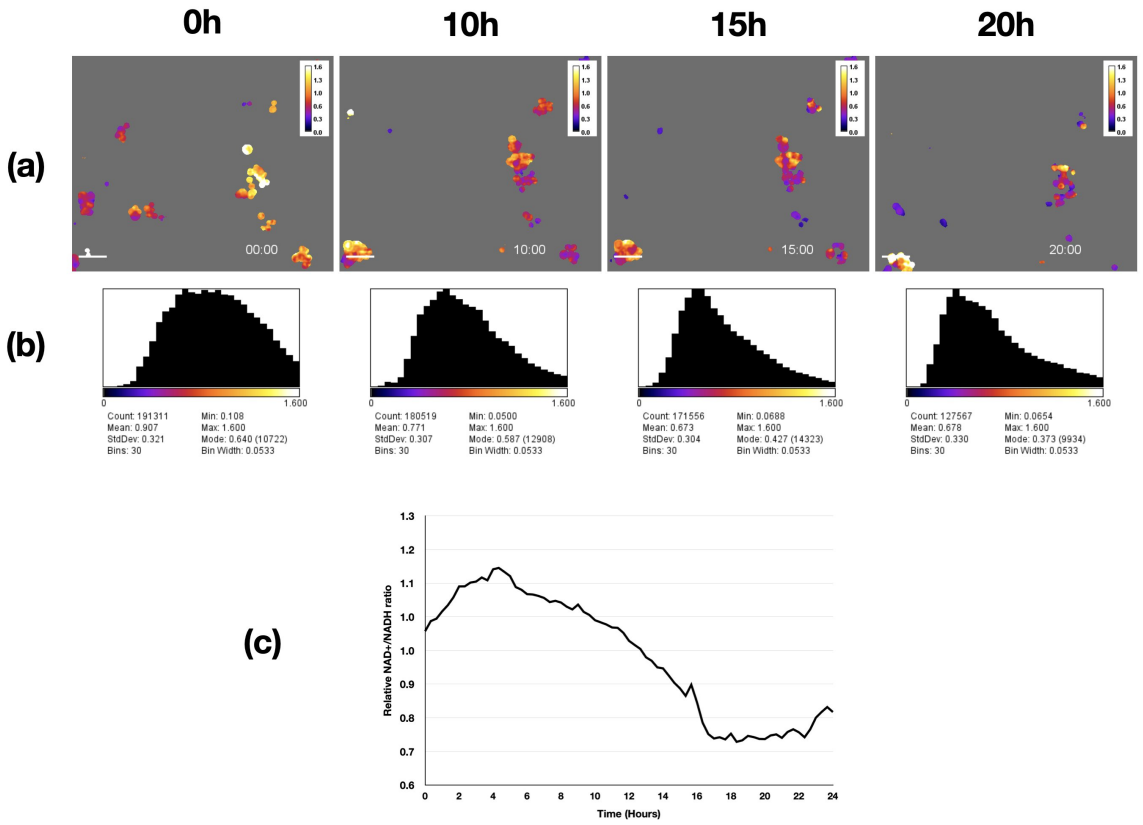

Figure 40: SK-BR3 cells expressing the SoNar sensor, treated with 1.3µM lapatinib

This experiment was repeated twice, once with the 10x lens to visualise multiple structures at once, and once with the 25x lens, to view cells at a higher resolution (Supplementary Figure S.11). Results were consistent between both of the experiments, with the addition of lapatinib causing overall reductions in the NAD+/NADH ratio of these cells. In contrast, the cpYFP control flourophore showed only very little change in its overall fluorescence ratio.

2.7.9 Lapatinib and EMBL-703625 act synergistically to reduce the NAD+/NADH ratio of SK-BR3 cells

Results from biochemical assays and re-growth experiments demonstrated that EMBL-703625 and lapatinib synergistically reduced the viability of BT-474 and SK-BR3 cells, and compromised the ability of BT-474 cells to re-grow. In order to gain an understanding from a metabolic perspective, light-sheet experiments were conducted with doses of lapatinib and EMBL-703625 that caused relatively modest reductions in viability, but stronger reductions when combined together. Cells were either treated with lapatinib alone (0.2µM), EMBL-703625 alone (1µM) or together, and images were taken every 20 minutes until widespread cell death was apparent after approximately 24 hours.

When treated with both inhibitors together, the vast majority of cells saw a steady decrease in their NAD+/NADH ratio, and the majority eventually fell below the intensity threshold, indicative that sensor expression itself had stopped. At the end of the 24 hour imaging

period, a very small number cells were still able to maintain their initial ratio, whereas most either had a decreased ratio or had fallen below the intensity threshold (Fig. 40 (a) and (b)). Treatment with lapatinib (Fig. 40 (c) and (d)) or EMBL-703625 (Fig. 40 (e) and (f)) alone lead to a much less pronounced decrease in the ratio, with a far higher number of cells able to maintain their initial ratio throughout the imaging period, and with only minor changes in their overall mean ratio compared to the combination treatment in the first 24 hours (Fig. 40(g)). The experiment was also repeated with the 25x lens (Supplementary Figure S.12) with consistent results.

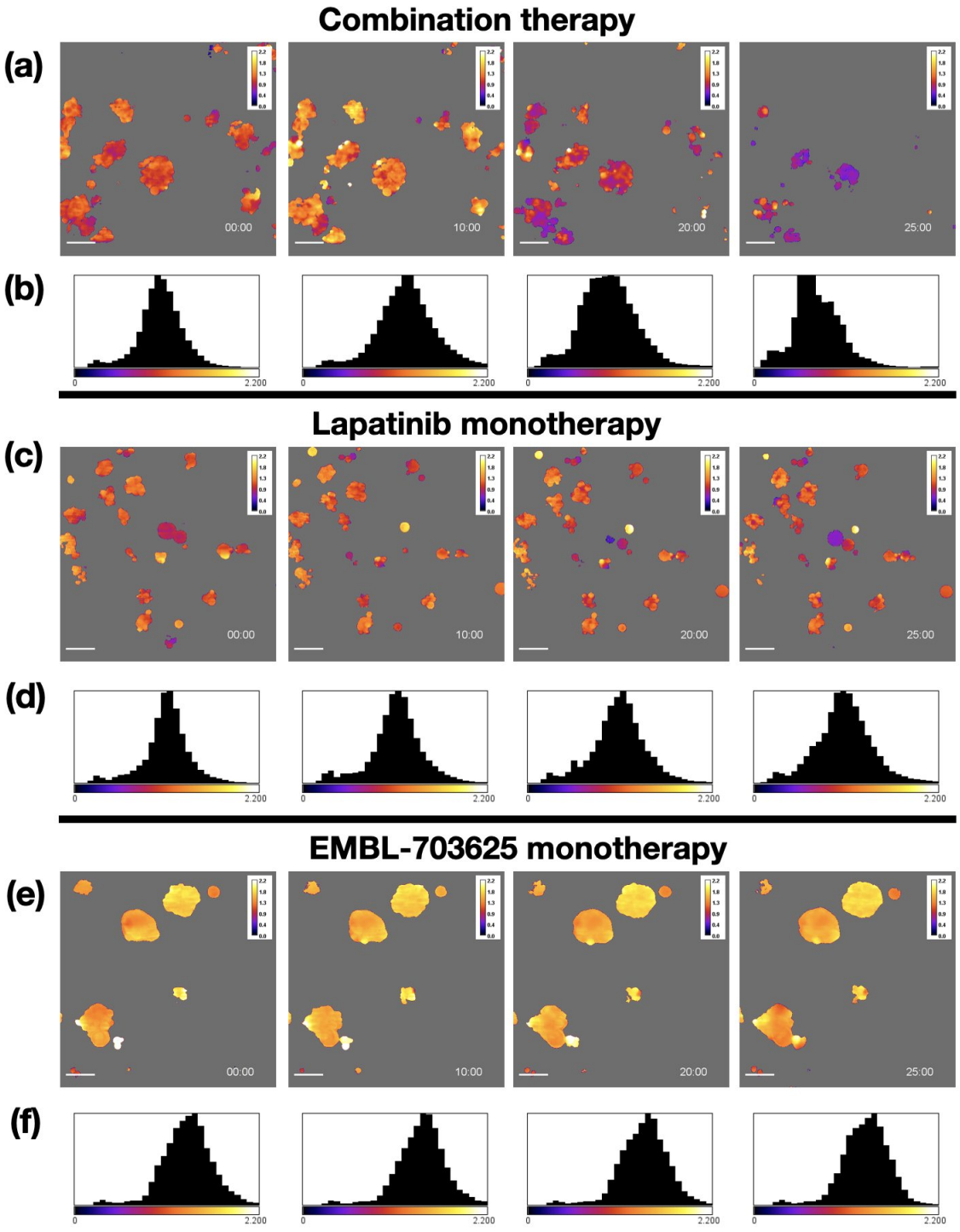
Combination therapy
(a)
00:00
10:00
20:00
25:00
(b)
0
2.200
Lapatinib monotherapy
(c)
00:00
10:00
20:00
25:00
(d)
0
2.200
EMBL-703625 monotherapy
(e)
00:00
10:00
20:00
25:00
(f)
0
2.200

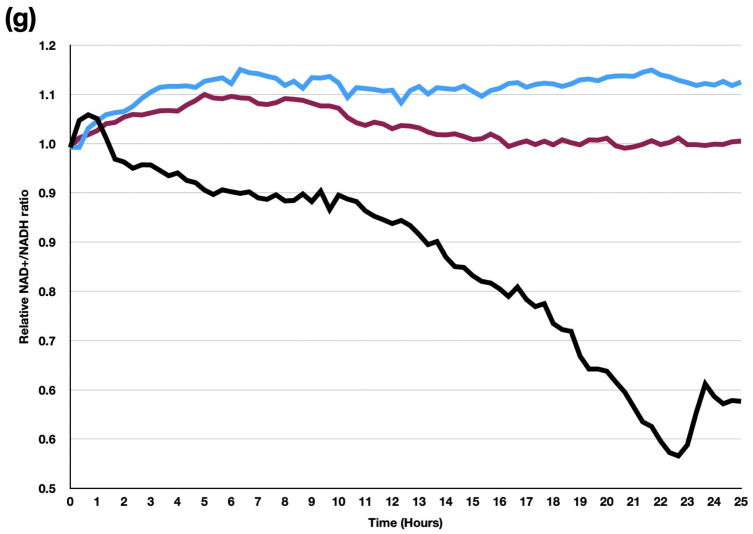

Figure 40: **The NAD+/NADH ratio of SK-BR3 cells treated with combination therapy, or Lapatinib, or EMBL-703625 monotherapy at 0, 10, 20 and 25 hours.** (a), (c) and (e) show representative ratio images for SoNar-expressing SK-BR3 cells treated with combination therapy, lapatinib monotherapy, and EMBL-703625 monotherapy, respectively. Time points in hours and minutes are shown at the bottom right of each image. (b), (d) and (f) show overall histograms for the ratio Z-stacks of each corresponding time point.

2.7.10 Image fusion and deconvolution, aimed to be able to improve image resolution to visualise cell-cell heterogeneity

2.7.10.1 Background and Theory

The results presented so far have been able to generate a general understanding of how the NAD+/NADH ratio of cells respond to different treatments over time. However, because of issues with resolving cells in 3D, this has not yet been able to provide a read-out on cell-cell heterogeneity, which was the original project aim. Because of this, a further pipeline was established that performed 3D image deconvolution using Huygens software (http://svi.nl). Marko Lampe (ALMF, EMBL) performed the merging and deconvolution of the Leica SP8 DLS raw data using Huygens software.

Deconvolution is a computational image analysis process that uses mathematical functions to improve image resolution. This works by accounting for patterns of light diffraction. All images taken under a microscope are subject to light diffraction, which occurs when a light wave encounters an object, causing them to spread or curve around the object. These diffracted wavelengths of light are then detected by the objective of the microscope and are interpreted as the final image. This diffraction is a form of interference, and often manifests as image blurring or smearing. The pattern of this diffraction can be mathematically defined based on a combination of the wavelength of light emitted, and the numerical aperture of the microscope, which known as the point spread function (PSF). In simple terms, the real-life specimen, multiplied by the PSF, results in the convolved image that is detected by the microscope. In practice, this can mean that two objects in close proximity to each other cannot be resolved if their proximity is closer together than

the PSF.

Deconvolution is designed to partially account for the PSF in the final image, and therefore generate images that have a higher resolution and contrast. This can help to resolve structures that would have otherwise not been resolved because they were in closer proximity than the PSF.

In the context of this experiment, deconvolution was aimed to be able to resolve individual cells in 3D, which was not possible from the raw images generated by the Leica SP8 DLS, particularly because of blurring or smearing in the Z-plane, which was dealt with in the "fast" workflow by using a 3D mean blur, at the compromise that cell-cell resolution was lost. As discussed previously (see Section 2.7.5), the Leica SP8 generates 3 separate images of the same structure; 2 images resulting from light-sheets coming from the left or right mirrors, and a merged version based from both of these images automatically using Leica software. In the previous sections, this merged version was used to conduct these experiments. However, to properly perform deconvolution, the raw images from the left and right light sheets were merged using Huygens software, and deconvolution was performed on these merged images. Prior to deconvolution a specific region of interest was selected to reduce the computational time needed for these proof-of-principle experiments.

2.7.10.2 Image deconvolution is able to better resolve cells in 3D

As shown in Figure 41(a), deconvolution improved image resolution, particularly in the Z-plane, which is influenced by a large amount of light diffraction, particularly in the 405 excitation channel (shown). This allowed cells to be more resolved and distinguished from one another in 3D. This presents an encouraging precedent for the image analysis pipeline, as this makes cells possibly more amenable to processes such as segmentation and 3D rendering, which could allow a greater understanding of cell-cell heterogeneity. An example of this 3D rendering is shown in Figure 41(b).

This experiment was designed as a proof-of-principle, and therefore processed a single channel (405nm excitation) in a particular region of interest, at a single time point, which was practically feasible because of time constraints. However, this approach can be extrapolated to multiple time-points, channels, and larger regions of interest, at the compromise that this takes time and a large amount of computational power; typically over the scale of 1-2 weeks for a single experiment, using up to 1TB of computer RAM. It is also important to note that this approach is subject to further optimisation. A discussion of the next steps in this regard, as well as the applicability of this approach with other sensors or experimental systems follows in Section 2.7.11.

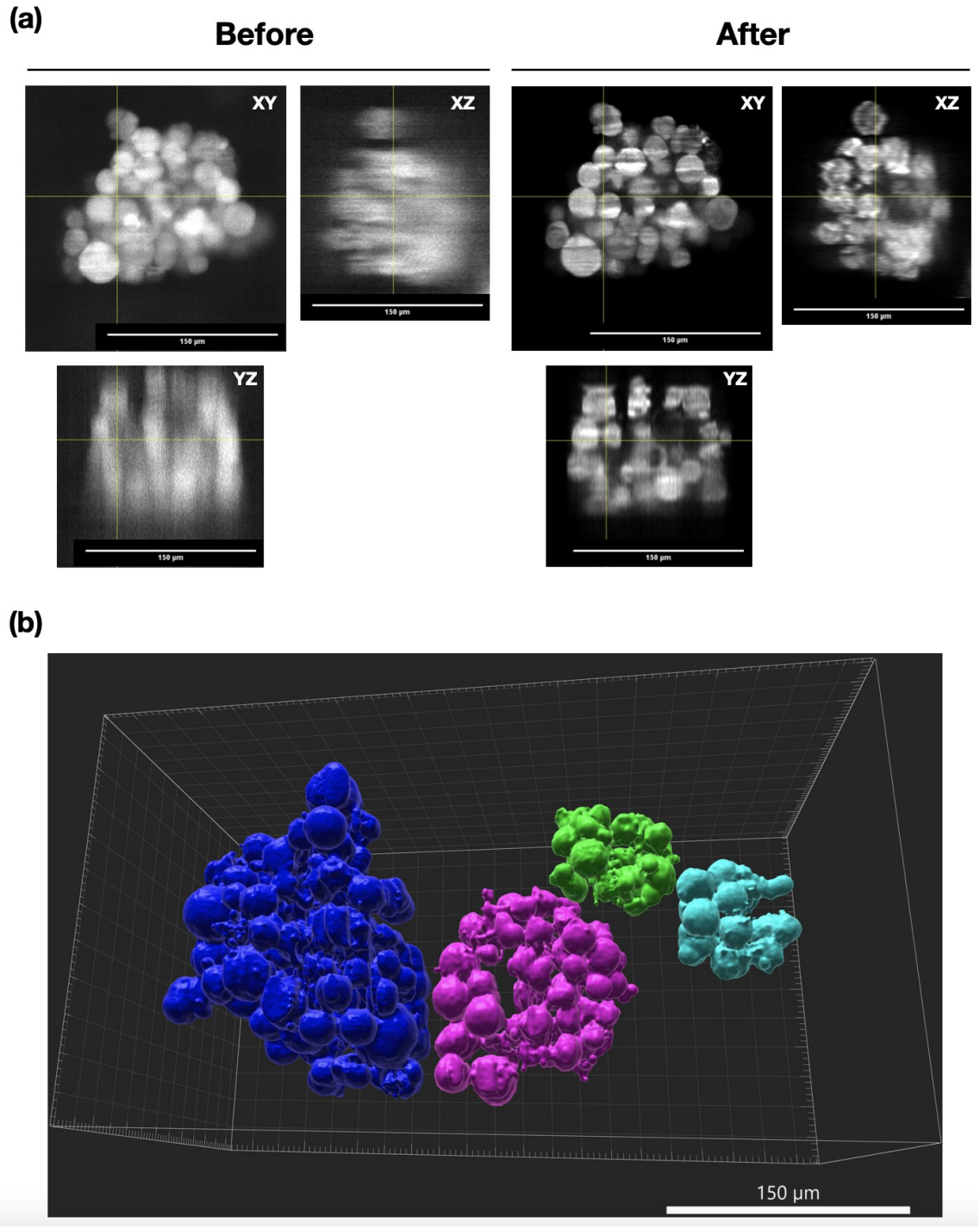

Figure 41: **3D deconvolution of SoNar expressing SK-BR3 cells taken with excitation at 405nm** (a) Images taken in the XY, XZ, and YZ planes showing improvements in resolution following deconvolution. Yellow lines show the planes of view for their perpendicular images. The left 3 images (under "Before" heading) are the merged images that are generated from the Leica SP8 DLS software, which is used in the "fast" pipeline (outlined in Figure 34). The images under the "After" heading were generated following fusion of the raw images generated by illumination from the right and left mirror caps of the Leica SP8 DLS and deconvolved, both using Huygens software. (b) 3D rendering of fused and deconvolved images of SoNar-expressing SK-BR3 cells excited at SoNar's 405nm excitation peak. This image was taken by Marko Lampe (EMBL ALMF) using Huygens deconvolution software. For reference, the organoid shown in part (a) is shown here in pink. Scale bars = 150µm.

2.7.11 Discussion of Section 2.7: Light-sheet imaging of breast cancer cells to obtain a spatial and temporal read-out of the redox status of cells on cell-cell resolution

2.7.11.1 Discussion of results and further directions to further develop and optimise the microscopy and image analysis pipeline

To our knowledge, this light-sheet microscopy-based experimental pipeline is the first that could potentially resolve cancer metabolic heterogeneity simultaneously on a spatial and temporal basis, although a similar approach that was recently published allows light-sheet redox imaging of patient-derived organoids on a high-throughput, non-temporal basis[246] (not using the SoNar sensor). Heterogeneity is of critical importance when assessing cell responses, and the methodology established in this project could allow for a wide range of different experimental approaches to be applied into this system.

To find a trade-off between experimental convenience and detail, two separate experimental workflows were established. Both approaches are outlined in Figure 34 (Page 121). The “fast” approach (described in Section 2.7.5) allows for a convenient and automated general read-out of cellular NAD+/NADH ratios in response to different conditions. This allows a first assessment of experiments or experimental designs that may show results of further interest. The image fusion and deconvolution approaches (outlined in Section 2.7.10.2) then allow a more intricate and detailed assessment on a cell by cell resolution, with possible implications for studying cell heterogeneity. This comes with the compromise of relatively long (1-2 weeks) image analysis timelines, with the requirement for powerful computational memory (up to 1TB of RAM).

Using the “fast” approach, we showed that the NAD+/NADH ratio of cells decrease in treatment conditions known to cause cell death from other experiments (Figures 40 and 2.7.9). Previous results suggest that increases or decreases in the NAD+/NADH ratio are both predictive of cell death because of fundamental changes in cell metabolism. For example, the high-throughput screening approaches with the SoNar sensor by Zhao *et al.* (2017) found compounds that led to apoptosis in H1299 cells through ratio changes in both directions[1]. In fact, changes in the NAD+/NADH ratio may also indicate that the cell has acquired a more aggressive phenotype; at non-lethal levels, reductions in the cellular NAD+/NADH ratio significantly increased *in vivo* metastasis in MDA-MB-231 and MDA-MB-435 cells[247].

Future experiments using the fusion and deconvolution pipeline will aim to understand the degree of heterogeneity that these cells may experience when subjected to the same treatments as in Figure 40. However, it is expected that human cell lines, such as SK-BR3, are likely to be relatively homogenous compared to other experimental systems such as mouse or patient derived organoids, particularly in the context of DNA stability. In this context, it would be of interest to also image mouse-derived or patient-derived organoids. To this end, attempts to generate mouse lines that stably express SoNar or cpYFP were already attempted, but unfortunately failed and could not be repeated before

the submission of this thesis. However, it is also possible to use the lentiviral approaches also established in this lab to transfect primary *in vitro* mouse cells with the SoNar sensor, as previously established by Alladin *et al.* (2020). Conveniently, this same approach was used to originally generate the SoNar/cpYFP expressing SK-BR3 (and BT-474) expressing cells, meaning that the lentiviral vectors (including similar vectors using pCAG or pEF1α as the promoter) to be used in this approach have already been generated.

It is of importance to note that the image deconvolution approaches are still in early stages of development; the pipeline is subject to optimisation, which may further improve image resolution. However, Figure 41 has shown that, as a proof of principle, it is possible to resolve these cells to a degree that allows them to be distinguished from one another. To optimally visualise these cells and understand heterogeneity, it is likely that cell segmentation approaches would be important. Using segmentation, each cell could be given a "mask" and the ratiometric voxels within could be averaged to provide a mean NAD+/NADH SoNar ratio for each cell. This would likely make for easier visualisation and cell tracking. To this end, further approaches are planned to experiment with using live nuclear and/or surface membrane dyes at red or far-red wavelengths (as to not interfere with the SoNar sensor), which may further enhance cell segmentation approaches. Similar approaches were previously undertaken in this project using lentivirally-transfected mCardinal linked to Glycosylphosphatidylinositol (GPI) in order to anchor it to the cell membrane, but the mCardinal unfortunately did not express at levels that allowed a usable intensity for these experiments.

If cells were able to be segmented and tracked, this would have large implications for experiments that could be performed, as it would allow an understanding of how different cellular phenotypes respond to different treatments. For example, if SoNar-expressing SK-BR3 cells were treated with a concentration of lapatinib that led to certain cells having different NAD+/NADH ratios than other cells, it could be assessed if these cells were more resilient or sensitive to subsequent EMBL-703625 treatment. If primary mouse cells were used, the level of pre-existing heterogeneity could be enough to make these conclusions without a prior sensitising treatment.

2.7.11.2 Other possible future uses for the SoNar sensor, or similar sensors

This project focused on imaging and characterising the SoNar sensor using light-sheet microscopy. However, there are multiple other experimental contexts that the SoNar sensor could be used in. It was originally characterised in the context of high-throughput screening, which makes it applicable for cancer drug discovery, an approach that is beyond the scope of this project. However, attempts were made to use the SoNar sensor in the context of the synergy experiments described in Section 2.1.2, to understand in a high-throughput way how the NAD+/NADH ratio would be affected by these drug combinations. However, at the resolution of a plate reader, the intensity of the flourescence signal coming from the SoNar-expressing cells was not intense enough over the autoflourescence coming from the matrigel to produce accurate or sensitive results. However,

preliminary approaches were established in collaboration with the EMBL ALMF to attempt to do this using high-throughput confocal approaches, which had the added benefit that there could be some basic read-outs of heterogeneity (although likely between organoids rather than individual cells). These approaches appeared feasible, but had not been extensively characterised at the point of this thesis submission. Nonetheless, if these approaches continued to yield usable results, then there are different experimental workflows that could be applied. Not only could high-throughput experiments be conducted that may give a read-out on drug interactions, they could also be used for experiments on a longer time-scale than is possible on the Leica SP8 DLS. In the context of cell re-growth, this approach would be valuable to understand if any metabolic phenotype (with respect to the NAD+/NADH ratio) correlates with re-growth ability.

On top of this, the authors of the SoNar sensor have also demonstrated that this sensor is applicable for *in vivo* approaches in mice[244]. With this in mind, attempts were made to generate transgenic mice that express SoNar or cpYFP, with the dual aim of being able to do *in vivo* and *in vitro* approaches (see previous sub-section). Unfortunately, although founder mice were generated, no flourescent signal for SoNar was observed in any PCR-positive mice. However, in the future, this could be performed by transducing cells at the ROSA-26 locus, which has been previously demonstrated to yield strong flourescent expression[248].

Finally, in a more general context, other metabolic sensors of interest could also be amenable to the approaches described in this section. Of relevance, the authors that created the SoNar sensor have since also generated a very similar sensor of NADP+/NADPH known as iNAP[249], which uses identical excitation and wavelengths, making it directly applicable to the experimental pipeline established in this project. Understanding this ratio is of relevance to the transcriptomic results in this project, described in Section 2.2. This is because many of the pathways that were de-regulated by combination lapatinib and EMBL-703625 treatment are known to be directly or in-directly involved in ROS detoxification, which NADPH plays an integral role in, in cancer cells[250]. This could further give a read-out on a spatial and temporal basis in this context.

2.8 Changes in tumor cells and during the formation of minimal residual disease

2.8.1 Gene expression changes during tumor regression towards a residual state

The results in this section were generated, and also analysed separately by Ashna Alladin and Ksenija Radic Shechter. Ksenija Radic-Shechter further developed these results using a multi-omics based approach. At the time of this thesis submission, these results have been submitted for publication; a pre-print can be found at Reference[175].

The results of lapatinib and EMBL-703625 synergy provide an encouraging pre-clinical rationale for movement into a clinical setting, pending *in vivo* data. However, it is important to also understand how residually surviving cells differ from their normal counterparts. This could inform on further clinical targeting strategies outside of lapatinib or EMBL-703625. As well as this, some clinical strategies now focus on giving maintenance treatment regimens in order to prevent relapse after initial treatment; understanding possible vulnerabilities of residual cells could help to inform which strategies could be better.

To assess this the differences between normal, tumor and residual cells, Ksenija Radic-Shechter and Ashna Alladin designed and conducted transcriptomic experiments that compared the transcriptional profile of induced primary mouse tumor cells to their normal counterparts. These experiments transcriptionally profiled cells that resembled a tumorigenic state (5 days on DOX) and cells that were transitioning from a tumorigenic state to a residual state, following oncogene de-induction (see Figure 42(a)).

Gene expression over this time course was analysed, and adjusted p-values were generated for each gene (performed by Ashna Alladin, and analysed by Katharina Zirngibl using the "R" package "DeSeq2"). Cellular processes that are de-regulated may act as potential targetable nodes. Because of this, it was of interest to perform a parallel analysis to identify pathways that had large numbers of de-regulated genes. From this, pathways of interest could be selected, and further analysed. To assess which pathways that over-represented with de-regulated genes, gene ontology analysis was performed on these data by Matt Rogon (EMBL: Bio-IT).

Metabolic pathways were of particular interest to this project (See Section 1.5.3 for a full explanation). Because of this, certain metabolic pathways, and signalling pathways related to metabolism were selected for further analysis (shown as part of higher order networks in Figure 42 (c-f)).

Observing how these pathways may interact with each other is important to further understand how cell metabolism is altered as cells regress towards a residual state. To achieve this, the genes in these pathways were analysed and visualised by Matt Rogon, using the ClueGO plug-in, in Cytoscape. This plug-in allows a visualisation of all the known interactions of expressed proteins in these networks. Significantly de-regulated pathways with high degrees of interaction could suggest higher-order de-regulation, and suggest a

fundamental change in a certain area of the biology of the cell.

From this analysis, networks involving sugar metabolism (Figure 42(c)), amino acid metabolism (Figure 42(d)), mitophagy (Figure 42(e)), and cellular signalling pathways such as FoxO, TGF-β, adipocytokine and Ras signalling (Figure 42(f)) were manually selected as pathways of particular interest.

A description and interpretation of the data shown in Figure 42 follows after the figure.

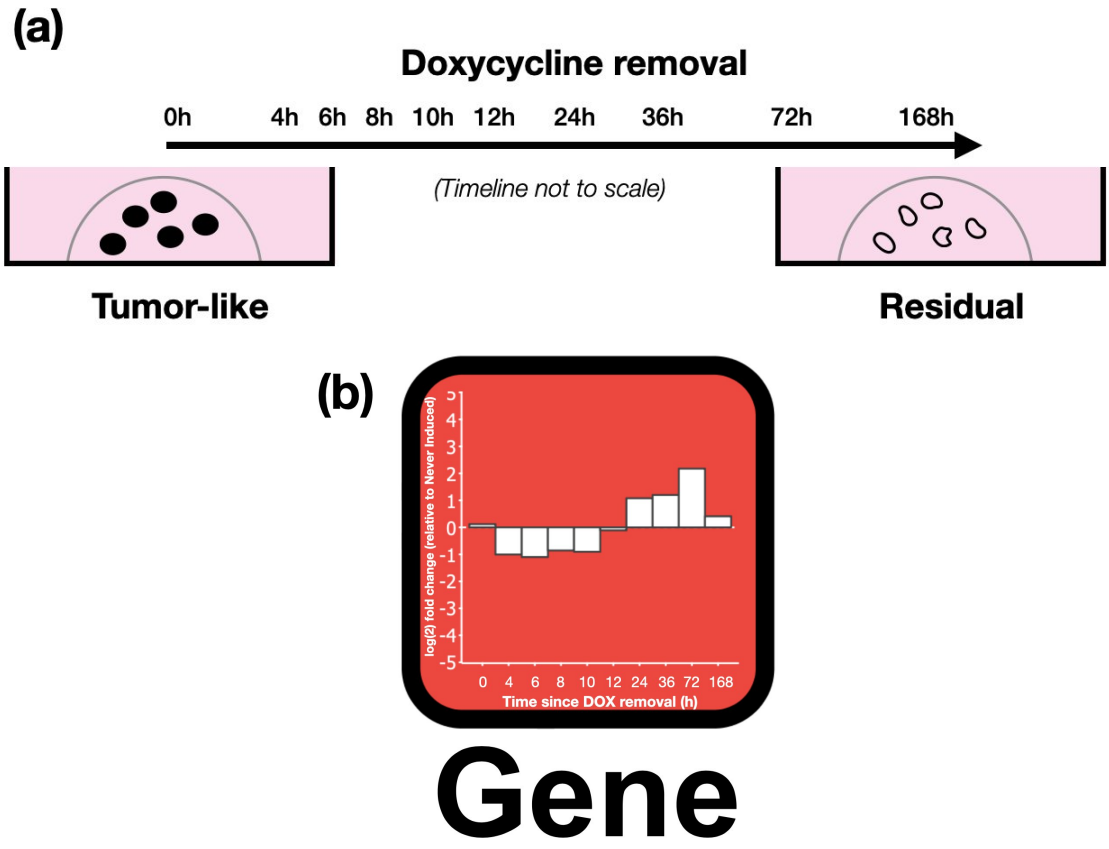

Figure 42: **Experimental schematic and zoomed-in data display example (a)** Schematic of the experiment detailed in this figure. Primary cells derived from mouse mammary glands were seeded in matrigel and kept on DOX for 5 days to induce a tumor-like state. Following this, the DOX was removed, causing oncogene (HER2 and MYC) over-expression to stop, meaning that tumor cells regressed to a residual-like state. At the time points shown, RNA samples were taken and gene expression was analysed. **(b)** An example of a significantly de-regulated gene (adjusted p-value $<$0.01) profiling the log(2)fold gene expression changes (relative to never induced) at the profiled time points. It is increased in size as genes in the rest of the figure are not possible to read.

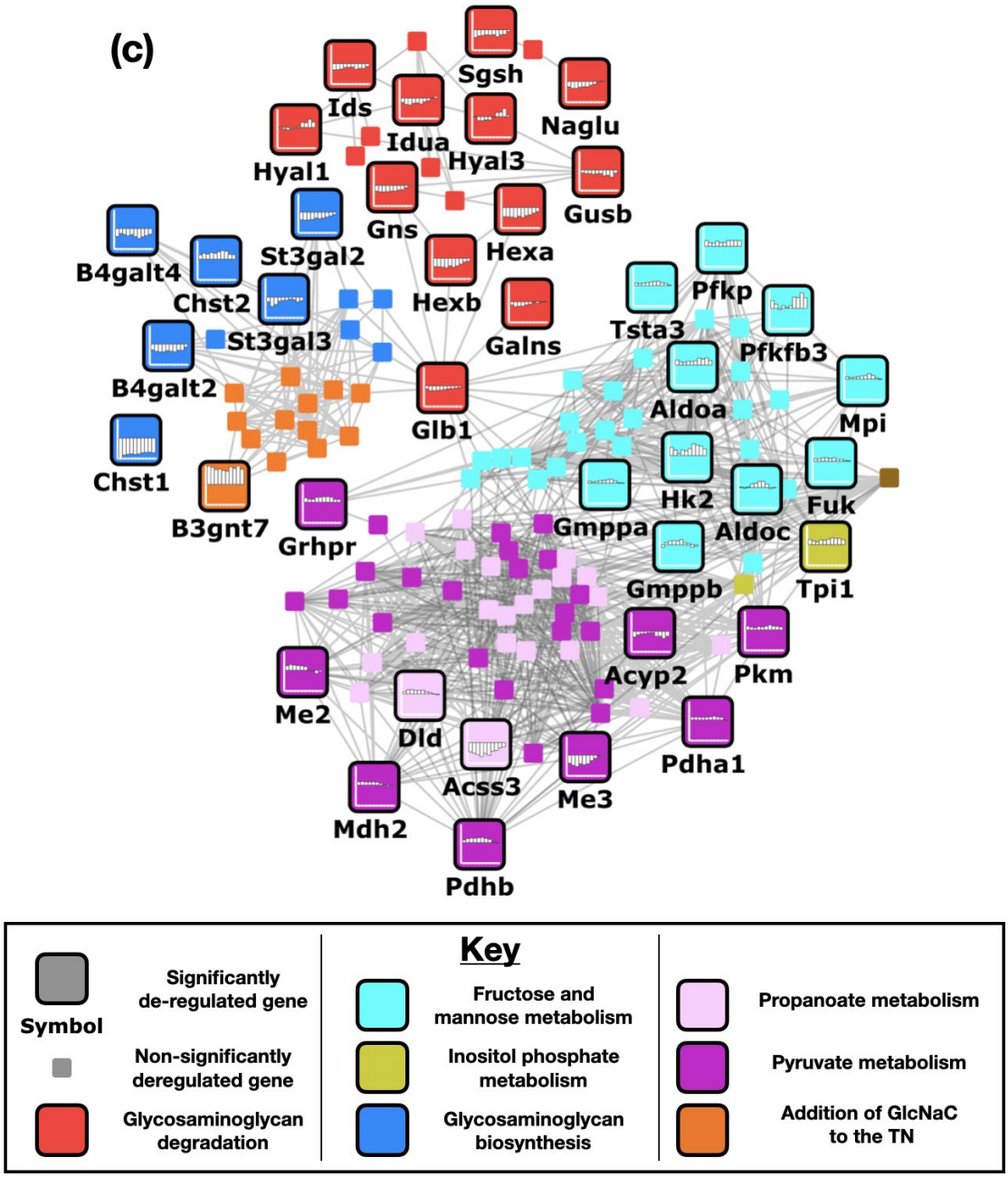

Figure 42: **(c) Sugar metabolism**
Continued on next pages.

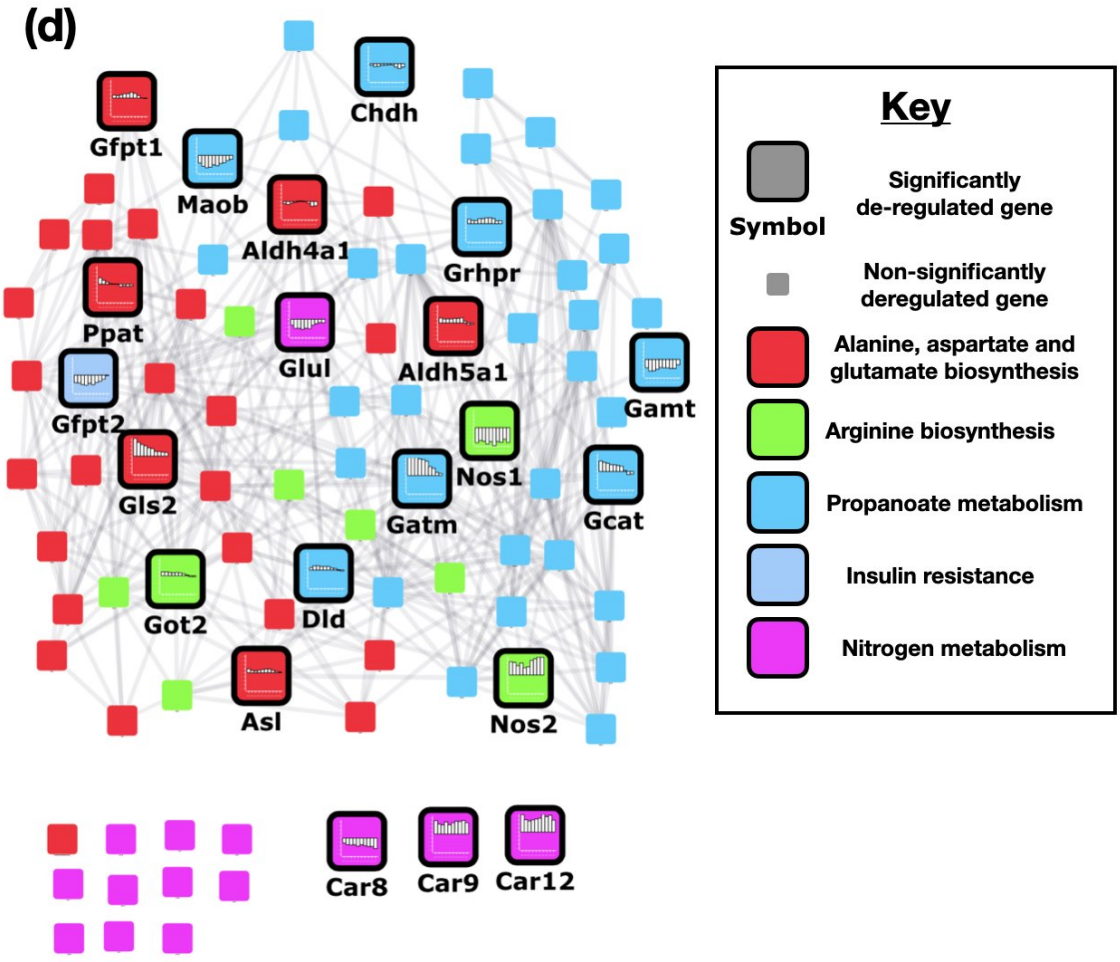

Figure 42: **(d) Amino acid metabolism**
Continued on next pages.

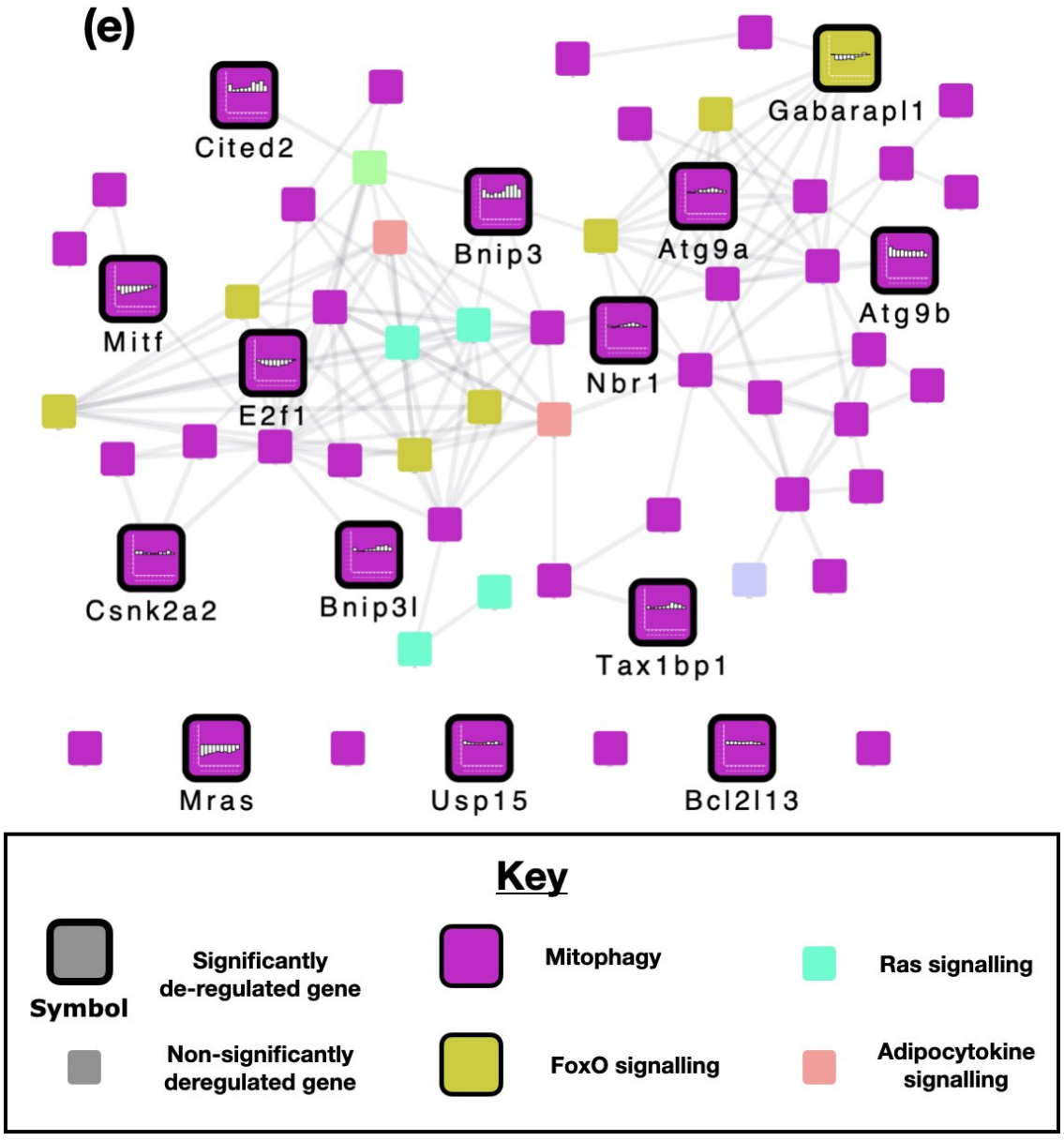

Figure 42: **(e) Mitophagy**
Continued on next page.

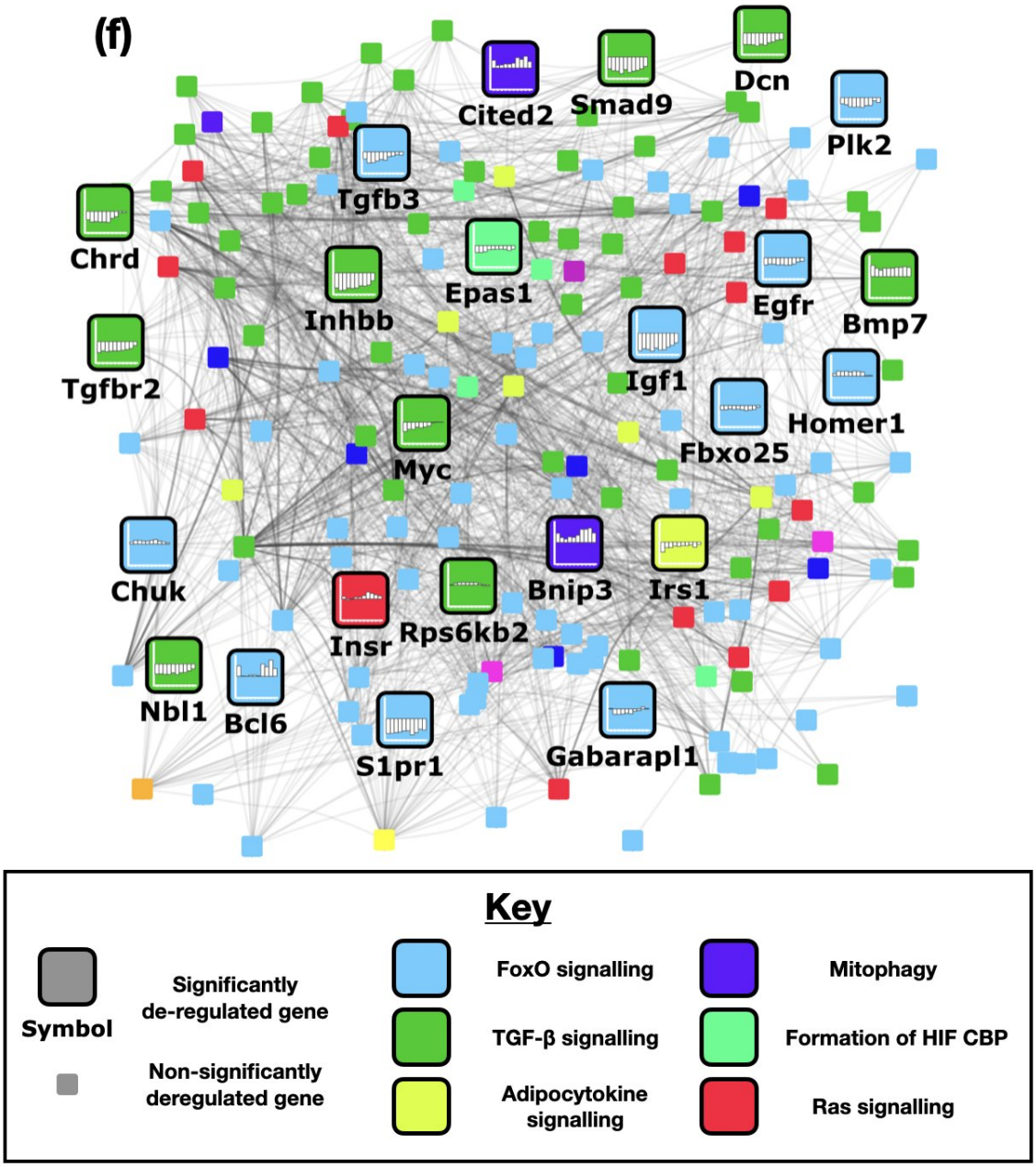

Figure 42: **Significantly de-regulated genes in sugar (c), amino acid (d), mitophagy (e), and TGF-β and FoxO signalling pathways (f) during tumorigenesis and tumor de-induction**. Known gene-gene interactions are shown with grey lines. Significantly de-regulated genes are enlarged and have their corresponding gene symbol below. Non-significantly de-regulated genes are shown as smaller squares, and their symbols are omitted for figure readability. In each significantly de-regulated gene node, a graph is shown of the log(2) fold change, relative to never induced for each time-point. These experiments were designed and performed by Ashna Alladin and Ksenija-Radic Shechter. Analysis of the data and clustering of gene trajectories was performed by Katharina Zirngibl. Based on these trajectories, Matt Rogon performed gene ontology analysis to decipher de-regulated pathways. I (Matthew Boucher) chose pathways of interest for further analysis, and analysis on ClueGO, and importing of the results into cytoscape was performed by Matt Rogon. I directed which pathways should be analysed, and performed visualisation of these pathways.

As shown across Figure 42 for all the pathways included in this analysis, multiple genes across the analysed pathways were de-regulated. As expected, the majority of genes, whether up- or down-regulated, tended to show expression levels that were altered in the tumor state (bar on the far left) and returning to levels comparable with never induced cells, in line with the notion that they are largely re-acquiring typical mammary epithelial characteristics. However, a subset of genes appeared to have atypical expression levels, either on a transient basis, or staying de-regulated for the duration of the time points assessed. These genes could indicate altered cellular characteristics that could serve as points of interference, both as the cell is transitioning, and also as a longer-term residual state.

As shown in Figure 42(c), networks involved in sugar metabolism included glycosaminoglycan degradation, fructose and mannose metabolism, inositol phosphate metabolism, glycosaminoglycan biosynthesis, propanoate metabolism, and pyruvate metabolism. Fructose and mannose, pyruvate and propanoate metabolism have high degrees of intra- and inter-connectivity, along with Glycosaminoglycan biosynthesis and Addition of GlcNaC to the TN antigen. Genes involved in fructose and mannose metabolism had increases in expression as cells regressed towards a residual state, for example in Hk2, Pfkfb3, Aldoa and Mpi. This suggests a shift towards using these two sugars as a source of energy production in the cell. Hk2 and Pfkfb3 showed increased expression levels in the tumor state - both of these genes promote glycolytic metabolism, in line with the notion that tumor cells have increased glycolytic flux.

In contrast, pyruvate and propanoate metabolism had increases and decreases in the expression of different genes. Focusing on cells in the tumor state (bar on the far left of each graph), genes such as Me3 and Acss3 were down-regulated, which are both mitochondrial enzymes. Acyp2, which hydrolyses acyl phosphates, was also down-regulated, although its wider physiologial role remains unclear. The other genes had small increases or decreases in their expression.

As cells regressed towards a residual state, the majority of genes, such as Me2, Me3, Mdh2, Acss3 and Dld appeared to return to expression levels comparable to normal, whereas certain genes, such as Pkm, Grhpr and Acyp2 had small fluctuations (although still statistically significant), the first two being involved in pyruvate production. Pdha1 appeared to have increased expression levels across the time series, with a small increase during cell regression - this is involved in the production of acetyl-coA from pyruvate.

The majority of genes that were significantly altered in glycosaminoglycan biosynthesis and degradation were down-regulated in tumor cells, but appeared to taper back towards a log(2) fold change of 0 as cells regressed towards a residual state, for example, Hexa, Hexb, St3gal2, and St3gal3.

Interestingly, certain gene expression signatures suggested a shift towards the production of keratan sulfate in tumor and residual cells. For example B3gnt7, which was up-regulated in tumor and residual cells, is involved in keratan sulfate biosynthesis, and Chst1, which was strongly down-regulated in tumor and residual cells, is involved in break-

down of keratan sulfate through sulfation, although Chst2, which has a similar function was moderately up-regulated as cells regressed.

Hyal1 and Hyal3, which are both involved in hyaluronic acid breakdown were moderately decreased in tumor cells, but had an increase in expression as cells began to regress. Hyaluronic acid is associated with breast cancer motility. Therefore its breakdown in line with the notion that these cells are acquiring a more "normal" epithelial breast like state.

The majority of significantly deregulated genes in glycosaminoglycan biosynthesis or degradation returned to "normal" expression levels (relative to never induced cells) suggesting that residual cells acquire relatively typical mammary epithelial like characteristics, in this respect.

Focusing on tumor cells (far left bar), many of the gene expression changes in relation to amino acid metabolism (Figure 42(d)) were associated with the urea cycle and creatine biosynthesis in tumor cells. For example, Got2, Gls2, Gatm, Nos1, Nos2, Car8, Car9 and Car12 (all of which, apart from Nos1 and Car8, are significantly up-regulated) are all associated with the urea cycle. The down-regulation of Nos1 and Car8 could be because cancer cells are preferentially using their isoforms for the urea cycle.

Gamt, which is part of the creatine biosynthesis pathway, is significantly down-regulated in tumor cells. In contrast with this, Ppat is up-regulated. Ppat is involved in purine biosynthesis.

Taken together, the shift of sugar metabolism towards fructose and mannose metabolism, and away from pyruvate and propanoate metabolism, as well as an apparent flux through the urea cycle, down-regulation of creatine biosynthesis and up-regulation of genes involved in biosynthesis, suggests a shift away from cellular energy production, and towards macromolecule biosynthesis.

As cells regressed towards a more residual state, certain genes, such as Nos1, Nos2, Car8, Car9 and Car12 appeared to stay de-regulated, and other genes, such as Gfpt1, Gfpt2, Glul, Gamt and Maob appeared to have transient fluctuations in their expression. The changes in Nos1, Nos2, Car8, Car9, Car12 would appear to suggest that the urea cycle remains altered in residual cells, consistent with results from the parralel analysis done by Ksenija Radic-Shechter *et al.* (2020)[175]. The changes in Gfpt1, Gfpt2, Glul, Gamt and Maob suggest transient changes to metabolic pathways as cells become re-polarised and adjust to becoming more epithelial in characteristics.

Mitophagy was also a pathway that had multiple genes that were de-regulated. In contrast to sugar metabolism and amino acid biosynthesis pathways, many of these genes had an expression trajectory where expression was increased, relative to the tumorigenic and never induced state, when regressing towards a residual state. These include genes such as Cited2, Bnip3, Nbr1, Bnip2l, Bnip3l, Mras, Mitf, Gabarapl1 and Atg9a. Genes such as Bnip3 and Bnip3l are involved with apoptosis, consistent with the fact that the majority of oncogene addicted cells undergo cell death following oncogene de-induction. Many of these genes are also involved in autophagy such as Bnip3, Bnip3l, Nbr1, Gabarapl1 and

Mitf are associated with autophagy. This suggests that mitochondrial components could be used as sources of molecules for macromolecular production, and also for energy production as cells acquire a residual state.

Many genes involved in FoxO signalling and TGF-β signalling were down-regulated in the tumor state and had an upwards trajectory towards comparatively normal levels as they progressed towards a residual state, for example, Chrd, Nbl1, Tgfbr2, TgfB3, Egfr and Myc. Other genes, such as Inhbb and Epas1 and Igf1 also had similar trajectories but stayed at down-regulated levels at the end of the time course - it is possible that these genes could also return to comparatively normal levels over a longer time period.

However, in contrast, certain genes appeared to consistently stay de-regulated in a tumor-like state, such as S1pr1, which stayed down-regulated, and Bmp7, which stayed up-regulated. As well as Smad9, Dcn and Igf1, which also stayed de-regulated at the end of the time course, but could possibly be decreasing at a slower rate than the time parameters in this experiment. Interestingly, Bcl6, which is implicated in breast cancer proliferation, appeared to increase in the residual state after initially decreasing.

2.8.2 Residual cells resemble tumors, but have a unique metabolic phenotype

In order to have an accurate and comprehensive understanding of how tumor and residual cells differ from their normal mammary epithelium counterparts, Ksenija Radic-Shechter, in collaboration with Eleni Kakifa, conducted metabolomic experiments, utilising GCMS and LCMS to profile the intracellular and extracellular metabolites. Using a combination of the GCMS, LCMS and transcriptomic data of tumor cells (5 days on DOX) and residual cells (7 days off DOX) (Figure 43(a)). Matt Rogon (EMBL) performed an integrated analysis of the GCMS, LCMS and transcriptomic data to visualise cellular networks that differed in these cells, relative to their normal counterparts. A detailed overview of how this was performed is available in the materials and methods (Section 4.10).

This analysis created networks for intracellular and extracellular metabolites for each cellular state (tumor and residual). These networks contained the altered metabolites, significantly altered genes, and first and second neighbours of these genes, as well as associated enzymes and reactions. These networks for intracellular and extracellular metabolites were combined in a union, to display a combination of both, and then the data were subsetted to observe which networks are consistent between the tumor and residual state (Figure 43(b)) and which are unique to the residual state (Figure 43(c)).

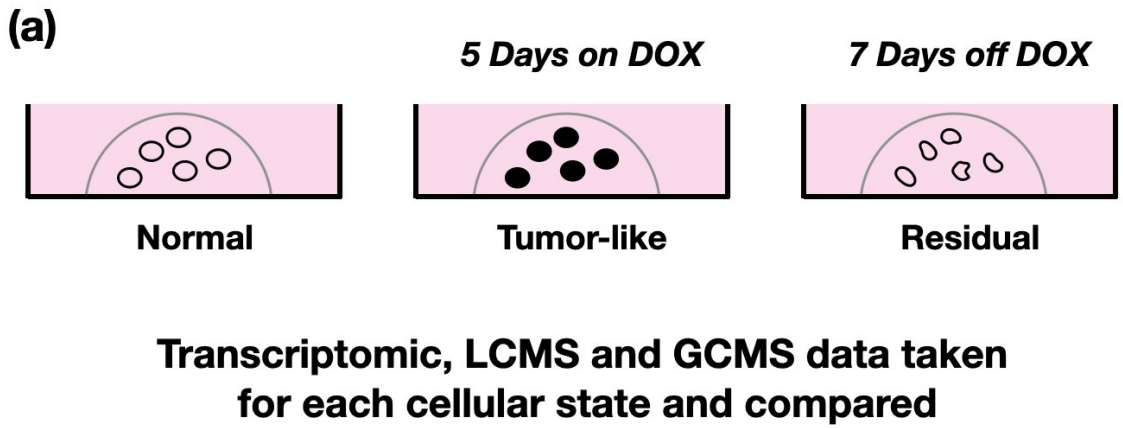

Figure 43: *Continued on next pages.* **(a) Schematic for the experiment.** Mouse mammary primary cells that were tumorigenic (5 days on DOX or residual (A further 7 days off DOX) had transcriptomic, and LCMS and GCMS data taken for metabolomic experiments. These data were then processed and analysed (see Section 4.10) and compared to normal cells (Never Induced). The networks that were consistently de-regulated in tumour and residual cells (b) and uniquely de-regulated in only residual cells (c) are displayed on the following pages.

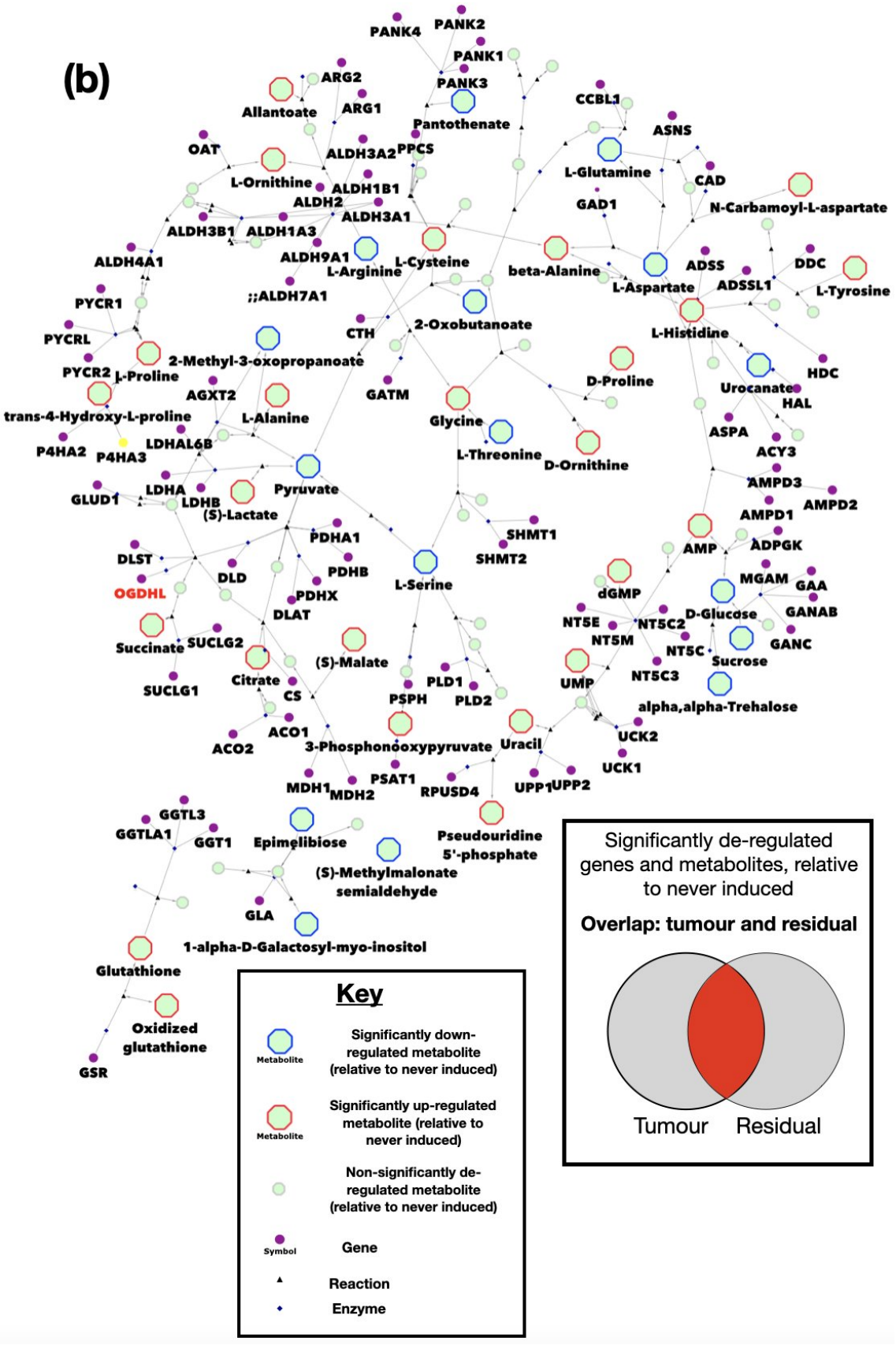

Figure 43: *Continued on next page.*

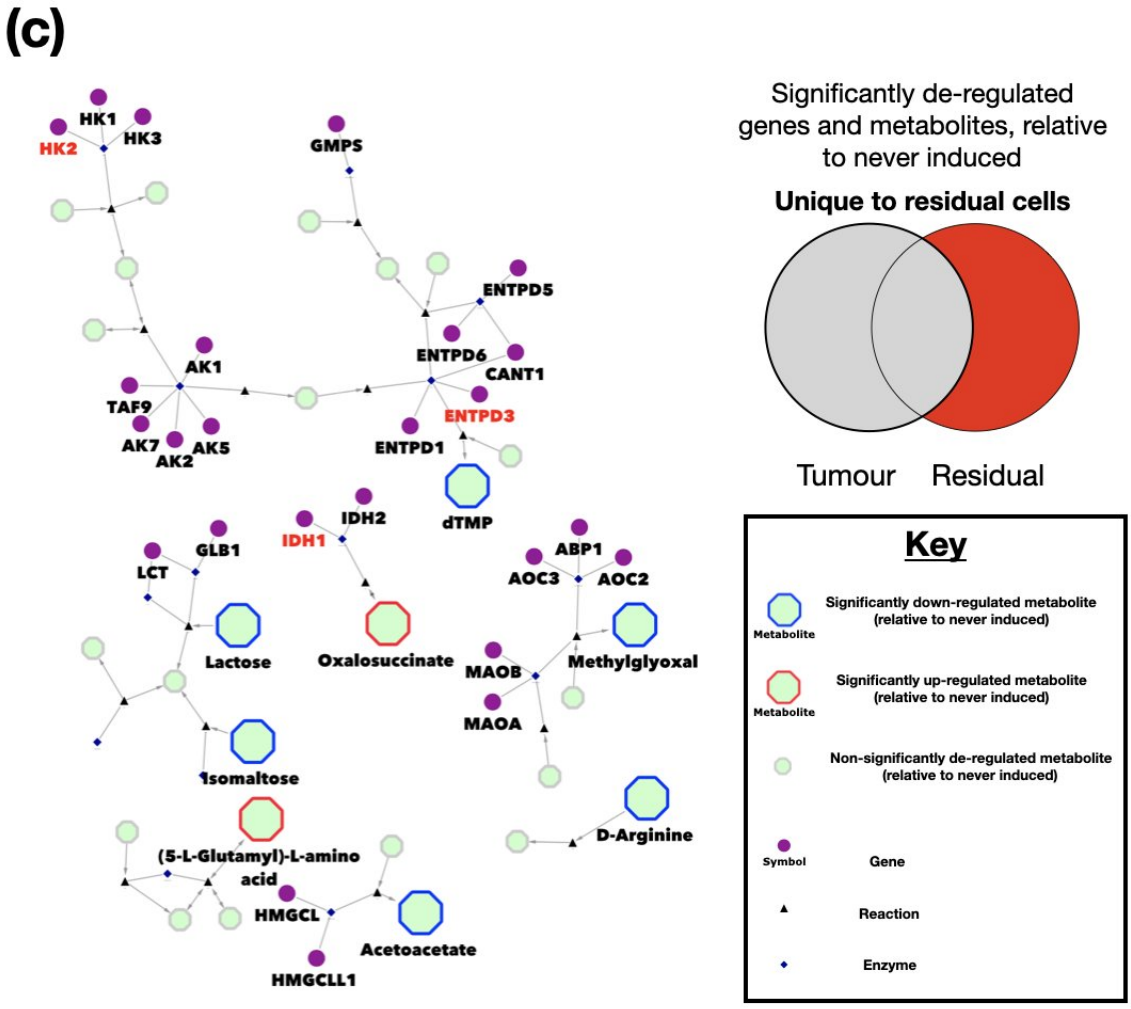

Figure 43: **Overlap of significantly de-regulated Compound-Reaction-Enzyme-Gene networks. (a) between tumor cells (5 days on DOX) and residual cells (7 days off DOX), (b)Compound-Reaction-Enzyme-Gene networks unique to residual cells**. GCMS, LCMS and Transcriptomic data were integrated (see Section 4.10 for a comprehensive explanation). Followed by simulated annealing algorithms in jActiveModules to generate Compound-Reaction-Enzyme-Gene networks, visualised in Cytoscape. Networks found in both 7 days off DOX and 5 days on DOX networks are displayed. Interactions between metabolites, genes, reactions and enzymes are visualised by grey lines, with arrows signifying the direction of the reaction. Significantly changed metabolites (relative to never-induced) are shown as enlarged octagons, and their border signifies up-regulation (red) or down-regulation (blue). Non-significantly changed metabolites are shown as smaller octagons, with their names omitted for figure readability. Significantly altered genes, and their first and second neighbours are shown in the figure. Significantly altered genes are written in red.

As shown in Figure 43(b) and consistently with parallel analyses done by Radic-Shechter *et al.* 2020[175], there was a significant overlap between the tumor and residual states, with respect to the networks that were altered. Consistent with the time-course transcriptomic data, networks related to the urea cycle appeared to be significantly altered, with both isoforms of Ornithine (L- and D-) and L-Arginine significantly de-regulated.

On top of this, multiple sugars and amino acids were significantly up- or down-regulated. The vast majority of metabolites were not associated with signficantly de-regulated genes,

with only OGDHL (shown on the left of Figure 43(b))) being changed. This implies that the transcriptomic changes and metabolic changes happened over different timescales, with metabolic changes changing more slowly. The interplay between transcriptomics and metabolomics is complex, also meaning that changes in metabolically related enzymes and the actual metabolites themselves may not necessarily be consistent.

Figure 43(c) shows significantly altered metabolic networks that were just unique to residual cells. The size of the network was smaller than the overlap (Figure 43(b)), suggesting that the metabolism of residual cells is partially unique, but largely reminiscent of tumor cells. Also compared to Figure 43(b), the size of the extracted metabolic networks tended to be smaller, implying smaller high order metabolic changes.

2.8.3 Discussion of section 2.8: Metabolic differences of tumor and residual cells, compared to normally mammary epithelial cells

Ksenija Radic-Shechter and Ashna Alladin conducted the experiments detailed in this section with the aim to understand how tumor cells, residual cells and normal mammary epithelial cells differed from one another, and led transcriptional and metabolomic experiments on inducible and de-inducible transgenic murine experimental systems in order to understand this further. As part of a parallel analysis, this project also independently analysed these data with a particular focus on metabolism to understand how metabolism differed in tumour and residual cells compared to normal. Metabolic differences that carry over to residual cells after initial tumor regression could be particularly important to target, possibly as part of a maintenance therapy treatment regimen.

This difference was assessed in two ways: temporally using transcriptomic data, based on already generated time-adjusted p-values from a prior analysis of the data (performed by Katharina Zirngibl), and an integrated analysis, using a combination of metabolomics and transcriptomics.

2.8.3.1 Sugar metabolism: potential shifting towards an altered state of sugar metabolism in residual cells

As shown in Figure 42, a large number of genes across multiple different pathways appeared to return to comparatively similar expression levels as never induced cells over time. These results are consistent with previous microarray gene expression data from our lab[176] and also a separate analysis of these data that have been submitted by Radic-Shechter *et al.* for a preprint[175]. Overall, these results are indicative that these cells regress towards a “dormant” state, which is reminiscent of “normal” cells but still maintain unique properties.

Focusing more specifically, some genes involved in sugar metabolism appeared to increase in their expression, either transiently, or as long as the time series was assessed for (168h), possibly meaning that these particular genes remain up-regulated indefinitely in these cells. In particular, this was the case in genes involved in fructose and mannose

metabolism. Without more in depth functional analysis of the particular genes involved, it is difficult to speculate on what specific cellular characteristics may be affected by this. However, a number of genes with this expression trajectory, including Hk2, Aldoa, Aldoc and Pfkfb3 have been associated with treatment resistance across different cancers, implying that they may have a functional role rather than being expression artefacts as cells undergo regression and re-polarisation. On a pathway level, increased utilisation of fructose metabolism (fructolysis) has also been positively associated with breast cancer development[251]. This means that fructolysis may also play a functional role in the eventual re-initiation of tumorigenesis, and partially account for why residual cells are drastically more likely to form tumors than their normal counterparts.

Genes involved in pyruvate and propanoate metabolism, as well as glycosaminoglycan and degradation pathways had transient increases or decreases in their expression, but returned to similar levels compared to never induced cells by the end of the time course. This implies that changes of the genes involved in these networks are either transiently required in the regression towards a residual state, or are artefacts from other cellular processes.

2.8.3.2 Sugar metabolism: up-regulation of keratan sulfate biosynthesis in tumor and residual cells

Interestingly, B3gnt7 and Chst1 were highly up- and down-regulated in the tumor state and during the whole of the regression time course, respectively. B3gnt7 is implicated in keratan sulfate biosynthesis, and Chst1 is implicated in its metabolism, suggesting an up-regulation of keratan sulfate (KS) in tumor and regressing cells. KS is a glycosaminoglycan that has a wide range of physiological roles, including in the cornea of the eye, the central and peripheral nervous system and has some implications in tumorigenesis. Its characterisation in cancer is limited, but plays roles in the malignancy of pancreatic cancer. A publication by Miyamoto *et al* (2011)[252] also performed histological staining on multiple different human tumor samples, and found expression in multiple cancer types, including cancer of the breast, lung, pancreas, thyroid, mesothelium, endometrium, ovary and cervix, with particularly high expression in thyroid, endometrial and ovarian cancer.

Overall, these results on sugar metabolism suggest that there are transient and perhaps longer-term changes in the expression of metabolic enzymes, which may be indicative of a metabolic shift during tumor regression, whilst maintaining certain tumor characteristics. Maintaining these tumor characteristics could mean that cells are in a metabolic state that is more likely to be permissive of a transition back to a neoplastic phenotype, compared to their normal (not previously cancerous) mammary epithelial cell counterparts.

2.8.3.3 Amino acid metabolism: potential for a deregulated urea cycle contributing to HER2+ breast cancer relapses

In amino acid metabolism, many of the genes that were de-regulated were involved with the urea (ornithine) cycle. In a normal setting, this pathway is primarily functional in the

liver as a part of amino acid catabolism, where toxic ammonia is converted into urea for secretion. De-regulation of the urea cycle has been characterised across many different cancers; with a wide variety of cancers having at least two enzymes involved in the urea cycle that are de-regulated[253]. In cancer patients, this is reflected by the changes in the ratio of nitrogenous compounds, for example, increased an increase pyrimidines such as uracil and thymidine is observed in the urine of prostate cancer patients. In the results from this project, many of the genes involved in the urea cycle stayed de-regulated as far as the experimental time series measured, indicative of more permanent changes to the urea cycle in these cells. De-regulation of the urea cycle is associated with increased cell proliferation, mutagenesis and cell migration, and leads to worse patient prognosis. Taken together, these results could indicate that a de-regulated urea cycle is a potential way that residual tumor cells could eventually be re-induced into a neoplastic state through accumulation of further mutations and already retaining previous cancer hallmarks.

2.8.3.4 Mitophagy: a source of macromolecule production as cells enter a residual state

Similarly to the gene expression trajectories found in sugar and amino acid metabolism, the expression characteristics of genes involved mitophagy were predominantly transient, with most expression trajectories appearing to tend towards a comparatively normal state as the time course progressed. Some genes, such as Cited2, Bnip3 and Nbr1, Atg9a and Tax1bp1 appeared to increase in their expression part way through the time course. It is possible that Bnip3 and Cited2 may stay expressed for longer time periods.

Overall, these expression signatures are likely to be due to the majority of cells undergoing autophagy as the main oncogene drivers are removed. However, it is also important to consider that the link between mitophagy and cellular metabolic reprogramming in cancer cells is well characterised. As mitochondria are broken down and metabolised, this means that more of the cells energy production has to come through glycolysis, contributing to the Warburg effect. If there is any retained metabolic characteristics with respect to mitophagy, it would help to put dormant cells in a metabolic state that is geared towards macromolecule production and away from energy efficient ATP synthesis. Interestingly, Cited2 and Bnip3, which are two genes that look as though they could potentially stay upregulated beyond the experimental time course, are both implicated in breast cancer progression and also resistance.

2.8.3.5 TGF-β and FoxO signalling pathways: regulators of tumor metabolism

TGF-β and FoxO both play roles in regulating cellular metabolism, and are both implicated in tumor metabolism. TGF-β normally acts as a tumor suppressor, but in the context of HER2 over-expression, acts to promote different cancer hallmarks, including migration, invasion and survival characteristics. In the context of metabolism, TGF-β and cell metabolism interact with one another, with TGF-β signalling stimulating glycolysis during EMT, with an upregulation of HK2.

Almost all the significantly deregulated genes in TGF-β and FoxO signalling were down-regulated in the tumor state, which remained the case during regression, with expression appearing to slowly return to normal levels, although it is possible that signalling remained down, reminiscent of tumor signalling. The notable exception to this is BCL-6, which was up-regulated in tumor state, and then quickly lost expression before regaining it after 24h. BCL-6 acts as a transcriptional repressor, and the high expression shown in this experiment is consistent with breast cancer cell line data, including SK-BR3 cells, which functionally characterised BCL-6 as being important for cancer cell growth across multiple breast cancer sub-types.

Chapter 3

General Discussion and Future Perspectives

3.1 Recap and overview of results

Recently, multiple new targeted therapeutic options have been approved for HER2+ breast cancer patients. These are likely to improve patient prognosis as the licensing of HER2 targeted drugs such as trastuzumab, pertuzumab and lapatinib have already done (See Table 2, Page 35). However, an unmet need remains in HER2+ breast cancer, with regard to problematic tumor recurrences[98;99;100;101]. Tumors that have recurred have a worse prognosis, and tumors that have been able to metastasise are still considered incurable. Tumors that have metastasized after therapy relapse are regarded as having a particularly poor prognosis[98].

Therefore, it is important to develop treatments that minimize the risk of tumor relapses, as well as treatments that are effective during initial treatment. With regard to HER2 and Pirin inhibition, this project aimed to conduct experiments to address both of these criteria. Lapatinib, an already approved HER2 and EGFR tyrosine kinase inhibitor[94], was used to inhibit the function of the HER2 driver oncogene. EMBL-703625 is an inhibitor of the function of the Pirin protein, which is relatively poorly characterized, but acts as a transcriptional regulator, and interacts with NF-$\kappa\beta$ and BCL-3[188;190]. Data from the EMBL CBCF characterizing this inhibitor on HeLa cells and A549 lung tumor xenografts showed encouraging efficacy, tolerability in mice, and appeared to have deregulate areas of cell biology that are known to be involved in HER2+ breast cancer relapses and/or resistance, such as effects related to glycolysis, heat shock protein expression, and the expression of solute carriers.

Rather than establishing a lapatinib resistant line and then treating with EMBL-703625, which is reminiscent of an already relapsed setting, this project instead focused on mimicking a combination first-line approach. The data from this project showed that lapatinib and EMBL-703625 had a synergistic effect with each other (Section 2.1) and that they had a largely individual transcriptomic effect which led to a larger overall combination effect (Section 2.2). Re-growth experiments suggested that in one cell line, BT-474, this may compromise re-growth (Section 2.3). As well as this, experiments that co-inhibited lactate dehydrogenase (LDH) with oxamate suggested that these two drugs could both kill cells, in part, through a blockade mechanism on glycolysis (Section 2.4). In mouse primary cells, a direct comparison between neoplastic and non-neoplastic cells from the same source suggested that lapatinib and EMBL-703625 predominantly target neoplastically transformed cells (Section 2.5). In succession, it appears possible that EMBL-703625 could sensitise BT-474 for subsequent treatment with lapatinib also (Section 2.6). For the future, this project also aimed to establish a microscopy experimental pipeline that could image cell-cell heterogeneity in 3D over time (Section 2.7). Finally, data generated from experiments led by Ashna Alladin and Ksenija Radic-Shechter were analysed to identify any areas of vulnerability for tumor and residual cells; consistently with the pre-print submitted by Radic-Shechter *et al.* (2020)[175], areas of cell metabolism were identified as particular nodes of vulnerability, which could inform on future experimental approaches related to understanding mechanisms of tumor heterogeneity and treatment evasion or

resistance (Section 2.8).

3.2 Future directions: Characterising synergy between dual HER2 and Pirin inhibition, or pirin inhibition monotherapy across other cancer types

The future directions outlined in this section are directions this project could take over a medium-longer term time scale in order to expand upon the results found in this thesis. More immediate and specific future directions can be found at the end of each results and discussion section (Sections 2.1 - 2.8).

3.2.1 Multiple different tumor types over-express or express HER2 and therefore could be susceptible to dual HER2 and pirin inhibition

There are currently a plethora cancer types addicted to the HER2 oncogene that HER2 and pirin inhibition synergy could carry over to. These include gastric cancer, non-small cell lung cancer, biliary tract cancer, ovarian, endometrial, cervical, prostate, bladder, colorectal, and pancreatic. In all of these tumor types, HER2-targeted therapies are being developed and clinically tested, but currently, only breast cancer (See Table 2 (Page 35) for full details) and gastric cancer (trastuzumab and trastuzumab deruxtecan[254]), have HER2-targeted licensed therapies against them.

In many of HER2 over-expressing cancer sub-types, clinical trials have found no significant benefit for classical HER2 targeted agents in monotherapy. For example, trastuzumab in HER2 over-expressing NSCLC found no statistically significant clinical benefit compared to the standard of care[255]. However, with the recent development of multiple new, more effective HER2 targeted therapeutics, including antibody-drug conjugates such as trastuzumab emtansine and trastuzumab deruxtecan, multiple clinical trials across these various tumour subtypes are now ongoing, often in combination with other targeted agents. Preliminary data appear encouraging across different tumour types, for example, trastuzumab emtansine monotherapy in HER2+ salivary gland cancer[256], and trastuzumab deruxtecan in monotherapy against HER2 over-expressing metastatic NSCLC[257].

As more targeted agents are characterised and approved in HER2+ over-expressing cancers, it gives rise to the possibility of more agents being combined with them to further increase treatment efficacy, such as agents like EMBL-703625.

As well as this, as HER2-targeted agents continue to improve, it is possible that HER2-low patients (those that express HER2, but not at high levels) in cancers such as breast cancer and gastric cancer may also benefit from HER2-targeted therapies. This could largely extend the niche for HER2-targeted therapeutics, and by extension, extend the potential for combination therapies. Currently, multiple different clinical trials aim to assess this with different HER2-targeted agents, including in breast cancer, for example, with trastuzumab deruxtecan in the Phase 3 DESTINY-Breast04[258] (HR-) and DESTINY-Breast06 (HR+)

trials[259]. Although these trials have not yet presented any preliminary data, and will take at least two more years to reach their primary endpoint, other HER2-low trials have reported encouraging preliminary data (Reviewed in Eiger *et al.,* 2012[260]). The majority of these trials are testing HER2-targeted drugs in combinations with other drugs. However, it is also important to note that this synergy between HER2 and pirin inhibition may not carry over to tumor types where HER2 is not a driver of a neoplastic phenotype.

Taken together, this means that the clinical landscape is showing benefit of expanding HER2-targeted therapies in combination with other targeted agents across multiple different cancer types, and in sub-types that were previously considered not amenable to HER2 targeted therapy. This presents a large potential niche for HER2 and Pirin inhibition synergy, and presents an exciting rationale when considering the wide reaching function that pirin appears to have across different cancers.

3.2.1.1 An example of a cancer type that dual HER2 and Pirin inhibition may benefit: Non-Small Cell Lung Cancer

An example of an important cancer for which dual HER2 and pirin inhibition could carry over to is non-small cell lung cancer (NSCLC). NSCLC is characterised by poor prognosis and survival rates, and very high rates of relapse. Many different sub-types of NSCLC that are addicted to a particular oncogenic driver exist, including those driven by mutant EGFR (15% of cases in Europe, 40% of cases in Asia) and mutant HER2 (approximately 2% of cases). There is currently no standard of care for HER2 driven NSCLC, and although EGFR-targeted tyrosine kinases such as osimertinib are licensed for EGFR-driven NSCLC, tumor relapses often occur. This means that there is a large unmet need for these patients.

Many of the nodes that were found to be affected by pirin inhibiton are relevant in lung cancer. Firstly, data using EMBL-703625 on A549 lung xenografts by the EMBL CBCF have demonstrated potent tumor inhibitor activity (data not shown). The incidence of lung cancer is majorly increased by cigarette smoking. A study by Gelbman *et al.* (2007)[261] found that pirin expression is up-regulated in the bronchial epithelial cells of smokers, and appears to have a role in promoting the apoptosis of these cells. Further evidence for the role of pirin in lung cancer comes through the current data on NF-$\varkappa\beta$ signalling. Similarly to breast cancer, NF-$\varkappa\beta$ signalling is also implicated as a therapeutic target in lung cancer therapy across multiple experimental models (Reviewed in Rasmi *et al.,* 2020[262]). Critically, a meta-analysis of clinical patients found that NF-$\varkappa\beta$ expression is associated with a shorter overall survival in non-small cell lung cancer (NSCLC) patients[263].

Specifically to EGFR/HER2 signalling, NF-$\varkappa\beta$ is a known player in EGFR-targeted therapy resistance. Single cell transcriptomic studies show an upregulation of NF-$\varkappa\beta$ signalling genes in persister sub-populations after EGFR TKI treatment[264]. As well as this, other nodes that are affected by pirin inhibition are also relevant here. HSP90 inhibition in NSCLC has an effect on EGFR, HER2, and HER3 expression[265] and is shown to have strong tumor inhibitory effects[266]. Clinical data using the HSP90 inhibitor 2,4-

dimethoxychalcone sensitises T790M mutant EGFR NSCLC (a particularly prevalent mutant) to EGFR targeted therapy[267]. As well as this, glycolysis, which appears to also be a node that pirin acts through to encourage tumor resistance, has been also demonstrated to support cell survival and growth in EGFR mutant NSCLC by inhibiting EGFR turnover pathways[268;269].

3.2.2 Evidence to support further characterisation of pirin inhibiton in monotherapy, or alongside other targeted treatments, across multiple tumor types

Currently, there is very limited characterisation of the function of pirin in cancer therapy, but there is evidence to suggest that pirin could play a potential role across multiple cancers, including: breast, lung, prostate, ovarian, head/neck, gastrointestinal, oral, and cervical[193]. All of these cancers, with the exception of breast (this project) and lung (EMBL CBCF data) , have not yet been functionally characterised through pirin inhibition in a cancer setting, but expression and interaction data suggest that pirin expression and function could be responsible for the development of many cancer properties across these different indications. Perez-Dominguez *et al*. (2021)[193] recently published an excellent review of the evidence to support the role of pirin in epithelial carcinogenesis across these cancer types

Notably, this project demonstrated that pirin inhibition appears to be important for multiple cellular functions, including protein degradation, NF-$\varkappa\beta$ signalling, and heat shock protein networks. These same networks are often to be important for carcinogenesis and therapy resistance across multiple cancer types. NF-$\varkappa\beta$ signalling is highly complex, and its downstream targets can be implicated across almost every hallmark of cancer. In breast cancer, NF-$\varkappa\beta$ activation is implicated with resistance to lapatinib and endocrine therapy in ER+ sub-types, and in lung cancer, NF-$\varkappa\beta$ activation is implicated in resistance to EGFR TKIs.

One downstream network from NF-$\varkappa\beta$ activation is ubiquitin mediated protein degradation. In the results from BT-474 and SK-BR3 cells, pirin-inhibition caused widespread expression changes in genes involved in this process. The importance of these pathways in carcinogenesis and therapy resistance is well characterised, and multiple FDA approved drugs have been approved that inhibit genes involved in these pathways, although the majority only in haematological cancers. However, multiple research efforts are now being undertaken to characterise this across a range of tumor types.

Heat shock proteins have also been well characterised in a cancer setting, and (outside of the inhibitions already shown for breast cancer) have been widely implicated in many different types of cancer, and aspects of the neoplastic phenotype[270].

In summary, there are multiple lines of evidence to suggest that pirin inhibiton should be functionally characterised across a wide range of tumor types, which would support clinical development in this setting. Firstly, functional characterisation in breast cancer in this project, as well as lung cancer and HeLa cells from the EMBL-CBCF demonstrate that

pirin inhibition has anti-tumor effects. Expression evidence across a wide range of tumor types suggest that pirin plays a role in tumorigenesis, and widely characterised functional evidence in clinical and pre-clinical settings from demonstrated downstream targets of pirin inhibition support the notion that it could be important for tumorigenesis, and therapy resistance, and therefore an attractive therapeutic target.

3.2.3 Methods to characterise HER2 and Pirin inhibition across other tumor types

3.2.3.1 Cell lines

To characterise whether dual HER2 and Pirin inhibition show synergistic interactions across other HER2 positive tumor types, applying the synergistic models used in this thesis could be a highly useful tool to observe which tumor types this synergy affects. Each of the tumor types that have HER2+ driven or positive sub-types (described in Section 3.2.1) have corresponding HER2+ cell lines that have been characterised and are available for use[271]. Using the methodology established in this project to seed large quantities of cells in 3D, treat with different drug concentrations, conduct biochemical assays on them, and perform synergy measurements, it would be relatively convenient and fast to apply generate data similar in nature to this project across multiple different cell lines.

3.2.3.2 *In vivo* approaches

To progress to in-human trials, data from an *in vivo* setting are essential. *In vivo* approaches in mice allow for an important pre-clinical validation step of safety and efficacy, before characterisation in humans in clinical trials.

A logical next step for this project in a practically feasible experimental workflow and on a reasonable time scale would be to characterise dual lapatinib and EMBL-703625 treatment in the inducible mouse models that are used in the Jechlinger Lab[77]. To this end, *in vivo* experiments are already planned and have been discussed with the EMBL Animal (LAR) facility, with the aim of the experiment to generate overall survival and relapse-free survival Kaplain-Meyer curves of monotherapy compared to combination therapy in primary tumors after induction.

On a larger practical and temporal scale, *in vivo* mouse approaches could also be used to characterise EMBL-703625 efficacy, with or without HER2 inhibition in a variety of other tumor types. Recently, Lundin *et al*. (2020)[272] reported on the development of a Doxycycline inducible mouse system that allows convenient gene editing and conditional expression in different tissues in an *in vitro* setting, making it an ideal *in vivo* method for cancer drug characterisation.

This convenient method of mouse gene editing would allow conditional induction of tumors through oncogene expression across multiple tissue types. After initial *in vitro* validation with cell lines, these mice would present a valuable pre-clinical model to generate *in vivo* data, that could inform future clinical trial design.

3.2.4 Patient-derived organoids

Using 3D organoids that are derived from patient tumor cells is an approach that has been utilised commonly in recent years, and present an encouraging experimental approach for characterising patient responses. Of particular relevance for the implications from this project is that patient-derived organoids have a higher degree of heterogeneity than cell lines, making them important in understanding the mechanisms behind patient relapses. This is discussed in detail by Liu *et al.* (2021)[273]. In the Jechlinger Lab, Sylwia Gawrzak has pioneered approaches to optimising 3D growth conditions from patient derived organoids.

3.3 Future directions: Single cell -omics based approaches to understand cell heterogeneity in response to drug treatment

The results presented in this thesis demonstrate that HER2 and Pirin inhibition synergise with one another in HER2+ breast cancer cells. However, tumor resistance occurs because of tumor heterogeneity, meaning that certain sub-populations within a tumor could be less susceptible to this drug synergy. One method that this project aimed to establish to understand heterogeneity was through the light-sheet microscopy approaches aim to characterise spatially and temporally how cells differ from one another (See Section 2.7 (Page 115)).

An important way to provide additional insight to the results already generated and understand lapatinib-EMBL-703625 synergy with more granularity is through single cell -omics based approaches. Single-cell transcriptomics, in particular, has seen the most innovation in understanding cancer. This is particularly important in the context of treatment relapses because it allows a more precise overview of initial cell sub-populations before and how these evolve during treatment. An experimental design that compares lapatinib or EMBL-703625 monotherapy to combination therapy will be able to understand how each monotherapy gives rise to persister sub-populations, and how this differs in combination therapy. The re-growth experiments suggest that SK-BR3 cells also had surviving sub-populations even after combination therapy; these approaches could provide some insight as to how these cells were able to survive, and therefore how to kill these cells.

An excellent example of how an experimental design like this could be utilised comes from a recently published study by Aissa *et al*. (2021)[274]. They used single-cell transcriptomics on EGFR mutant NSCLC cells that were treated with EGFR TKIs and ALK/ROS1 TKIs. Their analysis found a diverse array of different drug tolerant cell states to EGFR TKIs, with high amounts of heterogeneity, which was the case in cell lines, xenograft tumors and patient samples.

On top of solely performing transcriptomic experiment on tumor cells, samples that come from *in vivo* or patient samples, allow stratification and analysis of neoplastic and non-

neoplastic samples into different sub-populations, allowing an understanding of the interplay between tumor cells, and cells in the local micro-environment. This can be important for understanding tumor relapses, as demonstrated in a study in HER2+ breast cancer by Wang *et al.* (2019)[275]. They characterised a CDK4/6 inhibitor Palbociclib, which is currently under review in HER2+ breast cancer by the FDA after demonstrating encouraging data in clinical trials. In tumors that are resistant to this inhibitor, they found a immature myeloid cell population that helped these resistant sub-populations avoid this response. Targeting these myeloid cell populations with TKIs and also introducing immune checkpoint therapy (anti-PD(L)1 or CTLA4 antibodies) overcame this resistance.

In vivo mouse experiments for this project are planned at the time of this thesis submission. Tumor samples that are taken from mice in primary tumors, or after disease remission in a primary or metastatic site could be applicable to a single cell transcriptomic workflow to allow an intricate understanding of the neoplastic sub-populations that give rise to recurrent tumors, and also how non-neoplastic cells in the surrounding micro-environment contribute to this. This could inform on how to optimise dual lapatinib and EMBL-703625 treatment to maximise efficacy and minimise probabilities of relapses.

3.4 Future directions: Progressing with HER2 and Pirin inhibition into a clinical setting

This project has aimed to assess whether dual HER2 and Pirin inhibition could display a synergistic effect in HER2+ breast cancer, and whether it could potentially reduce the risk of problematic relapses, as well as developing light-sheet microscopy based methods aimed at eventually understanding cell-cell heterogeneity in 3D space over time. The data from these aims has put forward an encouraging rationale for progressing into a clinical setting, pending results from *in vivo* experiments. It is highly important for any project that characterises drugs efficacy or interactions to consider the therapeutic situation, which starts with clinical trials. Surrounding clinical trials are both scientific and business-related considerations, which are both discussed here.

3.4.1 HER2+ breast cancer clinical trials involving Pirin inhibiton

Characterising whether a drug combination, such as lapatinib and EMBL-703625, reduces the risk of tumor relapses takes an inherently long amount of time, possibly over a scale of decades to obtain statistically meaningful data. Whilst long-term follow ups are important, to progress through clinical trials and be approved, drug combinations would have to show a efficacy and safety profile at least as good as the current standard of care. That is why this project aimed to establish if HER2 and pirin inhibiton displayed synergy with one another, which provides evidence that they may have strong efficacy.

From a commercial aspect, pharmaceutical companies may see limited investment opportunities for drug combinations that are unlikely to gain a large market share, given the high costs of clinical research and development. This could be the case if the HER2/Pirin

inhibition combination did not yield significant initial clinical benefit over the current standard of care, meaning that these combinations would never reach a clinical setting, even if this combination realistically lowered the rate of relapses over the long term.

From this standpoint, it could be commercially more attractive to test EMBL-703625 (or equivalent) in a basket clinical trial design, which tests this drug in an early clinical phase setting (Phase 1 or 2) across multiple different HER2-(over)expressing tumor types (listed in Section 3.2.1, in combination with a HER2 (or potentially EGFR) inhibitor to assess safety and provide a first insight to how clinical efficacy, although normally with a sample size too small to generate meaningful statistics. This trial design is common for first-in-human characterisations of new drugs. If pirin inhibition could potentially be used across multiple different tumor types, then this would provide increased commercial attractiveness. This is why testing EMBL-703625 across multiple other HER2-(over)expressing tumor types (discussed in Section 3.2.1) is an attractive rationale for future experiments, based off the data from this project.

Chapter 4

Materials and Methods

4.1 Biochemical Assays

4.1.1 Cell Toxicity Assay

The CellTox™ Green Cytotoxicity Assay (Promega) was used in order to assess relative cell toxicity. The CellTox™ Green Cytotoxicity Dye was added to flourobrite media in a concentration of 0.06µl of dye for every 10µl of media. 10µl of this solution was then added to 50µl of flourobrite media already in each well, making a total volume of 60µl of flourobrite media, with the working concentration of the CellTox™ Green Cytotoxicity Dye at 1:1000.

Measurements were taken using a Tecan Infinite® M1000 PRO plate reader. Fluorescence measurements were taken at 485nm excitation and 525nm emission, with both bandwidths set as 10nm. Readings were taken from the bottom, and gain was set manually at 100. Multiple reads were taken from different positions in each well, in a 4x4 pattern (type: Square, Border: 50um (in the Tecan software)).

4.1.2 3D Cell Viability Assay

The CellTiter-Glo® 3D Cell Viability Assay (Promega) was used in order to assess relative ATP levels as a read-out of relative cell viability. This assay can be multiplexed with the CellTox™ Green Cytotoxicity Assay and was therefore performed directly after Cell Toxicity readings were taken. 50µl of CellTiter-Glo® 3D Reagent was added to each well of a black-walled 96 well plate (Corning), covered in aluminium foil and shaken for 5 minutes at room temperature at approximately 550RPM on a bench-top shaker to facilitate full homogeneising of each gel. The plate was then left in the aluminium foil for a further 25 minutes before luminescence measurements were taken. Measurements were taken using a Tecan Infinite® M1000 PRO plate reader, to measure luminescence. Integration time was set as 1000ms and settle time was 0ms. Attenuation was set to none.

4.2 General cloning methods

4.2.1 Restriction Digestions

Restriction digestions of plasmid DNA were all carried out at 37°C for in a thermo-cycler for one hour. For each reaction, DNA concentration was measured via a NanoDrop, and 1200ng of DNA was added to each 20µl reaction volume. A table showing the components of a restriction digest used is below:

Reagent	Volume
Plasmid DNA	*Appropriate volume to make up 1200ng*
Restriction enzyme 1	1µl
Restriction enzyme 2	1µl
rSAP*	1µl
FastDigest green buffer	2µl
Water	*Added to make a final reaction volume of 20µl*

*rSAP was added to plasmid vectors in order to prevent re-annealing, but not added to digestions of inserts.

Table 11: Typical restriction digestion reaction conditions

4.2.2 Ligation Reactions

Digested vectors and inserts were added at a ratio of 7:1; Insert:Vector. This was calculated using the NEBioCalculator (https://nebiocalculator.neb.com/!/ligation). Two separate control reactions containing no ligase enzyme and no insert, respectively, were used to verify colony formation was likely to be genuine, and not due to background growth. A table showing the components of a ligation reaction is below.

Reagent	Volume
Ligase buffer	1µl
Insert	Appropriate volume to make up 175ng
Vector	Appropriate volume to make up 25ng
T4 DNA ligase enzyme	1µl*
Nuclease free water	Added to make a final reaction volume of 10µl

Table 12: Ligation reaction conditions when ligating cut vector and insert. *In the control reactions, either the vector or T4 DNA Ligase enzyme were not added; the volume was replaced with water.

4.2.3 Heat Shock Transformation of competent *E. coli*

Transformation of *E. coli* was carried out using heat shocking. 2 µl of ligation mix was added to 50µl of competent cells and kept on ice for 30 minutes. The cells were then included in a 42C water bath for 45 seconds, followed by a further 2 minutes on ice. 50µl of SOC media at 37°C was then added and incubated at 37°C for 30 minutes, before streaking on an agar plate with an appropriate antibiotic, and overnight storage at 37°C.

4.3 Transfection and imaging of the SoNar Sensor in SK-BR3 cells

4.3.1 Cloning of lentiviral vectors to generate SoNar or cpYFP-expressing BT-474 and SK-BR3 cells

Lentiviral transfection methods were used in order to express the SoNar sensor and cpYFP flourophore in BT-474 and SK-BR3 cells. The respective sensors were first cloned into lentiviral pLOVE backbones under the control of the CMV promoter. The SoNar and cpYFP gene constructs (pCDNA 3.1-SoNar and pcDNA 3.1-cpYFP) were provided as a gift by Yuzheng Zhao, East China University of Science and Technology. The SoNar and cpYFP genes were amplified from their original construct using primers to introduce an EcoRI and NheI restriction site to the 5' and 3' end of each gene and ligated into the lentiviral pLOVE vector. These sequence of these primers (5' - 3') was TAAGCAGAATTC-CGATGAACCGG to add the EcoRI site, and TAAGCAGCTAGCGGGCCCTCTAGACTC to add the NheI site. pLOVE-SoNar and pLOVE-cpYFP were then transfected into Top 10 *E. coli* cells using heat-shock transformation and plated on ampicillin containing agar plates. After colony selection, frozen stocks containing half LB suspension and half 50% glycerol were used for both plasmids. Sanger sequencing was used to verify that no genetic mutation had taken place on miniprep (Qiagen) extracted DNA.

4.3.2 Production and counting of lentiviral particles for transduction

To produce the lentiviruses, a protocol developed by Lucas Chaible (Jechlinger Lab, EMBL) was followed. 3.2 x 10^7 HEK-293T cells (Lenti-X, Clonetech Catalogue C6628) were thawed from frozen stocks and seeded in 500cm^2 cell culture dishes. The cell media was DMEM High Glucose supplemented with 1% glutamine, 1% sodium pyruvate, 10% FCS, and cells were passaged for 3 passages. The morning of the lentiviral transfection of HEK-293T cells, the media was supplemented with 25mM chloroquine diphosphate (Sigma-Aldrich Cat. - C6628). The HEK-293T cells were incubated with this media for 5 hours. The cells were then transfected with backbone plasmids: 20µg pMD2.G (Addgene Cat. - 8454) and 30µg psPAX2 (Addgene Cat. -12260), 1mg/ml of PEI (Poly-Science Cat. 23966-1), 40µg of pLOVE-pCMV-SoNar or pLOVE-pCMV-cpYFP, which was transferred with 9ml of Opti-MEM. After 2, 3 and 4 days post-transfection, the media was harvested (and replaced by fresh media), and pelleting of the lentiviruses was performed using an ultracentrifuge Beckman Sw32 rotor) at 25,000RPM for 2 hours at 4°C. The lentivirus pellet was then re-suspended in 1ml of HBBS buffer, which was then aliquoted and stored at -80°C. Quantification of the amount of viable lentiviral particles in the solution was performed by seeding 75000 HEK-293T cells in each well of a 6-well plate. After 24 hours, one well trypsinised and counted, to be used for calculations. For the other 5 wells, medium was removed and fresh DMEM was added at 10µl, 5µl, 1µl, 0.5µl, 0.1µl to each well for 2 days, with medium changed every 18 hours. The cells were then trypsinised and counted by FACS sorting. This was then compared to the amount of

virus pipetted and number of cells that were counted after the trypsinisation step.

4.3.3 Production and counting of lentiviral particles for transduction

The lentiviral vectors expressing pLOVE-SoNar or pLOVE-cpYFP were transfected into BT-474 and SK-BR3 cells in the following method. Each cell line was seeded onto a collagen coated 6 well plate, 24 hours prior to transfection. The media was then removed, and replaced with fresh medium containing the lentirviral particles, and was incubated for 24 hours, followed by a media change and incubation for a further 24 hours. Cells were briefly checked for a fluorescent signal, passaged onto a 175cm^2 tissue culture flask with filter cap (ThermoFisher Nunc^{TM} - Cat. #178985) to increase numbers, and briefly checked under a fluorescence microscope to confirm fluorescence. The cells were then sorted through FACs, selecting for GFP fluorescence, to select for the 5% of brightest cells. Before and after FACs sorting, cells were frozen as liquid nitrogen stocks. FACs-sorted cells were used for all described experiments.

4.4 Light-sheet Microscopy on the Leica SP8 DLS

4.4.1 Mounting for Light-Sheet Microscopy

To mount samples for the Leica SP8 DLS microscope, glass cover slips were cut into slices 1.4-1.8mm in width and elevated into place at approx 2mm in height with Picodent Twinsil® glue. The Picodent Twinsil® glue was prepared by adding the two elements, the base and catalyst, in a 1:1 ratio, mixing, and applying to the bottom of a MatTek glass bottom microwell dish, either side of the circular glass bottom. The cut glass was then applied on top of this glue, and was allowed to set for at least one hour. The imaging dish was then sterilised with 70% ethanol and UV light. Matrigel containing cells expressing either SoNar or cpYFP could then be seeded adjacent to one another on the glass slice, over the circular glass bottom. To delinate one end from the other, a dot was drawn on the side of the plate nearest to the cells expressing the SoNar sensor.

4.4.2 Light-sheet imaging on the Leica SP8 DLS

Light-sheet imaging on SK-BR3 cells expressing SoNar or cpYFP was conducted using the Leica TCS SP8 DLS microscope, primarily using 10x magnification. Conditions were kept at 37°C and 5% atmospheric CO_2 for the duration of the imaging. The imaging chamber was surrounded with water, which was also heated to 37°C to prevent media evaporation; this water was replaced every 24 hours to ensure it did not evaporate itself.

4.5 Cell Lines

4.5.1 Cell line authentication

SK-BR3 cells were obtained from the Cell Lines Service in Heidelberg, and BT-474 cells were obtained as a kind gift from the Edward Lemke lab at EMBL Heidelberg. Both lines were authenticated by STR profiling (Multiplexion), including SoNar or cpYFP expressing cells. Cells were also routinely checked for 2D and 3D morphology and growth characteristics, and tested for mycoplasma contamination through PCR testing.

4.5.2 Culturing of cell lines (2D)

4.5.2.1 Media

Cell lines were routinely grown in 2D on collagen coated plates - 3D culture was used purely for experimental purposes, whereas 2D was used for cell cultivation in preparation for experiments, or to create frozen stocks. The media conditions used were as follows: Phenol Red containing high glucose DMEM (Gibco - Cat. #41965120), supplemented with 10% heat-inactivated FBS, 2mM (final concentration) L-glutamine (Gibco - Cat. #25030149), HEPES buffer (made in-house at EMBL), 100x concentrated non-essential amino acids (NEAAs) (Gibco - Cat. #11140050), penecillin/streptomycin (Gibco - Cat. #15070063) and 1mM (final concentration) sodium pyruvate (Gibco - Cat. #11360070). Cells were grown typically on a collagen-coated 175cm^2 tissue culture flask with filter cap (ThermoFisher Nunc^{TM} - Cat. #178985).

4.5.2.2 Passaging

After cell lines reached approximately 70-80% confluency, both lines were split in a 1:3 ratio onto a new 175cm^2 tissue culture dish. This was performed in the following way. Firstly, media was aspirated off and the flask was washed with an equivalent amount of PBS (10ml for a 175cm^2 flask). The PBS was then aspirated off, and 0.25% trypsin (Gibco - Cat. #25200056) was added at enough volume to cover the bottom of the flask (typically 2ml for a 175cm^2 flask). The flask was then incubated at 37°C for 3 minutes. After this, the cells were briefly checked for detachment under a microscope, and then cell culture media (See Section 4.5.2.1) was added 5:1 media:trypsin and circulated to ensure the trypsin was deactivated by the FCS in the media. One third (typically 3ml) of this volume was then put onto a new flask, with a further 2 parts (typically 6ml) of fresh media added, being placed back in the 37°C incubator. The remaining cells were either discarded or frozen as liquid nitrogen stocks (see following section).

4.5.2.3 Generating liquid nitrogen stocks of cell lines or primary mouse cells

To generate liquid nitrogen stocks, cells were passaged as in the previous subsection. Instead of being put into a new flask, the cell containing media was introduced into a 15ml centrifuge tube, and centrifuged at 1000RPM for 5 minutes. The media was then removed

from the resulting pellet. For each 175cm^2 flask, three 2ml cryotubes were prepared for liquid nitrogen storage. For a 175cm^2 flask, this meant the pellet was resuspended in 6ml of CELLBANKER 2 (AMSBio) mediun, before 2ml was pipetted into a 2ml cryotube. These were then frozen in a -80°C freezer for 24 hours, before long-term storage in liquid nitrogen.

4.6 Mouse Genotyping

The Jechlinger Lab has bred mice to develop tri-transgenic mouse strains for TetO-MYC, TetO-Neu, MMTV-rtTA. All mice were bred into an FVB background. All mice were bred and housed in the EMBL Laboratory Animal Resources (LAR) in accordance with the European Commission Guidelines, revised Directive 2010/63/EU and AVMA Guidelines 2007, under vetinary supervision. Mice had constant access to drinking water and food, kept in cages of up to 6 other mice. In the animal facility, mouse were kept on a 12 hour light and dark cycle, with a constant temperature and air humidity (23C +/- 1C and 60% +/- 8%). The EMBL LAR facility provided tail cuts which were used to provide PCR results on the presence or absence of MYC, Neu and rtTA. Each tail clipping was kept in a 1.5ml centrifuge tube. This was firstly digested to obtain genomic DNA. 70ul of Na0H 25mM, EDTA 0.2mM was added and heated to 98C for at least 30 minutes at 650rpm shaking. After this, the cells were briefly centrifuged to ensure all liquid was at the bottom of the tube, and then 70ul of Tris-HCl (40mM, pH 5.5) was added to neutralise, before a 5 minute centrifuge (1000 RPM). 1.1ul of this solution was then used in the genotyping PCR reactions. The primer sequences and the size of the PCR product are shown in the Table 13. PCR products were subjected to agarose gel electrophoresis, using a gel consisting of 1.5% agarose (Sigma, Cat. A9539-500G), eith 0.5µg/ml (Sigma, Cat. E1510-10ML). The gels were imaged under UV light to test for the presence of a band at the correct size (band length shown in Table 13), using Quantam-Capt1 (Peqlab).

Gene	Forward primer (5' - 3')	Reverse primer (5' - 3')	PCR product size (bp)
TetO-Neu	GACTCTCTCTCCTGCGAA-GAATGG	CCTCACATTGCCAAAA-GACGG	630
TetO-Myc	TAGTGAACCGTCAGATCGC-CTG	TTTGATGAAG-GTCTCGTCGTCC	386
MMTV-rtTA	GTGAAGTGGGTCCGCG-TACAG	GTACTCGTCAATTC-CAAGGGCATCG	380

Table 13: Primer sequences used in mouse genotyping

4.7 Harvesting of primary mouse mammary gland cells and culturing

Female mice of the required genotype were sacrificed 8-10 weeks old, and sacrificed by cervical dislocation. The skin was cut along the front of the mouse, starting at the chin

and ending at the pubis, this was then pinned outwards, exposing the subcutaneous mammary glands. All 10 mouse mammary glands were isolated and put into a 50ml polypropylene centrifuge tube. These were then digested in 5ml of digestion media consisting of DMEM/F12 (Lonza) buffered with HEPES, and supplemented with L-glutamine (Gibco - Cat. #25030149), and 20µg/ml liberase blendzyme 2 (Roche- Cat. 05401020001) and 5ml penecillin/streptomycin (Gibco - Cat 15140-122). These were digested for 16 hours at 37°C, 5% atmospheric CO_2 with the tube cap screwed on loosely. After this digestion, 45ml of PBS was added, and centrifuged for 5 min at 1000 RPM. This formed a cell pellet, an interphase, and a top layer of fat that still contains some mammary gland cells. The interphase was aspirated away. 5ml of 0.25% trypsin (Gibco - Cat. #25200056) was added and incubated for 40 minutes at 37°C, 5% atmospheric CO_2 with the tube cap screwed on loosely. The trypsin was then inactivated with the addition of 25ml of DMEM/F12 containing 10% tetracycline-free FCS, as well as HEPES and L-glutamine (Gibco - Cat. #25030149), and 5-15 mg/ml of DNase I (ThermoFisher - Cat. EN0525) (here-on-in referred to as STOP media) to prevent cells from sticking to one another. This was then centrifuged for another 5 min at 1000 RPM, and dissociated cells were suspended in MEBM media (Lonza - Cat. CC-3151), which was supplemented with the MEGM BulletKit (Lonza - Cat. CC-3150) and plated onto collagen coated 6-well plates. 24 hours later, the media was aspirated, cells were washed with pre-warmed PBS, and cells were detached using 0.25% trypsin-EDTA until detachment. Once again, trypsin was inactivated with STOP media, and the cells were pipetted into a 15ml centrifuge tube and centrifuged at 1000 RPM for 5 minutes. Cell pellets were then quantified by counting on a hemocytometer and seeded in black-walled 96 well plates, as described in Section 4.7.3.

4.7.1 3D seeding of Cell lines

To seed cell lines in Matrigel, cells were pelleted as in Section 4.5.2.2. The pellet was then re-suspended in an appropriate amount of PBS to facilitate accurate cell counting on a hemocytometer before suspension in matrigel. For every 5µl of matrigel, 625 cells were seeded. The PBS-cell mix was further diluted or re-centrifuged to obtain a concentration of cells that could be added at 1 part PBS to 4 parts matrigel. Before mixing with matrigel, the PBS-cell mix was incubated on ice for 5 minutes. The PBS and matrigel were then mixed, with gentle pipetting as to not introduce bubbles, before pipetting. The matrigel droplets containing the cells were allowed to polymerise at room temperature for 30 minutes, before media was added, and incubation at 37°C.

4.7.2 3D seeding of primary mouse cells

Primary mouse cells were seeded in a very similar method as described above (Section 4.7.1), using the same numbers of cells and matrigel conditions, but grown in MEBM supplemented with 10% FCS. To induce the primary mouse cells into a tumourigenic state, 200ng/ml of doxycycline was added to the MEBM media after 6 days of growth in normal MEBM. Media containing doxycycline was replenished every 48 hours.

4.7.3 High-throughput seeding

To ensure accuracy and convenience, high throughput experiments that used 96 well plates were seeded using a multi-channel multi-dispenser pipette (Integra). Matrigel containing cells were prepared as described in Section 4.7.1 or 4.7.2. An extra 30-40% of Matrigel-cell mix was prepared to account for dead volume. This was pipetted into a cell culture reagent reservoir, and kept on ice in a metal 3-D printed trough that was made by the EMBL Workshop in collaboration with Slywia Gawrzak to allow stability and also keep the mix at temperatures below 4°C to prevent Matrigel polymerisation. The multi-channel multi-dispenser was then used to take up the matrigel into 8 separate pipette tips, and each was dispensed at 5µl. No more than 6 wells worth of matrigel was taken into each tip to prevent polymerisation before plating. There was also 5µl of dead volume before and after the pipetting, which allowed for accuracy and decreased the likelihood of bubbles in the matrigel. The plates were incubated for 30 minutes at room temperature before 100µl media was added and incubation at 37°C. Media was changed every 2-3 days using a manual multi-channel pipette, taking the media from the corners in order to not disturb or break the matrigel pellet containing the cells.

4.7.4 Re-seeding of cell lines for re-growth experiments

For re-seeding experiments, cells were initially seeded as above, but in 40µl droplets. Cells were grown for 7 days, with media changes every 2-3 days. Drugs were then added as above. Re-seeding took place on day 14. Media was aspirated off, and the matrigel droplets were washed with ice cold PBS, with pipetting up and down in order to homogenise the gel as much as possible. They were transferred to a 15ml centrifuge tube, which was filled up with more PBS, and then centrifuged for 5 min at 1000RPM to create a matrigel-cell pellet. The PBS was then removed, and the pellet was re-suspended in 1.5ml of 0.25% trypsin, and incubated at 37°C for 5 minutes. FCS containing media was then added to the centrifuge tube up to a volume of 10ml, and further centrifuged for 5 minutes at 1000RPM. The cell pellet was then appropriately diluted in matrigel and cell media to have a concentration of cells that was appropriate for re-seeding. Cells were reseeded by manual pipetting, as 5µl matrigel droplets

4.7.5 High throughput imaging: Olympus ScanR

96 well plates were imaged on the Olympus ScanR using the 10x lens, with Z-stack increments 100µm apart, typically taken over 21 Z-planes. The imaging chamber was kept at 37°C and 5% atmospheric CO_2 for the duration of imaging.

4.8 Transcriptomic experiments

4.8.1 RNA isolation, processing and analysis

Total RNA was isolated using the mirVana miRNA Isolation Kit, using the total RNA isolation procedure outlined in the protocol of the kit. At each time point, 400µl of lysis buffer was added to each matrigel pellet after media was removed, pipetted up and down to homogenize, and then transferred to a centrifuge tube, where it was immediately frozen at -20°C until thawing and processing with the mirVana kit. Each RNA sample was quality checked for integrity on a Bioanalyzer (Aligent Technologies) using RNA NanoChips (Aligent Technologies) before stranded mRNA sequencing on the Illumina NextSeq 500 platform. Read length was set at NextSeqHigh75 single-ended, 1-laned.

4.8.2 Transcriptomic Data analysis

Raw RNA sequencing reads were pre-processed by the EMBL Genomics Core Facility to generate BAM files and reads-to-genes tables. Briefly, the raw sequencing reads were quality checked by FastQC version 0.11.3, processed using CutAdapt (version 1.9.1) to remove adapter sequences, followed by quality trimming and filtering with FaQCs version 1.34 (Code parameters: -q, -minL = 25, -n=5, -discard=1). Reads were then alighted to a human reference genome (hs hg38) using Tophat2 version 2.0.10. Differential expression analysis only used reads with unique mappings (not that appeared in multiple genomic positions), and HTSeq was used to obtain reads-to-genes tables. The "R" package DESeq2 (version 3.13) was used to perform differential analysis on these reads-to-genes tables. The workflow, including time course designed workflow, outlined by Love *et al.* (2019)[276] was used to perform the analysis. Data were normalised using a variance stabilising transformation (VST) the first two surrogate variables were removed using the "R" package "sva". The "R" package "PathfindR" was used to generate significantly altered GO-terms, using the "GO-All" database using the Bonferroni method. P-value thresholds were set as 0.01. Hierarchical clustering was performed using the default parameters; 1-$\varkappa$ was used as the distance metric.

4.8.3 Image fusion and deconvolution

All images were fused and deconvolved with Huygens Professional version 19.04 (Scientific Volume Imaging, The Netherlands, http://svi.nl). Deconvolution parameters were set as the following: Maximum iterations - 40; Signal to noise ratio - 20; Quality threshold-0.1; Iteration mode - Optimised, Brick layout - Auto; Area radius (micron) - 0.7; Estimation mode - Lowest; Numerical apeture - 0.300, Excitation wavelength (nm) - 488, Emission wavelength (nm) - 520; X and Y voxel size (nm) - 358; Z voxel size (nm)- 1000; Multiphoton excitation - 1. Images were output as an Imaris File format, and were converted to TIFF files using ImageJ, which were then visualised using orthagonal viewing. The 3D visualisation that features in Figure 41(b) was visualised by Marco Lampe using Huygens.

4.9 Inhibitors: lapatinib, EMBL-703625 and Oxamate

Lapatinib was acquired from Selleckchem (Cat #S2111) as 10mM DMSO solution, and stored at 20µl aliquots at -80°C. EMBL-703625 was prepared by the EMBL-CBCF and stored as 20µl aliquots of 100mM stock solution at -20°C. Sodium oxamate was acquired from Sigma-Aldrich and stored as powder form at room temperature.

4.10 Analysis and integration of GCMS, LCMS and transcriptomic data

LRPath was used to perform a metabolic pathway enrichment analysis against metabolism-focused databases: EHMN, KEGG and Reactome. This LRPath output was then inputted into MetScape, a cytoscape plug-in designed for visualisation and analysis of metabolomic data. Gene filtering was applied at the Metscape level at cut-off values of a log(2) fold change of at least 1.5, and a p-value of 0.05. To integrate the metabolomic data, the data from the GCMS and LCMS analysis were combined by using Fisher's method to obtain a combined p-value and a median log(2) fold change for each cellular state (tumor and residual) and used for down-stream analysis. The complete dataset for GCMS was used, along with significant values from the higher throughput LCMS data. Metscape was then used to integrate the transcriptomic and metabolomic data. jActiveModules, another cytoscape plug-in that generates expression activated sub-networks was used to sub-set this data, using a simulated annealing algorithm with the following parameters: 2500 to 10000 iterations tested, start temp 1, end temp 0.01, quenching and hubfinding, non-random starting graph seed 1623495108.

Chapter 5

Supplementary Figures

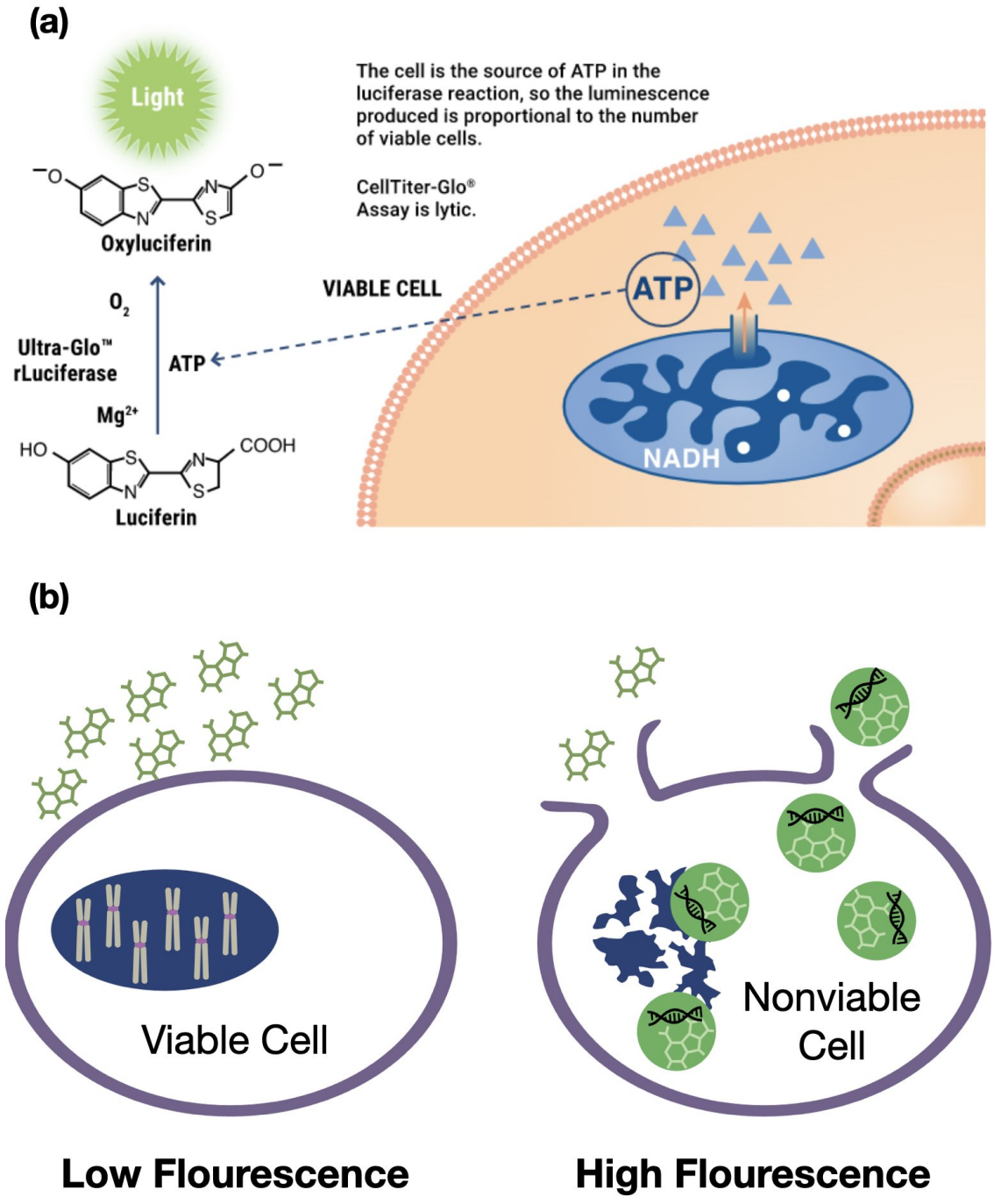

Figure S.1: The CellTiter Glo (a) and CellTox Green Cytotoxicity (b) Assays

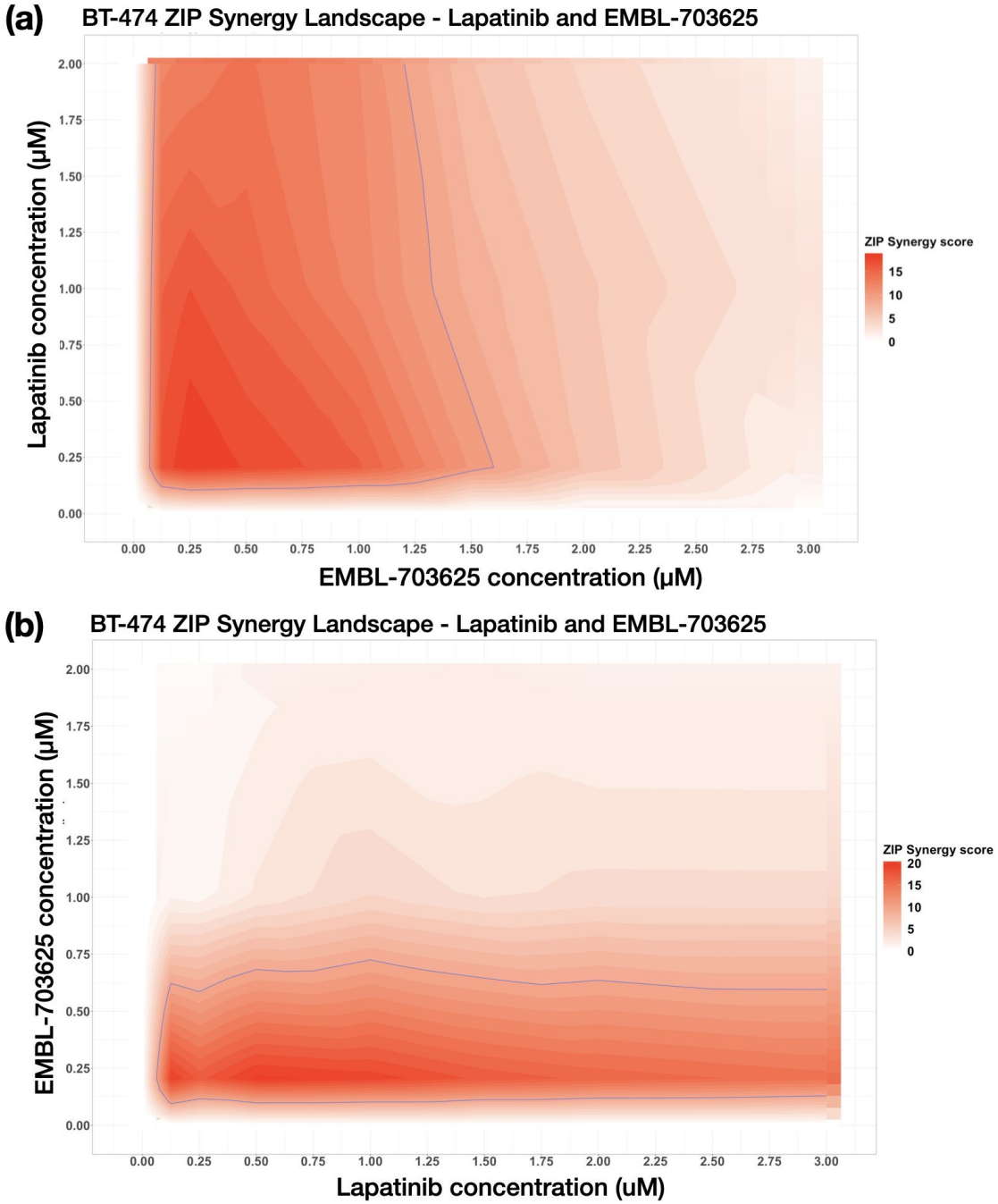

Figure S.2: Supplementary figure continued on next page

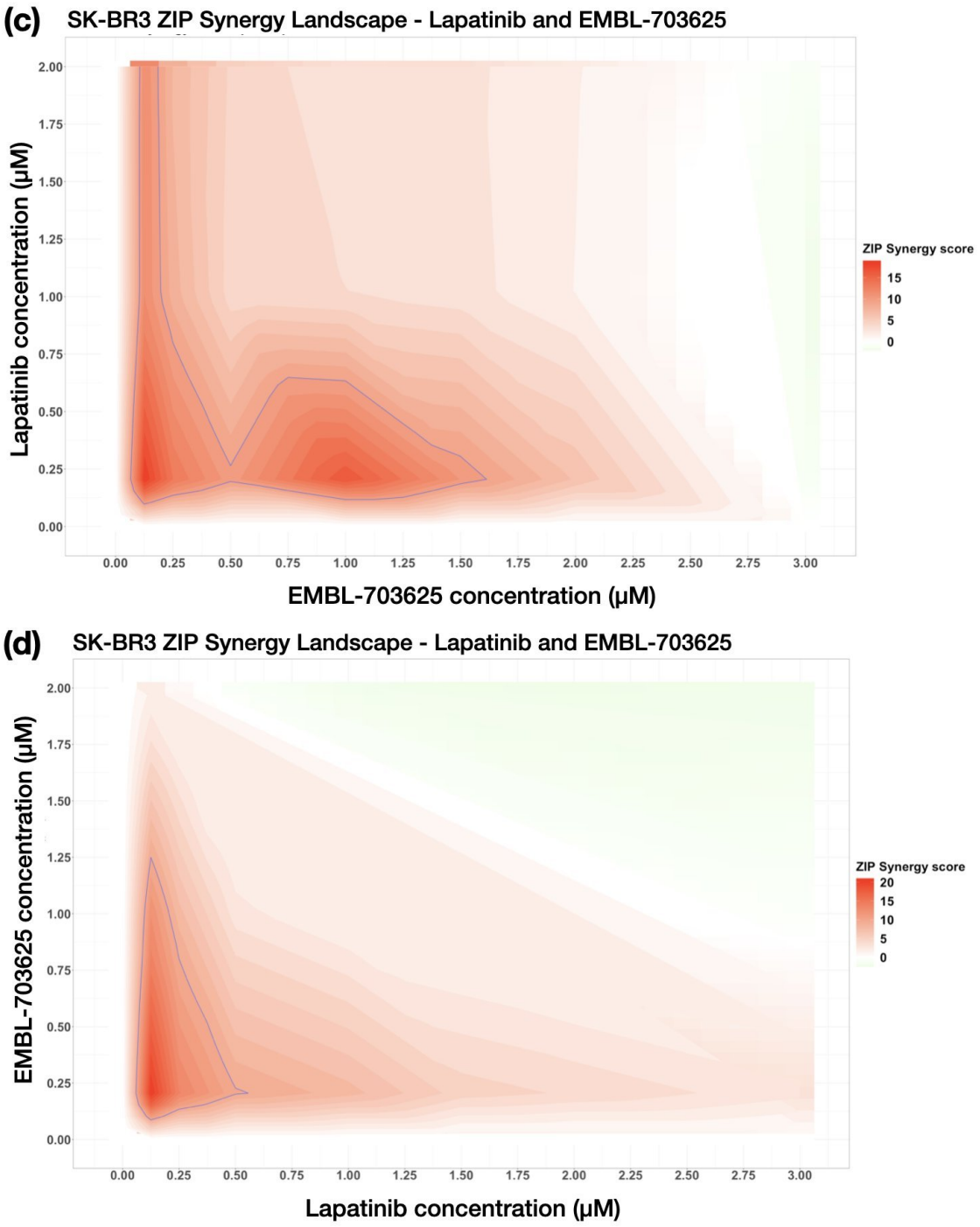

Figure S.2: **Non-interpolated ZIP synergy landscapes for BT-474 or SK-BR3 cells treated with lapatinib and EMBL-703625**

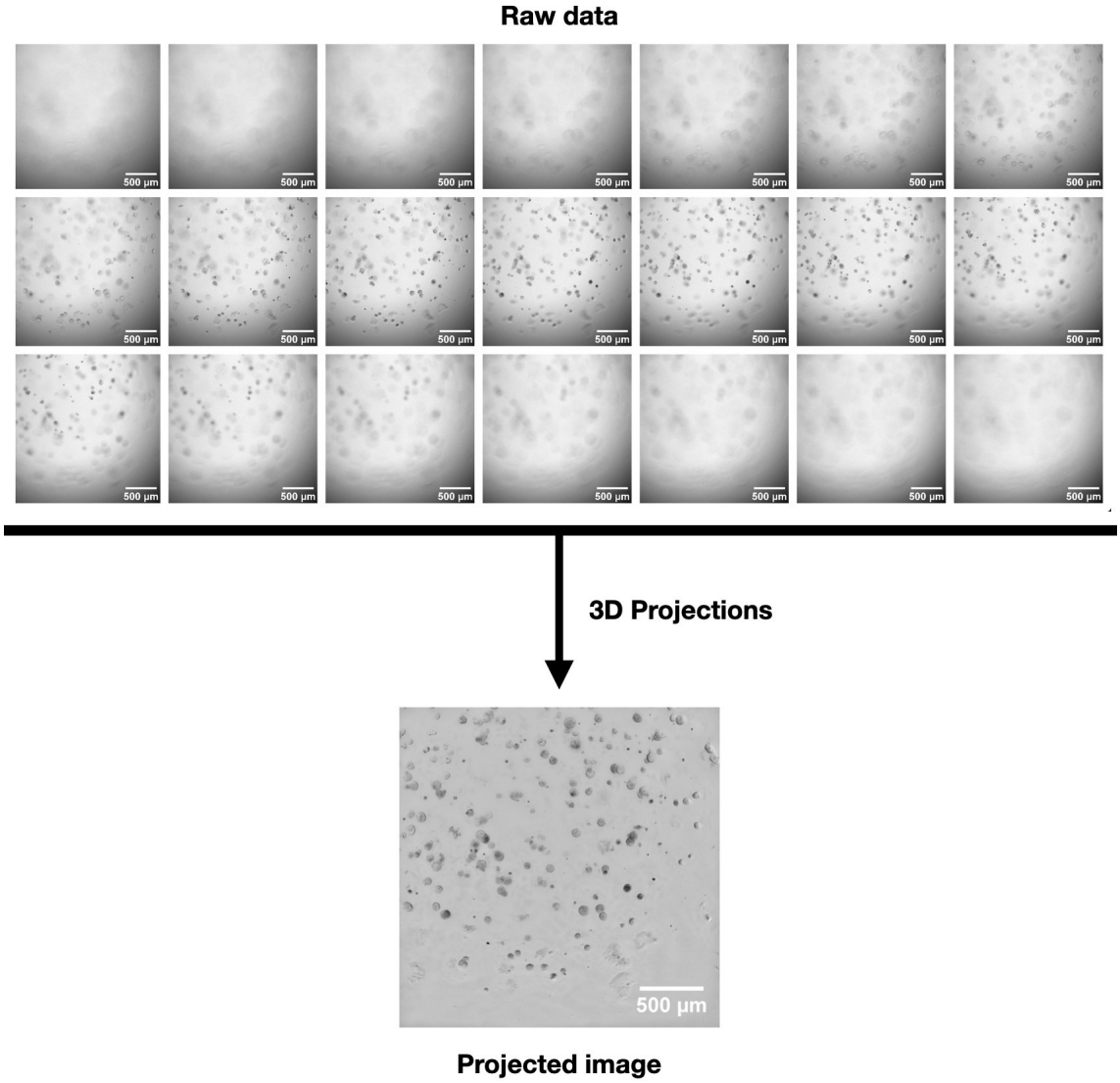

Figure S.3: **3D Image projection pipeline for high-throughput ScanR data.** Transmission images of BT-474 cells grown for 7 days in normal growth conditions are shown. Each Z-stack is taken 100µm apart and combined using extended depth of field projections. This pipeline was developed by Sylwia Gawrzak in collaboration with the EMBL ALMF. The ImageJ macro was produced by Anna Lladó and Sébastian Tosi (IRB Barcelona). All scale bars = 500µm

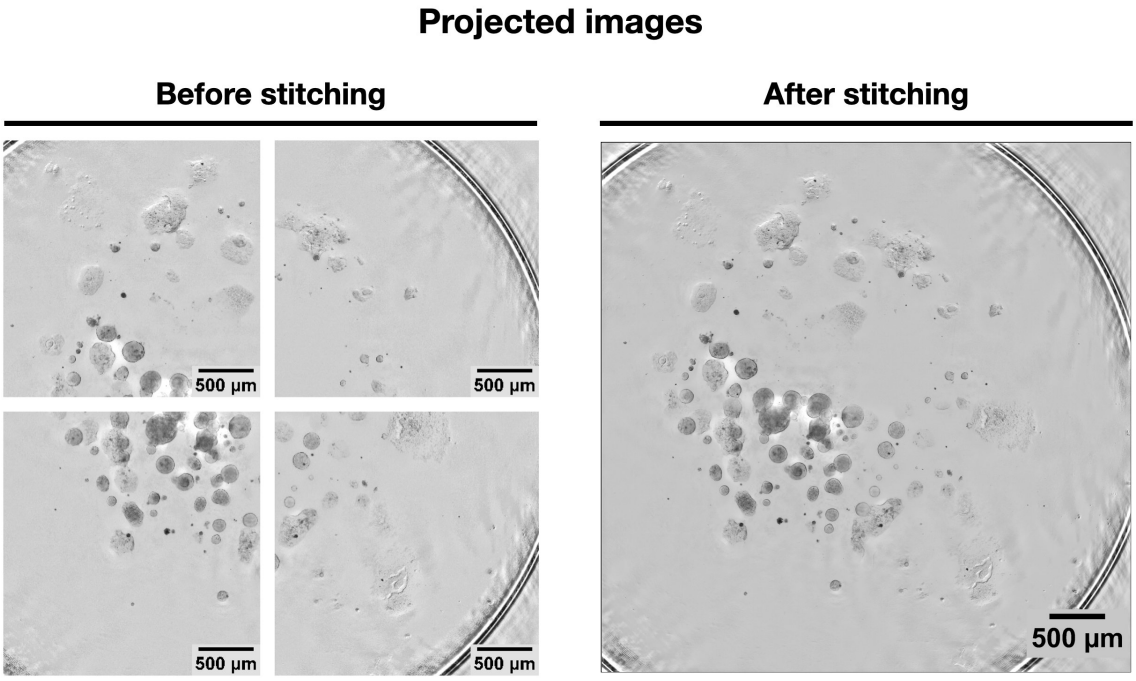

Figure S.4: **Stitching of projected images to obtain a whole-well overview of a 96-well plate.** Projected images (see Figure S.3) were stitched together to allow a single image overview from a well of a 96-well plate, allowing a more convenient and comprehensive overview of how cells have re-grown over time. This pipeline was developed by Sylwia Gawrzak in collaboration with the EMBL ALMF. The ImageJ macro was produced by Anna Lladó and Sébastian Tosi (IRB Barcelona). All scale bars = 500µm

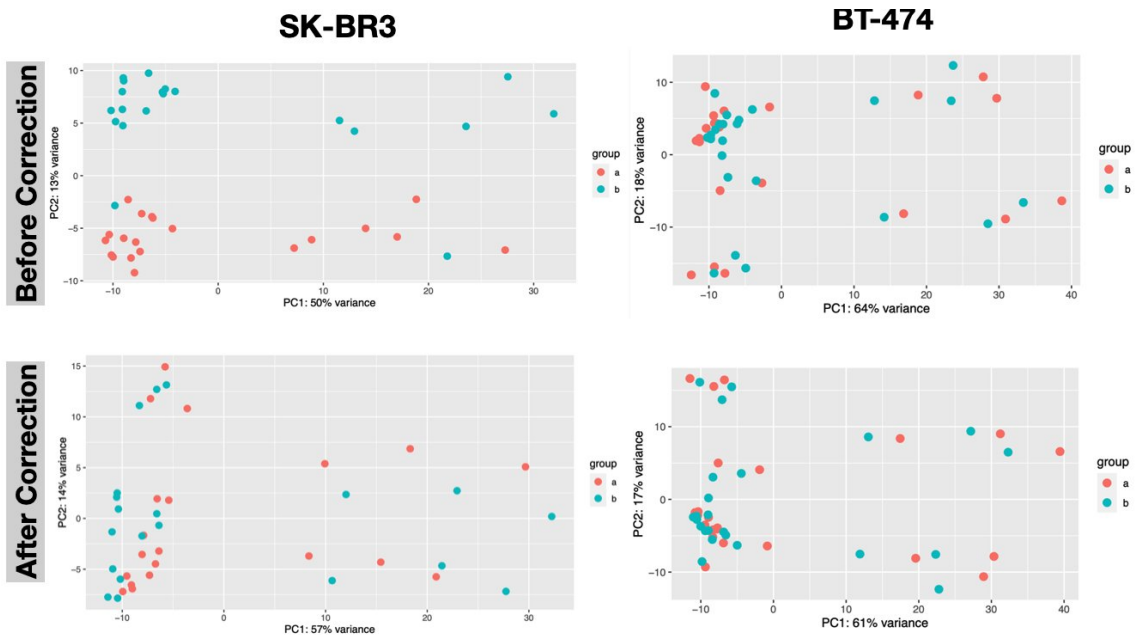

Figure S.5: **Batch correction of transcriptomic data using limma to correct for variance between technical replicates before subsequent analysis.** Group a and b refer to each experimental replicate.

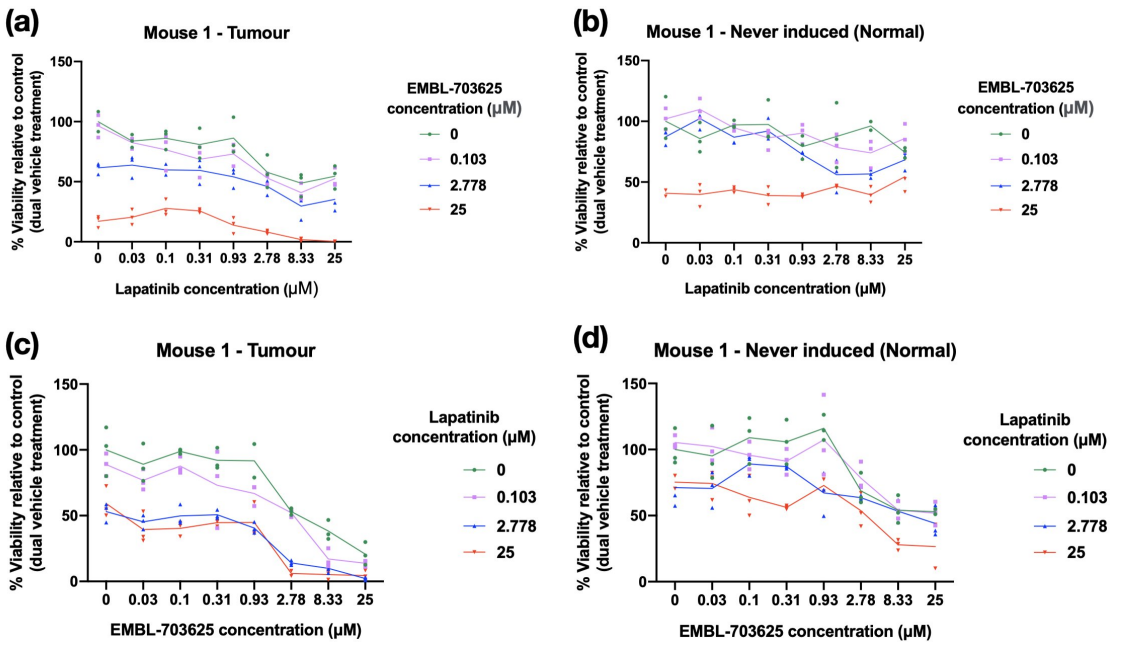

Figure S.6: Individual effects on cell viability of lapatinib and EMBL-703625 treatment, at different concentrations, for mouse 1. Dots represent technical replicates, the line passes through the mean at each point

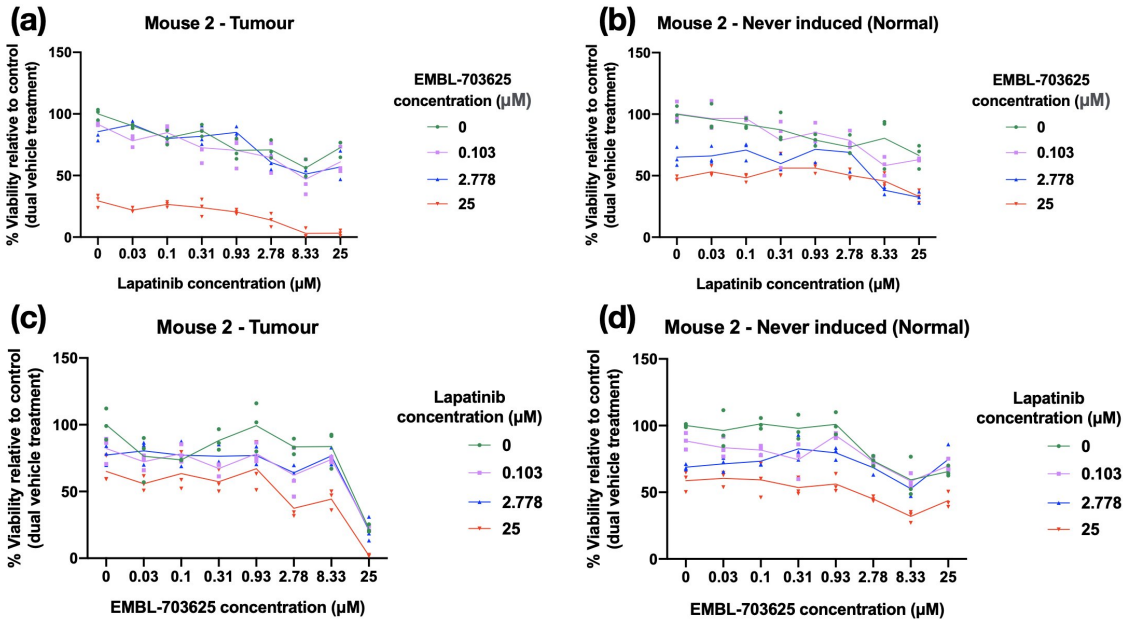

Figure S.7: Individual effects on cell viability of lapatinib and EMBL-703625 treatment, at different concentrations, for mouse 2. Dots represent technical replicates, the line passes through the mean at each point

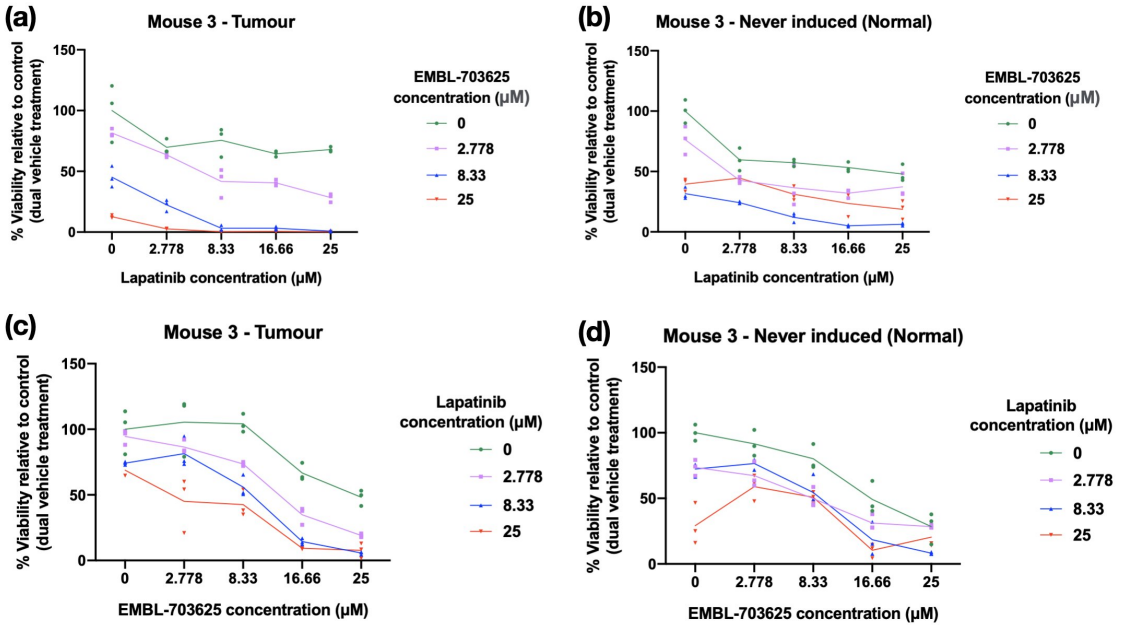

Figure S.8: Individual effects on cell viability of lapatinib and EMBL-703625 treatment, at different concentrations, for mouse 3. Dots represent technical replicates, the line passes through the mean at each point

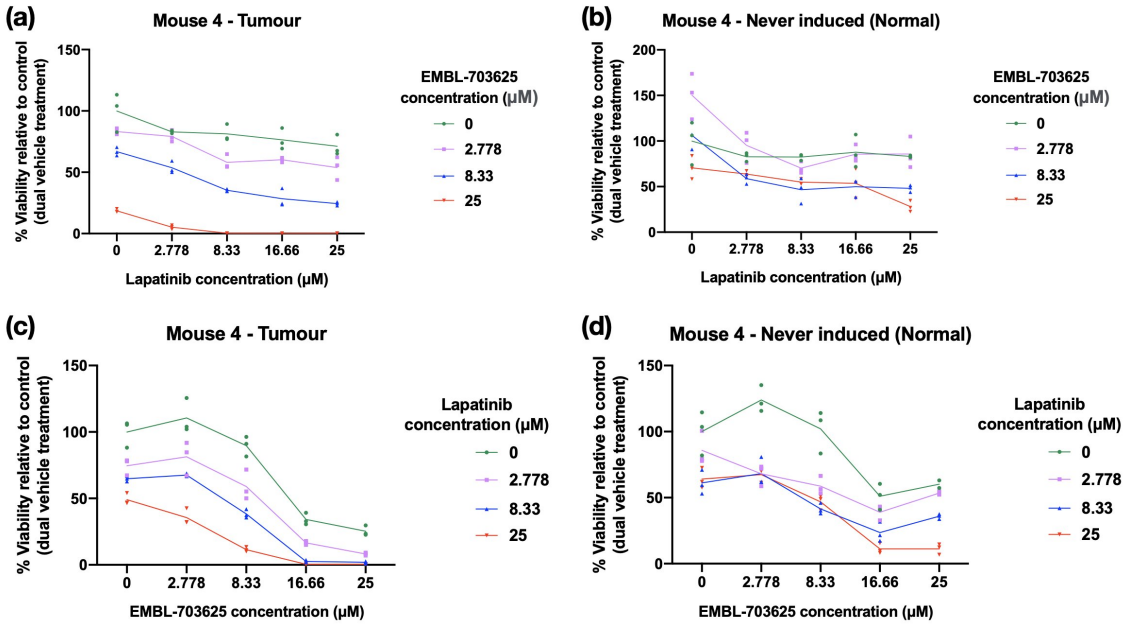

Figure S.9: Individual effects on cell viability of lapatinib and EMBL-703625 treatment, at different concentrations, for mouse 4. Dots represent technical replicates, the line passes through the mean at each point

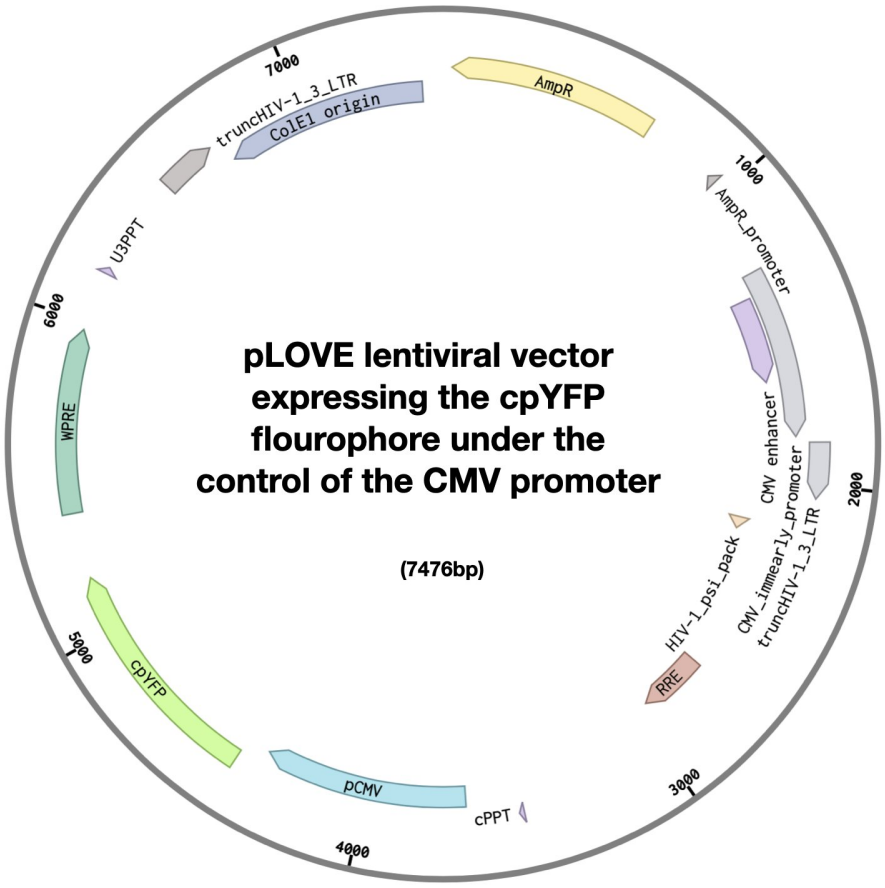

Figure S.10: pLOVE lentiviral vector containing cpYFP under the control of the CMV promoter

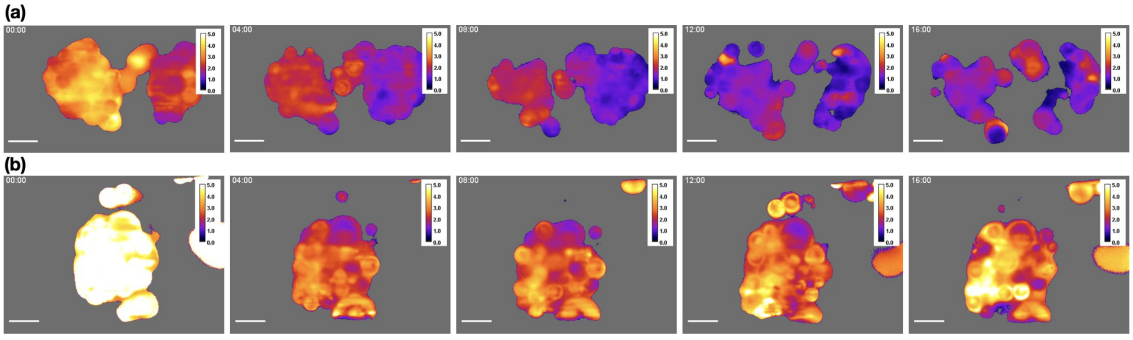

Figure S.11: **SK-BR3 expressing SoNar or cpYFP treated with 1.3µM** lapatinib.

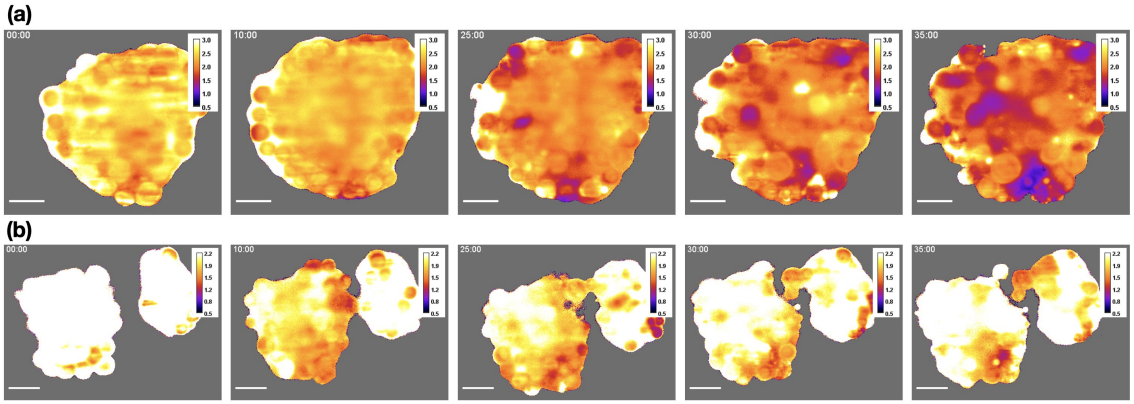

Figure S.12: **SK-BR3 expressing SoNar or cpYFP treated with 1µM EMBL-703625 and 0.2µM lapatinib**

Table 14 BT-474 - Lapatinib monotherapy: Hierarchical clustering

ID	Term_Description	Fold_Enrichment	Support	Adj p value	Up_regulated	Down_regulated	Cluster	Status
GO:0004672	protein kinase activity	1.762	0.032	1.910E-11	MAP3K3, PDK2, MAP2K5, DYRK1B, RPS6KA5, TESK2, MAP4K1, SGK3, HSPB8, PINK1	AKT1, MAP3K5, PRKAA2, SRPK1, MAP3K14, TNIK, MMD, TRIB2	1	Representative
GO:0004674	protein serine/threonine kinase activity	1.346	0.032	4.492E-10	PIM1, MAP3K12, ULK1, STK19, RPS6KA5, TESK2, MAP4K1, PINK1	AKT1, PLK3, LIMK1, MAP3K5, MAP3K9, PRKAA2, SRPK1, MAPKAPK3, RPS6KA4, MAP3K14, PLK2, NEK6, TNIK, STK39	1	Member
GO:0005524	ATP binding	1.436	0.043	1.303E-05	INSR, PDK2, PIM1, TAP1, RPS6KA5, CLPX, CLP1, MAP4K1, PINK1	ACLY, AKT1, CDK6, HSPA8, MAP3K5, NME1, NVL, OAS3, SRPK1, TDG, RPS6KA4, NEK6, FICD	1	Member
GO:0016301	kinase activity	1.939	0.032	1.045E-03	PIK3C3, ULK1, PINK1	AKT1, MAP3K14, STK39, TRIB3	1	Member
GO:0004842	ubiquitin-protein transferase activity	1.103	0.011	2.211E-11	TRIM23, SIAH2, TRIM21, KLHL21, RNF13, TRIM2, RNF135	BIRC3, BARD1, TRAF3, DTX4, KLHL42, TRIM47	2	Representative
GO:0061630	ubiquitin protein ligase activity	0.644	0.005	1.101E-02	SIAH2, RNF125, RNF122, RNF135, TRIM52		2	Member
GO:0008013	beta-catenin binding	1.780	0.022	1.676E-08	FOXO3, SMAD7, FOXO4, CALCOCO1	PXN, VCL, GSKIP, AMER1	3	Representative
GO:0051018	protein kinase A binding	3.671	0.005	1.013E-02	WASF1, AKAP10	EZR, AKAP5, GSKIP	3	Member
GO:0003779	actin binding	1.455	0.005	3.076E-02	GSN, AVIL, SYNE1, SCIN	ALDOA, CEACAM1, TPM1, VCL, EZR, MICAL2, CORO1A	3	Member
GO:0045296	cadherin binding	1.049	0.005	4.483E-02	NDRG1	VCL	3	Member
GO:0031625	ubiquitin protein ligase binding	1.782	0.177	1.941E-08	CAMLG, CLU, ERBB3, JAK1, SMAD7, ATXN3, SPOP, BCL10, TXNIP, DDX58, GABARAPL1, ANKRA2, MOAP1, PINK1	ACTG1, HSPA8, PA2G4, TRAF3, VCL, FZD4, FZD6, MFHAS1, TRAF4, TUBA1B, NEK6, TRIB2, TRIB3, UBE2J2, TUBB	4	Representative
GO:0031996	thioesterase binding	2.670	0.005	5.571E-04		TRAF3, TRAF4	4	Member
GO:0050699	WW domain binding	3.092	0.005	4.241E-03	CDC25C, SCNN1G, WBP1	TRAF4	4	Member
GO:0003713	transcription coactivator activity	1.541	0.016	4.064E-08	HMGB2, PRMT2, SMARCA2, BCL10, DYRK1B, CITED2, WBP2, WWTR1, NUPR1, ING4, CALCOCO1, JMY	PER2, SRA1, TCERG1, RRP1B, JMJD6	5	Representative
GO:0030331	estrogen receptor binding	2.025	0.005	4.677E-02	PRMT2, WBP2	NKX3-1, PPARGC1B	5	Member
GO:0008134	transcription factor binding	1.708	0.091	1.061E-07	HMGB2, FOXO4, PIM1, TFDP2, THRA, TWIST1, BCL10, HDAC5, RBFOX2, BCAS3	CCND1, BCL3, E2F4, FHL2, GATA2, GTF2A2, NKX3-1, PIK3R1, PPARG, MAPK9, LMO4, TNFRSF10A, HDAC4, PDCD11, TRIB2	6	Representative
GO:0000976	transcription regulatory region sequence-specific DNA binding	1.836	0.043	2.950E-06	ATF6B, ERBB4, FOXO3, HMGB2, SMAD7, SMARCA2, THRA, HDAC5, HINFP, ZBTB20, SOX6, CALCOCO1, FOXK1	EGR1, ETV5, NKX3-1, PPARG, SOX11, PER2, HDAC4, SOX18, SUV39H2, GLIS2	6	Member
GO:0000978	RNA polymerase II proximal promoter sequence-specific DNA binding	1.367	0.022	1.093E-04	CHD2, ATF6B, ELF1, FOXO3, HOXC4, TBX2, TGIF1, KLF7, HDAC5, PRDM4, KLF8, WBP2, EHF, CALCOCO1	E2F4, ELK3, ETS2, ETV1, ETV4, MYCN, NKX3-1, SOX11, FOSL1, ONECUT2, CLOCK, HDAC4, SOX18	6	Member
GO:0043565	sequence-specific DNA binding	1.561	0.016	3.639E-04	FOXO3, IRF6, FOXO4, TBX2, ZNF224, HOXB13, HEY2, CALCOCO1, FOXP2	CBFB, E2F3, EGR1, HNRNPAB, HOXA13, NKX3-1, PPARG, ZNF35, CLOCK, HDAC4, MAFF, GRHL3, PBX4	6	Member
GO:0001228	DNA-binding transcription activator activity, RNA polymerase II-specific	1.878	0.022	6.998E-04	ATF6B, DBP, ELF1, FOXO3, FOSL2, GTF2I, HOXC4, IRF2, FOXO4, RXRB, STAT6, TFDP2, KLF7, PRDM4, HINFP, EHF, CREBRF	E2F3, E2F4, EGR1, ELK3, ETV1, ETV4, ETV5, MYCN, SOX11, ONECUT2, CLOCK, MAFF, SOX18, GRHL3, GLIS2, MACC1	6	Member
GO:0042826	histone deacetylase binding	1.285	0.005	1.035E-03	CIR1, HDAC5, HEY2, ANKRA2	CCND1, NKX3-1, HDAC4	6	Member
GO:0000977	RNA polymerase II regulatory region sequence-specific DNA binding	1.748	0.005	1.337E-03	DBP, FOSL2, IRF2, MXI1, RXRB, SATB1, STAT6, TFDP2, HINFP, CREBRF	E2F3, EGR1, ETV5, LMX1B, MACC1	6	Member
GO:0001227	DNA-binding transcription repressor activity, RNA polymerase II-specific	1.546	0.011	1.394E-03	FOXO3, MXI1, NFATC4, SATB1, TBX2, TGIF1, ZNF224, HOXB13, KLF8, HEY2, ZNF350, FOXK1	ELK3, ETS2, BHLHE40, CHCHD3	6	Member
GO:0000981	DNA-binding transcription factor activity, RNA polymerase II-specific	1.708	0.005	4.528E-02	SP100, TWIST1, KLF7, HEY2	GATA2, LMX1B, BHLHE40, CLOCK, KLF2, FOXO6	6	Member
GO:0051087	chaperone binding	2.512	0.086	1.122E-06	CLU, GRN, TSC1, DNAJB4, GET4, FNIP1	CDC25A, HSPA8, DNAJB1, UBL4A, FICD, DNAJB5, SACS	7	Representative
GO:0051082	unfolded protein binding	1.708	0.038	2.192E-04	CLU	HSPA2, HSPA8, DNAJB1, GRPEL1	7	Member
GO:0051117	ATPase binding	1.534	0.011	8.827E-03	ATXN3, BBC3, SNX10, SLC2A13	DNAJB1, EZR, METTL21A	7	Member
GO:0030544	Hsp70 protein binding	3.147	0.011	3.416E-02	TSC1	DNAJB1, FICD, SACS, DNAJC2, METTL21A	7	Member
GO:0031072	heat shock protein binding	1.546	0.005	4.584E-02	TPR	HSPA8, LIMK1, METTL21A	7	Member

Table 14 continued: BT-474 - Lapatinib monotherapy

ID	Term_Description	Fold_Enrichment	Support	Adj p value	Up_regulated	Down_regulated	Cluster	Status
GO:0004843	thiol-dependent ubiquitin-specific protease activity	1.566	0.011	4.260E-05	ATXN3, USP19, OTUD5, VCPIP1, OTUD1	USP18, UCHL5, USP38	8	Representative
GO:0061578	Lys63-specific deubiquitinase activity	4.005	0.005	8.801E-03	ATXN3, OTUD5	STAMBPL1	8	Member
GO:0070628	proteasome binding	2.937	0.005	4.395E-02		SACS, UCHL5	8	Member
GO:0004713	protein tyrosine kinase activity	1.658	0.038	4.713E-05	ERBB3, ERBB4, IGF1R, INSR, JAK1	RET, SRMS	9	Representative
GO:0004714	transmembrane receptor protein tyrosine kinase activity	2.937	0.016	1.305E-03	ERBB4	EPHA2, RET	9	Member
GO:0005154	epidermal growth factor receptor binding	3.496	0.005	2.281E-02	EGF, ERBB4, FAM83B	AGR2, EPGN	9	Member
GO:0003714	transcription corepressor activity	2.190	0.027	6.126E-05	EZH1, SIAH2, SAP30, CIR1, CITED2, RBFOX2	CCND1, CBFA2T3, FHL2, DNAJB1, RBBP8, NR0B2, LIMD1, TCERG1, LMCD1, WNT4, TRIB3	10	Representative
GO:0001103	RNA polymerase II repressing transcription factor binding	2.554	0.005	6.306E-03	BBS2, BBS4	RBBP8, TCERG1	10	Member
GO:0019903	protein phosphatase binding	2.068	0.022	9.368E-05	CDKN1B, JAK1, STAT6, KIFAP3	CEACAM1, MAP3K5, PIK3R1, PXN, TRAF3, ANAPC7	11	Representative
GO:0030332	cyclin binding	1.088	0.016	3.553E-03	CDKN1B	CDK6	11	Member
GO:0004861	cyclin-dependent protein serine/threonine kinase inhibitor activity	1.468	0.005	4.121E-02	CDKN1B		11	Member
GO:0003684	damaged DNA binding	2.368	0.016	1.034E-04	HMGB2, CUL4B	RBBP8, TDG, AUNIP	12	Representative
GO:0008144	drug binding	1.433	0.005	9.004E-03	HMGB2	MT2A, PNP, PPARG	12	Member
GO:0003690	double-stranded DNA binding	1.108	0.005	1.092E-02	HMGB2, SATB1	PPARG, TDG	12	Member
GO:0043621	protein self-association	2.570	0.005	2.802E-02	AGXT, BCL10, FOXP1	NKX3-1, PPARG, TDG, FHOD1	12	Member
GO:0004879	nuclear receptor activity	2.719	0.005	3.841E-02	RXRB, THRA	NKX3-1, PPARG, VDR	12	Member
GO:0046965	retinoid X receptor binding	2.937	0.016	4.677E-02		PPARG, VDR	12	Member
GO:0019904	protein domain specific binding	2.514	0.027	1.630E-04	CAPG, GUSB, INSR, KCNN2, NUMA1, RAB27B, SP100, TFDP2, THRA, CITED2, VPS11, CHMP1B, CNTROB	E2F4, ETS2, KPNB1, MAP3K5, PLAUR, SRSF7, EZR, NR0B2, BHLHE40, RAPGEF3, PLXND1, FHOD1	13	Representative
GO:1990841	promoter-specific chromatin binding	1.224	0.005	1.246E-02	RBL2	E2F4, EGR1	13	Member
GO:0019843	rRNA binding	3.671	0.005	1.571E-03		DDX21, FASTKD2, NGRN	14	Representative
GO:0030515	snoRNA binding	4.895	0.005	3.669E-02		NOP14, DDX21, NOP56, NUDT5	14	Member
GO:0005198	structural molecule activity	1.708	0.065	1.732E-03	NUMA1	ASPH, TUBA1B, TUBA1C, TUBB	15	Representative
GO:0008022	protein C-terminus binding	1.345	0.005	1.826E-03	FOXN3, NUMA1, PEX12, BCL10, MAGI1, VPS4B, OPTN, CALCOCO1	HRAS, PPARG, FBLN5, CORO1A	15	Member
GO:0097718	disordered domain specific binding	1.915	0.005	1.611E-02	NUMA1	HSPA2, PPIL1	15	Member
GO:0043022	ribosome binding	2.937	0.011	2.875E-03		EIF2S1, SRP72, NAA10, GEMIN5, NAA15	16	Representative
GO:0003743	translation initiation factor activity	2.719	0.005	4.747E-02	EIF2D, EIF3F	EIF2S1, EIF4G2, EIF2B3	16	Member
GO:0005159	insulin-like growth factor receptor binding	6.119	0.005	3.858E-03	IGF1, INSR, SOCS2	PIK3R1, YWHAG	17	Representative
GO:0005080	protein kinase C binding	1.224	0.005	1.358E-02	HDAC5	PKP2, YWHAG	17	Member
GO:0060090	molecular adaptor activity	1.984	0.005	2.902E-02	AKAP9, ISCU	PKP2, PSMG1, CHCHD3	17	Member
GO:0005085	guanyl-nucleotide exchange factor activity	2.098	0.005	4.204E-03	SOS1, VAV3, ARFGEF1, TIAM2, FGD3, FNIP1	EIF2B3, RAPGEF3, DOCK5, MON1A, FGD5	18	Representative
GO:0005096	GTPase activator activity	2.021	0.011	1.662E-02	SOS1, RABGAP1L, VAV3, ARFGEF1, TBC1D15, ARAP1	RAP1GAP, RGS3, RGS16, CDC42EP2, TBC1D30, ERRFI1, RALGAPA2, SGSM1, ARHGAP27	18	Member
GO:0050431	transforming growth factor beta binding	5.140	0.005	4.134E-02	LTBP1, TWSG1, WFIKKN1, CD109	TGFB3, HYAL2, VASN	19	Representative
GO:0004708	MAP kinase kinase activity	1.468	0.005	4.677E-02		MAPKAPK3	20	Representative

Table 14 continued: BT-474 - Lapatinib monotherapy

ID	Term_Description	Fold_Enrichment	Support	Adj p value	Up_regulated	Down_regulated	Cluster	Status

Table 14: De-regulated genes and networks (see section 2.2 for details on how significance was calculated) in BT-474 cells treated with 1µM lapatinib.

Table 15 BT-474 - EMBL-703625 monotherapy: Hierarchial clustering

ID	Term Description	Fold Enrichment	support	Adj p-value	Up regulated	Down regulated	Cluster	Status
GO:0005516	calmodulin binding	2.169	0.013	1.04E-10	VAMP2, TRPV6	CEACAM1, MBP, MYO9B, PPP3CB, TRPV1, CAMKK2, UNC13A, PLCB1, IQCG	1	Representative
GO:0035091	phosphatidylinositol binding	2.232	0.020	3.45E-02	ITPR1, SNX5, SNX12	HIP1, MAPT, PITPNA, TRPV1, MCF2L	1	Member
GO:0031625	ubiquitin protein ligase binding	1.292	0.288	1.54E-10	ARRB2, ATP6V0C, BAG1, CDKN1A, GPR37, PCBP2, PML, POLR2A, VCP, CXCR4, FZD5, BCL10, CASC3, FBXW7, OTUB1, RNF20	BRCA1, CASP8, EGFR, PRKACB, RB1, TP53, IKBKE, TANK, ERLIN2, NLK, DET1	2	Representative
GO:0051087	chaperone binding	1.354	0.052	2.20E-07	DNAJB9, SOD1, BAG3	MAPT, TBCE, TP53, BAG2, TIMM9, RNF207	2	Member
GO:0002020	protease binding	1.271	0.020	6.29E-04	TNFAIP3, BCL10, RNF139	BRCA2, TP53, FADD, PYCARD, LONP2, THAP5	2	Member
GO:0043621	protein self-association	2.859	0.039	1.10E-03	DYRK1A, SLC2A1, VAMP2, TNFAIP3, BCL10, KCTD9, ZFYVE27	ADAM8, TP53, RNF112	2	Member
GO:0019903	protein phosphatase binding	1.289	0.059	1.19E-03	LGALS3, VCP, MTMR9	CEACAM1, EGFR, MET, TP53, IKBKE	2	Member
GO:1990841	promoter-specific chromatin binding	1.588	0.059	2.29E-03	PRDM1, HNRNPU, POLR2A, KLF4	TP53	2	Member
GO:0097718	disordered domain specific binding	0.995	0.007	8.74E-03		RB1, TP53	2	Member
GO:0035035	histone acetyltransferase binding	1.806	0.007	3.31E-02	EPAS1, ECD	TP53	2	Member
GO:0001085	RNA polymerase II transcription factor binding	1.173	0.007	3.40E-02	PITX1, KLF4	HCLS1, TP53	2	Member
GO:0004402	histone acetyltransferase activity	3.812	0.046	6.15E-10	TAF9, SRCAP, KAT7, TAF5L, ING3	BRCA2, TADA2A, TAF10, TAF12, KAT8	3	Representative
GO:0003713	transcription coactivator activity	1.130	0.013	2.95E-03	TAF9, TAF11, BCL10, AIP, MED21, MED6, SRCAP, TAF5L, HCFC2, RNF20, TADA1	BRCA1, TAF12, RUVBL1, TRIP11, HTATIP2	3	Member
GO:0070063	RNA polymerase binding	2.859	0.020	3.06E-03	ANP32B, PHRF1	BRCA1, TAF10	3	Member
GO:0016251	RNA polymerase II general transcription initiation factor activity	2.745	0.007	1.43E-02	GTF2E2	GTF2E1, GTF2H3, TAF10, TAF12, SNAPC5	3	Member
GO:0004843	thiol-dependent ubiquitin-specific protease activity	1.830	0.020	1.07E-08	TNFAIP3, USP4, OTUD3, OTUD6B, OTUB1, USP35, USP36, ZC3H12A, OTULIN	TANK, USP30, USP51	4	Representative
GO:0003682	chromatin binding	1.557	0.078	1.40E-06	BCL6, HNRNPU, BRD2, ATF5, PELP1, GMNN, SIRT7, ZC3H12A, PWWP2A	EGFR, MLH1, SMARCE1, TFAP2A, TP53, MORC2, POLR1A, NUCKS1, NKAP, ZKSCAN3, GLYR1, USP51, ZNF431, PRIMPOL	4	Member
GO:0042393	histone binding	1.654	0.007	2.49E-02	ANP32B, COPRS, RNF20, PWWP2A, UHRF2	MLLT6, PRMT6, SAP30L, PARP9, GLYR1, DTX3L, USP51	4	Member
GO:0000976	transcription regulatory region sequence-specific DNA binding	1.119	0.052	5.06E-08	ATF3, FOS, NFE2L2, NFYC, SOX4, TAF9, TCF7L2, KLF4, NR1D1, ATF5	BRCA1, MEN1, TAF2, TFAP2A, TP53, NR1H3, ZNF658, GABPB2	5	Representative
GO:0000978	RNA polymerase II proximal promoter sequence-specific DNA binding	0.986	0.020	1.14E-05	PRDM1, KLF5, KLF6, ETS2, HNRNPU, IRF7, MXD1, MTF1, NFYC, SOX4, TCF7L2, NR1D1, NKRF, ZGPAT	ESR2, ESRRB, MYBL1, TFAP2A, TP53, IRF9, TCFL5, BHLHE41, ZKSCAN3, NLRC5, ZNF431	5	Member
GO:0008134	transcription factor binding	1.489	0.052	1.14E-05	EPAS1, FOS, IGHMBP2, PIM1, TCF7L2, TLE1, BCL10, AIP, MAFB, MED6, PELP1, CXXC5, HDAC8	E2F5, ESRRB, PURA, PURB, RB1, TAF12, TP53, ATG7, ATF7, IRF2BP1, NLK, NUCKS1, HDAC11, KAT8, METTL23	5	Member
GO:0043565	sequence-specific DNA binding	1.160	0.007	1.33E-04	BCL6, EGR4, EPAS1, NFE2L2, POLRMT, TCF7L2, USF1, MAFB, ATF5, CXXC5, ZGPAT, OSR2, YY2	ESRRB, MAPT, TFAP2A, ZNF76, SPDEF, ZBTB4, ZKSCAN3, ZC3H8	5	Member
GO:0001228	DNA-binding transcription activator activity, RNA polymerase II-specific	0.842	0.020	7.00E-04	ATF3, KLF5, CDC5L, KLF6, EGR4, MTF1, NR4A2, SOX4, BARX2, KLF4, ATF5, NKRF, YY2	ESRRB, MYBL1, TFAP2A, TP53, ZNF76, ZNF175	5	Member
GO:0001102	RNA polymerase II activating transcription factor binding	1.173	0.007	3.40E-02	FOS, NFE2L2	IFI27, BHLHE41	5	Member
GO:0004842	ubiquitin-protein transferase activity	1.521	0.072	2.64E-05	TNFAIP3, UBE2D2, RNF139, RNF115, MYLIP, UBE2R2, CHFR, RNF20, ZNRF1, UHRF2, ZNF738	XIAP, BRCA1, DZIP3, FBXW2, FBXW8, FBXO4, UBE2D4, TRIM56, RNF135, TRIM69, DTX3L, NHLRC1	6	Representative

Table 15 continued: BT-474 - EMBL-703625 monotherapy

ID	Term Description	Fold Enrichment	support	Adj p-value	Up regulated	Down regulated	Cluster	Status
GO:0061631	ubiquitin conjugating enzyme activity	1.634	0.013	4.43E-03	UBE2D2, UBE2R2	UBE2D4	6	Member
GO:0061630	ubiquitin protein ligase activity	1.605	0.013	2.86E-02	RNF139, RNF115, MYLIP, ASB1, PELI1, IRF2BPL, ZNRF1, UHRF2, RNF19B	XIAP, RNF112, RNF113A, TRAF3IP2, IRF2BP1, RNF135, SH3RF2	6	Member
GO:0003723	RNA binding	1.587	0.111	3.63E-05	HNRNPU, IGHMBP2, PCBP2, PSMA6, RBM4, SRSF6, SNRNP70, SNRPD3, DUSP11, PKP3, RBM15, RPF1, ZC3H12A	BRCA1, IREB2, MAPT, RNASEL, SRSF1, NOL3, DZIP3, ADAT1, RBM15B, CPSF3, APOBEC3F	7	Representative
GO:0003729	mRNA binding	2.287	0.026	6.14E-03	RBM4, ARC, LUC7L3, RBM25, RBM15, ZC3H12A, RBPMS2	DHFR, PURB, SRSF1, TDRD7, NSRP1, NUDT16	7	Member
GO:0047485	protein N-terminus binding	1.613	0.026	2.46E-04	GADD45A, GLRX, TAF11, ALG2	ATM, ERCC4, GTF2H3, MEN1, SMARCE1, TP53, THAP7	8	Representative
GO:0003684	damaged DNA binding	1.107	0.007	2.06E-02	XPA	ERCC4, OGG1	8	Member
GO:0004861	cyclin-dependent protein serine/threonine kinase inhibitor activity	4.575	0.020	4.35E-04	CDKN1A, CDKN2D, HEXIM1	HEXIM2	9	Representative
GO:0030332	cyclin binding	2.542	0.013	8.36E-03	CDKN1A, RBM4, CDK12, FBXW7	CDK6, PROCA1	9	Member
GO:0044877	protein-containing complex binding	1.220	0.007	4.60E-04	CDKN1A, HNRNPU, USF1, FZD5, NAPA, SPATA2, NOD1, PSMG4	ATM, ITGA2, MTHFR, PEX1, PEX6, TERF2, CBX5, DET1	10	Representative
GO:0008022	protein C-terminus binding	1.310	0.026	4.94E-03	POLR2A, COIL, KSR1, BCL10	BRCA2, CDC20, ERCC4, PEX1, PEX6, PEX12, TERF2, XRCC4, MDC1, TNNI3K, IFT46	10	Member
GO:0042162	telomeric DNA binding	1.634	0.026	7.00E-03		TERF2, POT1, TINF2	10	Member
GO:0004722	protein serine/threonine phosphatase activity	1.733	0.007	5.85E-04	PPM1D, CDC14B	PPP1R3D, PTEN, RPAP2	11	Representative
GO:0003697	single-stranded DNA binding	2.062	0.007	7.48E-04	HNRNPU, IGHMBP2, WBP11	BRCA2, ERCC4, MAPT, MLH1, PURA, PURB, NABP1, SWSAP1	12	Representative
GO:0000993	RNA polymerase II complex binding	2.042	0.007	2.15E-02	HNRNPU, SMYD2, RPRD1B	ESRRB, ELP4	12	Member
GO:0036002	pre-mRNA binding	3.119	0.007	3.63E-02	HNRNPU, SRSF6, RBM22		12	Member
GO:0004674	protein serine/threonine kinase activity	1.001	0.020	9.84E-04	ACVR1, MAP3K8, DYRK1A, GSK3A, PDK3, PIM1, PRKCD, SGK1, PPM1D, STK17A	ATM, ATR, MAP3K10, MAP3K11, SYK, MKNK1, HTATIP2, STK38, IRAK4, NLK, ALPK1	13	Representative
GO:0005524	ATP binding	1.372	0.013	5.47E-03	ACVR1, ATP1B1, HNRNPU, IGHMBP2, PDK3, PIM1, KSR1, STK17A, CLP1, YARS2, PRKAG2, PI4K2A	CAD, CDK6, MYO9B, PEX1, PEX6, PRKACB, TP53, TRPV1, MKNK1, ABCB8, STK38, MORC2, PPIP5K2, NLK, SRR	13	Member
GO:0031593	polyubiquitin modification-dependent protein binding	2.018	0.007	1.69E-03	VCP, TNIP2	DZIP3	14	Representative
GO:0016887	ATPase activity	1.549	0.033	5.67E-03	ATP1B1, PSMC1, RFC3, VCP	MYH3, MYO9B, PEX1, PEX6, RUVBL1, ABCC3, MORC2, C10orf88, SWSAP1	14	Member
GO:0044389	ubiquitin-like protein ligase binding	2.691	0.007	9.97E-03	VCP	CCNB1, PARP9, DTX3L	14	Member
GO:0050700	CARD domain binding	4.399	0.007	1.82E-03	BCL10, NOD1	CARD8, MAVS, CARD14	15	Representative
GO:0019900	kinase binding	1.307	0.007	3.28E-02	GADD45A, POLR2A, PRKCD, BCL10, ATF5	CEACAM1, RB1, WWC3	15	Member
GO:0004713	protein tyrosine kinase activity	1.476	0.020	3.26E-03	DYRK1A, LYN	EGFR, MET, PTK6, SRMS, SYK, CAMKK2	16	Representative
GO:0004715	non-membrane spanning protein tyrosine kinase activity	2.199	0.013	7.19E-03	DYRK1A, LYN, TEC	PTK6, SYK	16	Member
GO:0000149	SNARE binding	2.542	0.007	3.58E-03	VAMP2, NAPA, CAPN10	SNAPIN	17	Representative
GO:0008092	cytoskeletal protein binding	2.859	0.013	3.58E-02	CAPN10, MYLIP	ALDOA, ANK3, PKD2, RPH3AL, MYPN	17	Member
GO:0004879	nuclear receptor activity	1.694	0.007	7.18E-03	NR4A2	ESR2, THRB, NR1H3	18	Representative
GO:1990756	protein binding, bridging involved in substrate recognition for ubiquitination	4.765	0.007	1.01E-02	SKP1, SPSB1, ARRDC4	DET1, SPSB2	18	Member
GO:0008013	beta-catenin binding	0.693	0.007	1.70E-02	NR4A2, SKP1, TCF7L2	CBY1	18	Member
GO:0030674	protein binding, bridging	1.400	0.007	1.67E-02	FBXW7	ANK3, MAPT, MEN1, CBX5, MLPH	19	Representative
GO:0035064	methylated histone binding	1.225	0.007	3.89E-02	ING3, SPIN3	CBX5, THAP7, KAT8, GLYR1	19	Member

Table 15 continued: BT-474 - EMBL-703625 monotherapy

ID	Term Description	Fold Enrichment	support	Adj p-value	Up regulated	Down regulated	Cluster	Status
GO:0051015	actin filament binding	0.852	0.007	1.70E-02		EGFR, HIP1, MYH3, FSCN2, DBNL, POF1B, ANTXR1	20	Representative
GO:0051117	ATPase binding	1.195	0.007	2.61E-02	ATP1B1, ATP1B3, TAF9	EGFR, PKD2, TRPC1, TMTC4	20	Member
GO:0043015	gamma-tubulin binding	2.859	0.007	4.33E-02	TUBGCP3, RAB11FIP5, BLOC1S2	BRCA2	21	Representative

Table 15: De-regulated genes and networks (see section 2.2 for details on how significance was calculated) in BT-474 cells treated with 1µM EMBL-703625

Table 16 BT-474 - Lapatinib + EMBL-703625 combination therapy: Hierarchical clustering

ID	Term Description	Fold Enrichment	Support	Adj p-value	Up regulated	Down regulated	Cluster	Status
GO:0004842	ubiquitin-protein transferase activity	1.941	0.28	4.207E-58	AMFR, BIRC2, TRIM23, TRIM37, CNOT4, RNF2, SIAH1, SIAH2, TNFAIP3, TRAF6, UBE2B, UBE2D1, UBE2D3, UBE2G1, UBE2H, UBE2L3, VHL, RNF103, BRAP, CUL3, CDC23, PJA2, KLHL21, TRIM28, TOPORS, WWP2, RNF139, RNF13, PDZRN3, TRIM2, NEDD4L, FBXO7, ARIH1, FBXL3, FBXO2, FBXO3, RNF115, MYLIP, RLIM, FANCL, TRIM36, RNF20, SMURF1, HACE1, UBE2O, SMURF2, RMND5A, CBLL1, KCTD10, UBE2Q2, UHRF2, UBR3, ZNF738, RC3H1, RNF168, RNF152	BIRC3, XIAP, BRCA1, ERCC8, TRIM27, TNFAIP1, UBE2A, RNF40, RNF41, DTX4, FBXW8, FBXO4, UBE2T, UBE2D4, RNF43, TRIM62, KLHL42, RNF213, RNF25, TRIM56, TRIM47, TRIM69, FBXL14, DTX3L, KCTD13, NHLRC1	1	Representative
GO:0061630	ubiquitin protein ligase activity	1.796	0.095	3.409E-40	AMFR, CDC42, TRIM37, SIAH1, SIAH2, TRAF6, RNF103, BRAP, CUL3, TRIM24, TRIP12, RNF10, TOPORS, WWP2, RNF139, MKRN1, RNF11, RNF115, MYLIP, MEX3C, UBR5, ASB1, RNF125, FANCL, SMURF1, PELI1, UBE2O, IRF2BPL, SMURF2, RNF122, TMEM129, UHRF2, RNF19B, RC3H1, RNF38, RNF152, ZNRF2	XIAP, NFX1, TRIM27, PPP1R11, RNF112, RNF144A, RNF41, TRAF3IP2, PPIL2, IRF2BP1, RNF43, RFWD3, SH3RF3	1	Member
GO:0004674	protein serine/threonine kinase activity	1.775	0.165	4.133E-36	ACVR1, ACVR1B, ACVR2A, ACVR2B, AKT2, BRAF, CDK1, CDK7, CLK1, CLK3, MAP3K8, CSNK1A1, CSNK1E, CSNK1G3, CSNK2A2, DYRK1A, MKNK2, GSK3A, ILK, MAP3K1, NEK2, PIM1, PRKCE, PKN2, MAPK1, MAPK8, MAP2K1, RAF1, ROCK1, SGK1, SRPK2, STK3, STK4, CDKL5, TGFBR1, ULK1, STK24, MAP4K3, PPM1D, RIPK2, RIOK3, MAP3K13, RPS6KA5, MAPKAPK2, STK17B, STK17A, EIF2AK3, SLK, TLK1, OXSR1, AKT3, HIPK3, TESK2, MAP3K2, TLK2, PIM2, LMTK2, STK38L, SIK3, ULK3, TBK1, MINK1, SNRK, CLK4, UHMK1, ACVR1C, NEK7, TTBK2, SIK1, CDK11A	ATR, IRAK1, LIMK1, MAP3K5, MAP3K9, MAP3K10, MAP3K11, PHKG2, PRKACA, PRKCA, PRKD1, MAPK13, EIF2AK2, RPS6KA3, MAPK12, NEK4, STK10, SYK, VRK2, MAPKAPK3, MAPKAPK5, MKNK1, RIPK1, RPS6KA4, MAP3K14, PLK2, TNIK, DAPK2, PRKD2, IRAK4, FAM20C, MARK4, MASTL, EIF2AK4	2	Representative
GO:0004672	protein kinase activity	1.693	0.135	3.398E-25	ABL1, ACVR1, BRAF, CDK1, CDK7, CDK8, CSNK1A1, CSNK1E, CSNK1G3, DYRK1A, EPHA4, MAP3K1, MAP3K3, NEK2, CDK17, PDK2, PRKAA1, PKN2, MAP2K1, ROCK1, STK3, STK4, CDKL5, TGFBR1, STK24, MAP4K3, CDK13, DYRK1B, RPS6KA5, MAPKAPK2, STK17B, AKT3, HIPK3, TESK2, MAP3K2, HSPB8, TBK1, MINK1, CDK12, STK26, TTBK2	ATR, CAD, EPHA1, IRAK1, MAP3K5, PRKACA, PRKCA, EIF2AK2, RPS6KA3, SYK, CDC7, RIPK1, MAP3K14, DCLK1, IKBKE, RASSF2, TNIK, PRKD2, TRIB2, IRAK4, MLKL	2	Member
GO:0016301	kinase activity	1.391	0.02	3.224E-10	ABL1, CDK7, CSNK1A1, EPHA4, PIK3C3, PIK3CA, PKN2, MAPK1, MAPK8, CDKL5, WEE1, ULK1	IRAK1, PRKD1, CDC7, MAP3K14, TRIB3, MASTL	2	Member
GO:0005524	ATP binding	1.402	0.045	4.010E-06	ABCA1, ABCA2, ABL1, ACVR1, ACVR1B, AKT2, ATP1A1, ATP1B1, ATP7B, ERCC6, MKNK2, HNRNPU, HSPA1B, HSPA5, INSR, MYO1B, PDK2, PIM1, TWF1, ABCD3, SRPK2, STK3, STK4, CDKL5, TGFBR1, MAP4K3, KSR1, RPS6KA5, STK17B, STK17A, TLK1, OXSR1, AKT3, CLPX, PAPOLA, CLP1, TLK2, STK38L, SIK3, MINK1, YARS2, STK26, SNRK, PI4K2A, PANK3, SIK1, CDK11A	ACLY, ABCD1, BLM, CAD, CDK6, GALK1, GSS, KCNJ11, MAP3K5, MVK, MYO9B, NVL, OAS3, TP53, TRPV1, MKNK1, EIF2B2, RPS6KA4, LONP1, ABCB6, PMVK, FICD, ABCB8, MORC2, DAPK2, VPS4A, SRR, NOL9, MLKL, MYO18A	2	Member
GO:0008134	transcription factor binding	1.714	0.405	2.605E-28	APBB1, ARNT, CCNT1, CEBPG, CENPF, CREBBP, CTNNB1, EP300, FOSB, GATA6, GTF2B, HMGB1, HMGB2, RBPJ, SMAD2, SMAD3, FOXO4, NFKBIA, NPM1, PAX6, PIM1, PPID, REST, RORA, RPS3, TRAPPC2, STAT3, STK4, TCF7L2, TFDP2, THRA, TWIST1, SUMO1, VHL, ZBTB17, USP7, KAT6A, HDAC3, KAT2B, BCL10, AIP, PIAS2, HDAC9, MAFB, MED6, HDAC5, ARID5A, PPARGC1A, WWP2, KDM1A, SIRT1, KAT6B, RBFOX2, UBXN7, CXXC5, HDAC8, MED25	CCND1, BCL3, CEBPA, DDIT3, DNMT3A, E2F5, ESRRB, FHL2, NKX3-1, PPARG, MED1, MAPK9, PURB, RARA, RB1, SMARCA4, TAF12, MLX, TP53, LMO4, TNFRSF10A, HDAC4, SNF8, PDCD11, CAMTA2, IRF2BP1, TRIB2, PARD6A, NUCKS1, HDAC11, METTL23, SDR16C5, KCTD1	3	Representative

Table 16 continued: BT-474 - Lapatinib + EMBL-703625 combination therapy

ID	Term Description	Fold Enrichment	Support	Adj p-value	Up regulated	Down regulated	Cluster	Status
GO:0003713	transcription coactivator activity	1.871	0.325	1.369E-22	ABL1, BIRC2, BRDT, CREBBP, CTNNB1, DAXX, EP300, HMGB1, HMGB2, JUP, LMO2, NFKBIB, NPM1, PSMD9, KDM5A, RFXAP, SMARCA2, TAF9, UBE2L3, KAT6A, NCOA3, NRIP1, NCOA1, TRIM24, KAT2B, BCL10, AIP, DYRK1B, MED21, MED23, MED17, MED26, LPIN2, MAML1, THRAP3, MED6, TRIM28, CITED2, YAP1, ZBTB18, NCOA2, KAT5, SRCAP, PPARGC1A, SUB1, RBPMS, SNW1, PRPF6, WWTR1, TAF5L, MED4, HCFC2, ING4, RNF20, ENY2, JADE1, MED30, TADA1, JMY, CITED4, ASXL1	BRCA1, DDIT3, MED1, SMARCA4, TAF12, RUVBL1, PER2, TRIP11, SRA1, CAMTA2, JMJD6, ARL2BP, CCAR1	3	Member
GO:0003714	transcription corepressor activity	1.976	0.225	5.019E-19	CREBBP, DAXX, EZH1, HNRNPU, PAWR, PFDN5, SIAH2, NRIP1, PIAS1, URI1, CREG1, SAP30, HDAC3, CBFA2T2, CDYL, CIR1, NCOR1, HDAC9, TRIM28, SAP18, CITED2, YAP1, KDM5B, ARID5A, SNW1, SIRT1, RBFOX2, ZMYND8, TBL1XR1	CCND1, CBFA2T3, DNMT3A, ATN1, FHL2, MAP3K10, MED1, SMARCA4, NR0B2, CASP8AP2, PRMT5, MYBBP1A, EID1, IRF2BP1, LMCD1, WNT4, CCAR1, TRIB3, NSD1, PARP9, AJUBA, TCP10L, SDR16C5, BEND6, KCTD1, IRF2BP2	3	Member
GO:0000976	transcription regulatory region sequence-specific DNA binding	1.447	0.205	4.455E-27	ARNTL, ATF3, ERBB4, FOXO3, GABPA, GATA6, HMGB1, HMGB2, IRF1, JUND, SMAD3, SMAD4, SMAD7, NFE2L2, NFYA, NFYC, KDM5A, RBBP5, REST, RXRA, SIX1, SMARCA2, SOX4, STAT3, TAF9, TCF7L2, THRA, YY1, ZNF217, MAFK, KLF11, KLF4, NR1D1, NCOR1, RNF10, HDAC5, YAP1, CTCF, ATF5, GRHL1, SOX6, CREB3L2, TBL1XR1, FOXK1, ZNF568	BRCA1, RUNX1, CEBPA, DDIT3, ETV5, SMAD6, NKX3-1, PPARG, TAF2, TFAP2A, TP53, TFEB, KMT2D, PER2, HDAC4, NR1H3, ZNF658, SOX18, CREB3L1, GABPB2	4	Representative
GO:0000978	RNA polymerase II proximal promoter sequence-specific DNA binding	1.497	0.16	1.085E-26	ARNTL, ZFHX3, PRDM1, KLF5, CHD2, KLF6, ATF2, ELF1, ELK4, FOXO3, GABPA, NR3C1, HNRNPU, HOXA5, HOXB7, HSF2, RBPJ, IRF1, IRF7, MXD1, SMAD1, SMAD2, SMAD3, SMAD4, SMAD5, MITF, MTF1, NFIL3, NFYA, NFYC, NONO, PAX6, PER1, POU2F1, REL, REST, RORA, RXRA, SAFB, SIX1, SOX4, SOX9, STAT3, TBX2, TCF7L2, TFAP2C, TGIF1, NR2C2, UBP1, ZNF148, ZBTB17, ZNF217, NRIP1, YBX3, KLF7, ZBED1, LRRFIP1, LITAF, TBPL1, NR1D1, THRAP3, NR1D2, HDAC5, CTCF, NFAT5, KLF8, EHF, GRHL1, ZNF219, THAP1, ZNF395, NKRF, ZBTB2, ZNF750	RUNX1, DDIT3, DNMT3A, ELK3, ESRRB, ETV1, ETV4, SMAD6, MYCN, NKX3-1, POU4F3, RARA, RELB, TFAP2A, TP53, XBP1, ZNF202, FOSL1, ONECUT2, CLOCK, HDAC4, IRF9, CREB3, TCFL5, FOXP3, SOX18, CCAR1, NSD1, BHLHE41, E2F8, NLRC5, ZNF431	4	Member
GO:0001228	DNA-binding transcription activator activity, RNA polymerase II-specific	1.381	0.095	1.075E-19	ATF1, ATF3, KLF5, CDC5L, CEBPG, KLF6, ATF2, DBP, ELF1, ELF3, ELK4, FOXO1, FOXO3, FOSL2, GABPA, NR3C1, GTF2I, HOXA5, HOXB7, HSF2, RBPJ, IRF1, SMAD1, SMAD2, SMAD3, SMAD4, MITF, FOXO4, MTF1, NR4A2, REL, RFXAP, RXRB, SIX1, SOX4, SOX9, STAT3, TFAP2C, TFDP2, NR2C2, UBP1, ZNF24, ZBTB17, PRDM2, BARX2, KLF7, ZBED1, KLF4, LITAF, TBPL1, NFAT5, ATF5, MLXIP, FOXJ3, ATMIN, EHF, GRHL1, NKRF, ZNF750, CREBRF, YY2	RUNX1, CEBPA, DDIT3, E2F3, ELK3, ESRRB, ETV1, ETV4, ETV5, HLF, MYCN, NHLH1, PLAGL2, PLSCR1, POU4F3, TFAP2A, TP53, ZNF175, ONECUT2, CLOCK, CREB3, SOX18, GRHL3, GRHL2, CREB3L1, MACC1	4	Member
GO:0001227	DNA-binding transcription repressor activity, RNA polymerase II-specific	1.509	0.045	1.473E-12	ZFHX3, BACH1, PRDM1, FOXO3, NR3C1, HOXD9, MXD1, MAX, MNT, MXI1, NFIL3, REST, SKI, TBX2, TFAP2C, TGIF1, YY1, CNBP, ZNF148, ZNF217, PRDM2, MAFK, LRRFIP1, NR1D1, ZBTB5, ZNF263, ZBTB18, HOXB13, CTCF, KLF8, ZNF219, THAP1, ZBTB2, OVOL2, ZNF350, IKZF5, HMBOX1, IRX2, FOXK1	CREM, ELK3, NFX1, MLX, TFAP2A, ZNF85, ZNF140, ZNF175, ZNF202, BHLHE40, TCFL5, ZBTB21, ZNF589, ZBTB4, BHLHE41, E2F8, CREB3L1	4	Member
GO:0043565	sequence-specific DNA binding	1.424	0.075	6.433E-11	ARNT, ARNTL, BCL6, CEBPG, FOXD1, FOXO1, FOXO3, RBPJ, IRF6, SMAD3, SMAD4, FOXO4, NFE2L2, POLRMT, POU2F1, RORA, RXRA, SIX1, SOX9, SP4, TBX2, TCF7L2, NR2F2, NR2C2, USF1, ZNF24, ZNF148, PRDM2, MAFK, ZBED1, MAFB, ZBTB33, ZNF263, TRIM28, ZBTB18, HOXB13, CTCF, ARID5A, PPARGC1A, ATF5, FOXJ3, GRHL1, CXXC5, THAP1, HMBOX1, OSR2, IRX2, YY2	CENPB, E2F3, ESRRA, ESRRB, FOXD4, HLF, HOXA13, MAPT, NKX3-1, PLAGL2, PPARG, TFAP2A, ZNF35, ZNF140, LONP1, CLOCK, HDAC4, ZNF274, SPDEF, FOXP3, ZBTB4, GRHL3, GRHL2, ZC3H8	4	Member

Table 16 continued: BT-474 - Lapatinib + EMBL-703625 combination therapy

ID	Term Description	Fold Enrichment	Support	Adj p-value	Up regulated	Down regulated	Cluster	Status
GO:0000977	RNA polymerase II regulatory region sequence-specific DNA binding	1.495	0.055	4.345E-07	ATF1, ATF3, CDC5L, ATF2, DBP, EP300, FOSL2, NR3C1, HOXD9, HSF2, MAX, MEF2D, MNT, MXI1, NFIL3, RORA, RPS3, RXRA, RXRB, SP3, TFDP2, NR2C2, CNBP, PRDM2, BARX2, NR1D1, ZBTB5, ATF5, MLXIP, IKZF5, CREBRF	RUNX1, CREM, E2F3, ETV5, LMX1B, NFX1, NHLH1, RARA, MLX, ZNF175, CREB3, ZNF589, ZBTB4, STOX1, MACC1	4	Member
GO:0031625	ubiquitin protein ligase binding	1.731	0.605	2.751E-26	APBB1, APC, ARRB2, ATP6V0C, BAG1, CALR, CAMLG, CDKN1A, CKB, CLU, DAXX, FOXO1, GPR37, HSPA1B, HSPA5, JAK1, SMAD2, SMAD3, SMAD5, SMAD7, ATXN3, TRIM37, NFKBIA, PCBP2, PER1, PML, POLR2A, PRKAR1A, RPL5, RPL11, SKI, SUMO2, TMBIM6, TRAF6, UBE2B, UBE2G1, UBE2L3, SUMO1, VCP, YWHAE, CXCR4, FZD5, USP7, BAG6, SPOP, CUL3, BCL10, BAG4, PRDX6, SCAMP3, TRIM28, TXNIP, PPARGC1A, GABARAP, GABARAPL2, CASC3, SYT11, GABARAPL1, FBXO7, ARIH1, UBXN7, USP25, SNX9, UBE2J1, FANCL, FBXW7, LAPTM4B, AMBRA1, RNF20, RTN4, MOAP1, DERL1, MAP1LC3B, MAP1LC3A, CCDC50, ZNF675	BRCA1, CASP8, EGFR, HSPA1L, LTBR, SMAD6, MID1, SLC22A18, PRKACA, RB1, TP53, UBE2A, FZD8, RIPK1, TRAF4, IKBKE, RNF40, RRAGA, TRIOBP, FAF2, TRIB2, UBE2T, TRIB3, HM13, ARRDC1	5	Representative
GO:0002039	p53 binding	1.668	0.17	8.763E-20	PTTG1IP, CREBBP, DAXX, TAF9, TP53BP2, USP7, TRIM24, KDM1A, SIRT1, BRD4, RNF125, RNF20, SMYD2	BLM, SMARCA4, TP53, MAPKAPK5, TP63, PSME3, PRMT5, RFWD3, SETD7	6	Representative
GO:0070577	lysine-acetylated histone binding	1.950	0.01	8.300E-06	BRDT, MLLT3, BRD2, YEATS4, TRIM24, BRD4, ZMYND8, PHIP	SMARCA4, THAP7	6	Member
GO:0003723	RNA binding	1.917	0.37	2.494E-18	ACO1, FMR1, HNRNPU, CAPRIN1, MBNL1, NPM1, PCBP2, PPP1R8, PSMA1, PSMA6, RBM4, UPF1, RPL19, RPL30, RPL34, RPL37, RPL38, RPL39, RPL41, RPS3, RPS14, RPS16, SRSF6, SNRNP70, SNRPA, SSB, HSP90B1, YY1, DUSP11, RAE1, RNMT, PUM1, RBM7, C1D, KHDRBS1, CELF1, PPARGC1A, RBPMS, NUDT21, CPSF6, RCAN3, SCAF8, EXOSC7, PUM2, SF3B1, RBFOX2, PRPF6, PABPC1, SND1, MEX3C, CWC15, RBM15, RPF1, ZC3H12A, MEX3B, YTHDC1, NAF1, RBM20	BRCA1, IREB2, MAPT, RANGAP1, RNASEL, MRPL12, SRSF1, SRSF3, SURF6, NOL3, EMG1, DHX30, JMJD6, TARDBP, ADAT1, RBM15B, CPSF3, XPO5, NIFK, PHF5A, MEX3A, JAKMIP1, APOBEC3F	7	Representative
GO:0003729	mRNA binding	2.205	0.185	8.050E-08	ZFP36L1, CALR, DXO, FMR1, RBM4, RPL7, RPS2, RPS3, RPS5, RPS13, SSB, TPR, RBM5, CELF1, NUDT21, CPSF6, ARC, SF3B6, LUC7L3, METTL14, RBM25, RBM15, ZC3H12A, FYTTD1, HNRNPLL	DHFR, PURB, SRSF1, IGF2BP1, TDRD7, ESRP1, XPO5, ESRP2, NSRP1, NUDT16	7	Member
GO:0003730	mRNA 3'-UTR binding	1.410	0.12	1.108E-07	AUH, CIRBP, FMR1, HNRNPU, RBM4, RPL5, RPL41, RPS7, YBX3, PUM1, PUM2, CARHSP1, PABPC1, RNF20, ZC3H12A, RC3H1	TP53, RNF40, IGF2BP1, TARDBP, DND1	7	Member
GO:0048027	mRNA 5'-UTR binding	1.862	0.065	6.824E-05	FMR1, RPL5, RPL26, RPL41, RPS3A, RPS7, RPS13, RPS14	SHMT1, IGF2BP1	7	Member
GO:0035198	miRNA binding	1.695	0.02	1.125E-04	FMR1, RBM4, PUM1, MATR3, PUM2, ZC3H12A, RC3H1, NEAT1	ZNF346, ZC3H10, PNPT1, DND1	7	Member
GO:0004843	thiol-dependent ubiquitin-specific protease activity	1.693	0.035	4.541E-17	CYLD, ATXN3, TNFAIP3, USP4, USP7, USP15, USP3, USP19, OTUD3, USP24, USP49, USP25, DESI2, USP53, OTUD4, ZRANB1, USP35, USP28, USP46, VCPIP1, ZC3H12A, USP42, OTULIN, USP12, OTUD1	USP18, BRCC3, USP38, USP32, USP51, USP27X	8	Representative
GO:0061578	Lys63-specific deubiquitinase activity	2.978	0.05	3.138E-04	CYLD, ATXN3, TNFAIP3, DESI2, OTUD4	STAMBPL1, BRCC3, USP27X	8	Member
GO:1990380	Lys48-specific deubiquitinase activity	2.048	0.015	1.376E-02	ATXN3, USP7, USP15, DESI2	USP27X	8	Member
GO:0004197	cysteine-type endopeptidase activity	1.251	0.005	4.649E-02	CASP3, CASP9, CTSB, CTSL, PDIA3, LGMN, USP7, USP15, USP49, USP12	CASP8	8	Member

Table 16 continued: BT-474 - Lapatinib + EMBL-703625 combination therapy

ID	Term Description	Fold Enrichment	Support	Adj p-value	Up regulated	Down regulated	Cluster	Status
GO:0003682	chromatin binding	1.817	0.375	1.168E-16	APBB1, ATRX, BCL6, CCNT2, CREBBP, CTNNB1, ELK4, EP300, ERCC6, EZH1, FOXO1, FMR1, GPER1, HNRNPU, JARID2, MLLT3, NONO, PRKAA1, UPF1, REST, RNF2, BRD2, SAFB, SHMT2, SOX9, TOP2B, TPR, MLLT10, URI1, TRIM24, HDAC3, KAT2B, CDYL, TRIM28, CITED2, CBX1, ATF5, BAHD1, KDM1A, BRD4, GMNN, SIRT7, ZC3H12A, PWWP2A, KLHDC3, PHF13, RNF168	RCC1, EGFR, SMAD6, MLH1, PPARG, MED1, RARA, TFAP2A, TP53, ZNF274, MORC2, DHX30, CAMTA2, POLR1A, UBE2T, APTX, FANCM, NSD1, NUCKS1, NKAP, KDM8, GRWD1, MCM8, GLYR1, CREB3L1, USP51, ZNF431, PRIMPOL	9	Representative
GO:0035064	methylated histone binding	1.682	0.04	9.529E-11	ATRX, FMR1, ING1, PHF1, KDM5A, RBBP5, TRIM24, CDYL, SPIN1, MTF2, ZMYND8, CXXC1, ING4, ING3, KMT2E, SPIN4, SPIN3	CBX5, PHF19, KDM8, THAP7, L3MBTL2, GLYR1	9	Member
GO:0042393	histone binding	2.023	0.105	6.130E-09	APBB1, ATRX, BRDT, CHD2, CTSL, DAXX, MLLT3, NASP, NPM1, KDM5A, MLLT10, TNKS, SART3, USP3, ANP32B, KDM5B, SIRT1, BRD1, USP49, UIMC1, RSF1, COPRS, RNF20, TBL1XR1, ANP32E, PWWP2A, UHRF2, SPTY2D1, RNF168	RCC1, MLLT6, PRMT6, IPO9, SFMBT2, PARP9, GRWD1, L3MBTL2, GLYR1, DTX3L, USP51, KDM1B	9	Member
GO:0019003	GDP binding	2.409	0.06	1.257E-15	TRIM23, GNAI1, GNAI3, RAB2A, RAB4A, RAB27B, RAB5C, RAP1B, RAP2B, RHEB, SRP54, RAB7A, RAB11B, RAB9A, RAB35, RAB18, RAB21, DYNC1LI1, RAB14, RAB8B, ARL8B, RRAGD, RRAGC, RAB17	ARL3, RAB8A, RAB3B, MIEF1, RERG, RASEF	10	Representative
GO:0003924	GTPase activity	1.591	0.07	8.119E-09	TRIM23, ARF1, ARF3, ARL1, CDC42, GNAI1, GNAI3, RAB1A, RAB2A, RAB4A, RAB6A, RAB27B, RAB5C, RAC1, RAP1B, RASA1, RGS2, RHEB, SRP54, RAB7A, RAB11A, RAB11B, RAB9A, GTPBP1, RRAGB, RAB35, TPPP, RAB21, RAB14, RRAGD, RRAGC, RAB17, RAB33B, RAB6C	ARHGDIB, RAB8A, RAB3B, RGS3, RNF112, ARFRP1, RGS19, RGS14, RRAGA, MTG2, MFN1, RERG, DIRAS1	10	Member
GO:0005525	GTP binding	1.781	0.05	9.217E-08	TRIM23, ARL1, CDC42, EEF1A1, GLUD1, GNAI1, INSR, RAB2A, RAB4A, RAB6A, RAB27B, RAC1, RAP1B, RAP2B, RHEB, SRP54, RAB7A, RAB11B, RAB9A, ARL4A, RRAGB, RAB35, RAB21, DYNC1LI1, RAB14, ARL8B, RRAGD, RRAGC, RHEBL1	RHOH, ARL3, RAB8A, MX2, RNF112, EIF2B2, RRAGA, ARFIP2, NUDT16, DIRAS1, RASEF	10	Member
GO:0031489	myosin V binding	2.184	0.025	1.549E-04	RAB6A, RAB27B, RAB11A, RAB11B, RAB14	RAB8A, RAB3B, RAB3D	10	Member
GO:0004713	protein tyrosine kinase activity	1.189	0.065	8.982E-14	ABL1, DYRK1A, EPHA7, ERBB2, ERBB4, FGFR1, IGF1R, INSR, JAK1, LYN, TWF1	EGFR, EPHB2, MET, PTK6, SRMS, SYK, CAMKK2	11	Representative
GO:0001784	phosphotyrosine residue binding	1.084	0.025	1.104E-06	ABL1, CRKL, GRB2, RASA1, NCK2	PTPN3, SH3BP2, SYK, LDLRAP1	11	Member
GO:0004715	non-membrane spanning protein tyrosine kinase activity	1.260	0.03	7.666E-06	ABL1, CLK1, DYRK1A, JAK1, LYN, TEC	PTK6, SYK	11	Member
GO:0046875	ephrin receptor binding	1.445	0.005	3.003E-05	ABL1, EFNA1, EFNA5, EFNB3, GRB2, LYN		11	Member
GO:0070064	proline-rich region binding	1.575	0.01	1.978E-02	ABL1, APBB1, CYLD	CCND1, WBP4	11	Member
GO:0070411	I-SMAD binding	3.276	0.09	6.495E-13	CTNNB1, SMAD1, SMAD2, SMAD4, SMAD7, TGFBR1, SMURF1	SMAD6	12	Representative
GO:0070412	R-SMAD binding	1.509	0.03	4.963E-06	SMAD2, SMAD3, SMAD4, PAX6, PPM1A, SMURF1	SMAD6	12	Member
GO:0070410	co-SMAD binding	1.638	0.025	2.008E-04	SMAD1, SMAD2, SMAD3	SMAD6	12	Member
GO:0001223	transcription coactivator binding	1.638	0.01	1.978E-02	CCNT2, SMAD3, SMAD4, RORA, ZBTB17, MED25		12	Member
GO:0048156	tau protein binding	0.945	0.005	3.903E-02	CLU, DYRK1A, SMAD2		12	Member
GO:0004402	histone acetyltransferase activity	2.594	0.11	9.724E-13	ATF2, CREBBP, EP300, TAF9, KAT6A, NCOA3, KAT2B, KAT5, SRCAP, KAT7, KAT6B, TAF5L, ING3, EPC1	BRCA2, TADA2A, TAF12, CLOCK, BAZ1A	13	Representative
GO:0016407	acetyltransferase activity	3.003	0.09	1.309E-07	CREBBP, EP300, GTF2B, KAT6A, KAT2B, KAT5, KAT6B, ELP3, ESCO1	NAA10, ESCO2	13	Member
GO:0005516	calmodulin binding	1.200	0.005	6.681E-12	MYO6, PPP3CA, RGS2, STRN, VAMP2, UNC13B, TRPV6	CEACAM1, MBP, MYO9B, PPP3CB, TRPV1, IQCB1, CAMKK2, DAPK2, IQCG, MYLK2	14	Representative
GO:0051059	NF-kappaB binding	1.706	0.02	7.810E-12	EP300, NFKBIA, NPM1, PSMA6, TAF4B, TP53BP2, HDAC3, BCL10	RNF25, SETD6	15	Representative

Table 16 continued: BT-474 - Lapatinib + EMBL-703625 combination therapy

ID	Term Description	Fold Enrichment	Support	Adj p-value	Up regulated	Down regulated	Cluster	Status
GO:0033613	activating transcription factor binding	1.575	0.06	8.868E-08	EP300, GABPA, SMAD2, MEF2D, NPM1, PTMA, TAF9	PPARG, HDAC4, SDR16C5	15	Member
GO:0030957	Tat protein binding	1.638	0.015	6.790E-03	NPM1, CTDP1, GABARAPL1	SMARCA4	15	Member
GO:0035257	nuclear hormone receptor binding	2.315	0.17	9.920E-12	CRY1, CTNNB1, EP300, TCF7L2, NCOA3, NRIP1, NCOA1, BUD31, NCOR1, NCOA2, SNW1, SIRT1	MED1	16	Representative
GO:0030374	nuclear receptor transcription coactivator activity	1.989	0.065	6.703E-07	SS18, NCOA1, BUD31, MED17, RBM14, NCOA2, PPARGC1A, BRD8, KDM1A, ENY2	MED1, PSMC3IP, CCAR1, WDR77, ZMIZ2, SFR1, PPARGC1B	16	Member
GO:0003712	transcription coregulator activity	2.176	0.08	2.134E-06	CNOT2, PTPN14, KAT2B, MED17, MED26, THRAP3, PPARGC1A, RALY, BRD4, SND1, MED4, HES6, MED30	MED1, TRIP13, NSD1, PPARGC1B	16	Member
GO:0046966	thyroid hormone receptor binding	2.389	0.055	4.922E-06	GTF2B, TACC1, TRIP12, ZNHIT3, MED17, THRAP3, ARID5A, BRD8, MED4, MED30, JMJD1C	GTF2H1, MED1, NSD1	16	Member
GO:0016922	nuclear receptor binding	1.911	0.04	9.793E-06	RXRA, TACC1, NCOA3, NCOA1, NCOA2, PPARGC1A	MED1	16	Member
GO:0030331	estrogen receptor binding	1.836	0.025	1.907E-05	CTNNB1, PPID, STRN, TACC1, NRIP1, NCOA1, ARID5A	NKX3-1, MED1, PADI2, NSD1, PAGR1, PPARGC1B	16	Member
GO:0046965	retinoid X receptor binding	2.867	0.015	7.769E-03	NR4A2, TACC1, ARID5A, MED25	PPARG, VDR, NSD1	16	Member
GO:0042974	retinoic acid receptor binding	2.234	0.005	2.368E-02	TACC1, SNW1, MED25, ASXL1	MED1, NSD1	16	Member
GO:0000981	DNA-binding transcription factor activity, RNA polymerase II-specific	1.333	0.03	2.165E-11	ARNT, ARNTL, ZFHX3, ELF2, GATA6, IRF1, IRF7, SMAD3, MAX, MEF2D, PAX6, POU2F1, SOX9, SP100, TWIST1, USF1, KLF11, KLF7, ZMYM5, ARX	ESRRB, LMX1B, TFAP2A, TP53, BHLHE40, CLOCK, CREB3, BHLHE41	17	Representative
GO:0001102	RNA polymerase II activating transcription factor binding	1.575	0.125	3.418E-09	ATF2, CREBBP, CTNNB1, EP300, GTF2I, ID2, LMO2, SMAD3, NFE2L2, LDB1, NCOR1, SIN3A	TBX6, BHLHE40, BHLHE41	17	Member
GO:0070888	E-box binding	1.199	0.015	3.547E-05	ARNTL, MAX, MITF, NONO, PER1, TWIST1, PSPC1	PPARG, BHLHE40, CLOCK, PRMT5, BHLHE41	17	Member
GO:0043425	bHLH transcription factor binding	2.048	0.02	2.911E-03	LMO2, SMAD3, PSMD9, TWIST1, USF1, SIRT1	FHL2, MAP3K10, BHLHE40, BHLHE41	17	Member
GO:0047485	protein N-terminus binding	2.153	0.185	2.771E-11	BIRC2, CSNK2A2, DAXX, GADD45A, EPB41, ERCC5, ERCC6, GLRX, HSPA1B, EIF3E, PPP1CC, MAP2K1, PEX5, RPS21, SDCBP, TARBP2, TRAF6, TSC1, NCOA3, NCOA1, MORF4L1, YWHAQ, PDCD10, PHB2, NIPBL, DCTN4, TBL1XR1, ALG2	ERCC2, ERCC4, GTF2H2, GTF2H3, PEX19, SMARCA4, TP53, VWF, SNF8, APTX, CHMP6, THAP7, VPS25	18	Representative
GO:0008022	protein C-terminus binding	1.563	0.215	3.925E-09	ABL1, DST, CDK7, CENPF, FOXN3, CTNNB1, EP300, EPB41, ERBB2, ERCC6, FBLN1, BCAM, NUMA1, POLR2A, MAP2K1, SIAH1, TOP2B, USP7, YEATS4, COIL, KSR1, BCL10, MAGI1, VPS4B, OPTN, PRDX3, PHB2, PRRC2C, SASH1, SIRT1, NIPBL, PABPC1, VTA1, PCGF1	BRCA2, CDC20, ERCC1, ERCC2, ERCC4, LIG4, PPARG, TERF2, MDC1, SNX17, PIAS3, FBLN5, CORO1A, SNF8, VPS4A, MIF4GD	18	Member
GO:0051087	chaperone binding	1.832	0.155	4.544E-11	AMFR, BIRC2, ATP1A1, CALR, CLU, GRN, HLA-B, HSPA5, DNAJB9, PFDN4, SOD1, TSC1, BAG3, DNAJB6, DNAJA2, ERP29, DNAJB4, GET4, FNIP2, FNIP1	CDC25A, MAPT, TBCE, TP53, VWF, UBL4A, PFDN6, FICD, DNAJB5, SACS, TIMM10, TIMM9, TSACC, RNF207	19	Representative
GO:0051879	Hsp90 protein binding	1.152	0.01	1.730E-04	ARNTL, CYP1A1, NR3C1, PPID, RPS3, TSC1, USP19, HDAC8	MAPT	19	Member
GO:0030544	Hsp70 protein binding	1.755	0.01	2.404E-02	CYP1A1, GPR37, PPID, RPS3, TSC1, HDAC8	FICD, SACS, DNAJB12, IQCG, METTL21A, RNF207	19	Member
GO:0050681	androgen receptor binding	1.820	0.07	5.557E-11	CALR, DAXX, EP300, ARID5A, SNW1, KDM1A, KDM4C, PRPF6, FOXP1, KDM3A	SMARCA4, NSD1	20	Representative
GO:0042162	telomeric DNA binding	1.170	0.005	7.891E-03	UPF1, KDM1A, TERF2IP, HMBOX1	TERF2, TINF2	20	Member
GO:0032454	histone demethylase activity (H3-K9 specific)	1.638	0.01	1.074E-02	KDM1A, KDM4C, KDM3A, JMJD1C		20	Member
GO:0019903	protein phosphatase binding	1.903	0.245	5.773E-11	CTNNB1, ERBB2, JAK1, JUP, LGALS3, NEK2, MAP2K7, STAT3, HSP90B1, VCP, SHOC2, MTMR3, MTMR4, EIF2AK3, KIF3A, TBK1, ANAPC5, PPP6R3, MTMR9	CEACAM1, CDC27, CDH5, EGFR, KCNN4, MAP3K5, MET, PPP1R3C, TP53, IKBKE, PPME1, ANAPC7, STYXL1, SIRPA	21	Representative
GO:0004714	transmembrane receptor protein tyrosine kinase activity	1.638	0.03	1.047E-03	ERBB2, ERBB4	EGFR, EPHA2, EPHB4, DDR2	21	Member

Table 16 continued: BT-474 - Lapatinib + EMBL-703625 combination therapy

ID	Term Description	Fold Enrichment	Support	Adj p-value	Up regulated	Down regulated	Cluster	Status
GO:0042826	histone deacetylase binding	1.536	0.13	5.986E-11	HSPA1B, MEF2D, PKN2, MAPK8, TOP2B, TRAF6, USF1, YWHAB, YWHAE, HDAC3, KAT2B, CIR1, NCOR1, HDAC9, HDAC5, NUDT21, NIPBL, AKAP8L, GMNN, BEX4, MIER1	CCND1, NKX3-1, TP53, HDAC4, CAMTA2, FOXP3, BHLHE41, THAP7, KCTD21	22	Representative
GO:0033558	protein deacetylase activity	1.862	0.04	2.854E-06	HDAC3, HDAC9, HDAC5, SIRT1	HDAC4	22	Member
GO:0004407	histone deacetylase activity	2.048	0.035	2.625E-05	HDAC3, HDAC9, HDAC5, SIRT1, HDAC8, MIER1	HDAC4, HDAC11	22	Member
GO:0070491	repressing transcription factor binding	1.502	0.05	2.999E-04	ARNTL, HMGB1, RBPJ, SKI, HDAC9, HDAC5, KAT5, ZMYND8	HDAC4, CBX5, TCP10L	22	Member
GO:0005080	protein kinase C binding	1.365	0.015	1.143E-02	ABL1, DSP, HINT1, HSPB1, ITGAV, TOP2B, ADAM9, HDAC9, HDAC5	PKP2, PRKD2, TIRAP	22	Member
GO:0019789	SUMO transferase activity	2.048	0.035	1.837E-10	PIAS1, PIAS2, ZBED1, TRIM28, TOPORS	HDAC4, PIAS3	23	Representative
GO:0046332	SMAD binding	1.872	0.055	7.514E-10	ACVR1, ACVR1B, CTNNB1, FKBP1A, SMAD2, SKI, TGFBR1, TGFBR2, TGFBR3, YY1, TGFBRAP1, USP15, IPO7, SNW1, SMURF2	CREB3L1	24	Representative
GO:0019838	growth factor binding	1.686	0.005	1.758E-03	ACVR1B, ACVR2B, ERBB2, IL6ST, LIFR, TGFBR1, ACVR1C		24	Member
GO:0008013	beta-catenin binding	1.179	0.04	3.589E-09	APC, SHROOM2, CDH1, CDH2, CTNNA1, CTNNB1, EP300, FOXO1, FOXO3, SMAD7, FOXO4, NR4A2, PTPRK, SKP1, TCF7L2, TBL1XR1	CDH5, CBY1, BCL9L	25	Representative
GO:0045295	gamma-catenin binding	2.457	0.015	4.292E-09	APC, CDH1, CDH2, CTNNA1, PTPRK, TCF7L2		25	Member
GO:0045296	cadherin binding	1.170	0.035	3.126E-04	ACVR1, APC, CTNNA1, CTNNB1, CTNND1, JUP, CD46, NDRG1		25	Member
GO:0003735	structural constituent of ribosome	2.168	0.06	2.124E-08	RPL10, RPL19, RPL30, RPL37, RPL39, RPLP0, RPLP1, RPLP2, RPS4X, RPS23	MRPS12, MRPS16, MRPS7, MRPS18A, MRPS15, MRPS11, MRPL57, MRPL52	26	Representative
GO:0061631	ubiquitin conjugating enzyme activity	1.755	0.045	6.926E-08	UBE2D1, UBE2D3, UBE2G1, UBE2L3, UBE2J1, UBE2O	UBE2A, UBE2T, UBE2D4	27	Representative
GO:0051015	actin filament binding	1.002	0.03	2.548E-07	SHROOM2, MYO1B, MYO6, MYO10, FSCN1, SPTB, HIP1R, DSTN, BLOC1S6, LIMA1, MAP1S, CAMSAP3, SCIN	EGFR, HIP1, MYH3, TPM1, TRIOBP, CORO1A, DBNL, POF1B, AIF1L, MYO18A	28	Representative
GO:0003779	actin binding	1.181	0.04	2.417E-04	ANG, SHROOM2, EPS8, GSN, HNRNPU, ITGB1, MYO6, P4HB, PAWR, TWF1, FSCN1, SPTB, CXCR4, PDLIM1, MAEA, SORBS1, SYNE2, SCIN, GAS2L3	ALDOA, CEACAM1, DMD, MAPT, MYO9B, TNNT2, TPM1, MICAL2, CORO1A, MSRB2, DBNL, MSRB1, MYO19	28	Member
GO:0008092	cytoskeletal protein binding	2.194	0.01	1.273E-02	ABI1, SORBS1, CAPN10, TOR1AIP1, MYLIP, LIN7C	ALDOA, DUSP3, TOR1A, PKD2, TPM1, RPH3AL, CORO1A, PACSIN3, MYPN	28	Member
GO:0031593	polyubiquitin modification-dependent protein binding	2.409	0.06	2.984E-07	EPS15, RAD23B, VCP, BAG6, OPTN, ZFAND6, TNIP2	RAD23A, BRCC3, SHARPIN	29	Representative
GO:1990381	ubiquitin-specific protease binding	2.340	0.09	3.099E-05	AMFR, SUMO1, VCP, BAG6, SART3, SPATA2, DERL1	RAD23A	29	Member
GO:0003697	single-stranded DNA binding	1.746	0.035	5.159E-07	ERCC5, HMGB1, HMGB2, HNRNPU, RAD23B, SUB1, RTF1, WBP11	BLM, BRCA2, ERCC1, ERCC4, MAPT, MLH1, POLR2H, PURB, RAD23A, RAD51D, SETMAR, TOP3A, POLR3C, NEIL3, REXO4, NABP1, NABP2, SWSAP1	30	Representative
GO:0003684	damaged DNA binding	1.717	0.08	1.678E-06	CREBBP, DDB1, EP300, HMGB1, HMGB2, RPS3, XPA, CUL4B, SDE2	ERCC1, ERCC4, OGG1, APTX	30	Member
GO:0003690	double-stranded DNA binding	1.545	0.045	2.405E-06	CRY1, ERCC5, HMGB1, HMGB2, HNRNPU, SMAD2, RXRA, SAFB, YBX3	HLF, MAPT, PPARG, SETMAR, POLR3F, TARDBP, ZNF638, APTX, NEIL3, REXO4, NUCKS1	30	Member
GO:0043130	ubiquitin binding	1.274	0.025	6.490E-07	BIRC2, HSPB1, SMAD3, TNFAIP3, CXCR4, USPL1, FBXO7, UBXN7, UBAP1, DDI2, RNF19B, RNF168	FAF2, NUP62	31	Representative
GO:0003743	translation initiation factor activity	1.365	0.02	6.853E-07	EIF2D, EIF3E, EIF3F, EIF3H, EIF3L	EIF2S1, EIF2B4, EIF2B2, EIF2B5	32	Representative
GO:0031369	translation initiation factor binding	2.048	0.005	2.693E-03	FMR1, RPS24	EIF2B4, EIF2B5, TBL2	32	Member

Table 16 continued: BT-474 - Lapatinib + EMBL-703625 combination therapy

ID	Term Description	Fold Enrichment	Support	Adj p-value	Up regulated	Down regulated	Cluster	Status
GO:0005096	GTPase activator activity	1.353	0.005	9.019E-07	ALDH1A1, BNIP2, ARHGAP35, LLGL1, RASA1, RGS2, EVI5, RAPGEF2, RABGAP1L, DLC1, VAV3, ARFGEF1, RALBP1, ACAP2, TBC1D7, ALS2, TBC1D15, SYDE2, ARHGAP11B, ARAP1, TBC1D20, ARHGAP42, FLCN	ABR, ARHGAP1, MYO9B, RANGAP1, RGS3, CDC42EP2, RGS14, GMIP, RALGAPA2, ARAP3, ELMOD3, EVI5L, SGSM1	33	Representative
GO:0017137	Rab GTPase binding	1.675	0.005	1.286E-02	ATP6AP1, CHML, EVI5, ULK1, RABGAP1L, OPTN, NDRG1, KIF3A, BICD2, TBC1D7, HACE1, RIC1, ALS2, RILP, RAB11FIP4, IFT20, TBC1D20	ARHGAP1, RAB8A, NSF, RGP1, GOLGA5, AP3M1, HPS6, MICALL1, EVI5L, SGSM1	33	Member
GO:0016887	ATPase activity	1.706	0.135	1.346E-06	ABCA2, ATP1B1, ATP2B1, CHD3, CLU, EIF4A2, HSPA1B, HSPA5, PSMC2, PSMC6, ABCD3, RFC3, VCP, WRN, DDX39B, VPS4B, ATP8A1, CLPX, KIF1B, ATP13A2, RSF1, WRNIP1	ABCD1, BLM, DNA2, TOR1A, MYH3, MYO9B, NSF, DHX16, RUVBL1, ABCC3, LONP1, MORC2, VPS4A, RNF213, C10orf88, MYO19, SWSAP1, MYO18A	34	Representative
GO:0004386	helicase activity	2.048	0.015	1.041E-04	EIF4A2, SUPV3L1, WRN, SNRNP200	BLM, DNA2, DDX23	34	Member
GO:0003678	DNA helicase activity	1.609	0.03	1.888E-04	CHD3, ERCC6, SUPV3L1, WRN, RAD54B	BLM, ERCC8, DNA2, RUVBL1, SETX, ZRANB3	34	Member
GO:0008094	DNA-dependent ATPase activity	1.950	0.02	2.379E-04	CDK7, ERCC6, SMARCA2, CHD6	BLM, ERCC8, RAD51D, SMARCA4, TTF2, SMARCAL1	34	Member
GO:0003724	RNA helicase activity	1.792	0.015	3.605E-04	UPF1, SUPV3L1, DDX39B, SNRNP200, RAD54B	DDX23, DHX30	34	Member
GO:0000400	four-way junction DNA binding	2.816	0.015	1.640E-03	ABL1, HMGB1, HMGB2, WRN, YY1	BLM, RAD51C, RAD51D, XRCC2, XRCC3, GEN1	34	Member
GO:0000987	proximal promoter sequence-specific DNA binding	1.698	0.01	1.762E-06	ARNT, ATF2, HMGB2, SMAD3, MTF1, SOX9, SP3, YY1, KLF4, ZNF516, TIPARP, YY2	E2F3, ESRRB, XBP1, E2F8, E2F7	35	Representative
GO:0070530	K63-linked polyubiquitin modification-dependent protein binding	2.633	0.02	2.149E-06	ZBTB1, TAB2, UIMC1, ZRANB1, RNF168, RNF169	IKBKE, ZRANB3, ATRIP	36	Representative
GO:0031491	nucleosome binding	2.835	0.02	4.227E-03	NAP1L4, MLLT10, HP1BP3, RNF168, RNF169	RCC1, MLLT6, GLYR1, DNTTIP1	36	Member
GO:0001085	RNA polymerase II transcription factor binding	0.945	0.135	3.100E-06	CREBBP, CTNNB1, KLF4, HDAC5, WWP2, KDM1A	TBX6, TP53, HDAC4	37	Representative
GO:0097718	disordered domain specific binding	1.781	0.035	3.940E-04	CALM1, CALM3, SMAD2, NUMA1, NCOA3, FKBP8	BCL2L2, RB1, TP53, PPIL1	37	Member
GO:1990841	promoter-specific chromatin binding	1.251	0.065	8.641E-04	PRDM1, GTF2B, HNRNPU, POLR2A, KLF4, TRIM28, KDM1A, NIPBL, ZNF304, ZNF750	TP53	37	Member
GO:0035035	histone acetyltransferase binding	1.293	0.005	2.208E-03	PAX6, CITED2, ECD	TP53, EID1, FOXP3	37	Member
GO:0004879	nuclear receptor activity	1.972	0.065	4.805E-06	NR3C1, NR4A2, RXRA, RXRB, STAT3, NR2F2, THRA, NR1D2	NKX3-1, PPARG, RARA, VDR, NR1H3	38	Representative
GO:0031490	chromatin DNA binding	1.733	0.005	5.513E-04	FOXO3, HNRNPU, PER1, STAT3, ZIC2, PPARGC1A, GRHL1	RARA, CLOCK, GRHL3, GRHL2	38	Member
GO:0051393	alpha-actinin binding	1.365	0.005	3.881E-02	KCNN2, MAGI1	PPARG, RARA	38	Member
GO:0030332	cyclin binding	1.668	0.03	4.835E-06	CDK1, CDKN1A, PTCH1, RBM4, CDK13, HDAC3, CDK12, FBXW7, FBXO31	CDK4, CDK6	39	Representative
GO:0004861	cyclin-dependent protein serine/threonine kinase inhibitor activity	2.048	0.02	1.233E-02	CDKN1A, CDKN2D, KAT2B, HEXIM1	HEXIM2	39	Member
GO:0004860	protein kinase inhibitor activity	2.048	0.005	4.125E-02	CDKN1A, CDKN1C, GMFB, NCK1, NPM1, DNAJC3, SOCS3, SH3BP5, MBIP	DUS2, PPP1R1B	39	Member
GO:0044325	ion channel binding	1.305	0.005	5.671E-06	CALM1, CALM3, AP2M1, CTNNB1, FKBP1A, FMR1, ID2, LYN, TRAPPC2, SLC5A3, SRI, YWHAE, HERPUD1, RIMS3, AKAP9, GPD1L, NEDD4L	BAK1, CDH5, FGF12, KCNJ11, PDE4B, PDE4D, PKD2, PKP2, HOMER1, RIMS2, GOPC, RNF207	40	Representative
GO:0017080	sodium channel regulator activity	1.117	0.005	2.581E-02	SGK1, GPD1L, NEDD4L	FGF12, PKP2, PTPN3	40	Member

Table 16 continued: BT-474 - Lapatinib + EMBL-703625 combination therapy

ID	Term Description	Fold Enrichment	Support	Adj p-value	Up regulated	Down regulated	Cluster	Status
GO:0008270	zinc ion binding	1.405	0.06	2.182E-05	ALPP, BIRC2, CA2, CALR, CBLB, CYLD, FNTB, GTF2B, LTA4H, SMAD3, MMP13, PAM, PGGT1B, PHEX, KDM5A, RNF2, RPS29, RXRA, SIAH1, SKI, SOD1, KAT6A, KLF7, TNKS, TNFSF10, TRIM24, LITAF, TRIM28, LANCL1, SEC24B, SLU7, CTCF, KDM5B, SMPDL3A, KDM4C, ATP13A2, ZMYND8, ARIH1, RNF11, CXXC5, SIRT6, TET2, RNF125, THAP1, IKZF5, ESCO1, RC3H1, ZDHHC20	ADAM8, BLM, CAD, GALT, KPNB1, MBD1, MT2A, NQO2, ENPP3, PPARG, TK1, TP53, ZNF185, HDAC4, SEC24D, MORC2, MSRB2, SIRT5, TIMM10, TIMM9, TIMM8B, ZCCHC4, APIP, LACTB2, MSRB1, FBXL19, ACER3, NSD1, PHF5A, APOBEC3F, PRIMPOL, KDM1B, MSRB3, ZACN	41	Representative
GO:0019888	protein phosphatase regulator activity	2.048	0.01	2.223E-05	PPP2R2A, PPP2R5A, PPP2R5D, SHOC2, ARPP19, PPP4R2	PPP1R7, EIF2AK2, ANKLE2, PPME1, PPP1R1B	42	Representative
GO:0051721	protein phosphatase 2A binding	1.950	0.005	6.475E-04	FOXO1, STRN, ARPP19, BOD1, DAB2IP	MAPT, TP53, ANKLE2, PPME1, MASTL	42	Member
GO:0044877	protein-containing complex binding	1.420	0.05	2.422E-05	CDKN1A, CDKN1C, CLU, DDB1, ERCC5, ERCC6, FBLN1, HNRNPU, INSR, ITGB1, NDUFA4, NUMA1, SLC25A3, RAC1, RAP1A, RAP1B, RPS3, SPAST, STRN, USF1, WRN, FZD5, ULK1, NAPA, VPS4B, CIR1, IST1, SPATA2, NOD1, APPL1, LZTFL1, BRK1, ATG101, VIPAS39, HMBOX1, POLDIP3, MB21D2, DAB2IP, FLCN	ERCC8, EPHB2, ITGA2, NSF, PFKP, TERF2, RIPK1, CBX5, VPS4A, CHMP6, ADM2, TNKS1BP1, MLKL	43	Representative
GO:0000993	RNA polymerase II complex binding	1.609	0.02	3.222E-05	ERCC5, GTF2B, HNRNPU, NCOA3, URI1, ELP2, SMYD2, CCAR2, RPRD1B, CDC73	ESRRB	44	Representative
GO:0001046	core promoter sequence-specific DNA binding	1.638	0.03	5.968E-04	NR3C1, GTF2B, NPM1, ZBTB17, FOXP1	TP53	44	Member
GO:0000979	RNA polymerase II core promoter sequence-specific DNA binding	0.683	0.005	2.500E-02	GTF2B, POU2F1		44	Member
GO:0005154	epidermal growth factor receptor binding	1.950	0.015	7.139E-05	ERBB4, GRB2, SNX1, SNX2, SNX4, FAM83B	HIP1, PLSCR1, AGR2, EPGN	45	Representative
GO:0035091	phosphatidylinositol binding	1.898	0.005	8.520E-04	GRB7, NUMA1, SNX1, SNX4, HIP1R, SNX13, APPL1, SNX5, SNX8, SNX12, SNX9, MITD1	HIP1, MAPT, PITPNA, TRPV1, SNX17, C2CD2L, MCF2L	45	Member
GO:0005158	insulin receptor binding	1.792	0.005	6.631E-03	GRB10, IGF1, IGF1R, SNX1, SNX2, SNX4, SORBS1		45	Member
GO:1990459	transferrin receptor binding	1.638	0.01	1.677E-02	CD81, SNX1, SNX2, SNX4		45	Member
GO:0051020	GTPase binding	1.966	0.01	7.500E-05	BNIP3, GOLGA4, RASA1, ULK1, RRAGB, ATG14, FNBP1L, AMBRA1, RRAGD, RRAGC	STOML2, LAMTOR1	46	Representative
GO:0019904	protein domain specific binding	1.655	0.07	1.458E-04	ARF1, ARL1, CALM1, CALM3, GUSB, HSPA5, INSR, KCNN2, MLF1, NFE2L2, NUMA1, PPP3R1, PRKAR1A, RAB6A, RAB27B, SKI, SKP1, SP100, TFDP2, THRA, VCP, XPA, YWHAB, MBD2, HGS, VAPA, IST1, CITED2, NCOA2, KHDRBS1, DICER1, ZMYND8, LIN7C, RCC2, CHMP1B, IKZF5, CNTROB, MITD1, MPP7, OCLN	DFFA, ATN1, ERCC1, ESRRA, KPNB1, MAP3K5, PLAUR, RARA, VRK2, NR0B2, BHLHE40, AP4M1, RNF41, EFS, RAPGEF3, PLXND1, VPS4A, FHOD1, MRPL17	47	Representative
GO:0000149	SNARE binding	2.048	0.005	1.974E-04	VAMP2, STX7, NAPA, BAIAP3, CAPN10, GABARAPL2	NSF, SEC24D, SNAPIN	48	Representative
GO:0019905	syntaxin binding	1.877	0.005	2.661E-02	ABCA1, ABL1, PTPN2, VAMP2, STX7, BAIAP3, STX6, BLOC1S6	GOLGA2, VPS18, STXBP4	48	Member
GO:0051082	unfolded protein binding	1.333	0.065	2.189E-04	CALR, CLU, HSPA1B, HSPA5, NAP1L4, NPM1, AIP, TOMM20, DNAJB6, DNAJA2, AFG3L2, ERLEC1	HSPA1L, GRPEL1	49	Representative
GO:0031072	heat shock protein binding	1.401	0.01	2.453E-04	DAXX, GPR37, HSPA1B, PPID, TPR, DNAJB6, LMAN2	HSPA1L, ITGB2, LIMK1, METTL18, METTL23, METTL21A	49	Member
GO:0044183	protein binding involved in protein folding	2.048	0.02	3.053E-04	CALR, HSPA1B, HSPB1, PFDN1, FKBP8	DFFA	49	Member
GO:0016791	phosphatase activity	1.517	0.005	2.484E-04	ACPP, PPP1CB, PPP1CC, SBF1, DUSP11, DUSP10, SACM1L	DUSP3, DUSP4, DUSP16	50	Representative
GO:0004721	phosphoprotein phosphatase activity	1.424	0.02	5.180E-03	PPP1CC, PPP2CA, PPP2R5A, PPP2R5D, CTDP1	CDC25A, CDC25B, DUSP16	50	Member
GO:0004722	protein serine/threonine phosphatase activity	1.986	0.01	6.408E-03	PPM1A, PPM1B, PPP1CC, PPP2CA, PPP3CA, PPP4C, PPM1D, MTMR3, MTMR4, PDP1, PPTC7	CDKN3, PPP1R3C, PPP1R3D, PPM1F, RPAP2	50	Member
GO:0019900	kinase binding	1.463	0.03	2.535E-04	CTNNB1, GADD45A, EEF1A1, PER1, POLR2A, PPP2R5A, RPS3, SP100, TAX1BP1, BCL10, PRDX3, ATF5, CAB39, TOLLIP, PARP16, LAPTM4B, DAB2IP	CEACAM1, CDC6, CEBPA, MYCN, RAD23A, RB1, TRIP6, WWC3	51	Representative

Table 16 continued: BT-474 - Lapatinib + EMBL-703625 combination therapy

ID	Term Description	Fold Enrichment	Support	Adj p-value	Up regulated	Down regulated	Cluster	Status
GO:0017124	SH3 domain binding	1.450	0.025	3.199E-04	ABL1, CASP9, DPYSL3, GRB2, ADAM15, ADAM9, ABI1, WASF2, LANCL1, KHDRBS1, CD2AP, DAB2IP	MAPT, PLSCR1, AKAP5, RUFY1, MYPN	52	Representative
GO:0008237	metallopeptidase activity	0.921	0.005	2.436E-03	ADAM10, LNPEP, ADAM17, ADAM15, ADAM9, ECEL1, AFG3L2	ADAM8, BRCC3	52	Member
GO:0005178	integrin binding	1.001	0.01	4.530E-03	ANXA7, DST, CALR, CD81, HMGB1, IGF1, ITGAV, ITGB1, P4HB, PTPN2, ADAM17, ADAM15, ADAM9, F11R	S1PR3, ITGB2, PRKCA, CX3CL1, SYK, VWF, FBLN5, FERMT3	52	Member
GO:0003725	double-stranded RNA binding	1.191	0.015	3.567E-04	HNRNPU, ILF3, MBNL1, SUPV3L1, TARBP2, TLR3, LRRFIP1, RFTN1, DICER1, RC3H1	OAS3, EIF2AK2, DHX30, ZNF346, APTX, DUS2	53	Representative
GO:0036002	pre-mRNA binding	1.862	0.01	2.490E-03	HNRNPU, SRSF6, TARBP2, CELF1, RBM22		53	Member
GO:0097602	cullin family protein binding	1.536	0.005	3.909E-04	DDB1, SKP1, RNF7, KLHL21, KCTD9	KCTD21	54	Representative
GO:1990756	protein binding, bridging involved in substrate recognition for ubiquitination	2.389	0.02	1.006E-02	SKP1, VHL, PDCD6, FBXO7, SPSB1	SPSB2, ARRDC1	54	Member
GO:0051117	ATPase binding	1.467	0.015	4.782E-04	ABCA1, ATP1B1, ATP1B3, FBL, ATXN3, SNU13, PPP3CA, TAF9, GABARAPL2, NCSTN, TOR1AIP1, BBC3, USP25, SNX10, DERL1, SLC2A13	ATP6V0A1, EGFR, PDE4D, PKD2, PTPN3, PEX19, TMTC4, METTL21A	55	Representative
GO:0001671	ATPase activator activity	1.536	0.01	3.824E-03	ATP1B1, ATP1B3, DNAJB6, DNAJA2, DNAJB4, TOR1AIP1		55	Member
GO:0002020	protease binding	1.365	0.02	6.208E-04	ANXA2, COL1A1, CST3, CSTB, ITGAV, ITGB1, FURIN, SERPINA1, PSAP, SRI, STIM1, TNFAIP3, UBC, CFLAR, BCL10, ATP9A, RNF139, DERL1, SLC2A13	BRCA2, TP53, VWF, FADD, TNFRSF10A, FLOT1, PYCARD, TYSND1	56	Representative
GO:0031996	thioesterase binding	1.489	0.01	7.167E-04	CDC42, RAC1, TRAF6	TRAF4	57	Representative
GO:0031624	ubiquitin conjugating enzyme binding	2.048	0.005	4.157E-03	FOXL2, TRAF6, ARIH1, RNF125		57	Member
GO:0031435	mitogen-activated protein kinase kinase kinase binding	1.638	0.005	3.140E-02	TRAF6, SASH1, DAB2IP	MAP3K11	57	Member
GO:0035925	mRNA 3'-UTR AU-rich region binding	1.862	0.03	7.195E-04	ZFP36L1, ILF3, KHSRP, HNRNPA0, NUDT21, CPSF1, ZC3H12A, CPEB2	EXOSC9, EXOSC4	58	Representative
GO:0043022	ribosome binding	1.311	0.005	2.555E-02	FMR1, RPSA, BAG6, ZC3H12A, CPEB2, YTHDF3	EIF2S1, NAA10	58	Member
GO:0050700	CARD domain binding	2.205	0.015	7.882E-04	RIPK2, BCL10, NOD1	CARD8, MAVS, CARD9, CARD14	59	Representative
GO:0051219	phosphoprotein binding	2.205	0.025	8.654E-04	EPB41, YWHAB, YWHAE, URI1, THRAP3, MID2, TBK1	MID1, PKD2, RB1, TRPV1, RRAGA, TBL2, APTX	60	Representative
GO:0046982	protein heterodimerization activity	1.273	0.09	1.253E-03	ADRA2C, ARNT, ATF3, ATP1A1, ATP1B1, GADD45A, ERBB2, EXT2, FMR1, HEXA, ITGB1, MCL1, NR4A2, P4HB, PPP2CA, SDCBP, SNX1, SNX2, SRI, SUPT5H, TOP2B, USF1, YWHAE, FXR1, SMC3, VAPA, KATNA1, PHB2, ZBTB1, FBXO7, GCA, RRAGD, RRAGC, ALG2, MICU2	BAK1, RCC1, DDIT3, HIP1, IRAK1, CEACAM6, PDGFB, MLX, TCOF1, TP53, TPM1, XBP1, BHLHE40, PSMF1, GABBR2, PRMT5, RRAGA, LSM5, RALGAPA2, BHLHE41	61	Representative
GO:0030971	receptor tyrosine kinase binding	1.585	0.01	1.346E-03	GRB14, NCK1, PTPN2, PTPN14, SOCS5, DOCK4, TOB1	DUSP3, TP53, HYAL2, RNF41, PITPNM3	62	Representative
GO:0017160	Ral GTPase binding	1.024	0.005	2.779E-02	RALBP1	MYO1C, RNF41	62	Member
GO:0008143	poly(A) binding	1.463	0.05	1.588E-03	HNRNPU, PABPC4, KHDRBS1, RBPMS, PABPC1		63	Representative
GO:0008266	poly(U) RNA binding	1.792	0.015	2.852E-03	FMR1, SSB, PABPC4, KHDRBS1, PABPC1, DIS3L2	PNPT1	63	Member
GO:0017116	single-stranded DNA-dependent ATP-dependent DNA helicase activity	1.706	0.01	2.522E-03	RFC3	DNA2, RFC4, RFC5, CHTF8	64	Representative
GO:0050750	low-density lipoprotein particle receptor binding	1.433	0.005	2.708E-03	AP2M1, CLU, LRPAP1, HSP90B1, LANCL1	SNX17, LDLRAP1	65	Representative
GO:0034236	protein kinase A catalytic subunit binding	1.575	0.005	2.806E-03	GSK3A, PRKAR1A, SOX9, PJA2	PRKAR1B	66	Representative
GO:0050699	WW domain binding	1.724	0.01	3.531E-03	SCNN1G, LITAF, RAPGEF2, DAZAP2, WBP11, NDFIP2	TP63, TRAF4	67	Representative
GO:0008327	methyl-CpG binding	1.675	0.005	3.581E-03	MBD2, ZBTB33, HOXB13, CXXC5	MBD1, PRMT5, ZBTB21, ZBTB4, WDR77	68	Representative
GO:0097110	scaffold protein binding	0.683	0.005	7.057E-03	BRAF, DSP, MAP2K1, YWHAE	CASP8, PDE4D, TCOF1, AKAP5	69	Representative
GO:0004708	MAP kinase kinase activity	1.638	0.005	1.151E-02	MAP2K1, MAP2K7	MAPKAPK3, MAPKAPK5	69	Member

Table 16 continued: BT-474 - Lapatinib + EMBL-703625 combination therapy

ID	Term Description	Fold Enrichment	Support	Adj p-value	Up regulated	Down regulated	Cluster	Status
GO:0005102	signaling receptor binding	1.029	0.005	9.500E-03	ABCA1, ADM, ALCAM, ANG, ANXA1, APP, ARRB2, BMP3, CLU, CTNND1, EDA, EFNA1, F2RL1, GFRA1, GLG1, GSK3A, GUSB, HLA-A, HLA-B, HLA-E, HSPA1B, IGFBP2, LRP6, LRPAP1, NCK1, SERPINE2, RASA1, SCP2, SRI, BAG6, TNFSF10, RIPK2, TRIM24, AKAP9, SEMA4D, ARPP19, TMED1, PANX1, RND1, PCSK1N, RAB8B, LEPROT, CAPRIN2	CDH5, MYO1C, PKD2, PLAUR, RARA, CX3CL1, TNFSF15, ABCA12, STOML2	70	Representative
GO:0034450	ubiquitin-ubiquitin ligase activity	1.862	0.01	1.210E-02	AMFR, UBR5, PELI2, PELI1	PPIL2	71	Representative
GO:0070063	RNA polymerase binding	2.048	0.005	1.333E-02	CCNT1, CCNT2, STOM, PKN2, ANP32B, PHRF1	BRCA1, YTHDC2	72	Representative
GO:0019843	rRNA binding	1.365	0.005	1.906E-02	ANG, FASTKD5	PTCD3, DDX28	73	Representative
GO:0015631	tubulin binding	1.404	0.005	1.936E-02	DCTN1, STMN1, NUMA1, RPS3, TPR, TPPP, ATF5, MAP1S	ALDOA, TTLL12, EML2, RITA1	74	Representative
GO:0008017	microtubule binding	1.242	0.005	2.910E-02	APC, DCTN1, FMR1, NUMA1, RP1, RPS3, SPAST, ZNF207, RAE1, RAB11A, VAPA, KIF23, NDRG1, MID2, TPPP, KATNA1, SUN2, MAP1S, RCC2, REEP4, FAM83D, WHAMM, CCSAP, RMDN2, GAS2L3	ARL3, KRIT1, GAS8, GOLGA2, MAPT, MID1, RGS14, EML2, MAP10, MARK4, TUBGCP5, SKA2	74	Member
GO:0070840	dynein complex binding	1.927	0.005	4.397E-02	APC, CENPF, FMR1, NUMA1, TPR, SMC3, BICD2, ATMIN		74	Member
GO:0031994	insulin-like growth factor I binding	1.862	0.005	2.139E-02	IGF1R, IGFBP2, INSR, ITGAV	ITGB4	75	Representative
GO:0005509	calcium ion binding	1.080	0.005	2.180E-02	ANXA1, BNIP2, BRAF, C1R, CALM1, CALM3, CALR, CDH2, FBLN1, GSN, HSPA5, MMP13, PAM, SRI, STIM1, TKT, TPD52, TPT1, HSP90B1, BAIAP3, PGS1, PDCD6, MAN1B1, SYT11, GCA, GLCE, SDF4, STIM2, MEX3B, SCIN, AGRN	ADAM8, DNASE1L2, GJB2, IDS, ENPP3, PKD2, PLSCR1, PPP3CB, PSPH, TRPM2, DYSF, NOL3, SLC25A13, CAMKK2, PADI2, ACER3, MAN1C1, SRR, PITPNM3, CRACR2A, CANT1, S100A16	76	Representative
GO:0004857	enzyme inhibitor activity	1.170	0.005	2.831E-02	PPP1R12A, PRPSAP1, CCAR2	PRPSAP2, PARP9, DTX3L	77	Representative
GO:0048306	calcium-dependent protein binding	0.853	0.01	3.171E-02	ANXA1, ANXA2, ANXA7, VAMP2, PDCD6IP, PDCD6, VPS37C, RBM22, VPS37B, ALG2		78	Representative
GO:0004535	poly(A)-specific ribonuclease activity	1.862	0.005	3.444E-02	CNOT2, CNOT8, CNOT6L, PAN3	TOE1	79	Representative
GO:0000175	3'-5'-exoribonuclease activity	2.503	0.005	3.609E-02	CNOT8, XRN2, DIS3, EXOSC7, DIS3L2	ISG20, EXOSC2, ISG20L2, PNPT1, TOE1, DIS3L	79	Member
GO:0004601	peroxidase activity	1.260	0.005	3.671E-02	HBA1, PRDX1, PRDX5	GPX8	80	Representative
GO:0018024	histone-lysine N-methyltransferase activity	1.755	0.005	4.010E-02	SETD2, KMT2E, SMYD3	TTLL12, N6AMT1, SETD7	81	Representative
GO:0008047	enzyme activator activity	1.820	0.005	4.790E-02	TRIM23, ARL1, CASP9, DDOST, GMFB, PPP1R12B, CTSA, PRKCE, PSAP, RFC1, CFLAR	MMP17, DPM2, DBNL, SLX4, DTX3L	82	Representative

Table 16: De-regulated genes and networks (see section 2.2 for details on how significance was calculated) in BT-474 cells treated with 1µM lapatinib and 1µM EMBL-703625

Table 17 SK-BR3 - Lapatinib + EMBL-703625 combination therapy: Hierarchial clustering

ID	Term_Description	Fold_Enrichment	support	highest_p	Up_regulated	Down_regulated	Cluster	Status
GO:0004842	ubiquitin-protein transferase activity	2.352	0.132	5.906E-29	AMFR, TRIM23, SIAH1, TNFAIP3, TTC3, UBE2D1, UBE2G1, UBE2H, RNF103, PJA2, AREL1, TOPORS, UBE2C, RNF139, TRIM2, NEDD4L, FBXO7, ARIH1, FBXL3, FBXO3, RNF115, MYLIP, TRIM33, RNF20, SMURF1, HACE1, UBE2O, SMURF2, RMND5A, CBLL1, KCTD10, ZNRF1, UHRF2, UBR3, RC3H1, RNF168, RNF152, RNF144B	XIAP, BRCA1, ERCC8, RBBP6, TRIM27, TNFAIP1, UBE2A, RNF40, RNF41, TRIM13, STUB1, DTX4, UBE2T, RNF220, TRIM62, KLHL42, RNF213, RNF25, LRSAM1, TRIM69, DTX3L, NHLRC1	1	Representative
GO:0061630	ubiquitin protein ligase activity	2.320	0.085	2.037E-25	AMFR, CDC42, SIAH1, RNF103, TRIM24, TRIP12, RNF10, TOPORS, RNF139, MKRN1, RNF11, RNF115, MYLIP, MEX3C, UBR5, SMURF1, PELI1, UBE2O, IRF2BPL, SMURF2, ZNRF1, UHRF2, RNF19B, RC3H1, RNF38, RNF152, ZNRF2	XIAP, NFX1, RBBP6, TRIM27, RNF144A, RNF41, TRIM13, STUB1, TRAF3IP2, CBLC, RFWD3, LRSAM1	1	Member
GO:0004843	thiol-dependent ubiquitin-specific protease activity	2.170	0.058	2.760E-22	CYLD, ATXN3, TNFAIP3, USP4, USP7, USP9X, USP8, USP3, OTUD3, USP24, USP21, USP25, DESI2, USP53, OTUD4, ZRANB1, USP31, USP35, VCPIP1, USP42, OTULIN, OTUD1	UCHL1, BRCC3	2	Representative
GO:0061578	Lys63-specific deubiquitinase activity	4.316	0.058	1.427E-06	CYLD, ATXN3, TNFAIP3, DESI2, OTUD4	STAMBPL1, BRCC3	2	Member
GO:1990380	Lys48-specific deubiquitinase activity	2.713	0.005	4.493E-03	ATXN3, USP7, USP9X, DESI2		2	Member
GO:0004197	cysteine-type endopeptidase activity	1.130	0.005	8.657E-03	LGMN, USP7, USP8	CASP8, CTSK, UCHL1	2	Member
GO:0004674	protein serine/threonine kinase activity	1.922	0.116	2.025E-19	ACVR1, ACVR1B, ACVR2A, ACVR2B, BRAF, CDK7, CLK1, CLK3, MAP3K8, CSNK1A1, CSNK1E, CSNK1G3, CSNK2A2, DYRK1A, MKNK2, ILK, MARK3, MAP3K1, NEK2, PIM1, PRKCD, MAPK1, MAPK8, RAF1, ROCK1, SGK1, SRPK2, TGFBR1, MAP4K3, PPM1D, RIOK3, MAP3K13, STK17A, EIF2AK3, ROCK2, CDC42BPB, SLK, TLK1, OXSR1, HIPK3, MAP3K2, LMTK2, STK38L, UHMK1, NEK7, SIK1	ATR, CDK2, PLK3, LIMK1, MAP3K10, MAP3K11, PHKG2, PKN1, MAPK4, EIF2AK2, NEK4, STK10, SYK, VRK2, AURKB, HTATIP2, DAPK2, PRKD2, STK39, IRAK4, MASTL, NIM1K	3	Representative
GO:0004672	protein kinase activity	1.356	0.053	8.197E-10	ACVR1, BRAF, CDK7, CSNK1A1, CSNK1E, CSNK1G3, DYRK1A, MAP3K1, NEK2, CDK17, PRKAA1, PRKCD, PTK2, ROCK1, TGFBR1, MAP4K3, CDC42BPB, HIPK3, MAP3K2	ATR, CAD, EPHA1, PRKAB1, PKN1, EIF2AK2, SYK, IKBKE, PRKD2, IRAK4, MLKL	3	Member
GO:0005524	ATP binding	1.356	0.011	5.421E-03	ABCA1, ACVR1, ACVR1B, ATP1A1, ATP1B1, ERCC6, MKNK2, HNRNPU, INSR, MYO1B, PIM1, PRPS1, SRPK2, TGFBR1, SMARCA5, MAP4K3, KSR1, STK17A, CDC42BPB, TLK1, OXSR1, STK38L, PI4K2A, N4BP2, PANK3, PIF1, SIK1	ACLY, ABCD1, CAD, CDK6, GALK1, MVK, OAS3, PRKACB, PYGL, TRPV1, TNK1, EIF2B2, ABCB6, ABCB8, MORC2, DAPK2, NIM1K, MLKL	3	Member
GO:0000978	RNA polymerase II proximal promoter sequence-specific DNA binding	1.356	0.095	6.822E-16	ZFHX3, PRDM1, KLF5, CHD2, ATF2, ELF1, FOXO3, GABPA, NR3C1, HDAC1, HNRNPU, HSF2, RBPJ, IRF7, MXD1, SMAD1, SMAD4, SMAD5, MITF, NFATC3, NFYA, NFYC, NONO, PLAG1, REL, REST, SOX4, SOX9, STAT3, TFAP2C, TGIF1, NR2C2, UBP1, ZBTB17, ZNF217, NRIP1, KLF7, LRRFIP1, LITAF, THRAP3, NR1D2, HDAC5, CTCF, EHF, GRHL1	ASCL2, ETV1, ETV4, SMAD6, NFIC, NPAS2, RELB, ZNF202, HDAC4, RUVBL2, CCAR1, BHLHE41, E2F8	4	Representative
GO:0001228	DNA-binding transcription activator activity, RNA polymerase II-specific	1.341	0.037	1.427E-12	ATF1, KLF5, CDC5L, ATF2, ELF1, ELF3, FOXO3, FOSL2, GABPA, NR3C1, GTF2I, HIF1A, HOXC10, HSF2, RBPJ, SMAD1, SMAD4, MITF, FOXO4, NFATC3, PLAG1, REL, RXRB, SOX4, SOX9, STAT3, TFAP2C, NR2C2, UBP1, ZNF24, ZBTB17, PRDM2, BARX2, KLF7, LITAF, FOXJ3, ATMIN, EHF, GRHL1, CREBRF, YY2	E2F3, ETV1, ETV4, HLF, NFIC, PLSCR1, RFX5, ZNF76, ZNF175, SCX	4	Member
GO:0000976	transcription regulatory region sequence-specific DNA binding	1.253	0.095	1.467E-11	CRY2, FOXO3, GABPA, GATA6, HDAC1, SMAD4, SMAD7, MSX2, NFE2L2, NFYA, NFYC, REST, SOX4, STAT3, TAF9, YY1, ZNF217, KLF11, SOX13, NCOR1, RNF10, HDAC5, CTCF, GRHL1, CREB3L2, TBL1XR1	BRCA1, SMAD6, RFX5, TAF2, ZNF174, TFEB, HDAC4, GABPB2	4	Member

Table 17 continued: SK-BR3 - Lapatinib + EMBL-703625 combination therapy

ID	Term_Description	Fold_Enrichment	support	highest_p	Up_regulated	Down_regulated	Cluster	Status
GO:0001227	DNA-binding transcription repressor activity, RNA polymerase II-specific	1.472	0.021	3.094E-09	ZFHX3, BACH1, PRDM1, FOXO3, NR3C1, MXD1, MAX, MXI1, NFATC3, REST, TFAP2C, TGIF1, YY1, ZNF217, PRDM2, LRRFIP1, ZBTB5, ZNF263, CTCF, HEY1, ZNF350, IKZF5, HMBOX1, IRX2	ASCL2, CREM, NFX1, MLX, ZNF175, ZNF202, BHLHE41, E2F8, JDP2	4	Member
GO:0000977	RNA polymerase II regulatory region sequence-specific DNA binding	1.561	0.085	7.069E-07	ACTN4, ATF1, CDC5L, ATF2, EP300, FOSL2, NR3C1, HIF1A, HOXC10, HSF2, MAX, MEF2D, MXI1, RPS3, RXRB, SP3, NR2C2, TRPS1, PRDM2, BARX2, ZBTB5, IKZF5, CREBRF	CREM, E2F3, NFX1, MLX, ZNF175, STOX1	4	Member
GO:0043565	sequence-specific DNA binding	1.278	0.032	1.526E-05	ARNT, BCL6, EPAS1, FOXO3, HIF1A, RBPJ, IRF6, SMAD4, FOXO4, MSX2, NFE2L2, SOX9, NR2C2, USF1, ZNF24, PRDM2, SOX13, MAFB, ZNF263, CTCF, FOXJ3, GRHL1, CXXC5, HMBOX1, OSR2, IRX2, YY2	CENPB, E2F1, E2F3, FOXD4, HLF, RFX5, ZNF76, ZNF174, HDAC4, ZNF274, ZC3H8, SCX	4	Member
GO:0031625	ubiquitin protein ligase binding	1.646	0.238	2.834E-15	APC, CALR, CAMLG, CLU, DAXX, DIO2, GPR37, HIF1A, JAK1, SMAD5, SMAD7, ATXN3, POLR2A, PRKAR2B, RPL5, RPL11, TMBIM6, UBE2G1, CXCR4, USP7, BCL10, BAG4, LRPPRC, TXNIP, GABARAP, GABARAPL2, GABARAPL1, FBXO7, ARIH1, UBXN7, USP25, UBE2J1, AMBRA1, RNF20, RTN4, DERL1, MAP1LC3B, CCDC50	BRCA1, CASP8, LTBR, SMAD6, PRKACB, RB1, RPA2, UBE2A, UCHL1, VCL, FZD8, NAE1, TRAF4, IKBKE, RNF40, STUB1, FAF2, UBE2T, SMC6, UBE2J2	5	Representative
GO:0043130	ubiquitin binding	1.658	0.005	2.353E-07	TNFAIP3, CXCR4, FBXO7, UBXN7, UBAP1, DDI2, RNF19B, RNF168	UCHL1, FAF2, NUP62	5	Member
GO:0003714	transcription corepressor activity	1.725	0.127	4.049E-15	CREBBP, DAXX, DNMT3B, HDAC1, HNRNPU, PAWR, PFDN5, TLE1, NRIP1, URI1, CBFA2T2, CDYL, CIR1, NCOR1, CITED2, KDM5B, SIRT1, RBFOX2, SFMBT1, TBL1XR1	CCND1, MAP3K10, CASP8AP2, PRMT5, MYBBP1A, RUVBL2, CCAR1, TCP10L, KCTD1	6	Representative
GO:0002039	p53 binding	1.884	0.122	3.904E-13	PTTG1IP, CREBBP, DAXX, HDAC1, HIF1A, TAF9, TP53BP2, USP7, TRIM24, SIRT1, RNF20	PLK3, PSME3, PRMT5, RFWD3	6	Member
GO:0008134	transcription factor binding	1.609	0.243	9.514E-13	ADD1, ARNT, CCNT1, CENPF, CREBBP, CTNNB1, EP300, EPAS1, GATA6, GTF2B, HDAC1, HIF1A, RBPJ, FOXO4, ENPP2, PIM1, REST, RPS3, TRAPPC2, STAT3, TLE1, ZBTB17, USP7, BCL10, AIP, MAFB, HDAC5, SIRT1, KAT6B, RBFOX2, UBXN7, CXXC5, HDAC8	CCND1, E2F1, E2F5, HYAL1, MAPK9, PURB, RB1, TAF12, MLX, TFCP2, TNFRSF10A, HDAC4, ATG7, PDCD11, CAMTA2, NUCKS1, METTL23, KCTD1	6	Member
GO:0042393	histone binding	2.206	0.079	5.479E-14	ATRX, CHD2, DAXX, MLLT3, NASP, MLLT10, SMARCA5, USP3, KDM5B, BAZ2A, SIRT1, BRD1, SFMBT1, RSF1, RNF20, TBL1XR1, UHRF2, SPTY2D1, RNF168	PKN1, HIRA, PRMT6, GRWD1, L3MBTL2, GLYR1, DTX3L, KDM1B	7	Representative
GO:0003682	chromatin binding	1.726	0.153	1.209E-11	ATRX, BCL6, CCNT2, CREBBP, CTNNB1, EP300, ERCC6, FMR1, GPER1, HNRNPU, JARID2, MLLT3, NONO, PRKAA1, REST, BRD2, SOX9, TPR, MLLT10, URI1, TRIM24, CDYL, CITED2, CBX1, SIRT7, KLHDC3, PHF13, RNF168	SMAD6, PKN1, CHAF1B, ZNF274, MORC2, CAMTA2, POLR1A, UBE2T, WAC, APTX, NUCKS1, GRWD1, MCM8, GLYR1, LRWD1	7	Member
GO:0035064	methylated histone binding	2.180	0.048	8.690E-09	ATRX, FMR1, ING1, PHF1, TRIM24, CDYL, SPIN1, CXXC1, ING3, KMT2E, KDM7A, SPIN3	CBX5, PHF19, THAP7, L3MBTL2, GLYR1, LRWD1	7	Member
GO:0070577	lysine-acetylated histone binding	1.615	0.005	9.309E-03	MLLT3, BRD2, TRIM24, BAZ2A	THAP7	7	Member
GO:0003713	transcription coactivator activity	1.633	0.148	9.486E-14	ACTN4, CREBBP, CTNNB1, DAXX, EP300, TAF9, NCOA3, NRIP1, NCOA1, TRIM24, BCL10, AIP, MED14, MED26, LPIN2, MAML1, THRAP3, CITED2, NCOA2, SRCAP, WWTR1, USP21, TAF5L, RNF20, JADE1, MED30, TADA1, JMY, ASXL1	BRCA1, TAF12, RUVBL1, MED24, HTATIP2, CAMTA2, JMJD6, ARL2BP, CCAR1, ZMIZ1	8	Representative
GO:0035257	nuclear hormone receptor binding	2.949	0.185	1.410E-12	ACTN4, CTNNB1, EP300, HIF1A, NCOA3, NRIP1, NCOA1, NCOR1, NCOA2, SIRT1		8	Member
GO:0030374	nuclear receptor transcription coactivator activity	1.938	0.021	3.601E-06	ACTN4, TMF1, NCOA1, RBM14, NCOA2, BRD8	PKN1, CCAR1, WDR77, SFR1	8	Member
GO:0016922	nuclear receptor binding	1.809	0.016	6.139E-03	TACC1, NCOA3, NCOA1, NCOA2		8	Member
GO:0030331	estrogen receptor binding	1.169	0.005	4.776E-02	CTNNB1, STRN, TACC1, NRIP1, NCOA1		8	Member
GO:0070411	I-SMAD binding	4.748	0.090	5.634E-12	CTNNB1, SMAD1, SMAD4, SMAD7, TGFBR1, SMURF1	SMAD6	9	Representative
GO:0070410	co-SMAD binding	2.713	0.011	3.666E-05	SMAD1, USP9X, TRIM33	SMAD6	9	Member
GO:0070412	R-SMAD binding	1.785	0.011	6.559E-04	SMAD4, PPM1A, TRIM33, SMURF1	SMAD6	9	Member

Table 17 continued: SK-BR3 - Lapatinib + EMBL-703625 combination therapy

ID	Term_Description	Fold_Enrichment	support	highest_p	Up_regulated	Down_regulated	Cluster	Status
GO:0003723	RNA binding	1.803	0.180	1.422E-09	FMR1, HNRNPH1, HNRNPU, RPS3, RPS14, SRSF6, SON, HSP90B1, YY1, EIF3A, RNMT, PUM1, RBM7, C1D, CELF1, CPSF6, BAZ2A, SCAF8, PUM2, SF3B1, RBFOX2, AGO1, PABPC1, SND1, MEX3C, RBM15, MEX3B, YTHDC1	BRCA1, CSTF2, DRG2, RANGAP1, MRPL12, SRSF1, SURF6, NOL3, EMG1, JMJD6, ADAT1, GPKOW, RBM15B, CPSF3, XPO5, METTL16, PHF5A, PATL2	10	Representative
GO:0003729	mRNA binding	2.191	0.069	1.347E-04	ZFP36L1, CALR, FMR1, RPL7, RPS3, RPS5, TPR, CELF1, CPSF6, LUC7L3, METTL14, RBM15, HNRNPLL	DHFR, PURB, SRSF1, XPO5, UPF3B, ESRP2, NSRP1, NUDT16	10	Member
GO:0061631	ubiquitin conjugating enzyme activity	2.584	0.011	2.124E-09	UBE2D1, UBE2G1, UBE2C, UBE2J1, UBE2O	UBE2A, UBE2T, UBE2J2	11	Representative
GO:0044389	ubiquitin-like protein ligase binding	1.596	0.005	2.118E-02	STAM, UBE2C	CCNB1, DTX3L	11	Member
GO:0047485	protein N-terminus binding	2.174	0.074	2.441E-09	CSNK2A2, DAXX, GADD45A, ERCC6, HDAC1, MNAT1, PPP1CC, SDCBP, TSC1, NCOA3, NCOA1, MORF4L1, PDCD10, SRRM2, NIPBL, DCTN4, TBL1XR1	ERCC2, ERCC4, GTF2H3, STX5, ZWINT, APTX, THAP7, VPS25	12	Representative
GO:0004402	histone acetyltransferase activity	3.165	0.074	3.064E-09	ATF2, CREBBP, EP300, TAF9, NCOA3, SRCAP, KAT7, KAT6B, TAF5L, ING3, EPC1	TADA2A, TAF12, BAZ1A	13	Representative
GO:0001102	RNA polymerase II activating transcription factor binding	1.739	0.127	3.982E-09	ATF2, CREBBP, CTNNB1, EP300, GTF2I, NFE2L2, NCOR1, SIN3A	MAD2L2, BHLHE41	13	Member
GO:0016407	acetyltransferase activity	2.261	0.021	7.293E-03	CREBBP, EP300, GTF2B, KAT6B, ESCO1		13	Member
GO:0005516	calmodulin binding	1.403	0.005	3.724E-09	MYO6, STRN, VAMP2, IQGAP1, UNC13B, TRPV6	MIP, PPP3CB, TRPV1, IQCB1, DAPK2, IQCG	14	Representative
GO:0005096	GTPase activator activity	1.680	0.016	7.656E-09	ALDH1A1, ARHGAP35, RASA1, RGS10, IQGAP1, RAPGEF2, USP6NL, ARHGAP44, DLC1, VAV3, RALBP1, ACAP2, ARFGAP3, RACGAP1, TBC1D15, SYDE2, TBC1D20, FLCN	ABR, RANGAP1, NPRL3, DEPDC5, CDC42EP2, SH3BP1, GMIP, ELMOD3, TBC1D16	15	Representative
GO:0003779	actin binding	1.344	0.011	1.662E-08	ACTN4, ADD1, ANG, EPS8, HNRNPU, ITGB1, ABLIM1, MYO6, PAWR, PTK2, FSCN1, TNNI2, CXCR4, MICAL3, GAS2L3	TPM1, VCL, CORO1A, DBNL, MSRB1, CORO7, MYO19	16	Representative
GO:0051015	actin filament binding	1.154	0.016	1.466E-06	ACTN4, ADD1, MYO1B, MYO6, MYO10, FSCN1, LRPPRC, DSTN, CYFIP1, BLOC1S6, LIMA1	HIP1, TPM1, CORO1A, DBNL, AIF1L	16	Member
GO:0003684	damaged DNA binding	2.407	0.132	7.700E-08	CREBBP, CRY2, DDB1, EP300, RPS3, CUL4B, SDE2	ERCC4, OGG1, RPA2, APTX	17	Representative
GO:0003697	single-stranded DNA binding	1.779	0.016	8.158E-03	CRY2, HNRNPA1, HNRNPU, RAD23B, RTF1	ERCC4, POLR2H, PURB, RAD23A, RAD51D, RPA2, TOP3A, POLR3C, NEIL3, TDP1, NABP1	17	Member
GO:0046332	SMAD binding	1.744	0.042	8.464E-08	ACVR1, ACVR1B, CTNNB1, TGFBR1, YY1, IPO7, SMURF2	STUB1, ZMIZ1	18	Representative
GO:0019838	growth factor binding	2.394	0.005	8.889E-03	ACVR1B, ACVR2B, ERBB2, IL6ST, LIFR, TGFBR1		18	Member
GO:0051059	NF-kappaB binding	1.696	0.005	1.279E-07	EP300, HDAC1, TP53BP2, BCL10	RNF25, SETD6	19	Representative
GO:0042826	histone deacetylase binding	1.441	0.042	3.372E-06	HDAC1, MEF2D, MAPK8, USF1, CIR1, NCOR1, HDAC5, NIPBL, AKAP8L, MIER1	CCND1, PKN1, RAD9A, HDAC4, CAMTA2, BHLHE41, THAP7	19	Member
GO:0033558	protein deacetylase activity	2.466	0.106	3.208E-05	HDAC1, HDAC5, SIRT1	HDAC4	19	Member
GO:0004407	histone deacetylase activity	2.543	0.111	1.743E-04	HDAC1, HDAC5, SIRT1, HDAC8, MIER1	HDAC4	19	Member
GO:0001085	RNA polymerase II transcription factor binding	1.043	0.069	1.915E-04	CREBBP, CTNNB1, HDAC1, HDAC5	HIRA, HDAC4	19	Member
GO:0033613	activating transcription factor binding	1.826	0.032	5.345E-04	EP300, GABPA, HDAC1, MEF2D, PTMA, TAF9	HDAC4	19	Member
GO:0070491	repressing transcription factor binding	1.356	0.016	1.970E-03	HDAC1, RBPJ, HDAC5	HDAC4, CBX5, TCP10L	19	Member
GO:0000981	DNA-binding transcription factor activity, RNA polymerase II-specific	1.341	0.021	9.875E-07	ARNT, ZFHX3, ELF2, GATA6, HIF1A, IRF7, MAX, MEF2D, MSX2, SOX9, SP100, USF1, KLF11, KLF7, HEY1	E2F1, BHLHE41	20	Representative
GO:0000987	proximal promoter sequence-specific DNA binding	1.654	0.016	2.381E-04	ARNT, ATF2, SOX9, SP3, YY1, YY2	E2F1, E2F3, TFCP2, E2F8	20	Member
GO:0003712	transcription coregulator activity	1.696	0.011	3.685E-06	PTPN14, MED14, MED26, THRAP3, SND1, MED30	PIR, MED24	21	Representative

Table 17 continued: SK-BR3 - Lapatinib + EMBL-703625 combination therapy

ID	Term_Description	Fold_Enrichment	support	highest_p	Up_regulated	Down_regulated	Cluster	Status
GO:0046966	thyroid hormone receptor binding	2.543	0.011	3.942E-05	GTF2B, TACC1, TRIP12, ZNHIT3, THRAP3, BRD8, MED30, JMJD1C	MED24	21	Member
GO:0005154	epidermal growth factor receptor binding	2.584	0.021	4.418E-06	GRB2, SNX1, SNX2, SNX4	EFEMP1, HIP1, PLSCR1, CBLC	22	Representative
GO:0035091	phosphatidylinositol binding	2.316	0.005	9.756E-03	GRB7, NUMA1, SNX1, SNX4, SNX13, APPL1, SNX5, SNX12, APPL2, ESYT2	HIP1, PITPNA, TRPV1, PITPNC1	22	Member
GO:0005158	insulin receptor binding	1.696	0.005	2.748E-02	IGF1R, SNX1, SNX2, SNX4		22	Member
GO:0035198	miRNA binding	2.573	0.069	5.213E-06	FMR1, HNRNPA1, PUM1, MATR3, PUM2, AGO1, RC3H1, NEAT1	ZNF346, ZC3H10, PNPT1	23	Representative
GO:0003730	mRNA 3'-UTR binding	1.334	0.026	1.243E-04	CIRBP, FMR1, HNRNPU, RPL5, PUM1, PUM2, CARHSP1, PABPC1, RNF20, RC3H1	PARN, RNF40	23	Member
GO:0008266	poly(U) RNA binding	2.119	0.011	2.618E-02	FMR1, HNRNPH1, PABPC1	MCRS1, PNPT1	23	Member
GO:0043022	ribosome binding	1.356	0.011	2.650E-02	FMR1, YTHDF1, EIF2A, CPEB2, YTHDF3		23	Member
GO:0008013	beta-catenin binding	1.233	0.079	7.563E-06	APC, CTNNA1, CTNNB1, EP300, FOXO3, SMAD7, FOXO4, DLG5, TBL1XR1	VCL, RUVBL2, AJAP1	24	Representative
GO:0045296	cadherin binding	1.696	0.053	1.521E-05	ACVR1, APC, CTNNA1, CTNNB1, CTNND1, NDRG1	VCL	24	Member
GO:0070530	K63-linked polyubiquitin modification-dependent protein binding	3.391	0.021	8.954E-06	ZBTB1, TAB2, ZRANB1, RNF168, RNF169	IKBKE, ATRIP	25	Representative
GO:0031491	nucleosome binding	3.652	0.021	1.168E-03	NAP1L4, MLLT10, HP1BP3, RNF168, RNF169	GLYR1, DNTTIP1	25	Member
GO:0005085	guanyl-nucleotide exchange factor activity	1.762	0.011	1.032E-05	TIAM1, TRIO, LAMTOR3, ARHGEF7, NET1, VAV3, ARFGEF2, FNIP1, DOCK11, SPATA13	ABR, TBXA2R, VAV1, EIF2B4, EIF2B3, EIF2B2, PREB, RAPGEF3, TIAM2, MON1A	26	Representative
GO:0003743	translation initiation factor activity	2.010	0.011	4.461E-03	EIF3A, EIF3F, EIF3H, EIF3L, EIF2A	EIF2B4, EIF2B3, EIF2B2	26	Member
GO:0008022	protein C-terminus binding	1.553	0.111	1.101E-05	DST, CDK7, CENPF, FOXN3, CTNNB1, EP300, ERBB2, ERCC6, NUMA1, POLR2A, SIAH1, USP7, KSR1, BCL10, MAGI1, PRRC2C, SASH1, SIRT1, NIPBL, PABPC1, SDCBP2	ERCC2, ERCC4, LIG4, TERF2, XRCC4, PEX16, MDC1, CORO1A, MIF4GD	27	Representative
GO:0019900	kinase binding	1.744	0.095	1.148E-05	CTNNB1, GADD45A, DLG3, EEF1A1, POLR2A, PPP2R5A, PRKCD, RPS3, SP100, TIAM1, TAX1BP1, BCL10, PARP16	CDC6, RAD23A, RB1, AURKB, STUB1	28	Representative
GO:0001784	phosphotyrosine residue binding	1.596	0.026	2.997E-05	CRKL, GRB2, RASA1, NCK2	PTPN3, SYK, VAV1, CBLC	29	Representative
GO:0017124	SH3 domain binding	1.696	0.021	1.530E-04	GPX1, GRB2, ADAM9, ABI1, WASF2, CD2AP, REPS1	PLSCR1, RAD9A, CBLC, RUFY1, AFAP1L2	29	Member
GO:0050681	androgen receptor binding	1.758	0.011	3.946E-05	CALR, DAXX, EP300, TMF1, KDM4C, KDM3A	PKN1	30	Representative
GO:0044183	protein binding involved in protein folding	1.130	0.005	2.393E-02	CALR	DFFA	30	Member
GO:0019903	protein phosphatase binding	1.719	0.053	4.865E-05	CTNNB1, ERBB2, JAK1, NEK2, PTK2, STAT3, HSP90B1, IQGAP1, MTMR3, EIF2AK3, KIF3A, PPP6R3, MTMR9	RPA2, IKBKE, ANAPC7, STYXL1, PPP1R3F	31	Representative
GO:0004713	protein tyrosine kinase activity	1.094	0.032	6.060E-05	DYRK1A, ERBB2, IGF1R, INSR, JAK1, PTK2	CSF1R, PTK6, SYK, TNK1	32	Representative
GO:0048156	tau protein binding	1.565	0.005	8.729E-05	APOE, CLU, DYRK1A		32	Member
GO:0004715	non-membrane spanning protein tyrosine kinase activity	1.565	0.011	3.574E-02	CLK1, DYRK1A, JAK1, PTK2	PTK6, SYK	32	Member
GO:0048365	Rac GTPase binding	2.188	0.005	6.149E-05	EPS8, SOD1, WASF1, DOCK4, RALBP1, CYFIP1, RCC2, HACE1	PKN1, ARFIP2	33	Representative
GO:0036002	pre-mRNA binding	2.466	0.053	8.529E-05	HNRNPA1, HNRNPU, SRSF6, CELF1		34	Representative
GO:0031490	chromatin DNA binding	1.565	0.011	9.412E-03	ACTN4, FOXO3, HNRNPU, STAT3, GRHL1	RUVBL2	34	Member
GO:0043021	ribonucleoprotein complex binding	1.615	0.005	4.230E-02	HNRNPU, UHMK1	PRMT5, CBX5, GEMIN4	34	Member
GO:0000993	RNA polymerase II complex binding	2.180	0.005	9.428E-05	GTF2B, HNRNPU, NCOA3, URI1, AGO1, ELP2, RPRD1B, CDC73	WAC	35	Representative
GO:0001046	core promoter sequence-specific DNA binding	2.261	0.016	1.077E-04	NR3C1, GTF2B, HDAC1, ZBTB17, AGO1		35	Member

Table 17 continued: SK-BR3 - Lapatinib + EMBL-703625 combination therapy

ID	Term_Description	Fold_Enrichment	support	highest_p	Up_regulated	Down_regulated	Cluster	Status
GO:0000979	RNA polymerase II core promoter sequence-specific DNA binding	1.696	0.005	4.881E-03	GTF2B, HDAC1	RUVBL2	35	Member
GO:0017025	TBP-class protein binding	1.596	0.005	1.961E-02	DR1, GTF2B	RUVBL1, RUVBL2	35	Member
GO:0031489	myosin V binding	2.261	0.011	1.077E-04	RAB6A, RAB27B, RAB14	RAB8A, RAB3A	36	Representative
GO:0003924	GTPase activity	1.345	0.016	3.220E-03	TRIM23, ARF3, ARL1, CDC42, GNAI3, GNB1, RAB1A, RAB6A, RAB27B, RAB5C, RASA1, RGS10, RHEB, RAB9A, GTPBP1, RRAGB, TPPP, RAB14, RAB33B	DRG2, RAB8A, RAB3A, RGS19, RERG	36	Member
GO:0005525	GTP binding	1.474	0.011	4.876E-03	TRIM23, ARL1, CDC42, EEF1A1, GLUD1, INSR, RAB6A, RAB27B, RHEB, RAB9A, ARL4A, RRAGB, RAB14, ARL8B, ARL8A	RAB8A, EIF2B2, RAB31, ARFIP2, NUDT16	36	Member
GO:0019003	GDP binding	1.729	0.021	1.611E-02	TRIM23, GNAI3, RAB27B, RAB5C, RHEB, RAB9A, RAB18, RAB14, RAB8B, ARL8B	RAB8A, RAB31, RERG	36	Member
GO:0051879	Hsp90 protein binding	1.696	0.021	1.561E-04	CYP1A1, NR3C1, HIF1A, RPS3, TSC1, HDAC8	NPAS2, STUB1	37	Representative
GO:0030544	Hsp70 protein binding	2.180	0.005	3.643E-03	CYP1A1, GPR37, RPS3, TSC1, HDAC8	STUB1, IQCG, METTL21A, RNF207	37	Member
GO:0031072	heat shock protein binding	1.428	0.005	1.268E-02	DAXX, GPR37, TPR	FKBP4, LIMK1, STUB1, METTL23, METTL21A	37	Member
GO:0098505	G-rich strand telomeric DNA binding	2.713	0.021	3.256E-04	HNRNPA1, TERF2IP	RPA2, TERF2	38	Representative
GO:0042162	telomeric DNA binding	1.938	0.011	1.230E-03	TERF2IP, HMBOX1, PIF1	TERF2, TINF2, ACD	38	Member
GO:0016887	ATPase activity	1.413	0.005	3.689E-04	ATP1B1, ATP2B1, CHD3, CLU, EIF4A2, DDX39B, SMARCA5, VWA8, KIF1B, RSF1	ABCD1, TOR1A, NSF, RUVBL1, RUVBL2, MORC2, RNF213, C10orf88, MYO19, SLFN11	39	Representative
GO:0003678	DNA helicase activity	1.453	0.005	1.973E-02	CHD3, ERCC6, RAD54B	ERCC8, RUVBL1, RUVBL2	39	Member
GO:0051087	chaperone binding	1.517	0.021	4.466E-04	AMFR, ATP1A1, CALR, CLU, GRN, SOD1, TSC1, ERP29, GET4, DNAJA4, FNIP2, FNIP1, HSPB6	STUB1, PFDN6, TIMM9, RNF207	40	Representative
GO:0051082	unfolded protein binding	1.735	0.011	3.416E-03	CALR, CLU, NAP1L4, AIP, TOMM20, DNAJA4, UGGT1, HSPB6	CHAF1B, RUVBL2, GRPEL1	40	Member
GO:0005178	integrin binding	0.980	0.005	5.639E-04	ACTN4, ANXA7, DST, CALR, ITGAV, ITGB1, PTK2, PTPN2, ADAM17, ADAM9	S1PR3, ICAM1, SYK	41	Representative
GO:0004879	nuclear receptor activity	1.256	0.011	6.961E-04	NR3C1, RXRB, STAT3, NR1D2	VDR	42	Representative
GO:0001103	RNA polymerase II repressing transcription factor binding	1.180	0.011	1.269E-02	HDAC1, RBPJ, STAT3	MKKS	42	Member
GO:0044877	protein-containing complex binding	1.583	0.048	9.627E-04	APOE, CDKN1C, CLU, DDB1, ERCC6, GNB1, HNRNPU, INSR, ITGB1, NUMA1, RAP1A, RPS3, STRN, USF1, CIR1, CDC42BPB, IST1, NOD1, APPL1, STRN3, LZTFL1, APPL2, HMBOX1, POLDIP3, FLCN	ERCC8, NSF, PFKP, TERF2, DEPDC5, CBX5, AJAP1, ACD, SCAMP5, MLKL	43	Representative
GO:0030332	cyclin binding	0.754	0.005	1.272E-03		CDK2, CDK4, CDK6	44	Representative
GO:0031593	polyubiquitin modification-dependent protein binding	1.995	0.011	1.283E-03	EPS15, RAD23B, ZFAND6	RAD23A, BRCC3	45	Representative
GO:0008327	methyl-CpG binding	1.541	0.016	1.498E-03	CXXC5	PRMT5, MBD3, WDR77, LRWD1	46	Representative
GO:0070888	E-box binding	1.323	0.005	9.381E-03	MAX, MITF, NONO, PSPC1	ASCL2, PRMT5, BHLHE41, SCX	46	Member
GO:0003735	structural constituent of ribosome	1.596	0.011	1.618E-03	RPL10, RPLP0	MRPS12, MRPS16, MRPS7, MRPS11, MRPL57, MRPL55	47	Representative
GO:0034450	ubiquitin-ubiquitin ligase activity	2.466	0.016	2.348E-03	AMFR, UBR5, PELI1	STUB1	48	Representative
GO:1990381	ubiquitin-specific protease binding	1.453	0.011	5.105E-03	AMFR, DERL1	RAD23A	48	Member
GO:0030674	protein binding, bridging	1.799	0.011	1.081E-02	AMFR, DDB1, NCK1, ST13, CRADD, CDYL, CNKSR1, ICE1, SERINC1	ERCC2, FKBP4, STUB1, CBX5	48	Member
GO:0031267	small GTPase binding	2.035	0.016	3.107E-03	ABCA1, BRAF, RAF1, IQGAP1, RCC2, RNF152		49	Representative
GO:0097110	scaffold protein binding	0.424	0.005	2.861E-02	BRAF, DSP	CASP8	49	Member
GO:0070300	phosphatidic acid binding	3.768	0.005	5.559E-03	RAPGEF2, PACSIN2, SESTD1	PITPNC1, JPH2, GRAMD1B, MAPKAP1, PLEKHN1, MICALL1, UQCC3	50	Representative
GO:0005547	phosphatidylinositol-3,4,5-trisphosphate binding	2.593	0.016	9.088E-03	MYO1B, MYO10, OGT, IQGAP1, CYTH3, GAB2, RACGAP1, ZFYVE1, PLEKHB2, KIF16B, PARD3	JPH2, MAPKAP1	50	Member

Table 17 continued: SK-BR3 - Lapatinib + EMBL-703625 combination therapy

ID	Term_Description	Fold_Enrichment	support	highest_p	Up_regulated	Down_regulated	Cluster	Status
GO:0017080	sodium channel regulator activity	1.541	0.005	5.886E-03	SGK1, GPD1L, NEDD4L	PKP2, PTPN3	51	Representative
GO:0042800	histone methyltransferase activity (H3-K4 specific)	0.969	0.005	6.352E-03	CXXC1, KMT2C		52	Representative
GO:0005095	GTPase inhibitor activity	2.261	0.005	6.728E-03	IQGAP1, CPEB2	PDE6D, CDC42SE1	53	Representative
GO:0044548	S100 protein binding	1.565	0.016	8.144E-03	ANXA2, IQGAP1, AHNAK		53	Member
GO:0019904	protein domain specific binding	1.672	0.016	7.078E-03	ARL1, CALM3, DDX6, ACSL3, GUSB, HIF1A, HNRNPA1, INSR, MLF1, NFE2L2, NUMA1, OSBP, PPP3R1, RAB6A, RAB27B, SP100, TRPS1, IQGAP1, VAPA, IST1, CITED2, NCOA2, RCC2, IKZF5, MPP7, OCLN	CDK2, DFFA, DFFB, PLAUR, VRK2, AP4M1, RNF41, RAPGEF3, FHOD1, MRPL17	54	Representative
GO:0070840	dynein complex binding	3.192	0.032	1.178E-02	APC, CENPF, FMR1, NUMA1, PAFAH1B1, TPR, BICD2, ATMIN		55	Representative
GO:0015631	tubulin binding	1.744	0.005	2.754E-02	DCTN1, STMN1, NUMA1, RPS3, TPR, TPPP	TTLL12, IFT81, RITA1	55	Member
GO:0008017	microtubule binding	1.279	0.005	3.116E-02	APC, DCTN1, FMR1, KIF5B, NUMA1, PAFAH1B1, RPS3, ZNF207, VAPA, LRPPRC, NDRG1, TPPP, KATNA1, RAC-GAP1, RCC2, REEP4, FAM83D, CCSAP, GAS2L3	GAS8, REEP1, PSRC1, TUBGCP5	55	Member
GO:0031996	thioesterase binding	1.233	0.005	1.210E-02	CDC42	TRAF4	56	Representative
GO:0050699	WW domain binding	1.428	0.005	1.354E-02	LITAF, RAPGEF2	TRAF4, FAM189B	56	Member
GO:0008289	lipid binding	1.292	0.005	1.247E-02	APOE, HDLBP, PSAP	BAD, BAX, S1PR3, LPAR2, COQ9	57	Representative
GO:0005543	phospholipid binding	1.792	0.005	3.151E-02	JAG1, APOE, ARHGAP35, PSAP, VAMP2, ARHGAP44, SMURF1, SYTL4	BAD, F3, PAFAH2, PTAFR, DYSF, CPTP	57	Member
GO:0046982	protein heterodimerization activity	1.341	0.016	1.595E-02	ADD1, ARNT, ATP1A1, ATP1B1, GADD45A, EPAS1, ERBB2, EXT2, FMR1, HEXA, HIF1A, ITGB1, MCL1, SD-CBP, SNX1, SNX2, USF1, FXR1, VAPA, KATNA1, ZBTB1, FBXO7, GCA, SDCBP2	BAX, BOK, HIP1, PDGFB, MLX, TPM1, NAE1, GABBR2, PRMT5, ZHX2, BHLHE41	58	Representative
GO:0005089	Rho guanyl-nucleotide exchange factor activity	2.142	0.011	1.739E-02	TIAM1, TRIO, FARP2, FARP1, AKAP13, DNMBP		59	Representative
GO:0051721	protein phosphatase 2A binding	1.292	0.005	2.375E-02	STRN, ARPP19, STRN3	MASTL	60	Representative
GO:0016301	kinase activity	1.408	0.011	2.632E-02	CDK7, CSNK1A1, PIK3CA, MAPK1, MAPK8, WEE1, SCYL3	DGKE, PKMYT1, STK39, MASTL	60	Member
GO:0030971	receptor tyrosine kinase binding	2.188	0.005	3.001E-02	NCK1, PTPN2, PTPN14, SOCS5, DOCK4, TOB1	DUSP3, HYAL2, RNF41, PITPNM3	61	Representative
GO:0000146	microfilament motor activity	0.904	0.005	3.536E-02	MYO1B, MYO5B		62	Representative
GO:0035035	histone acetyltransferase binding	1.071	0.005	3.750E-02	EPAS1, HIF1A, CITED2		63	Representative
GO:0002020	protease binding	1.507	0.005	4.002E-02	ANXA2, COL1A1, ITGAV, ITGB1, PSAP, STIM1, TNFAIP3, CRADD, CFLAR, BCL10, ATP9A, RNF139, DERL1	F3, FADD, TNFRSF10A, ADAMTSL4, TYSND1	64	Representative
GO:0051219	phosphoprotein binding	1.826	0.005	4.015E-02	PAFAH1B1, URI1, THRAP3	RB1, TRPV1, TBL2, APTX	65	Representative
GO:0034236	protein kinase A catalytic subunit binding	2.087	0.005	4.062E-02	PRKAR2B, SOX9, PJA2	PRKAR1B	66	Representative
GO:0000149	SNARE binding	2.261	0.005	4.519E-02	VAMP2, STX7, VTI1B, GABARAPL2	NSF, SNAPIN	67	Representative
GO:0004535	poly(A)-specific ribonuclease activity	3.083	0.005	4.772E-02	CNOT8, CNOT6L, PAN3	PARN, TOE1	68	Representative

Table 17: De-regulated genes and networks (see section 2.2 for details on how significance was calculated) in SK-BR3 cells treated with 0.2µM lapatinib and 1µM EMBL-703625

Table 18 SK-BR3 - Lapatinib monotherapy: Hierarchial clustering

ID	Term_Description	Fold_Enrichment	support	highest_p	Up_regulated	Down_regulated	Cluster	Status
GO:0004842	ubiquitin-protein transferase activity	1.673	0.010	6.472E-06	PJA2, RNF13, TRIM2, RNF152	TRAF3, UHRF1	1	Representative
GO:0031996	thioesterase binding	4.385	0.010	5.985E-03		TRAF3	1	Member
GO:0034236	protein kinase A catalytic subunit binding	3.710	0.005	6.944E-03	PJA2		1	Member
GO:0061578	Lys63-specific deubiquitinase activity	8.770	0.128	1.002E-05	CYLD, ATXN3		2	Representative
GO:0004843	thiol-dependent ubiquitin-specific protease activity	3.216	0.046	6.096E-05	CYLD, ATXN3, USP53	USP2, USP18	2	Member
GO:0070064	proline-rich region binding	7.421	0.046	1.018E-02	CYLD	CCND1	2	Member
GO:1990841	promoter-specific chromatin binding	2.680	0.005	2.351E-04	RBL2	E2F4	3	Representative
GO:0008134	transcription factor binding	0.897	0.010	2.966E-03	KAT6B	CCND1, E2F1, E2F4	3	Member
GO:0003684	damaged DNA binding	4.668	0.015	6.876E-04	CRY2	FEN1, UNG	4	Representative
GO:0008409	5'-3' exonuclease activity	10.719	0.015	3.208E-03		FEN1, EXO1	4	Member
GO:0000987	proximal promoter sequence-specific DNA binding	5.882	0.031	8.323E-04	ATF2	E2F1, E2F3, UHRF1, E2F7	5	Representative
GO:0003779	actin binding	2.607	0.005	1.401E-03	IQGAP2, NCALD	EMD, TPM1, CORO1A, COTL1	6	Representative
GO:0051015	actin filament binding	2.566	0.005	1.993E-02	IQGAP2, LIMA1	BIN1, TPM1, CORO1A	6	Member
GO:0008092	cytoskeletal protein binding	3.445	0.005	3.352E-02		TPM1, CORO1A	6	Member
GO:0005159	insulin-like growth factor receptor binding	8.039	0.010	5.877E-03	SOCS2	YWHAG	7	Representative
GO:0031625	ubiquitin protein ligase binding	1.413	0.005	6.254E-03	CAMLG, ATXN3, GABARAPL1, ANKRA2	TRAF3, USP2, MFHAS1	8	Representative
GO:0030332	cyclin binding	3.573	0.005	3.114E-02		CDK2, USP2	8	Member
GO:0048156	tau protein binding	3.710	0.005	1.018E-02		BIN1	9	Representative
GO:0051087	chaperone binding	3.173	0.005	4.769E-02	GET4, FNIP1	BIN1, CDC25A, UBL4A	9	Member
GO:0001228	DNA-binding transcription activator activity, RNA polymerase II-specific	1.870	0.010	1.507E-02	ATF2, ZNF24, POU2F3, HINFP, EHF, CREBRF	E2F3, E2F4, ETV4, NFIC	10	Representative
GO:0000978	RNA polymerase II proximal promoter sequence-specific DNA binding	1.331	0.010	2.378E-02	ATF2, KLF8, POU2F3, EHF, CALCOCO1	E2F4, ETV4, NFIC	10	Member
GO:0001227	DNA-binding transcription repressor activity, RNA polymerase II-specific	0.952	0.005	2.512E-02	NFATC4, KLF8	JDP2	11	Representative
GO:0070412	R-SMAD binding	2.539	0.010	3.537E-02	LDLRAD4		12	Representative
GO:0051059	NF-kappaB binding	2.010	0.010	3.589E-02		BRMS1	13	Representative
GO:0001784	phosphotyrosine residue binding	1.419	0.005	4.968E-02	BCAR3		14	Representative

Table 18: De-regulated genes and networks (see section 2.2 for details on how significance was calculated) in SK-BR3 cells treated with 0.2µM lapatinib

Table 19 SK-BR3 - EMBL-703625 monotherapy: Hierarchial clustering

ID	Term_Description	Fold_Enrichment	Support	Adj p-value	Up_regulated	Down_regulated	Cluster	Status
GO:0004842	ubiquitin-protein transferase activity	3.342	0.165	1.553E-28	AMFR, RNF2, SIAH1, UBE2D1, UBE2D3, UBE2E1, UBE2L3, RNF103, AREL1, TOPORS, RNF139, ARIH1, RCHY1, FBXL3, FBXO22, FBXO3, RNF115, MYLIP, TRIM33, SMURF1, CBLL1, ZFP91, UBE2Q2, UHRF2, RC3H1	XIAP, BRCA1, RNF41, TRIM62, TRIM56, TRIM69, DTX3L, NHLRC1	1	Representative
GO:0061630	ubiquitin protein ligase activity	3.227	0.065	1.886E-17	AMFR, CDC42, SIAH1, RNF103, RNF10, TOPORS, RNF139, RCHY1, RNF11, RNF115, MYLIP, MEX3C, SMURF1, PELI1, UHRF2, RNF19B, RC3H1	XIAP, NFX1, RNF41, TRAF3IP2	1	Member
GO:0061631	ubiquitin conjugating enzyme activity	5.005	0.075	2.394E-10	UBE2D1, UBE2D3, UBE2E1, UBE2L3, UBE2J1	UBE2J2	2	Representative
GO:0031625	ubiquitin protein ligase binding	1.539	0.065	2.050E-05	FOXO1, GPR37, JAK1, SMAD5, POLR2A, TMBIM6, UBE2L3, BCL10, BAG4, TRIB1, ARIH1, USP25, UBE2J1, OTUB1, DERL1, CCDC50	BRCA1, LTBR, TP53, DET1, UBE2J2	2	Member
GO:0004843	thiol-dependent ubiquitin-specific protease activity	3.270	0.02	1.077E-09	USP4, USP15, USP3, OTUD3, USP24, USP25, DESI2, OTUD6B, OTUD4, OTUB1, USP46, USP42, USP45	BRCC3	3	Representative
GO:0000976	transcription regulatory region sequence-specific DNA binding	1.619	0.055	5.503E-08	AHR, MSX2, NFE2L2, NFYA, NFYC, REST, TAF9, YY1, KLF11, RNF10, GRHL1, TBL1XR1	BRCA1, RFX5, TAF2, TP53, GABPB2	4	Representative
GO:0000981	DNA-binding transcription factor activity, RNA polymerase II-specific	1.222	0.01	2.766E-03	MAX, MSX2, KLF11, HEY1	TP53, HIF3A	4	Member
GO:0004674	protein serine/threonine kinase activity	1.971	0.04	2.513E-07	ACVR2A, MAP3K8, CSNK1G3, DYRK1A, MAP3K1, MAPK1, MAPK6, MAPK8, RAF1, SGK1, SRPK2, DYRK2, PPM1D, MAP3K13, STK17A, SLK, TLK1, HIPK3, MAP3K2, PLK2, UHMK1, NEK7, SIK1	MAP3K10, SYK, DAPK2, IRAK4	5	Representative
GO:0004672	protein kinase activity	1.635	0.005	3.704E-02	CHUK, CSNK1G3, DYRK1A, MAP3K1, CDK17, PRKAA1, RPS6KB1, HIPK3, TRIB1, MAP3K2	CAD, SYK, IRAK4, MLKL	5	Member
GO:0042393	histone binding	2.533	0.015	1.870E-06	MLLT10, SMARCA5, USP3, KDM5B, SIRT1, SFMBT1, TBL1XR1, UHRF2, SPTY2D1	PRMT6, L3MBTL2, DTX3L	6	Representative
GO:0003714	transcription corepressor activity	1.690	0.005	4.297E-04	PAWR, NRIP1, URI1, KDM5B, SIRT1, RBFOX2, SFMBT1, TBL1XR1	MAP3K10, PPP1R13L, KCTD1	6	Member
GO:0003729	mRNA binding	3.234	0.035	2.687E-06	ZFP36L1, DDX3X, CELF1, CPSF6, LUC7L3, METTL14, RBM25, RBM15	PURB, UPF3B, NSRP1, NUDT16	7	Representative
GO:0003723	RNA binding	2.228	0.075	5.880E-05	DDX3X, HNRNPH1, AGFG1, SON, YY1, PUM1, RBM7, CELF1, CPSF6, SCAF8, RBFOX2, AGO1, MEX3C, RBM15, NAF1	BRCA1, RANGAP1, RNASEL, NOL3, EMG1, RBM15B, CPSF3	7	Member
GO:0003682	chromatin binding	1.659	0.035	1.121E-05	BCL6, CCNT2, CTNNB1, ELK4, FOXO1, PRKAA1, REST, RNF2, BRD2, MLLT10, URI1, CHD7	TP53, MORC2, CAMTA2, NUCKS1	8	Representative
GO:0008134	transcription factor binding	1.793	0.07	1.302E-05	AHR, CCNT1, CEBPG, CTNNB1, DDX3X, EPAS1, GTF2B, RBPJ, REST, BCL10, TRIB1, SIRT1, RBFOX2	PURB, TAF12, MLX, TP53, CAMTA2, NUCKS1, KAT8, METTL23, KCTD1	8	Member
GO:0008022	protein C-terminus binding	1.872	0.05	1.659E-05	CTNNB1, POLR2A, SIAH1, TAF13, BCL10, MAPRE1, SIRT1, NIPBL	ERCC4, PEX6, TERF2, XRCC4, MDC1, IFT46	9	Representative
GO:0019900	kinase binding	1.502	0.01	2.032E-03	CTNNB1, POLR2A, SNAI1, TAX1BP1, BCL10, UBQLN1		9	Member
GO:0000978	RNA polymerase II proximal promoter sequence-specific DNA binding	0.906	0.015	6.469E-05	KLF5, ELK4, HSF2, RBPJ, SMAD5, NFYA, NFYC, REST, TGIF1, UBP1, NRIP1, GRHL1, NKRF	TP53, HIF3A	10	Representative
GO:0001228	DNA-binding transcription activator activity, RNA polymerase II-specific	1.222	0.005	3.489E-02	ATF1, KLF5, CDC5L, CEBPG, ELK4, FOXO1, HSF2, RBPJ, UBP1, PRDM2, FOXJ3, GRHL1, NKRF, YY2	RFX5, TP53, ZNF76, SCX	10	Member
GO:0004402	histone acetyltransferase activity	4.088	0.02	1.292E-04	TAF9, SRCAP, KAT7, TAF5L	TADA2A, TAF12, KAT8	11	Representative
GO:0003713	transcription coactivator activity	1.406	0.01	1.515E-03	CTNNB1, TAF9, UBE2L3, NRIP1, BCL10, MED26, LPIN2, SRCAP, TAF5L, TADA1	BRCA1, TAF12, CAMTA2	11	Member

Table 19 continued: SK-BR3 - EMBL-703625 monotherapy

ID	Term_Description	Fold_Enrichment	Support	Adj p-value	Up_regulated	Down_regulated	Cluster	Status
GO:0047485	protein N-terminus binding	2.920	0.035	2.593E-04	GLRX, MNAT1, PPP1CC, SDCBP, MORF4L1, PDCD10, NIPBL, DCTN4, TBL1XR1	ERCC4, STX5, TP53, THAP7	12	Representative
GO:0042826	histone deacetylase binding	1.314	0.01	6.716E-03	MAPK8, NIPBL, MIER1	TP53, CAMTA2, THAP7	12	Member
GO:0001784	phosphotyrosine residue binding	2.061	0.015	3.396E-04	CRKL, GRB2	SYK, VAV1	13	Representative
GO:0002039	p53 binding	1.622	0.035	5.554E-04	TAF9, TP53BP2, SIRT1, RCHY1	TP53	14	Representative
GO:0035257	nuclear hormone receptor binding	2.285	0.015	1.952E-03	CTNNB1, NRIP1, SIRT1		14	Member
GO:0004407	histone deacetylase activity	2.190	0.005	5.704E-03	SIRT1, MIER1		14	Member
GO:0033558	protein deacetylase activity	1.593	0.005	4.094E-02	SIRT1		14	Member
GO:0044389	ubiquitin-like protein ligase binding	2.061	0.005	6.088E-04	STAM	DTX3L	15	Representative
GO:0004713	protein tyrosine kinase activity	2.543	0.015	1.070E-03	DYRK1A, JAK1, TWF1, RYK, DYRK2	CSF1R, PTK6, SYK, TNK1	16	Representative
GO:0035035	histone acetyltransferase binding	2.766	0.025	1.072E-03	EPAS1, ECD	TP53	17	Representative
GO:0051087	chaperone binding	0.692	0.005	1.826E-02	AMFR, BAG2	TP53	17	Member
GO:0051721	protein phosphatase 2A binding	2.503	0.005	1.850E-02	FOXO1, STRN	TP53	17	Member
GO:0043621	protein self-association	1.752	0.01	2.385E-02	DYRK1A, BCL10, KCTD9	TP53	17	Member
GO:0031369	translation initiation factor binding	5.256	0.005	1.207E-03	DDX3X	EIF2B4, TBL2	18	Representative
GO:0035613	RNA stem-loop binding	3.504	0.005	4.677E-02	DDX3X, RC3H1		18	Member
GO:0001046	core promoter sequence-specific DNA binding	3.504	0.005	1.321E-03	GTF2B, AGO1	TP53	19	Representative
GO:0000993	RNA polymerase II complex binding	3.754	0.005	7.416E-03	GTF2B, URI1, AGO1, RPRD1B, CDC73	ELP4	19	Member
GO:1990841	promoter-specific chromatin binding	1.947	0.025	7.774E-03	GTF2B, POLR2A, NIPBL	TP53	19	Member
GO:0003779	actin binding	0.789	0.005	1.589E-03	EPS8, ABLIM1, PAWR, TWF1, MICAL3		20	Representative
GO:0005516	calmodulin binding	1.812	0.005	1.673E-03	RGS2, STRN	PPP3CB, TRPV1, DAPK2, IQCG	21	Representative
GO:0070412	R-SMAD binding	2.766	0.005	2.218E-03	PPM1A, TRIM33, SMURF1		22	Representative
GO:0001227	DNA-binding transcription repressor activity, RNA polymerase II-specific	1.268	0.03	2.294E-03	BACH1, MAX, REST, SNAI1, TGIF1, YY1, PRDM2, HEY1, ZNF350	NFX1, MLX	23	Representative
GO:0070888	E-box binding	2.136	0.005	1.546E-02	AHR, MAX, SNAI1, PSPC1	SCX	23	Member
GO:0000977	RNA polymerase II regulatory region sequence-specific DNA binding	1.251	0.015	2.432E-02	ATF1, CDC5L, HSF2, MAX, SNAI1, SP3, PRDM2	NFX1, MLX	23	Member
GO:0071889	14-3-3 protein binding	5.005	0.005	2.573E-03	ZFP36L1, PPP1R12A, SRPK2, RBM7, SIK1	KLHL22	24	Representative
GO:0016791	phosphatase activity	2.595	0.005	2.596E-03	PPP1CB, PPP1CC, DUSP10	DUSP18	25	Representative
GO:0004722	protein serine/threonine phosphatase activity	3.185	0.005	1.041E-02	PPM1A, PPP1CC, PPP2CA, PPM1D	PPP1R3D, PPM1F	25	Member
GO:0004721	phosphoprotein phosphatase activity	2.285	0.005	1.455E-02	PPP1CC, PPP2CA	CDC25B	25	Member
GO:0008013	beta-catenin binding	1.062	0.015	3.119E-03	CTNNB1, FOXO1, TBL1XR1	CBY1	26	Representative
GO:0046332	SMAD binding	2.503	0.02	7.133E-03	CTNNB1, YY1, TGFBRAP1, USP15, IPO7		26	Member
GO:0001085	RNA polymerase II transcription factor binding	0.898	0.01	2.385E-02	CTNNB1	TP53	26	Member
GO:0070411	I-SMAD binding	3.504	0.015	3.856E-02	CTNNB1, SMURF1		26	Member
GO:0008270	zinc ion binding	1.173	0.01	3.503E-03	GTF2B, LIMS1, MNAT1, PGGT1B, RLF, RNF2, SIAH1, KDM5B, ARIH1, RCHY1, RNF11, RC3H1	CAD, TP53, MORC2, SIRT5	27	Representative
GO:0051020	GTPase binding	3.504	0.005	5.657E-03	BNIP3, GNB1, RRAGB, ATG14, FNBP1L		28	Representative

Table 19 continued: SK-BR3 - EMBL-703625 monotherapy

ID	Term_Description	Fold_Enrichment	Support	Adj p-value	Up_regulated	Down_regulated	Cluster	Status
GO:0043022	ribosome binding	2.102	0.005	7.089E-03	YTHDF1, EIF2A, YTHDF3		29	Representative
GO:0000049	tRNA binding	3.369	0.005	3.129E-02	EIF2A	PTCD1, THG1L, PUS1, SLFN11	29	Member
GO:0046982	protein heterodimerization activity	1.386	0.02	7.506E-03	AHR, ATP1B1, CHUK, EPAS1, PPP2CA, SDCBP, FXR1, VAPA, ZBTB1, GCA	MLX, TP53, GABBR2, ZHX2	30	Representative
GO:0019888	protein phosphatase regulator activity	1.593	0.005	8.594E-03	PPP2R5E	PPP2R3B	31	Representative
GO:1990381	ubiquitin-specific protease binding	3.754	0.005	8.973E-03	AMFR, SPATA2, DERL1		32	Representative
GO:0005525	GTP binding	2.285	0.01	1.056E-02	CDC42, RAB9A, RRAGB, DYNC1LI1, RAB14, ARL8B, LSG1, ARL8A	RAB31, ATL1, THG1L, NUDT16	33	Representative
GO:0019003	GDP binding	3.092	0.01	4.604E-02	GNAI3, RAB9A, RAB18, DYNC1LI1, RAB14, RAB8B, ARL8B	RAB31, RERG	33	Member
GO:0003924	GTPase activity	2.172	0.005	4.916E-02	ARF3, CDC42, DDX3X, GNAI3, GNB1, RGS2, RAB9A, RRAGB, RHOQ, RAB14, LSG1, RAB33B	RGS19, ATL1, RERG	33	Member
GO:0035064	methylated histone binding	2.503	0.01	1.441E-02	ING1, SPIN1, MTF2, SPIN3	CBX5, THAP7, L3MBTL2, KAT8	34	Representative
GO:0070530	K63-linked polyubiquitin modification-dependent protein binding	6.257	0.01	1.522E-02	ZBTB1, TAB2, RNF169	ZRANB3, ATRIP	35	Representative
GO:0031593	polyubiquitin modification-dependent protein binding	4.122	0.015	1.662E-02	RAD23B, UBQLN1, ZFAND6	BRCC3	36	Representative
GO:0016301	kinase activity	0.992	0.01	2.033E-02	MAPK1, MAPK8, RPS6KB1		37	Representative
GO:0003725	double-stranded RNA binding	1.911	0.005	2.272E-02	SUPV3L1, DICER1, AGO1, RC3H1	ZNF346, DUS2	38	Representative
GO:0044877	protein-containing complex binding	1.285	0.005	4.612E-02	GNB1, RAP1A, STRN, IST1, SPATA2, LZTFL1	PEX6, TERF2, CBX5, DET1, MLKL	39	Representative

Table 19: De-regulated genes and networks (see section 2.2 for details on how significance was calculated) in SK-BR3 cells treated with 1µM EMBL-703625

Bibliography

[1] Yuzheng Zhao, Qingxun Hu, Feixiong Cheng, Ni Su, Aoxue Wang, Yejun Zou, Hanyang Hu, Xianjun Chen, Hai-Meng Zhou, Xinzhi Huang, et al. SoNar, a highly responsive NAD+/NADH sensor, allows high-throughput metabolic screening of anti-tumor agents. *Cell metabolism*, 21(5):777–789, 2015.

[2] Sauid Ishaq and Lois Nunn. Helicobacter pylori and gastric cancer: a state of the art review. *Gastroenterology and hepatology from bed to bench*, 8(Suppl1):S6, 2015.

[3] Francesc X Bosch, Attila Lorincz, Nubia Muñoz, CJLM Meijer, and Keerti V Shah. The causal relation between human papillomavirus and cervical cancer. *Journal of clinical pathology*, 55(4):244–265, 2002.

[4] Jun Yun, Yang Li, Chang-Tai Xu, and Bo-Rong Pan. Epidemiology and Rb1 gene of retinoblastoma. *International Journal of Ophthalmology*, 4(1):103, 2011.

[5] Nancie Petrucelli, Mary B Daly, and Tuya Pal. BRCA1-and BRCA2-associated hereditary breast and ovarian cancer. In *GeneReviews®[Internet], year=2016, publisher=University of Washington, Seattle*.

[6] Lukáš Lacina, Matúš Čoma, Barbora Dvořánková, Ondřej Kodet, Nikola Melegova, Peter Gal, and Karel Smetana. Evolution of Cancer progression in the context of Darwinism. *Anticancer Research*, 39(1):1–16, 2019.

[7] Simon Baker, Imran Ali, Ilona Silins, Sampo Pyysalo, Yufan Guo, Johan Högberg, Ulla Stenius, and Anna Korhonen. Cancer Hallmarks Analytics Tool (CHAT): a text mining approach to organize and evaluate scientific literature on cancer. *Bioinformatics*, 33(24):3973–3981, 2017.

[8] Reza Bayat Mokhtari, Tina S Homayouni, Narges Baluch, Evgeniya Morgatskaya, Sushil Kumar, Bikul Das, and Herman Yeger. Combination therapy in combating cancer. *Oncotarget*, 8(23):38022, 2017.

[9] Joshua D Schiffman, Paul G Fisher, and Peter Gibbs. Early detection of cancer: past, present, and future. *American Society of Clinical Oncology Educational Book*, 35(1):57–65, 2015.

[10] Lynda Wyld, Riccardo A Audisio, and Graeme J Poston. The evolution of cancer surgery and future perspectives. *Nature Reviews Clinical Oncology*, 12(2):115, 2015.

[11] Krapcho M Miller D Brest A Yu M Ruhl J Tatalovich Z Mariotto A Lewis DR Chen HS Feuer EJ Cronin KA (eds). Howlader N, Noone AM. SEER cancer statistics review, 1975-2018. *National Cancer Institute*, pages 1–12, 2017.

[12] Freddie Bray, Jacques Ferlay, Isabelle Soerjomataram, Rebecca L Siegel, Lindsey A Torre, and Ahmedin Jemal. Global cancer statistics 2018: GLOBOCAN estimates of incidence and mortality worldwide for 36 cancers in 185 countries. *CA: a cancer journal for clinicians*, 68(6):394–424, 2018.

[13] KAREL SMETANA, LUKÁŠ LACINA, Pavol Szabo, BARBORA DVOŘÁNKOVÁ, PROKOP BROŽ, and ALEKSI ŠEDO. Ageing as an important risk factor for cancer. *Anticancer research*, 36(10):5009–5017, 2016.

[14] Aruna Surakasula, Govardhana Chary Nagarjunapu, and KV Raghavaiah. A comparative study of pre-and post-menopausal breast cancer: Risk factors, presentation, characteristics and management. *Journal of research in pharmacy practice*, 3(1):12, 2014.

[15] Michiko T Yasuda, Hiroyuki Sakakibara, and Kayoko Shimoi. Estrogen-and stress-induced DNA damage in breast cancer and chemoprevention with dietary flavonoid. *Genes and Environment*, 39(1):1–9, 2017.

[16] Steven A Narod, Javaid Iqbal, and Anthony B Miller. Why have breast cancer mortality rates declined? *Journal of Cancer Policy*, 5:8–17, 2015.

[17] Alfonso M Pluchinotta, Giorgio Macellari, and Gigliola Lodovichetti. Benign lesions of the breast. In *The Outpatient Breast Clinic*, pages 197–239. Springer, 2015.

[18] Teresa L Mastracci, Suzanna Tjan, Anita L Bane, Frances P O'Malley, and Irene L Andrulis. E-cadherin alterations in atypical lobular hyperplasia and lobular carcinoma in situ of the breast. *Modern Pathology*, 18(6):741–751, 2005.

[19] Marilyn J Borst and John A Ingold. Metastatic patterns of invasive lobular versus invasive ductal carcinoma of the breast. *Surgery*, 114(4):637–642, 1993.

[20] Helen Tower, Meagan Ruppert, and Kara Britt. The immune microenvironment of breast cancer progression. *Cancers*, 11(9):1375, 2019.

[21] Rebecca L Siegel, Kimberly D Miller, and Ahmedin Jemal. Cancer Statistics, 2019. *CA: a cancer journal for clinicians*, 69(1):7–34, 2019.

[22] Marissa C van Maaren, Linda de Munck, Luc JA Strobbe, Gabe S Sonke, Pieter J Westenend, Marjolein L Smidt, Philip MP Poortmans, and Sabine Siesling. Ten-year recurrence rates for breast cancer subtypes in the Netherlands: A large population-based study. *International journal of cancer*, 144(2):263–272, 2019.

[23] Pavan Kumar Jonnada, Cherukuru Sushma, Madhuri Karyampudi, and Anvesh Dharanikota. Prevalence of Molecular Subtypes of Breast Cancer in India: a Systematic Review and Meta-analysis. *Indian Journal of Surgical Oncology*, pages 1–12, 2020.

[24] Jennifer J Gao and Sandra M Swain. Luminal a breast cancer and molecular assays: a review. *The oncologist*, 23(5):556, 2018.

[25] Chihiro Hata, Hirofumi Nakaoka, Yu Xiang, Dong Wang, Anping Yang, Dahai Liu, Fang Liu, Qingfeng Zou, Li Wei, Ke Zheng, et al. Germline mutations of multiple breast cancer-related genes are differentially associated with triple-negative breast cancers and prognostic factors. *Journal of human genetics*, 65(7):577–587, 2020.

[26] Solene De Talhouet, Julien Peron, Aurelie Vuilleumier, Alex Friedlaender, Valeria Viassolo, Aurélie Ayme, Alexandre Bodmer, Isabelle Treilleux, Noemie Lang, Jean-Christophe Tille, et al. Clinical outcome of breast cancer in carriers of BRCA1 and BRCA2 mutations according to molecular subtypes. *Scientific reports*, 10(1):1–9, 2020.

[27] Giampaolo Bianchini, Justin M Balko, Ingrid A Mayer, Melinda E Sanders, and Luca Gianni. Triple-negative breast cancer: challenges and opportunities of a heterogeneous disease. *Nature reviews Clinical oncology*, 13(11):674, 2016.

[28] Tingting Jiang, Weiwei Shi, Vikram B Wali, Lőrinc S Pongor, Charles Li, Rosanna Lau, Balázs Győrffy, Richard P Lifton, William F Symmans, Lajos Pusztai, et al. Predictors of chemosensitivity in triple negative breast cancer: an integrated genomic analysis. *PLoS medicine*, 13(12):e1002193, 2016.

[29] François Bertucci, Pascal Finetti, Anthony Goncalves, and Daniel Birnbaum. The therapeutic response of ER+/HER2- breast cancers differs according to the molecular Basal or Luminal subtype. *NPJ breast cancer*, 6(1):1–7, 2020.

[30] Ben Tran and Philippe L Bedard. Luminal-B breast cancer and novel therapeutic targets. *Breast Cancer Research*, 13(6):221, 2011.

[31] Caroline J Witton. Structure of HER receptors and intracellular localisation of downstream effector elements gives insight into mechanism of tumour growth promotion. *Breast Cancer Research*, 5(4):206, 2003.

[32] Hyun-Soo Cho, Karen Mason, Kasra X Ramyar, Ann Marie Stanley, Sandra B Gabelli, Dan W Denney, and Daniel J Leahy. Structure of the extracellular region of HER2 alone and in complex with the Herceptin Fab. *Nature*, 421(6924):756–760, 2003.

[33] Samuel Bouyain, Patti A Longo, Shiqing Li, Kathryn M Ferguson, and Daniel J Leahy. The extracellular region of ErbB4 adopts a tethered conformation in the absence of ligand. *Proceedings of the National Academy of Sciences*, 102(42):15024–15029, 2005.

[34] Hyun-Soo Cho and Daniel J Leahy. Structure of the extracellular region of HER3 reveals an interdomain tether. *Science*, 297(5585):1330–1333, 2002.

[35] Kathryn M Ferguson, Mitchell B Berger, Jeannine M Mendrola, Hyun-Soo Cho, Daniel J Leahy, and Mark A Lemmon. EGF activates its receptor by removing interactions that autoinhibit ectodomain dimerization. *Molecular cell*, 11(2):507–517, 2003.

[36] Marlon R Schneider and Eckhard Wolf. The epidermal growth factor receptor ligands at a glance. *Journal of cellular physiology*, 218(3):460–466, 2009.

[37] Kermit L Carraway, Mark X Sliwkowski, Robert Akita, Jill V Platko, Pamela M Guy, Andrew Nuijens, A John Diamonti, Richard L Vandlen, Lewis C Cantley, and Richard A Cerione. The erbB3 gene product is a receptor for heregulin. *Journal of Biological Chemistry*, 269(19): 14303–14306, 1994.

[38] Kermit L Carraway III, Janet L Weber, Michelle J Unger, Jessica Ledesma, Naichen Yu, Martin Gassmann, and Cary Lai. Neuregulin-2, a new ligand of ErbB3/ErbB4-receptor tyrosine kinases. *Nature*, 387(6632):512–516, 1997.

[39] Kristina Goutsouliak, Jamunarani Veeraraghavan, Vidyalakshmi Sethunath, Carmine De Angelis, C Kent Osborne, Mothaffar F Rimawi, and Rachel Schiff. Towards personalized treatment for early stage HER2-positive breast cancer. *Nature Reviews Clinical Oncology*, pages 1–18, 2019.

[40] Diana Graus-Porta, Roger R Beerli, John M Daly, and Nancy E Hynes. ErbB-2, the preferred heterodimerization partner of all ErbB receptors, is a mediator of lateral signaling. *The EMBO journal*, 16(7):1647–1655, 1997.

[41] Jennifer L Macdonald-Obermann and Linda J Pike. Different epidermal growth factor (EGF) receptor ligands show distinct kinetics and biased or partial agonism for homodimer and heterodimer formation. *Journal of Biological Chemistry*, 289(38):26178–26188, 2014.

[42] Allison P Belsches-Jablonski, Jacqueline S Biscardi, Dena R Peavy, David A Tice, Davis A Romney, and Sarah J Parsons. Src family kinases and HER2 interactions in human breast cancer cell growth and survival. *Oncogene*, 20(12):1465–1475, 2001.

[43] Harold Kim, Richard Chan, David L Dankort, Dongmei Zuo, Monica Najoukas, Morag Park, and William J Muller. The c-Src tyrosine kinase associates with the catalytic domain of ErbB-2: implications for ErbB-2 mediated signaling and transformation. *Oncogene*, 24(51): 7599–7607, 2005.

[44] Richard Marcotte, Lixin Zhou, Harold Kim, Calvin D Roskelly, and William J Muller. c-Src associates with ErbB2 through an interaction between catalytic domains and confers enhanced transforming potential. *Molecular and cellular biology*, 29(21):5858–5871, 2009.

[45] Sara Sigismund, Daniele Avanzato, and Letizia Lanzetti. Emerging functions of the EGFR in cancer. *Molecular oncology*, 12(1):3–20, 2018.

[46] Min Yan, Maria Schwaederle, David Arguello, Sherri Z Millis, Zoran Gatalica, and Razelle Kurzrock. HER2 expression status in diverse cancers: review of results from 37,992 patients. *Cancer and Metastasis Reviews*, 34(1):157–164, 2015.

[47] Alan L Schechter, David F Stern, Lalitha Vaidyanathan, Stuart J Decker, Jeffrey A Drebin, Mark I Greene, and Robert A Weinberg. The neu oncogene: an erb-B-related gene encoding a 185,000-Mr tumour antigen. *Nature*, 312(5994):513–516, 1984.

[48] Dennis J Slamon, Gary M Clark, Steven G Wong, Wendy J Levin, Axel Ullrich, and William L McGuire. Human breast cancer: correlation of relapse and survival with amplification of the HER-2/neu oncogene. *science*, 235(4785):177–182, 1987.

[49] Ron Bose, Shyam M Kavuri, Adam C Searleman, Wei Shen, Dong Shen, Daniel C Koboldt, John Monsey, Nicholas Goel, Adam B Aronson, Shunqiang Li, et al. Activating HER2 mutations in HER2 gene amplification negative breast cancer. *Cancer discovery*, 3(2):224–237, 2013.

[50] Eldad Tzahar, Hadassa Waterman, Xiomei Chen, GIL Levkowitz, Devarajan Karunagaran, Sara Lavi, Barry J Ratzkin, and Yosef Yarden. A hierarchical network of interreceptor interactions determines signal transduction by Neu differentiation factor/neuregulin and epidermal growth factor. *Molecular and cellular biology*, 16(10):5276–5287, 1996.

[51] Ronit Pinkas-Kramarski, Lior Soussan, Hadassa Waterman, Gil Levkowitz, Iris Alroy, Leah Klapper, Sara Lavi, Rony Seger, Barry J Ratzkin, M Sela, et al. Diversification of Neu differentiation factor and epidermal growth factor signaling by combinatorial receptor interactions. *The EMBO journal*, 15(10):2452–2467, 1996.

[52] DJ 2nd Riese, TM Van Raaij, Gregory D Plowman, Glenn C Andrews, and David F Stern. The cellular response to neuregulins is governed by complex interactions of the erbB receptor family. *Molecular and cellular biology*, 15(10):5770–5776, 1995.

[53] Yasuo Kokai, Jeffrey N Myers, Takuro Wada, Valerie I Brown, Charles M LeVea, James G Davis, Kunio Dobashi, and Mark I Greene. Synergistic interaction of p185c-neu and the EGF receptor leads to transformation of rodent fibroblasts. *Cell*, 58(2):287–292, 1989.

[54] Maurizio Alimandi, Alfredo Romano, Maria Cristina Curia, Raffaella Muraro, Paolo Fedi, Stuart A Aaronson, Pier Paolo Di Fiore, and Matthias H Kraus. Cooperative signaling of ErbB3 and ErbB2 in neoplastic transformation and human mammary carcinomas. *Oncogene*, 10 (9):1813–1822, 1995.

[55] Christian Wallasch, FU Weiss, G Niederfellner, BAHIJA Jallal, W Issing, and A Ullrich. Heregulin-dependent regulation of HER2/neu oncogenic signaling by heterodimerization with HER3. *The EMBO journal*, 14(17):4267–4275, 1995.

[56] David B Vaught, Jamie C Stanford, Christian Young, Donna J Hicks, Frank Wheeler, Cammie Rinehart, Violeta Sánchez, John Koland, William J Muller, Carlos L Arteaga, et al. HER3 is required for HER2-induced preneoplastic changes to the breast epithelium and tumor formation. *Cancer research*, 72(10):2672–2682, 2012.

[57] Olli-P Kallioniemi, Anne Kallioniemi, Wayne Kurisu, Ann Thor, Ling-Chun Chen, Helene S Smith, Frederic M Waldman, Dan Pinkel, and Joe W Gray. ERBB2 amplification in breast cancer analyzed by fluorescence in situ hybridization. *Proceedings of the National Academy of Sciences*, 89(12):5321–5325, 1992.

[58] Diana B Peckys, Ulrike Korf, and Niels de Jonge. Local variations of HER2 dimerization in breast cancer cells discovered by correlative fluorescence and liquid electron microscopy. *Science advances*, 1(6):e1500165, 2015.

[59] Sean P Kennedy, Jeremy ZR Han, Neil Portman, Max Nobis, Jordan F Hastings, Kendelle J Murphy, Sharissa L Latham, Antonia L Cadell, Dushan Miladinovic, Gabriella R Marriott, et al. Targeting promiscuous heterodimerization overcomes innate resistance to ERBB2 dimerization inhibitors in breast cancer. *Breast Cancer Research*, 21(1):1–17, 2019.

[60] R Schulz, F Streller, AH Scheel, J Rüschoff, MC Reinert, M Dobbelstein, ND Marchenko, and UM Moll. HER2/ErbB2 activates HSF1 and thereby controls HSP90 clients including MIF in HER2-overexpressing breast cancer. *Cell death & disease*, 5(1):e980–e980, 2014.

[61] Ami Citri, Bose S Kochupurakkal, and Yosef Yarden. The achilles heel of ErbB-2/HER2: regulation by the Hsp90 chaperone machine and potential for pharmacological intervention. *Cell cycle*, 3(1):50–59, 2004.

[62] Bart S Hendriks, H Steven Wiley, and Douglas Lauffenburger. HER2-mediated effects on EGFR endosomal sorting: analysis of biophysical mechanisms. *Biophysical journal*, 85(4): 2732–2745, 2003.

[63] pi3k/akt/mtor signaling pathway in breast cancer: From molecular landscape to clinical aspects.

[64] Lynn B Eckert, Gretchen A Repasky, Aylin S Ülkü, Aidan McFall, Hong Zhou, Carolyn I Sartor, and Channing J Der. Involvement of Ras activation in human breast cancer cell signaling, invasion, and anoikis. *Cancer research*, 64(13):4585–4592, 2004.

[65] Myeongjin Jeon, Daeun You, Soo Youn Bae, Seok Won Kim, Seok Jin Nam, Hyeon Ho Kim, Sangmin Kim, and Jeong Eon Lee. Dimerization of EGFR and HER2 induces breast cancer cell motility through STAT1-dependent ACTA2 induction. *Oncotarget*, 8(31):50570, 2017.

[66] Byoungsan Choi, Minkwon Cha, Gee Sung Eun, Dae Hee Lee, Seul Lee, Muhammad Ehsan, Pil Seok Chae, Won Do Heo, YongKeun Park, and Tae-Young Yoon. Single-molecule functional anatomy of endogenous HER2-HER3 heterodimers. *Elife*, 9:e53934, 2020.

[67] Jeroen Claus, Gargi Patel, Flavia Autore, Audrey Colomba, Gregory Weitsman, Tanya N Soliman, Selene Roberts, Laura C Zanetti-Domingues, Michael Hirsch, Francesca Collu, et al. Inhibitor-induced HER2-HER3 heterodimerisation promotes proliferation through a novel dimer interface. *Elife*, 7:e32271, 2018.

[68] Gregory Weitsman, Paul R Barber, Lan K Nguyen, Katherine Lawler, Gargi Patel, Natalie Woodman, Muireann T Kelleher, Sarah E Pinder, Mark Rowley, Paul A Ellis, et al. HER2-HER3 dimer quantification by FLIM-FRET predicts breast cancer metastatic relapse independently of HER2 IHC status. *Oncotarget*, 7(32):51012, 2016.

[69] Andrew R Green, Fabrício FT Barros, Tarek MA Abdel-Fatah, Paul Moseley, Christopher C Nolan, Alice C Durham, Emad A Rakha, Stephen Chan, and Ian O Ellis. HER2/HER3 heterodimers and p21 expression are capable of predicting adjuvant trastuzumab response in HER2+ breast cancer. *Breast cancer research and treatment*, 145(1):33–44, 2014.

[70] Diana B Peckys, Ulrike Korf, Stefan Wiemann, and Niels De Jonge. Liquid-phase electron microscopy of molecular drug response in breast cancer cells reveals irresponsive cell subpopulations related to lack of HER2 homodimers. *Molecular biology of the cell*, 28(23): 3193–3202, 2017.

[71] Peter H Duesberg and Peter K Vogt. Differences between the ribonucleic acids of transforming and nontransforming avian tumor viruses. *Proceedings of the National Academy of Sciences*, 67(4):1673–1680, 1970.

[72] I Bernard Weinstein. Addiction to oncogenes–the Achilles heal of cancer. *Science*, 297 (5578):63–64, 2002.

[73] I Bernard Weinstein and Andrew K Joe. Mechanisms of disease: oncogene addiction—a rationale for molecular targeting in cancer therapy. *Nature clinical practice Oncology*, 3(8): 448–457, 2006.

[74] Timo Faltus, Juping Yuan, Brigitte Zimmer, Andrea Krämer, Sibylle Loibl, Manfred Kaufmann, and Klaus Strebhardt. Silencing of the HER2/neu gene by siRNA inhibits proliferation and induces apoptosis in HER2/neu-overexpressing breast cancer cells. *Neoplasia (New York, NY)*, 6(6):786, 2004.

[75] Yukiko Ueda, Shizhen Wang, Nancy Dumont, Jae Youn Yi, Yasuhiro Koh, and Carlos L Arteaga. Overexpression of HER2 (erbB2) in human breast epithelial cells unmasks transforming growth factor β-induced cell motility. *Journal of Biological Chemistry*, 279(23): 24505–24513, 2004.

[76] Song Li, Jie Zhou, Hongying Wu, Qianying Lu, Yanhong Tai, Qiang Liu, and Chenguang Wang. Oncogenic transformation of normal breast epithelial cells co-cultured with cancer cells. *Cell Cycle*, 17(16):2027–2040, 2018.

[77] Martin Jechlinger, Katrina Podsypanina, and Harold Varmus. Regulation of transgenes in three-dimensional cultures of primary mouse mammary cells demonstrates oncogene dependence and identifies cells that survive deinduction. *Genes & development*, 23(14):1677–1688, 2009.

[78] Ashna Alladin and Martin Jechlinger. Towards a holistic and mechanistic understanding of tumourigenesis via genetically engineered mouse models. *Current Opinion in Systems Biology*, 6:74–79, 2017.

[79] DJ Slamon, B Leyland-Jones, S Shak, H Fuchs, V Paton, A Bajamonde, T Fleming, W Eiermann, J Wolter, M Pegram, et al. Concurrent administration of anti-HER2 monoclonal antibody and first-line chemotherapy for HER2-overexpressing metastatic breast cancer. A phase III, multinational, randomized controlled trial. *N Engl J Med*, 344(783):2001–792, 2001.

[80] C Ginestier, J Adelaide, A Goncalves, L Repellini, F Sircoulomb, A Letessier, P Finetti, J Geneix, E Charafe-Jauffret, F Bertucci, et al. ERBB2 phosphorylation and trastuzumab sensitivity of breast cancer cell lines. *Oncogene*, 26(50):7163–7169, 2007.

[81] Marco Mazzotta, Eriseld Krasniqi, Giacomo Barchiesi, Laura Pizzuti, Federica Tomao, Maddalena Barba, and Patrizia Vici. Long-term safety and real-world effectiveness of trastuzumab in breast cancer. *Journal of clinical medicine*, 8(2):254, 2019.

[82] Sabine Schmid, Dirk Klingbiel, Stefan Aebi, Aron Goldhirsch, Christoph Mamot, Elisabetta Munzone, Franco Nolè, Christian Oehlschlegel, Olivia Pagani, Bernhard Pestalozzi, et al. Long-term responders to trastuzumab monotherapy in first-line HER-2+ advanced breast cancer: characteristics and survival data. *BMC cancer*, 19(1):1–7, 2019.

[83] Jun-Cheng Xuhong, Xiao-Wei Qi, Yi Zhang, and Jun Jiang. Mechanism, safety and efficacy of three tyrosine kinase inhibitors lapatinib, neratinib and pyrotinib in HER2-positive breast cancer. *American journal of cancer research*, 9(10):2103, 2019.

[84] Rashmi K Murthy, Sherene Loi, Alicia Okines, Elisavet Paplomata, Erika Hamilton, Sara A Hurvitz, Nancy U Lin, Virginia Borges, Vandana Abramson, Carey Anders, et al. Tucatinib, trastuzumab, and capecitabine for HER2-positive metastatic breast cancer. *New England Journal of Medicine*, 382(7):597–609, 2020.

[85] J Baselga. Clinical trials of Herceptin®(trastuzumab). *European Journal of Cancer*, 37: 18–24, 2001.

[86] Luca Gianni, Tadeusz Pienkowski, Young-Hyuck Im, Laslo Roman, Ling-Ming Tseng, Mei-Ching Liu, Ana Lluch, Elżbieta Staroslawska, Juan de la Haba-Rodriguez, Seock-Ah Im, et al. Efficacy and safety of neoadjuvant pertuzumab and trastuzumab in women with locally advanced, inflammatory, or early HER2-positive breast cancer (NeoSphere): a randomised multicentre, open-label, phase 2 trial. *The lancet oncology*, 13(1):25–32, 2012.

[87] Lynn J Howie, Nancy S Scher, Laleh Amiri-Kordestani, Lijun Zhang, Bellinda L King-Kallimanis, Yasmin Choudhry, Jason Schroeder, Kirsten B Goldberg, Paul G Kluetz, Amna Ibrahim, et al. FDA approval summary: pertuzumab for adjuvant treatment of HER2-positive early breast cancer. *Clinical Cancer Research*, 25(10):2949–2955, 2019.

[88] William J Gradishar, Seock-Ah Im, Fatima Cardoso, Javier Cortes, Giuseppe Curigliano, Mark D Pegram, Antonino Musolino, Rossana Berardi, Michelino De Laurentiis, and Shakeela W Bahadur. Phase 3 SOPHIA Study of Margetuximab+ Chemotherapy vs Trastuzumab+ Chemotherapy in Patients With HER2+ Metastatic Breast Cancer After Prior Anti-HER2 Therapies: Infusion Time Substudy Results. 2019.

[89] Sunil Verma, David Miles, Luca Gianni, Ian E Krop, Manfred Welslau, José Baselga, Mark Pegram, Do-Youn Oh, Véronique Diéras, Ellie Guardino, et al. Trastuzumab emtansine

for HER2-positive advanced breast cancer. *New England Journal of Medicine*, 367(19): 1783–1791, 2012.

[90] Gunter Von Minckwitz, Chiun-Sheng Huang, Max S Mano, Sibylle Loibl, Eleftherios P Mamounas, Michael Untch, Norman Wolmark, Priya Rastogi, Andreas Schneeweiss, Andres Redondo, et al. Trastuzumab emtansine for residual invasive HER2-positive breast cancer. *New England Journal of Medicine*, 380(7):617–628, 2019.

[91] Shanu Modi, Cristina Saura, Toshinari Yamashita, Yeon Hee Park, Sung-Bae Kim, Kenji Tamura, Fabrice Andre, Hiroji Iwata, Yoshinori Ito, Junji Tsurutani, et al. Trastuzumab deruxtecan in previously treated HER2-positive breast cancer. *New England Journal of Medicine*, 382(7):610–621, 2020.

[92] Fabrice André, Javad Shahidi, Caleb Lee, Kongming Wang, and Ian E Krop. Abstract OT1-07-04:[Fam-] trastuzumab deruxtecan (T-DXd; DS-8201a) vs investigator's choice of treatment in subjects with HER2-positive, unresectable and/or metastatic breast cancer who previously received T-DM1: A randomized, phase 3 trial (DESTINY-Breast02), 2020.

[93] Javier Cortés, Javad Shahidi, Caleb Lee, Yufen Zhang, and Sunil Verma. Abstract OT1-07-01:[Fam-] trastuzumab deruxtecan (T-DXd; DS-8201a) vs ado-trastuzumab emtansine (T-DM1) in subjects with HER2-positive, unresectable and/or metastatic breast cancer who previously received trastuzumab and a taxane: A phase 3, randomized trial (DESTINY-Breast03), 2020.

[94] Qin Ryan, Amna Ibrahim, Martin H Cohen, John Johnson, Chia-wen Ko, Rajeshwari Sridhara, Robert Justice, and Richard Pazdur. FDA drug approval summary: lapatinib in combination with capecitabine for previously treated metastatic breast cancer that overexpresses HER-2. *The oncologist*, 13(10):1114–1119, 2008.

[95] Cristina Saura, Mafalda Oliveira, Yin-Hsun Feng, Ming-Shen Dai, Shang-Wen Chen, Sara A Hurvitz, Sung-Bae Kim, Beverly Moy, Suzette Delaloge, William Gradishar, et al. Neratinib plus capecitabine versus lapatinib plus capecitabine in HER2-positive metastatic breast cancer previously treated with 2 HER2-directed regimens: phase III NALA trial. *Journal of Clinical Oncology*, 38(27):3138, 2020.

[96] Arlene Chan, Suzette Delaloge, Frankie A Holmes, Beverly Moy, Hiroji Iwata, Vernon J Harvey, Nicholas J Robert, Tajana Silovski, Erhan Gokmen, Gunter von Minckwitz, et al. Neratinib after trastuzumab-based adjuvant therapy in patients with HER2-positive breast cancer (ExteNET): a multicentre, randomised, double-blind, placebo-controlled, phase 3 trial. *The Lancet Oncology*, 17(3):367–377, 2016.

[97] Mirat Shah, Suparna Wedam, Joyce Cheng, Mallorie H Fiero, Huiming Xia, Fang Li, Jianghong Fan, Xinyuan Zhang, Jingyu Yu, Pengfei Song, et al. FDA approval summary: tucatinib for the treatment of patients with advanced or metastatic HER2-positive breast cancer. *Clinical Cancer Research*, 27(5):1220–1226, 2021.

[98] Debu Tripathy, Adam Brufsky, Melody Cobleigh, Mohammad Jahanzeb, Peter A Kaufman, Ginny Mason, Joyce O'Shaughnessy, Hope S Rugo, Sandra M Swain, Denise A Yardley, et al. De Novo Versus Recurrent HER2-Positive Metastatic Breast Cancer: Patient Characteristics, Treatment, and Survival from the SystHERs Registry. *The oncologist*, 25(2):e214, 2020.

[99] Adam M Brufsky, Musa Mayer, Hope S Rugo, Peter A Kaufman, Elizabeth Tan-Chiu, Debu Tripathy, Iulia Cristina Tudor, Lisa I Wang, Melissa G Brammer, Mona Shing, et al. Central nervous system metastases in patients with HER2-positive metastatic breast cancer: incidence, treatment, and survival in patients from registHER. *Clinical Cancer Research*, 17 (14):4834–4843, 2011.

[100] Johanna C Bendell, Susan M Domchek, Harold J Burstein, Lyndsay Harris, Jerry Younger, Irene Kuter, Craig Bunnell, Montse Rue, Rebecca Gelman, and Eric Winer. Central nervous system metastases in women who receive trastuzumab-based therapy for metastatic breast carcinoma. *Cancer*, 97(12):2972–2977, 2003.

[101] Erin M Olson, Julie S Najita, Jessica Sohl, Amal Arnaout, Harold J Burstein, Eric P Winer, and Nancy U Lin. Clinical outcomes and treatment practice patterns of patients with HER2-positive metastatic breast cancer in the post-trastuzumab era. *The Breast*, 22(4):525–531, 2013.

[102] Bálint Mészáros, Borbála Hajdu-Soltész, András Zeke, and Zsuzsanna Dosztányi. Mutations of Intrinsically Disordered Protein Regions Can Drive Cancer but Lack Therapeutic Strategies. *Biomolecules*, 11(3):381, 2021.

[103] Bo Chen, Guochun Zhang, Guangnan Wei, Yulei Wang, Liping Guo, Jiali Lin, Kai Li, Hsiaopei Mok, Li Cao, Chongyang Ren, et al. Heterogeneity of genomic profile in patients with her2-positive breast cancer. *Endocrine-related cancer*, 27(3):153–162, 2020.

[104] Tiansheng Shen, Hiroaki Nitta, Lai Wei, Anil V Parwani, and Zaibo Li. HER2 intratumoral heterogeneity is independently associated with distal metastasis and overall survival in HER2-positive breast carcinomas. *Breast cancer research and treatment*, 181(3):519–527, 2020.

[105] Inga H Rye, Anne Trinh, Anna B Sætersdal, Daniel Nebdal, Ole Christian Lingjærde, Vanessa Almendro, Kornelia Polyak, Anne-Lise Børresen-Dale, Åslaug Helland, Florian Markowetz, et al. Intratumor heterogeneity defines treatment-resistant HER 2+ breast tumors. *Molecular oncology*, 12(11):1838–1855, 2018.

[106] Search performed using trial trove (informa) for ongoing or recruiting her2+ breast cancer trials, phase ii/iii or phase iii. results were manually checked to remove any irrelevant results.

[107] Valentina Guarneri, Maria Vittoria Dieci, E Barbieri, Federico Piacentini, Claudia Omarini, G Ficarra, S Bettelli, and PF Conte. Loss of HER2 positivity and prognosis after neoadjuvant therapy in HER2-positive breast cancer patients. *Annals of oncology*, 24(12):2990–2994, 2013.

[108] Naoki Niikura, Jun Liu, Naoki Hayashi, Elizabeth A Mittendorf, Yun Gong, Shana L Palla, Yutaka Tokuda, Ana M Gonzalez-Angulo, Gabriel N Hortobagyi, and Naoto T Ueno. Loss of human epidermal growth factor receptor 2 (HER2) expression in metastatic sites of HER2-overexpressing primary breast tumors. *Journal of Clinical Oncology*, 30(6):593, 2012.

[109] Gabriel L Fiszman and María A Jasnis. Molecular mechanisms of trastuzumab resistance in HER2 overexpressing breast cancer. *International journal of breast cancer*, 2011, 2011.

[110] Saranya Chumsri, Jeff Sperinde, Heshan Liu, Joseph Gligorov, Jean-Philippe Spano, Martine Antoine, Alvaro Moreno Aspitia, Winston Tan, John Winslow, Christos J Petropoulos, et al. High p95HER2/HER2 ratio associated with poor outcome in trastuzumab-treated HER2-positive metastatic breast cancer NCCTG N0337 and NCCTG 98-32-52 (Alliance). *Clinical Cancer Research*, 24(13):3053–3058, 2018.

[111] Maurizio Scaltriti, Federico Rojo, Alberto Ocaña, Judit Anido, Marta Guzman, Javier Cortes, Serena Di Cosimo, Xavier Matias-Guiu, Santiago Ramon y Cajal, Joaquin Arribas, et al. Expression of p95HER2, a truncated form of the HER2 receptor, and response to anti-HER2 therapies in breast cancer. *Journal of the National Cancer Institute*, 99(8):628–638, 2007.

[112] A Gallardo, E Lerma, D Escuin, A Tibau, J Munoz, B Ojeda, A Barnadas, E Adrover, L Sánchez-Tejada, D Giner, et al. Increased signalling of EGFR and IGF1R, and deregulation of PTEN/PI3K/Akt pathway are related with trastuzumab resistance in HER2 breast carcinomas. *British journal of cancer*, 106(8):1367–1373, 2012.

[113] miR-182 regulates trastuzumab resistance by targeting MET in breast cancer cells, author=Yue, Dan and Qin, Xiaosong. *Cancer gene therapy*, 26(1):1–10, 2019.

[114] Yuhua Zhao, Hao Liu, Zixing Liu, Yan Ding, Susan P LeDoux, Glenn L Wilson, Richard Voellmy, Yifeng Lin, Wensheng Lin, Rita Nahta, et al. Overcoming trastuzumab resistance in breast cancer by targeting dysregulated glucose metabolism. *Cancer research*, 71(13): 4585–4597, 2011.

[115] Hirotaka Kanzaki, Nishit K Mukhopadhya, Xiaojiang Cui, V Krishnan Ramanujan, and Ramachandran Murali. Trastuzumab-resistant luminal B breast cancer cells show basal-like

cell growth features through NF-κB-activation. *Monoclonal antibodies in immunodiagnosis and immunotherapy*, 35(1):1–11, 2016.

[116] Jung Min Park, Yoon-Jae Kim, Soeun Park, Minsu Park, Lee Farrand, Cong-Truong Nguyen, Jihyae Ann, Gibeom Nam, Hyun-Ju Park, Jeewoo Lee, et al. A novel HSP90 inhibitor targeting the C-terminal domain attenuates trastuzumab resistance in HER2-positive breast cancer. *Molecular Cancer*, 19(1):1–8, 2020.

[117] Alexandra Canonici, Zulfiqar Qadir, Neil T Conlon, Denis M Collins, Neil A O'Brien, Naomi Walsh, Alex J Eustace, Norma O'Donovan, and John Crown. The HSP90 inhibitor NVP-AUY922 inhibits growth of HER2 positive and trastuzumab-resistant breast cancer cells. *Investigational new drugs*, 36(4):581–589, 2018.

[118] Julie C Friedland, Donald L Smith, Jim Sang, Jaime Acquaviva, Suqin He, Chaohua Zhang, and David A Proia. Targeted inhibition of Hsp90 by ganetespib is effective across a broad spectrum of breast cancer subtypes. *Investigational new drugs*, 32(1):14–24, 2014.

[119] Francis W Hunter, Hilary R Barker, Barbara Lipert, Françoise Rothé, Géraldine Gebhart, Martine J Piccart-Gebhart, Christos Sotiriou, and Stephen MF Jamieson. Mechanisms of resistance to trastuzumab emtansine (T-DM1) in HER2-positive breast cancer. *British journal of cancer*, 122(5):603–612, 2020.

[120] Yoriko Yamashita-Kashima, Sei Shu, Masahiro Osada, Takaaki Fujimura, Shigeki Yoshiura, Naoki Harada, and Yasushi Yoshimura. Combination efficacy of pertuzumab and trastuzumab for trastuzumab emtansine-resistant cells exhibiting attenuated lysosomal trafficking or efflux pumps upregulation. *Cancer chemotherapy and pharmacology*, 86(5):641–654, 2020.

[121] Carla Ríos-Luci, Sara García-Alonso, Elena Díaz-Rodríguez, Mercedes Nadal-Serrano, Joaquín Arribas, Alberto Ocaña, and Atanasio Pandiella. Resistance to the antibody–drug conjugate T-DM1 is based in a reduction in lysosomal proteolytic activity. *Cancer research*, 77(17):4639–4651, 2017.

[122] Xiaowei Xu, Carmine De Angelis, Kathleen A Burke, Agostina Nardone, Huizhong Hu, Lanfang Qin, Jamunarani Veeraraghavan, Vidyalakshmi Sethunath, Laura M Heiser, Nicholas Wang, et al. HER2 reactivation through acquisition of the HER2 L755S mutation as a mechanism of acquired resistance to HER2-targeted therapy in HER2+ breast cancer. *Clinical Cancer Research*, 23(17):5123–5134, 2017.

[123] Benjamin Ruprecht, Esther A Zaal, Jana Zecha, Wei Wu, Celia R Berkers, Bernhard Kuster, and Simone Lemeer. Lapatinib resistance in breast cancer cells is accompanied by phosphorylation-mediated reprogramming of glycolysis. *Cancer research*, 77(8):1842–1853, 2017.

[124] D Wetterskog, KK Shiu, I Chong, T Meijer, A Mackay, M Lambros, D Cunningham, JS Reis-Filho, CJ Lord, and A Ashworth. Identification of novel determinants of resistance to lapatinib in ERBB2-amplified cancers. *Oncogene*, 33(8):966–976, 2014.

[125] Sharon T Wilks. Potential of overcoming resistance to HER2-targeted therapies through the PI3K/Akt/mTOR pathway. *The Breast*, 24(5):548–555, 2015.

[126] Neil A O'Brien, Karen McDonald, Luo Tong, Erika von Euw, Ondrej Kalous, Dylan Conklin, Sara A Hurvitz, Emmanuelle Di Tomaso, Christian Schnell, Ronald Linnartz, et al. Targeting PI3K/mTOR overcomes resistance to HER2-targeted therapy independent of feedback activation of AKT. *Clinical Cancer Research*, 20(13):3507–3520, 2014.

[127] Xiangyi Kong, Kai Zhang, Xiangyu Wang, Xue Yang, Yalun Li, Jie Zhai, Zeyu Xing, Yihang Qi, Ran Gao, Xiaoli Feng, et al. Mechanism of trastuzumab resistance caused by HER-2 mutation in breast carcinomas. *Cancer management and research*, 11:5971, 2019.

[128] Utthara Nayar, Ofir Cohen, Christian Kapstad, Michael S Cuoco, Adrienne G Waks, Seth A Wander, Corrie Painter, Samuel Freeman, Nicole S Persky, Lori Marini, et al. Acquired HER2 mutations in ER+ metastatic breast cancer confer resistance to estrogen receptor–directed therapies. *Nature genetics*, 51(2):207–216, 2019.

[129] María F Mercogliano, Mara De Martino, Leandro Venturutti, Martín A Rivas, Cecilia J Proietti, Gloria Inurrigarro, Isabel Frahm, Daniel H Allemand, Ernesto Gil Deza, Sandra Ares, et al. TNFα-induced mucin 4 expression elicits trastuzumab resistance in HER2-positive breast cancer. *Clinical Cancer Research*, 23(3):636–648, 2017.

[130] Alex J Eustace, Neil T Conlon, Martina SJ McDermott, Brigid C Browne, Patrick O'Leary, Frankie A Holmes, Virginia Espina, Lance A Liotta, Joyce O'Shaughnessy, Clair Gallagher, et al. Development of acquired resistance to lapatinib may sensitise HER2-positive breast cancer cells to apoptosis induction by obatoclax and TRAIL. *BMC cancer*, 18(1):965, 2018.

[131] Erika Hamilton and Jeffrey R Infante. Targeting CDK4/6 in patients with cancer. *Cancer treatment reviews*, 45:129–138, 2016.

[132] Amanda J Walker, Suparna Wedam, Laleh Amiri-Kordestani, Erik Bloomquist, Shengui Tang, Rajeshwari Sridhara, Wei Chen, Todd R Palmby, Jeanne Fourie Zirkelbach, Wentao Fu, et al. FDA approval of palbociclib in combination with fulvestrant for the treatment of hormone receptor–positive, HER2-negative metastatic breast cancer. *Clinical Cancer Research*, 22(20):4968–4972, 2016.

[133] Richard S Finn, Miguel Martin, Hope S Rugo, Stephen Jones, Seock-Ah Im, Karen Gelmon, Nadia Harbeck, Oleg N Lipatov, Janice M Walshe, Stacy Moulder, et al. Palbociclib and letrozole in advanced breast cancer. *New England journal of medicine*, 375(20):1925–1936, 2016.

[134] DETECT V / CHEVENDO A Multicenter, Randomized Phase III Study to Compare Chemo- Versus Endocrine Therapy in Combination With Dual HER2-targeted Therapy of Herceptin® (Trastuzumab) and Perjeta® (Pertuzumab) Plus Kisqali® (Ribociclib) in Patients With HER2 Positive and Hormone-receptor Positive Metastatic Breast Cancer. *clinicaltrials.gov*, Identifier: NCT02344472, September 2015 - September 2021. URL https://clinicaltrials.gov/ct2/show/NCT02344472.

[135] A Phase II Trial of Pyrotinib Combination With CDK4/6 Inhibitor SHR6390 in Patients Prior Trastuzumab-treated Advanced HER2-Positive Breast Cancer (INPHASE). *clinicaltrails.gov*, Identifier: NCT04095390(10):2103, September 2019 - November 2021. URL https://clinicaltrials.gov/ct2/show/NCT04095390.

[136] Shom Goel, Sonia Pernas, Zhenying Tan-Wasielewski, William T Barry, Aditya Bardia, Rebecca Rees, Chelsea Andrews, Rie Kawabori Tahara, Lorenzo Trippa, Erica L Mayer, et al. Ribociclib plus trastuzumab in advanced HER2-positive breast cancer: results of a phase 1b/2 trial. *Clinical Breast Cancer*, 19(6):399–404, 2019.

[137] Ciara C O'Sullivan, Vera J Suman, and Matthew P Goetz. The emerging role of CDK4/6i in HER2-positive breast cancer. *Therapeutic Advances in Medical Oncology*, 11: 1758835919887665, 2019.

[138] Kai Zhang, Ruoxi Hong, Lee Kaping, Fei Xu, Wen Xia, Ge Qin, Qiufan Zheng, Qianyi Lu, Qinglian Zhai, Yanxia Shi, et al. CDK4/6 inhibitor palbociclib enhances the effect of pyrotinib in HER2-positive breast cancer. *Cancer letters*, 447:130–140, 2019.

[139] Shom Goel, Qi Wang, April C Watt, Sara M Tolaney, Deborah A Dillon, Wei Li, Susanne Ramm, Adam C Palmer, Haluk Yuzugullu, Vinay Varadan, et al. Overcoming therapeutic resistance in HER2-positive breast cancers with CDK4/6 inhibitors. *Cancer cell*, 29(3):255–269, 2016.

[140] Alisha Yallowitz, Amr Ghaleb, Lucas Garcia, Evguenia M Alexandrova, and Natalia Marchenko. Heat shock factor 1 confers resistance to lapatinib in ERBB2-positive breast cancer cells. *Cell death & disease*, 9(6):1–13, 2018.

[141] Harry Lee, Nipun Saini, Erin W Howard, Amanda B Parris, Zhikun Ma, Qingxia Zhao, Ming Zhao, Bolin Liu, Susan M Edgerton, Ann D Thor, et al. Ganetespib targets multiple levels of the receptor tyrosine kinase signaling cascade and preferentially inhibits ErbB2-overexpressing breast cancer cells. *Scientific reports*, 8(1):1–14, 2018.

[142] Hye Jin Lee, Seungho Shin, Jinho Kang, Ki-Cheol Han, Yeul Hong Kim, Jeoung-Won Bae, and Kyong Hwa Park. HSP90 Inhibitor, 17-DMAG, Alone and in Combination with Lapatinib Attenuates Acquired Lapatinib-Resistance in ER-positive, HER2-Overexpressing Breast Cancer Cell Line. *Cancers*, 12(9):2630, 2020.

[143] Christina K Galang, José J García-Ramírez, Patricia A Solski, John K Westwick, Channing J Der, Nickolay N Neznanov, Robert G Oshima, and Craig A Hauser. Oncogenic neu/ErbB-2 increases ets, AP-1, and NF-kB-dependent gene expression, and inhibiting ets activation blocks Neu-mediated cellular transformation. *Journal of Biological Chemistry*, 271(14): 7992–7998, 1996.

[144] Evan C Merkhofer, Patricia Cogswell, and Albert S Baldwin. Her2 activates NF-κB and induces invasion through the canonical pathway involving IKKα. *Oncogene*, 29(8):1238–1248, 2010.

[145] DK Sarkar, Debarshi Jana, PS Patil, KS Chaudhari, BK Chattopadhyay, BR Chikkala, S Mandal, and P Chowdhary. Role of NF-κB as a prognostic marker in breast cancer: a pilot study in Indian patients. *Indian journal of surgical oncology*, 4(3):242–247, 2013.

[146] Kazi M Ahmed, Ning Cao, and Jian Jian Li. HER-2 and NF-κB as the targets for therapy-resistant breast cancer. *Anticancer research*, 26(6B):4235–4243, 2006.

[147] Wei Wang, Subhasree A Nag, and Ruiwen Zhang. Targeting the NFκB signaling pathways for breast cancer prevention and therapy. *Current medicinal chemistry*, 22(2):264–289, 2015.

[148] Chuandong Ma, Wenshu Zuo, Xingwu Wang, Ling Wei, Qian Guo, and Xianrang Song. Lapatinib inhibits the activation of NF-κB through reducing phosphorylation of IκB-α in breast cancer cells. *Oncology reports*, 29(2):812–818, 2013.

[149] Adrián Sanz-Moreno, Sonia Palomeras, Kim Pedersen, Beatriz Morancho, Tomas Pascual, Patricia Galván, Sandra Benítez, Jorge Gomez-Miragaya, Marina Ciscar, Maria Jimenez, et al. RANK signaling increases after anti-HER2 therapy contributing to the emergence of resistance in HER2-positive breast cancer. *Breast Cancer Research*, 23(1):1–18, 2021.

[150] Otto Warburg, Franz Wind, and Erwin Negelein. The metabolism of tumors in the body. *The Journal of general physiology*, 8(6):519, 1927.

[151] Carl F Cori and Gerty T Cori. The carbohydrate metabolism of tumors II. Changes in the sugar, lactic acid, and CO2-Combining Power of Blood Passing through a tumor. *Journal of Biological Chemistry*, 65(2):397–405, 1925.

[152] Patrick S Ward and Craig B Thompson. Metabolic reprogramming: a cancer hallmark even warburg did not anticipate. *Cancer cell*, 21(3):297–308, 2012.

[153] Chandan Kumar-Sinha, Kathleen Woods Ignatoski, Marc E Lippman, Stephen P Ethier, and Arul M Chinnaiyan. Transcriptome analysis of HER2 reveals a molecular connection to fatty acid synthesis. *Cancer research*, 63(1):132–139, 2003.

[154] William W Feng, Owen Wilkins, Scott Bang, Matthew Ung, Jiaqi Li, Jennifer An, Carmen del Genio, Kaleigh Canfield, James DiRenzo, Wendy Wells, et al. CD36-mediated metabolic rewiring of breast cancer cells promotes resistance to HER2-targeted therapies. *Cell reports*, 29(11):3405–3420, 2019.

[155] Bryan C Nikolai, Rainer B Lanz, Brian York, Subhamoy Dasgupta, Nicholas Mitsiades, Chad J Creighton, Anna Tsimelzon, Susan G Hilsenbeck, David M Lonard, Carolyn L Smith, et al. HER2 signaling drives DNA anabolism and proliferation through SRC-3 phosphorylation and E2F1-regulated genes. *Cancer research*, 76(6):1463–1475, 2016.

[156] Luigi Mele, Marcella la Noce, Francesca Paino, Tarik Regad, Sarah Wagner, Davide Liccardo, Gianpaolo Papaccio, Angela Lombardi, Michele Caraglia, Virginia Tirino, et al. Glucose-6-phosphate dehydrogenase blockade potentiates tyrosine kinase inhibitor effect on breast cancer cells through autophagy perturbation. *Journal of Experimental & Clinical Cancer Research*, 38(1):1–13, 2019.

[157] Evan C Lien, Costas A Lyssiotis, and Lewis C Cantley. Metabolic reprogramming by the PI3K-Akt-mTOR pathway in cancer. In *Metabolism in Cancer, pages=39–72, year=2016, publisher=Springer*.

[158] Cedric Magaway, Eugene Kim, and Estela Jacinto. Targeting mTOR and Metabolism in Cancer: Lessons and Innovations. *Cells*, 8(12):1584, 2019.

[159] Anna Lewinska, Jagoda Adamczyk-Grochala, Ewa Kwasniewicz, Anna Deregowska, and Maciej Wnuk. Ursolic acid-mediated changes in glycolytic pathway promote cytotoxic autophagy and apoptosis in phenotypically different breast cancer cells. *Apoptosis*, 22(6): 800–815, 2017.

[160] Mingxiu Guan, Yingna Tong, Minghua Guan, Xiaobin Liu, Meng Wang, Ruifang Niu, Fei Zhang, Dong Dong, Jie Shao, and Yunli Zhou. Lapatinib inhibits breast cancer cell proliferation by influencing PKM2 expression. *Technology in cancer research & treatment*, 17: 1533034617749418, 2018.

[161] Rafaela Andrade-Vieira, Zhaolin Xu, Patricia Colp, and Paola A Marignani. Loss of LKB1 expression reduces the latency of ErbB2-mediated mammary gland tumorigenesis, promoting changes in metabolic pathways. *PloS one*, 8(2):e56567, 2013.

[162] YH Zhao, Ming Zhou, Hao Liu, Y Ding, HT Khong, Dihua Yu, Oystein Fodstad, and M Tan. Upregulation of lactate dehydrogenase A by ErbB2 through heat shock factor 1 promotes breast cancer cell glycolysis and growth. *Oncogene*, 28(42):3689–3701, 2009.

[163] Lorenzo Castagnoli, Egidio Iorio, Matteo Dugo, Ada Koschorke, Simona Faraci, Rossella Canese, Patrizia Casalini, Patrizia Nanni, Claudio Vernieri, Massimo Di Nicola, et al. Intratumor lactate levels reflect HER2 addiction status in HER2-positive breast cancer. *Journal of cellular physiology*, 234(2):1768–1779, 2019.

[164] Chen Huang, Shile Sheng, Rui Li, Xiaoguang Sun, Jianju Liu, and Gang Huang. Lactate promotes resistance to glucose starvation via upregulation of Bcl-2 mediated by mTOR activation. *Oncology reports*, 33(2):875–884, 2015.

[165] Marcus PD Hatfield and Sándor Lovas. Role of Hsp70 in cancer growth and survival. *Protein and peptide letters*, 19(6):616–624, 2012.

[166] Valentina Condelli, Fabiana Crispo, Michele Pietrafesa, Giacomo Lettini, Danilo Swann Matassa, Franca Esposito, Matteo Landriscina, and Francesca Maddalena. HSP90 molecular chaperones, metabolic rewiring, and epigenetics: impact on tumor progression and perspective for anticancer therapy. *Cells*, 8(6):532, 2019.

[167] LU Yue, Jin-Yu Xiang, Ping Sun, Ya-Sai Yao, Zhen-Ni Sun, Xiang-Ping Liu, Hai-Bo Wang, Zan Shen, and Ru-Yong Yao. Relationship between HSP70 and ERBB2 expression in breast cancer cell lines regarding drug resistance. *Anticancer Research*, 36(3):1243–1249, 2016.

[168] Breast cancer and HSP90 inhibitors: is there a role beyond the HER2-positive subtype?, author=De Mattos-Arruda, Leticia and Cortes, Javier. *The Breast*, 21(4):604–607, 2012.

[169] Komal Jhaveri, Rui Wang, Eleonora Teplinsky, Sarat Chandarlapaty, David Solit, Karen Cadoo, James Speyer, Gabriella D'Andrea, Sylvia Adams, Sujata Patil, et al. A phase I trial of ganetespib in combination with paclitaxel and trastuzumab in patients with human epidermal growth factor receptor-2 (HER2)-positive metastatic breast cancer. *Breast Cancer Research*, 19(1):89, 2017.

[170] Yaqing Chen, Jianchang Qian, Qun He, Hui Zhao, Lourdes Toral-Barza, Celine Shi, Xuesai Zhang, Jiang Wu, and Ker Yu. mTOR complex-2 stimulates acetyl-CoA and de novo lipogenesis through ATP citrate lyase in HER2/PIK3CA-hyperactive breast cancer. *Oncotarget*, 7(18):25224, 2016.

[171] Ufuk Degirmenci, Mei Wang, and Jiancheng Hu. Targeting Aberrant RAS/RAF/MEK/ERK Signaling for Cancer Therapy. *Cells*, 9(1):198, 2020.

[172] Daniel C Kirouac, Jinyan Du, Johanna Lahdenranta, Matthew D Onsum, Ulrik B Nielsen, Birgit Schoeberl, and Charlotte F McDonagh. HER2+ cancer cell dependence on PI3K vs. MAPK signaling axes is determined by expression of EGFR, ERBB3 and CDKN1B. *PLoS computational biology*, 12(4):e1004827, 2016.

[173] Eugen Kerkhoff, Roland Houben, Silke Löffler, Jakob Troppmair, Jong-Eun Lee, and Ulf R Rapp. Regulation of c-myc expression by Ras/Raf signalling. *Oncogene*, 16(2):211–216, 1998.

[174] Tyler Risom, Xiaoyan Wang, Juan Liang, Xiaoli Zhang, Carl Pelz, Lydia G Campbell, Jenny Eng, Koei Chin, Caroline Farrington, Goutham Narla, et al. Deregulating MYC in a model of HER2+ breast cancer mimics human intertumoral heterogeneity. *The Journal of clinical investigation*, 130(1), 2019.

[175] Ksenija Radic Shechter, Eleni Kafkia, Katharina Zirngibl, Sylwia Gawrzak, Ashna Alladin, Daniel Machado, Christian Lüchtenborg, Daniel C Sévin, Britta Brügger, Kiran R Patil, et al. Oncogenic memory underlying minimal residual disease in breast cancer. *bioRxiv*, 2020.

[176] Kristina M Havas, Vladislava Milchevskaya, Ksenija Radic, Ashna Alladin, Eleni Kafkia, Marta Garcia, Jens Stolte, Bernd Klaus, Nicole Rotmensz, Toby J Gibson, et al. Metabolic shifts in residual breast cancer drive tumor recurrence. *The Journal of clinical investigation*, 127(6):2091–2105, 2017.

[177] Jan Baumann, Mostafa Kokabee, Jason Wong, Rakshika Balasubramaniyam, Yan Sun, and Douglas S Conklin. Global metabolite profiling analysis of lipotoxicity in HER2/neu-positive breast cancer cells. *Oncotarget*, 9(43):27133, 2018.

[178] Adriana Blancafort, Ariadna Giró-Perafita, Glòria Oliveras, Sònia Palomeras, Carlos Turrado, Òscar Campuzano, Dolors Carrión-Salip, Anna Massaguer, Ramon Brugada, Marta Palafox, et al. Dual fatty acid synthase and HER2 signaling blockade shows marked antitumor activity against breast cancer models resistant to anti-HER2 drugs. *PloS one*, 10(6): e0131241, 2015.

[179] Teresa Puig, Helena Aguilar, Sílvia Cufí, Glòria Oliveras, Carlos Turrado, Sílvia Ortega-Gutiérrez, Bellinda Benhamú, María Luz López-Rodríguez, Ander Urruticoechea, and Ramon Colomer. A novel inhibitor of fatty acid synthase shows activity against HER2+ breast cancer xenografts and is active in anti-HER2 drug-resistant cell lines. *Breast Cancer Research*, 13(6):1–13, 2011.

[180] Genevieve Deblois, Harvey W Smith, Ingrid S Tam, Simon-Pierre Gravel, Maxime Caron, Paul Savage, David P Labbé, Louis R Bégin, Michel L Tremblay, Morag Park, et al. ERRα mediates metabolic adaptations driving lapatinib resistance in breast cancer. *Nature communications*, 7(1):1–14, 2016.

[181] Demet Candas, Chung-Ling Lu, Ming Fan, Frank YS Chuang, Colleen Sweeney, Alexander D Borowsky, and Jian Jian Li. Mitochondrial MKP1 is a target for therapy-resistant HER2-positive breast cancer cells. *Cancer research*, 74(24):7498–7509, 2014.

[182] Bharat KR Chaganty, Songbo Qiu, Anneliese Gest, Yang Lu, Cristina Ivan, George A Calin, Louis M Weiner, and Zhen Fan. Trastuzumab upregulates PD-L1 as a potential mechanism of trastuzumab resistance through engagement of immune effector cells and stimulation of IFNγ secretion. *Cancer letters*, 430:47–56, 2018.

[183] Kaitlin M Peace, Jennifer K Litton, Rashmi Murthy, Timothy J Vreeland, Diane F Hale, Doreen O Jackson, John S Berry, Alfred F Trappey, Garth S Herbert, Guy T Clifton, et al. Pre-specified interim analysis in a prospective, randomized phase II trial of trastuzumab vs trastuzumab plus NeuVax to prevent breast cancer recurrence in HER2+ breast cancer patients. volume 77. American Association of Cancer Research, 2017.

[184] Scott Parsons, Edward B Maldonado, and Vinay Prasad. Comparison of Drugs Used for Adjuvant and Metastatic Therapy of Colon, Breast, and Non–Small Cell Lung Cancers. *JAMA network open*, 3(4):e202488–e202488, 2020.

[185] Wolfgang MF Wendler, Elisabeth Kremmer, Reinhold Förster, and Ernst-Ludwig Winnacker. Identification of pirin, a novel highly conserved nuclear protein. *Journal of Biological Chemistry*, 272(13):8482–8489, 1997.

[186] Hai Pang, Mark Bartlam, Qinghong Zeng, Hideyuki Miyatake, Tamao Hisano, Kunio Miki, Luet-Lok Wong, George F Gao, and Zihe Rao. Crystal structure of human pirin: an iron-binding nuclear protein and transcription cofactor. *Journal of Biological Chemistry*, 279(2): 1491–1498, 2004.

[187] Charles Adeniran and Donald Hamelberg. Redox-Specific Allosteric Modulation of the Conformational Dynamics of κB DNA by Pirin in the NF-κB Supramolecular Complex. *Biochemistry*, 56(37):5002–5010, 2017.

[188] Fange Liu, Imran Rehmani, Shingo Esaki, Rong Fu, Lirong Chen, Vesna de Serrano, and Aimin Liu. Pirin is an iron-dependent redox regulator of NF-κB. *Proceedings of the National Academy of Sciences*, 110(24):9722–9727, 2013.

[189] Arghya Barman and Donald Hamelberg. Fe (II)/Fe (III) redox process can significantly modulate the conformational dynamics and electrostatics of Pirin in NF-κB Regulation. *ACS omega*, 1(5):837–842, 2016.

[190] Ralf Dechend, Fuminori Hirano, Kerstin Lehmann, Vigo Heissmeyer, Stephane Ansieau, F Gregory Wulczyn, Claus Scheidereit, and Achim Leutz. The Bcl-3 oncoprotein acts as a bridging factor between NF-κB/Rel and nuclear co-regulators. *Oncogene*, 18(22):3316–3323, 1999.

[191] Nanjun Hu, Lulu Bai, Enyong Dai, Leng Han, Rui Kang, Hongjun Li, and Daolin Tang. Pirin is a nuclear redox-sensitive modulator of autophagy-dependent ferroptosis. *Biochemical and Biophysical Research Communications*, 536:100–106, 2021.

[192] Po-Chi Soo, Yu-Tze Horng, Meng-Jiun Lai, Jun-Rong Wei, Shang-Chen Hsieh, Yung-Lin Chang, Yu-Huan Tsai, and Hsin-Chih Lai. Pirin regulates pyruvate catabolism by interacting with the pyruvate dehydrogenase E1 subunit and modulating pyruvate dehydrogenase activity. *Journal of bacteriology*, 189(1):109–118, 2007.

[193] Francisco Perez-Dominguez, Diego Carrillo-Beltrán, Rancés Blanco, Juan P Muñoz, Grettell León-Cruz, Alejandro H Corvalan, Ulises Urzúa, Gloria M Calaf, and Francisco Aguayo. Role of Pirin, an Oxidative Stress Sensor Protein, in Epithelial Carcinogenesis. *Biology*, 10 (2):116, 2021.

[194] Muhammad Suleman, Ai Chen, Huanhuan Ma, Shixiong Wen, Wentao Zhao, Donghai Lin, Guode Wu, and Qinxi Li. PIR promotes tumorigenesis of breast cancer by upregulating cell cycle activator E2F1. *Cell Cycle*, 18(21):2914–2927, 2019.

[195] Kuniya Komai, Yuki Niwa, Yukiko Sasazawa, and Siro Simizu. Pirin regulates epithelial to mesenchymal transition independently of Bcl3-Slug signaling. *FEBS letters*, 589(6):738–743, 2015.

[196] Juliette Sauveur, Louise Conilh, Sabine Beaumel, Kamel Chettab, Lars-Petter Jordheim, Eva-Laure Matera, and Charles Dumontet. Characterization of T-DM1-resistant breast cancer cells. *Pharmacology Research & Perspectives*, 8(4):e00617, 2020.

[197] Sigrid A Langhans. Three-dimensional in vitro cell culture models in drug discovery and drug repositioning. *Frontiers in pharmacology*, 9:6, 2018.

[198] Etienne Y Lasfargues, William G Coutinho, and Ernest S Redfield. Isolation of two human tumor epithelial cell lines from solid breast carcinomas. *Journal of the National Cancer Institute*, 61(4):967–978, 1978.

[199] Jørgen Fogh, Jens M Fogh, and Thomas Orfeo. One hundred and twenty-seven cultured human tumor cell lines producing tumors in nude mice. *Journal of the National Cancer Institute*, 59(1):221–226, 1977.

[200] Chester I Bliss. The toxicity of poisons applied jointly 1. *Annals of applied biology*, 26(3): 585–615, 1939.

[201] S Loewe. Effect of combinations: mathematical basis of problem. *Arch. Exp. Pathol. Pharmakol.*, 114:313–326, 1926.

[202] Bhagwan Yadav, Krister Wennerberg, Tero Aittokallio, and Jing Tang. Searching for drug synergy in complex dose–response landscapes using an interaction potency model. *Computational and structural biotechnology journal*, 13:504–513, 2015.

[203] Aleksandr Ianevski, Anil K Giri, and Tero Aittokallio. SynergyFinder 2.0: visual analytics of multi-drug combination synergies. *Nucleic acids research*, 48(W1):W488–W493, 2020.

[204] Ke-Da Yu, Jiong Wu, Zhen-Zhou Shen, and Zhi-Ming Shao. Hazard of breast cancer-specific mortality among women with estrogen receptor-positive breast cancer after five years from diagnosis: implication for extended endocrine therapy. *The Journal of Clinical Endocrinology & Metabolism*, 97(12):E2201–E2209, 2012.

[205] Niels Bentzon, Maria Düring, Birgitte Bruun Rasmussen, Henning Mouridsen, and Niels Kroman. Prognostic effect of estrogen receptor status across age in primary breast cancer. *International journal of cancer*, 122(5):1089–1094, 2008.

[206] Laurence Lousberg, Joëlle Collignon, and Guy Jerusalem. Resistance to therapy in estrogen receptor positive and human epidermal growth factor 2 positive breast cancers: progress with latest therapeutic strategies. *Therapeutic advances in medical oncology*, 8 (6):429–449, 2016.

[207] C Kent Osborne, Jiang Shou, Suleiman Massarweh, and Rachel Schiff. Crosstalk between estrogen receptor and growth factor receptor pathways as a cause for endocrine therapy resistance in breast cancer. *Clinical cancer research*, 11(2):865s–870s, 2005.

[208] Hitomi Sakai, Junji Tsurutani, Tsutomu Iwasa, Yoshifumi Komoike, Kazuko Sakai, Kazuto Nishio, and Kazuhiko Nakagawa. HER2 genomic amplification in circulating tumor DNA and estrogen receptor positivity predict primary resistance to trastuzumab emtansine (T-DM1) in patients with HER2-positive metastatic breast cancer. *Breast Cancer*, 25(5):605–613, 2018.

[209] Ravi S Narayan, Piet Molenaar, Jian Teng, Fleur MG Cornelissen, Irene Roelofs, Renee Menezes, Rogier Dik, Tonny Lagerweij, Yoran Broersma, Naomi Petersen, et al. A cancer drug atlas enables synergistic targeting of independent drug vulnerabilities. *Nature communications*, 11(1):1–14, 2020.

[210] Pavel Sidorov, Stefan Naulaerts, Jérémy Ariey-Bonnet, Eddy Pasquier, and Pedro J Ballester. Predicting synergism of cancer drug combinations using NCI-ALMANAC data. *Frontiers in chemistry*, 7:509, 2019.

[211] Brent M Kuenzi, Jisoo Park, Samson H Fong, Kyle S Sanchez, John Lee, Jason F Kreisberg, Jianzhu Ma, and Trey Ideker. Predicting drug response and synergy using a deep learning model of human cancer cells. *Cancer Cell*, 38(5):672–684, 2020.

[212] Norma O'Donovan, Annette T Byrne, Aisling E O'Connor, Sharon McGee, William M Gallagher, and John Crown. Synergistic interaction between trastuzumab and EGFR/HER-2 tyrosine kinase inhibitors in HER-2 positive breast cancer cells. *Investigational new drugs*, 29(5):752–759, 2011.

[213] G Brockhoff, B Heckel, E Schmidt-Bruecken, M Plander, F Hofstaedter, A Vollmann, and S Diermeier. Differential impact of Cetuximab, Pertuzumab and Trastuzumab on BT474 and SK-BR-3 breast cancer cell proliferation. *Cell proliferation*, 40(4):488–507, 2007.

[214] Gloria Fuentes, Maurizio Scaltriti, José Baselga, and Chandra S Verma. Synergy between trastuzumab and pertuzumab for human epidermal growth factor 2 (Her2) from colocalization: an in silico based mechanism. *Breast Cancer Research*, 13(3):1–9, 2011.

[215] Jeffrey T Leek. Svaseq: removing batch effects and other unwanted noise from sequencing data. *Nucleic acids research*, 42(21):e161–e161, 2014.

[216] Saranya Chumsri, Zhuo Li, Daniel J Serie, Afshin Mashadi-Hossein, Gerardo Colon-Otero, Nan Song, Katherine L Pogue-Geile, Patrick G Gavin, Soonmyung Paik, Alvaro Moreno-

Aspitia, et al. Incidence of late relapses in patients with HER2-positive breast cancer receiving adjuvant trastuzumab: combined analysis of NCCTG N9831 (Alliance) and NRG Oncology/NSABP B-31. *Journal of Clinical Oncology*, 37(35):3425, 2019.

[217] Adam C Palmer and Peter K Sorger. Combination cancer therapy can confer benefit via patient-to-patient variability without drug additivity or synergy. *Cell*, 171(7):1678–1691, 2017.

[218] Matthew D Cheeseman, Nicola EA Chessum, Carl S Rye, A Elisa Pasqua, Michael J Tucker, Birgit Wilding, Lindsay E Evans, Susan Lepri, Meirion Richards, Swee Y Sharp, et al. Discovery of a chemical probe bisamide (CCT251236): an orally bioavailable efficacious pirin ligand from a heat shock transcription factor 1 (HSF1) phenotypic screen. *Journal of medicinal chemistry*, 60(1):180–201, 2017.

[219] Florian Wegwitz, Evangelos Prokakis, Anastasija Pejkovska, Robyn Laura Kosinsky, Markus Glatzel, Klaus Pantel, Harriet Wikman, and Steven A Johnsen. The histone H2B ubiquitin ligase RNF40 is required for HER2-driven mammary tumorigenesis. *Cell death & disease*, 11(10):1–14, 2020.

[220] Takeda Announces U.S. FDA Breakthrough Therapy Designation Granted for Pevonedistat for the Treatment of Patients with Higher-Risk Myelodysplastic Syndromes (HR-MDS). Published July 30 2020. URL: https://www.takeda.com/newsroom/newsreleases/2020/takeda-announces-u.s.-fda-breakthrough-therapy-designation-granted-for-pevonedistat-for-the-treatment-of-patients-with-higher-risk-myelodysplastic-syndromes-hr-mds/, Accessed: 14-May-2021.

[221] Sonja Thaler, Marcus Schmidt, Sven Roβwag, Gitta Thiede, Arno Schad, and Jonathan P Sleeman. Proteasome inhibitors prevent bi-directional HER2/estrogen-receptor cross-talk leading to cell death in endocrine and lapatinib-resistant HER2+/ER+ breast cancer cells. *Oncotarget*, 8(42):72281, 2017.

[222] Kamil Brzóska and Marcin Kruszewski. Impact of Pirin Protein Expression Level on NF-κB Signaling Pathway Activation. In *AIP Conference Proceedings, volume=1204, number=1, pages=260–261, year=2010, organization=American Institute of Physics*.

[223] Diego Carrillo-Beltrán, Juan P Muñoz, Nahir Guerrero-Vásquez, Rancés Blanco, Oscar León, Vanesca de Souza Lino, Julio C Tapia, Edio Maldonado, Karen Dubois-Camacho, Marcela A Hermoso, et al. Human Papillomavirus 16 E7 Promotes EGFR/PI3K/AKT1/NRF2 Signaling Pathway Contributing to PIR/NF-κB Activation in Oral Cancer Cells. *Cancers*, 12 (7):1904, 2020.

[224] Daniel L Roden, Laura A Baker, Benjamin Elsworth, Chia-Ling Chan, Kate Harvey, Niantao Deng, Sunny Z Wu, Aurelie Cazet, Radhika Nair, and Alexander Swarbrick. Single cell transcriptomics reveals molecular subtype and functional heterogeneity in models of breast cancer. *bioRxiv*, page 282079, 2018.

[225] Benjamin G Neel, Chewei Anderson Chang, Shaowen Jiang, Azin Sayad, Kevin R Brown, Allison Nixon, Avantika Dhabaria, Kwan Ho Tang, Jason Moffat, Beatrix Ueberheide, et al. Ontogeny and Vulnerabilities of Lapatinib Drug-Tolerant Persisters in HER2+ Breast Cancer. *bioRxiv*, 2020.

[226] Merck KGaA. Merck Announces Fourth-Quarter and Full-Year 2020 Financial Results . 2020.

[227] Sherene Loi, Anita Giobbie-Hurder, Andrea Gombos, Thomas Bachelot, Rina Hui, Giuseppe Curigliano, Mario Campone, Laura Biganzoli, Hervé Bonnefoi, Guy Jerusalem, et al. Pembrolizumab plus trastuzumab in trastuzumab-resistant, advanced, HER2-positive breast cancer (PANACEA): a single-arm, multicentre, phase 1b–2 trial. *The Lancet Oncology*, 20(3):371–382, 2019.

[228] Synergistic tumoricidal effect of combined hPD-L1 vaccine and HER2 gene vaccine, author=Zhang, Wangqian and Wang, Shuning and Gu, Jintao and Gao, Yuan and Wang, Zhaowei and Zhang, Kuo and Mu, Nan and Huang, Tonglie and Li, Weina and Hao, Qiang

and others, journal=Biochemical and biophysical research communications, volume=497, number=1, pages=394–400, year=2018, publisher=Elsevier.

[229] Tiziana Triulzi, Viola Regondi, Loris De Cecco, Maria Rosa Cappelletti, Martina Di Modica, Biagio Paolini, Pier Luigi Lollini, Serena Di Cosimo, Lucia Sfondrini, Daniele Generali, et al. Early immune modulation by single-agent trastuzumab as a marker of trastuzumab benefit. *British journal of cancer*, 119(12):1487–1494, 2018.

[230] Elin Karlsson, Ulla Delle, Anna Danielsson, Björn Olsson, Frida Abel, Per Karlsson, and Khalil Helou. Gene expression variation to predict 10-year survival in lymph-node-negative breast cancer. *Bmc Cancer*, 8(1):1–14, 2008.

[231] Victor Aedo-Aguilera, Diego Carrillo-Beltrán, Gloria M Calaf, Juan P Muñoz, Nahir Guerrero, Julio C Osorio, Julio C Tapia, Oscar León, Hector R Contreras, and Francisco Aguayo. Curcumin decreases epithelial-mesenchymal transition by a Pirin-dependent mechanism in cervical cancer cells. *Oncology reports*, 42(5):2139–2148, 2019.

[232] Karina G Thomsen, Mikkel G Terp, Rikke R Lund, Rolf Søkilde, Daniel Elias, Martin Bak, Thomas Litman, Hans C Beck, Maria B Lyng, and Henrik J Ditzel. miR-155, identified as anti-metastatic by global miRNA profiling of a metastasis model, inhibits cancer cell extravasation and colonization in vivo and causes significant signaling alterations. *Oncotarget*, 6 (30):29224, 2015.

[233] Xiaoyu Xiang, Xiaoying Zhuang, S Ju, S Zhang, H Jiang, J Mu, L Zhang, D Miller, W Grizzle, and HG Zhang. miR-155 promotes macroscopic tumor formation yet inhibits tumor dissemination from mammary fat pads to the lung by preventing EMT. *Oncogene*, 30(31): 3440–3453, 2011.

[234] Matthew J Hangauer, Vasanthi S Viswanathan, Matthew J Ryan, Dhruv Bole, John K Eaton, Alexandre Matov, Jacqueline Galeas, Harshil D Dhruv, Michael E Berens, Stuart L Schreiber, et al. Drug-tolerant persister cancer cells are vulnerable to GPX4 inhibition. *Nature*, 551(7679):247–250, 2017.

[235] Tracy E Strecker, Qiang Shen, Yun Zhang, Jamal L Hill, Yuxin Li, Chunyu Wang, Hee-Tae Kim, Tona M Gilmer, Krystal R Sexton, Susan G Hilsenbeck, et al. Effect of lapatinib on the development of estrogen receptor–negative mammary tumors in mice. *Journal of the National Cancer Institute*, 101(2):107–113, 2009.

[236] Early and locally advanced breast cancer overview. *National Institute for Health and Care Excellence (NICE), United Kingdom*. URL: https://pathways.nice.org.uk/pathways/early-and-locally-advanced-breast-cancer, Accessed: 03-April-2021.

[237] Francisco P Branco, Duarte Machado, Filipa F Silva, Saudade André, Ana Catarino, Rosa Madureira, João M Pinto, João P Godinho, Pedro D Simões, Margarida Brito, et al. Loss of HER2 and disease prognosis after neoadjuvant treatment of HER2+ breast cancer. *American journal of translational research*, 11(9):6110, 2019.

[238] Paula R Pohlmann, Ingrid A Mayer, and Ray Mernaugh. Resistance to trastuzumab in breast cancer. *Clinical cancer research*, 15(24):7479–7491, 2009.

[239] Lola E Navas and Amancio Carnero. NAD+ Metabolism, stemness, the immune response, and cancer. *Signal Transduction and Targeted Therapy*, 6(1):1–20, 2021.

[240] Alba Luengo, Zhaoqi Li, Dan Y Gui, Lucas B Sullivan, Maria Zagorulya, Brian T Do, Raphael Ferreira, Adi Naamati, Ahmed Ali, Caroline A Lewis, et al. Increased demand for NAD+ relative to ATP drives aerobic glycolysis. *Molecular Cell*, 81(4):691–707, 2021.

[241] Pamela Becherini, Irene Caffa, Francesco Piacente, Patrizia Damonte, Valerio G Vellone, Mario Passalacqua, Andrea Benzi, Tommaso Bonfiglio, Daniele Reverberi, Amr Khalifa, et al. SIRT6 enhances oxidative phosphorylation in breast cancer and promotes mammary tumorigenesis in mice. *Cancer & Metabolism*, 9(1):1–16, 2021.

[242] Sonam Sinha, Sonal Sharma, Jaykant Vora, and Neeta Shrivastava. Emerging role of sirtu-

ins in breast cancer metastasis and multidrug resistance: Implication for novel therapeutic strategies targeting sirtuins. *Pharmacological Research*, page 104880, 2020.

[243] Sun M Hong, Sung W Hwang, Taejun Wang, Chang W Park, Yeon-Mi Ryu, Jin-Hak Jung, Ji H Shin, Sang-Yeob Kim, Jong L Lee, Chan W Kim, et al. Increased nicotinamide adenine dinucleotide pool promotes colon cancer progression by suppressing reactive oxygen species level. *Cancer science*, 110(2):629–638, 2019.

[244] Yuzheng Zhao, Aoxue Wang, Yejun Zou, Ni Su, Joseph Loscalzo, and Yi Yang. In vivo monitoring of cellular energy metabolism using SoNar, a highly responsive sensor for NAD+/NADH redox state. *Nature protocols*, 11(8):1345, 2016.

[245] YuZheng ZHAO, Zhuo ZHANG, and Yi YANG. Monitoring intracellular redox metabolism with genetically encoded fluorescent sensors. *SCIENTIA SINICA Vitae*, 47(5):508–521, 2017.

[246] Peter F Favreau, Jiaye He, Daniel A Gil, Dustin A Deming, Jan Huisken, and Melissa C Skala. Label-free redox imaging of patient-derived organoids using selective plane illumination microscopy. *Biomedical optics express*, 11(5):2591–2606, 2020.

[247] Antonio F Santidrian, Akemi Matsuno-Yagi, Melissa Ritland, Byoung B Seo, Sarah E LeBoeuf, Laurie J Gay, Takao Yagi, Brunhilde Felding-Habermann, et al. Mitochondrial complex I activity andNAD+/NADH balance regulate breast cancer progression. *The Journal of clinical investigation*, 123(3):1068–1081, 2013.

[248] Maryann Giel-Moloney, Daniela S Krause, Gang Chen, Richard A Van Etten, and Andrew B Leiter. Ubiquitous and uniform in vivo fluorescence in ROSA26-EGFP BAC transgenic mice. *genesis*, 45(2):83–89, 2007.

[249] Rongkun Tao, Yuzheng Zhao, Huanyu Chu, Aoxue Wang, Jiahuan Zhu, Xianjun Chen, Yejun Zou, Mei Shi, Renmei Liu, Ni Su, et al. Genetically encoded fluorescent sensors reveal dynamic regulation of NADPH metabolism. *Nature methods*, 14(7):720–728, 2017.

[250] Huai-Qiang Ju, Jin-Fei Lin, Tian Tian, Dan Xie, and Rui-Hua Xu. NADPH homeostasis in cancer: functions, mechanisms and therapeutic implications. *Signal Transduction and Targeted Therapy*, 5(1):1–12, 2020.

[251] Xiajing Fan, Hongru Liu, Miao Liu, Yuanyuan Wang, Li Qiu, and Yanfen Cui. Increased utilization of fructose has a positive effect on the development of breast cancer. *PeerJ*, 5: e3804, 2017.

[252] Tsutomu Miyamoto, Keiko Ishii, Ryouichi Asaka, Akihisa Suzuki, Akiko Takatsu, Hiroyasu Kashima, and Tanri Shiozawa. Immunohistochemical expression of keratan sulfate: a possible diagnostic marker for carcinomas of the female genital tract. *Journal of clinical pathology*, 64(12):1058–1063, 2011.

[253] Joo Sang Lee, Lital Adler, Hiren Karathia, Narin Carmel, Shiran Rabinovich, Noam Auslander, Rom Keshet, Noa Stettner, Alon Silberman, Lilach Agemy, et al. Urea cycle dysregulation generates clinically relevant genomic and biochemical signatures. *Cell*, 174(6): 1559–1570, 2018.

[254] Food and US Drug Administration. Drug Administration: FDA approves fam-trastuzumab deruxtecan-nxki for unresectable or metastatic HER2-positive breast cancer, 2021, 2021.

[255] Gerald Clamon, James Herndon, Jeffrey Kern, Ramaswamy Govindan, Jennifer Garst, Dorothy Watson, and Mark Green. Lack of trastuzumab activity in nonsmall cell lung carcinoma with overexpression of erb-B2: 39810: a phase II trial of Cancer and Leukemia Group B. *Cancer: Interdisciplinary International Journal of the American Cancer Society*, 103(8): 1670–1675, 2005.

[256] KL Jhaveri, XV Wang, V Makker, S-W Luoh, EP Mitchell, JA Zwiebel, E Sharon, RJ Gray, S Li, LM McShane, et al. Ado-trastuzumab emtansine (T-DM1) in patients with HER2-amplified tumors excluding breast and gastric/gastroesophageal junction (GEJ) adenocar-

cinomas: results from the NCI-MATCH trial (EAY131) subprotocol Q. *Annals of Oncology*, 30(11):1821–1830, 2019.

[257] K Nakagawa, M Nagasaka, E Felip, J Pacheco, C Baik, Y Goto, A Saltos, B Li, H Udagawa, S Gadgeel, et al. OA04. 05 Trastuzumab Deruxtecan in HER2-Overexpressing Metastatic Non-Small Cell Lung Cancer: Interim Results of DESTINY-Lung01. *Journal of Thoracic Oncology*, 16(3):S109–S110, 2021.

[258] Shanu Modi, Shoichiro Ohtani, Caleb Lee, Yibin Wang, Kapil Saxena, and David A Cameron. Abstract OT1-07-02: A phase 3, multicenter, randomized, open-label trial of [fam-] trastuzumab deruxtecan (T-DXd; DS-8201a) vs investigator's choice in HER2-low breast cancer (DESTINY-Breast04), 2020.

[259] Aditya Bardia, Carlos Barrios, Rebecca Dent, Xichun Hu, Joyce O'Shaughnessy, Kan Yonemori, Annie Darilay, Sarice Boston, Yufan Liu, Gargi Patel, et al. Abstract OT-03-09: Trastuzumab deruxtecan (T-DXd; DS-8201) vs investigator's choice of chemotherapy in patients with hormone receptor-positive (HR+), HER2 low metastatic breast cancer whose disease has progressed on endocrine therapy in the metastatic setting: A randomized, global phase 3 trial (DESTINY-Breast06), 2021.

[260] Daniel Eiger, Elisa Agostinetto, Evandro de Azambuja, et al. The Exciting New Field of HER2-Low Breast Cancer Treatment. *Cancers*, 13(5):1015, 2021.

[261] Upregulation of pirin expression by chronic cigarette smoking is associated with bronchial epithelial cell apoptosis, author=Gelbman, Brian D and Heguy, Adriana and O'Connor, Timothy P and Zabner, Joseph and Crystal, Ronald G, journal=Respiratory research, volume=8, number=1, pages=1–13, year=2007, publisher=Springer.

[262] Rajan Radha Rasmi, Kunnathur Murugesan Sakthivel, and Chandrasekaran Guruvayoorappan. NF-κB inhibitors in treatment and prevention of lung cancer. *Biomedicine & Pharmacotherapy*, 130:110569, 2020.

[263] Lijun Gu, Zhiyan Wang, Jing Zuo, Hongmei Li, and Lin Zha. Prognostic significance of NF-κB expression in non-small cell lung cancer: A meta-analysis. *PloS one*, 13(5):e0198223, 2018.

[264] Collin M Blakely, Evangelos Pazarentzos, Victor Olivas, Saurabh Asthana, Jenny Jiacheng Yan, Irena Tan, Gorjan Hrustanovic, Elton Chan, Luping Lin, Dana S Neel, et al. NF-κB-activating complex engaged in response to EGFR oncogene inhibition drives tumor cell survival and residual disease in lung cancer. *Cell reports*, 11(1):98–110, 2015.

[265] Young Ho Seo. Discovery of 2, 4-dimethoxychalcone as a Hsp90 inhibitor and its effect on iressa-resistant non-small cell lung cancer (NSCLC). *Archives of pharmacal research*, 38 (10):1783–1788, 2015.

[266] Tsuyoshi Ueno, Kazunori Tsukuda, Shinichi Toyooka, Midori Ando, Munenori Takaoka, Junichi Soh, Hiroaki Asano, Yuho Maki, Takayuki Muraoka, Norimitsu Tanaka, et al. Strong anti-tumor effect of NVP-AUY922, a novel Hsp90 inhibitor, on non-small cell lung cancer. *Lung cancer*, 76(1):26–31, 2012.

[267] Sho Watanabe, Yasushi Goto, Hiroyuki Yasuda, Takashi Kohno, Noriko Motoi, Yuichiro Ohe, Hiroyoshi Nishikawa, Susumu S Kobayashi, Kazuyoshi Kuwano, and Yosuke Togashi. HSP90 inhibition overcomes EGFR amplification-induced resistance to third-generation EGFR-TKIs. *Thoracic cancer*, 12(5):631–642, 2021.

[268] Sun Mi Kim, Mi Ran Yun, Yun Kyoung Hong, Flavio Solca, Joo-Hang Kim, Hyun-Jung Kim, and Byoung Chul Cho. Glycolysis inhibition sensitizes non–small cell lung cancer with T790M mutation to irreversible EGFR inhibitors via translational suppression of mcl-1 by AMPK activation. *Molecular cancer therapeutics*, 12(10):2145–2156, 2013.

[269] Ji Hye Kim, Boas Nam, Yun Jung Choi, Seon Ye Kim, Jung-Eun Lee, Ki Jung Sung, Woo Sung Kim, Chang-Min Choi, Eun-Ju Chang, Jae Soo Koh, et al. Enhanced glycolysis supports cell survival in EGFR-mutant lung adenocarcinoma by inhibiting autophagy-mediated EGFR degradation. *Cancer research*, 78(16):4482–4496, 2018.

[270] Daniel R Ciocca and Stuart K Calderwood. Heat shock proteins in cancer: diagnostic, prognostic, predictive, and treatment implications. *Cell stress & chaperones*, 10(2):86, 2005.

[271] Mahmoud Ghandi, Franklin W Huang, Judit Jané-Valbuena, Gregory V Kryukov, Christopher C Lo, E Robert McDonald, Jordi Barretina, Ellen T Gelfand, Craig M Bielski, Haoxin Li, et al. Next-generation characterization of the cancer cell line encyclopedia. *Nature*, 569 (7757):503–508, 2019.

[272] Anders Lundin, Michelle J Porritt, Himjyot Jaiswal, Frank Seeliger, Camilla Johansson, Abdel Wahad Bidar, Lukas Badertscher, Sandra Wimberger, Emma J Davies, Elizabeth Hardaker, et al. Development of an ObLiGaRe Doxycycline Inducible Cas9 system for preclinical cancer drug discovery. *Nature communications*, 11(1):1–16, 2020.

[273] Lisa Liu, Lei Yu, Zhichao Li, Wujiao Li, and WeiRen Huang. Patient-derived organoid (PDO) platforms to facilitate clinical decision making. *Journal of Translational Medicine*, 19(1):1–9, 2021.

[274] Alexandre F Aissa, Abul BMMK Islam, Majd M Ariss, Cammille C Go, Alexandra E Rader, Ryan D Conrardy, Alexa M Gajda, Carlota Rubio-Perez, Klara Valyi-Nagy, Mary Pasquinelli, et al. Single-cell transcriptional changes associated with drug tolerance and response to combination therapies in cancer. *Nature communications*, 12(1):1–25, 2021.

[275] Qingfei Wang, Ian H Guldner, Samantha M Golomb, Longhua Sun, Jack A Harris, Xin Lu, and Siyuan Zhang. Single-cell profiling guided combinatorial immunotherapy for fast-evolving CDK4/6 inhibitor-resistant HER2-positive breast cancer. *Nature communications*, 10(1):1–12, 2019.

[276] Michael I Love, Simon Anders, Vladislav Kim, and Wolfgang Huber. RNA-Seq workflow: gene-level exploratory analysis and differential expression. *F1000Research*, 4, 2019.

List of Tables

1 Breast cancer sub-types 28
2 Currently approved HER2-targeted therapies, along with the mechanism of action, the therapeutic setting the drug is used in, year of original regulatory approval, and the key data that led to that approval 35
3 Ongoing or planned phase II or III clinical trials in the neoadjuvant or adjuvant setting of HER2-targeted agents in combination with non-HER2-targeted agents 46

4 Table of chosen lapatinib and EMBL-703625 concentrations that were used in monotherapy and combination therapy for transcriptomic and consecutive experiment treatments. 71
5 BT-474 cells: GO-terms and corresponding cancer Hallmarks, as per Mészáros et al. (2021)[102], for significantly de-regulated GO-terms 84
6 SK-BR3 cells: GO-terms and corresponding cancer Hallmarks, as per Mészáros et al. (2021)[102], for significantly de-regulated GO-terms. 85
7 Future experimental directions with regard to the data discussed in Section 2.2 . . 88
8 Future experimental directions with regard to the data discussed in Section 2.3 . . 96
9 Future experimental directions with regard to the data discussed in Section 2.4 . . 102
10 Future experimental directions with regard to the data discussed in Section 2.6 . . 114

11 Showing typical restriction digestion reaction conditions 167
12 Ligation reaction conditions 167
13 Primer sequences used in mouse genotyping 171

14 De-regulated genes and networks (see section 2.2 for details on how significance was calculated) in BT-474 cells treated with 1µM lapatinib. 189
15 De-regulated genes and networks (see section 2.2 for details on how significance was calculated) in BT-474 cells treated with 1µM EMBL-703625 192
16 De-regulated genes and networks (see section 2.2 for details on how significance was calculated) in BT-474 cells treated with 1µM lapatinib and 1µM EMBL-703625 202
17 De-regulated genes and networks (see section 2.2 for details on how significance was calculated) in SK-BR3 cells treated with 0.2µM lapatinib and 1µM EMBL-703625208
18 De-regulated genes and networks (see section 2.2 for details on how significance was calculated) in SK-BR3 cells treated with 0.2µM lapatinib 209
19 De-regulated genes and networks (see section 2.2 for details on how significance was calculated) in SK-BR3 cells treated with 1µM EMBL-703625 212

List of Figures

1 The hallmarks of cancer, with examples of sub-hallmarks 23
2 Cross sections showing the anatomy of the breast, Terminal Ductal Lobular Units and the cell types in a duct or lobule 26
3 Different stages of intitial breast cancer development, originating from the mammary duct 27
4 The HER-family of receptors, showing how protein domains interact with ligands to induce dimer formation. 31
5 The binding and mechanisms of action of currently licensed HER2-targeted therapeutics 36
6 Mechanisms of drug resistance to currently licensed therapeutics 40
7 Top and side view of pirin (crystal structure) 47
8 Comparison of results found from the Jechlinger Lab (Radic-Shechter *et al.* (2020)[175] with transcriptomic results found on HeLa cells by the EMBL Chemical Biology Core Facility 49
9 BT-474 and SK-BR3 organoids grown for 14 days in matrigel. 53
10 The transgenic, doxycycline inducible mouse experimental system utilised by the Jechlinger Lab 54

11 Changes in cell viability measured over 72 hours in BT-474 and SK-BR3 cells, comparing singular drug treatment to combination treatment. 58
12 Representations of Bliss Independence, Loewe Additivity and ZIP synergy models of drug interaction testing 60
13 Schematic of how viability data was processed and outputted as synergy landscapes 63
14 Heat-maps of relative cell viability (using the Promega CellTitre Glo^{TM} 3D cell viability assay) and toxicity (using the CellTox^{TM} green fluorescent cytotoxicity assay) for BT-474 and SK-BR3 cells treated with varying concentrations of lapatinib and EMBL-703625 66
15 ZIP Synergy landscape of Lapatinib and EMBL-703625 for BT-474 and SK-BR3 68
16 Schematic of transcriptomic experiment 72
17 PCA plot of VST transformed transcriptomic data and sample-sample distances for BT-474 and SK-BR3 cells treated with lapatinib and/or EMBL-703625, or vehicle (DMSO) 75
18 Gene expression changes (relative to non-treated) for the top 500 de-regulated genes for BT-474 or SK-BR3 cells treated with EMBL-703625, Lapatinib or a combination of both 79

19 Venn diagrams of the number significantly de-regulated clusters ($p<0.01$) for BT-474 or SK-BR3 cells treated with Lapatinib, EMBL-703625, or a combination of both, with the corresponding representative terms for each cluster listed below . . . 82
20 Schematic of experimental design for BT-474 and SK-BR3 re-growth removal following EMBL-703625/Lapatinib monotherapy or combination therapy . . . 89
21 Projected and stitched ScanR images showing re-growth following treatment removal in BT-474 and SK-BR3 cells. . . . 92
22 Time lapse of BT-474 cells re-growing in the presence of 2.3µM of EMBL-703625 . . . 93
23 BT-474 and SK-BR3 ZIP Synergy landscape of cells co-treated with oxamate and Lapatinib, and of cells co-treated with oxamate and EMBL-703625 100
24 Schematic of experiments performed on non-neoplastic or induced-neoplastic mouse mammary gland cells . . . 103
25 Dose response curves for each of the four mice used in the experiments, in tumor and never induced cells treated with either lapatinib or EMBL-703625 105
26 Dose response curves of Never Induced (Normal) or Induced (Tumor) cells at varying concentrations of lapatinib and EMBL-703625 . . . 106
27 Schematic of consecutive treatment experiments . . . 110
28 Viability readings (percentage normalised to vehicle treated) for BT-474 and SK-BR3 cells treated with EMBL-703625 that have been pre-treated for 72h with either vehicle (DMSO), Lapatinib or EMBL-703625. . . . 111
29 Viability readings (percentage normalised to vehicle treated) for BT-474 and SK-BR3 cells treated with Lapatinib that have been pre-treated for 72h with either vehicle (DMSO), Lapatinib or EMBL-703625. . . . 112
30 SoNar sensor diagram, and excitation peaks, adapted from Zhao *et al*. (2015)[1] . . . 116
31 A schematic, adapted from Zhao *et al*., (2017)[245] of how cpYFP can be used to normalise the ratio of SoNar to account for pH or other imaging artefacts . . . 117
32 SoNar plasmid . . . 118
33 Sample mouting for the Leica SP8 DLS . . . 120
34 Workflow of the two image analysis pipelines for the Leica SP8 DLS . . . 121
35 Processing of raw Leica SP8 DLS data with the ImageJ plug in, BigDataProcessor 2 . . . 123
36 Creation and visualisation of ratio-metric images using the Lazy Ratio Viewer (ImageJ plug-in) . . . 124
37 3D mean blurring of light sheet images to reduce noise and correct for image artefacts . . . 125
38 Histogram generation from 3-D ratio images . . . 126
39 *Figure continued on next page.* . . . 128
39 Ratio changes in SK-BR3 cells expressing the SoNar sensor after the addition of Oxamate . . . 129
40 SK-BR3 cells expressing the SoNar sensor, treated with 1.3µM lapatinib . . 130
40 The NAD+/NADH ratio of SK-BR3 cells treated with Combination therapy, or Lapatinib or EMBL-703625 monotherapy at 0, 10, 20 and 25 hours . . . 133
41 3D deconvolution of SoNar expressing SK-BR3 cells taken with excitation at 405nm . . . 135
42 Significantly de-regulated genes in sugar, amino acid, mitophagy, and TGF-β and FoxO signalling pathways during tumorigenesis and tumor de-induction 144

43 Overlap of significantly de-regulated Compound-Reaction-Enzyme-Gene networks between tumor cells (5 days on DOX) and residual cells (7 days off DOX) and Compound-Reaction-Enzyme-Gene networks unique to residual cells 150

S.1 The CellTiter Glo (a) and CellTox Green Cytotoxicity (b) Assays 178
S.2 Supplementary figure continued on next page 179
S.2 Non-interpolated ZIP synergy landscapes for BT-474 or SK-BR3 cells treated with lapatinib and EMBL-703625 180
S.3 3D Image projection pipeline for high-throughput ScanR data. 181
S.4 Stitching of projected images to obtain a whole-well overview of a 96-well plate. 182
S.5 Batch correction of transcriptomic data using limma 182
S.6 Individual effects on cell viability of lapatinib and EMBL-703625 treatment, at different concentrations, for mouse 1 183
S.7 Individual effects on cell viability of lapatinib and EMBL-703625 treatment, at different concentrations, for mouse 2. 183
S.8 Individual effects on cell viability of lapatinib and EMBL-703625 treatment, at different concentrations, for mouse 3. 184
S.9 Individual effects on cell viability of lapatinib and EMBL-703625 treatment, at different concentrations, for mouse 4 184
S.10 pLOVE lentiviral vector containing cpYFP under the control of the CMV promoter 185
S.11 SK-BR3 expressing SoNar or cpYFP treated at 1.3µM 185
S.12 SK-BR3 expressing SoNar or cpYFP treated with 1µM EMBL-703625 and 0.2µM lapatinib 186

List of Abbreviations

E. coli *Escherichia coli*. 19, 167

ADC Antibody-drug Conjugate. 34, 35

ALMF Advanced Light Microscopy Facility. 118, 122–124, 133, 135, 138

ANOVA Analysis of variance. 110–112

ATP Adenosine triphosphate. 42, 115

BRCA1 BReast CAncer Gene 1. 25

BRCA2 BReast CAncer Gene 2. 25

CBCF Chemical Biology Core Facility. 16, 48, 50, 56, 97, 101, 102, 156, 158, 159

CMV Human cytomegalovirus. 168

cpYFP circularly permutated Yellow Flourescent Protein. 17, 19, 116–120, 123, 125–127, 129, 130, 136–138, 168–170, 236

DCIS Ductal Carcinoma In Situ. 27

DFS Disease Free Survival. 35

DLS Digital Light Sheet. 17, 19, 118–121, 123, 133–135, 138, 169, 236

DMSO Dimethyl sulfoxide. 63, 71, 77, 84, 85, 109–113, 235, 236

DNA Deoxyribose Nucleic Acid. 166–168, 171

EGFR Epidermal Growth Factor Receptor (also known as HER1). 30–32, 35, 43, 44, 48, 156, 158, 159, 161, 163

EMBL European Molecular Biology Laboratory. 18, 19, 48–50, 56, 70, 101, 102, 118, 122–124, 130, 131, 135, 138, 156, 158–160, 168, 170, 171, 173–175, 235

EMT Epithelial to mesenchymal transition. 95

ER Estrogen Receptor. 25, 28, 40, 46, 69

FDA Food and Drug Administration. 34, 35, 87, 159, 162

GCMS Gas chromatography mass spectrometry. 19, 147, 148, 150, 175

HER1 Human Epidermal Growth Factor Receptor 1 (also known as EGFR). 30, 31

HER2 Human Epidermal Growth Factor Receptor 2. 15–19, 24, 25, 28–48, 50–52, 56, 69, 70, 85–88, 93–95, 97, 98, 101, 103, 107, 111–113, 129, 140, 152, 153, 156–158, 160–163, 233, 235

HER3 Human Epidermal Growth Factor Receptor 3. 30–32, 43

HER4 Human Epidermal Growth Factor Receptor 4. 30, 31

HR Hazard Ratio. 35

HR+ Hormone Receptor (Estrogen and/or Progesterone Receptor) positive. 93, 94, 157

HSP Heat Shock Protein. 15, 32, 41, 43, 87

IDC Invasive Ductal Carcinoma. 27

LCIS Lobular Carcinoma In Situ. 27

LCMS Liquid chromatography mass spectrometry. 19, 147, 148, 150, 175

MMTV Mouse mammary tumor virus. 44, 54, 103, 171

NAD+ Nicotinamide adenine dinucleotide (oxidised form). 17, 18, 115, 116, 120, 125, 126, 129, 130, 133, 136–138, 236

NADH Nicotinamide adenine dinucleotide (reduced form). 17, 18, 115, 116, 120, 125, 126, 129, 130, 133, 136–138, 236

NADP+ Nicotinamide adenine dinucleotide phosphate (oxidised form). 138

NADPH Nicotinamide adenine dinucleotide phosphate (reduced form). 138

NF-$\kappa\beta$ Nuclear factor kappa-light-chain-enhancer of activated β-cells. 42, 47, 50, 56, 80, 84, 87, 88, 156, 158, 159

nm Nanometer. 118, 124, 126, 134, 135, 236

NSCLC Non-small cell lung cancer. 157–159, 161

ORR Overall Response Rate. 35

PBS Phosphate buffered saline. 170, 172, 173

PCR Polymerase chain reaction. 170, 171

pCR Pathological Complete Response. 35, 38, 46

PFS Progression Free Survival. 35

PI3K Phosphoinositide 3-kinase. 32, 40, 43, 44

PR Progesterone Receptor. 28

PSF Point Spread Function. 133, 134

RNA Ribose nucleic acid. 19, 174

RPM Revolutions per minute. 166, 168, 170, 172, 173

rSAP recombinant Shrimp Alkaline Phosphatase. 167

rtTA Reverse tetracycline transactivator. 44, 54, 103, 171

SEM Standard error of the mean. 105, 106

SoNar Sensor of NAD(H) redox. 17–19, 116–120, 123, 125, 126, 129, 130, 133, 135–138, 168–170, 236

SVA Surrogate Variable Analysis. 76

TDLU Terminal Ductal Lobular Unit. 26, 27

TetO Tetracycline Operon. 54, 103

TKI Tyrosine Kinase Inhibitor. 35, 52, 158, 159, 161, 162

TNBC Triple Negative Breast Cancer. 28, 29

ZIP Zero Interaction Potency. 60–63, 66–68, 235